

ELECTRICALLY CONDUCTIVE BACTERIAL CELLULOSE FOR TISSUE- ENGINEERED NEURAL INTERFACES

By

Ana Margarida Rodrigues Rebelo

MSc

A Doctoral Thesis

Submitted in partial fulfilment of the requirements

for the award of

Doctor of Philosophy (PhD) of Loughborough University

December 2018

© by Ana R. Rebelo, 2018

Keywords

Bacterial cellulose, functionalisation, poly(4-vinylniline)/polyaniline bilayer, carbon nanotubes, bioelectronic neural interfaces, tissue engineering.

Abstract

Bacterial cellulose (BC) with its high crystallinity, tensile strength, degree of polymerisation, and water holding capacity (98%) becomes increasingly attractive as 3D nanofibrillar material for biomedical applications. Such multi-scale fibrillary BC networks can be potentially functionalised with electrically conductive moieties to facilitate the conductive properties required for various smart biomedical devices, in particular, in the construction of bioelectronic neural interfaces.

In this thesis, BC fibres are chemically modified with poly(4-vinylaniline) (PVAN) interlayer for further enhancement of electrical conductivity and cell viability of subsequent polyaniline (PANI) coatings as a bilayer grafted BC nanocomposite. This functional poly(4-vinylaniline)/polyaniline (PVAN/PANI) bilayer can be efficiently anchored onto BC fibrils through successive surface-initiated atom transfer radical polymerisation and *in situ* chemical oxidative polymerisation. PVAN is found to have promoted the formation of a uniform PANI layer with 1D nanofiber- and nanorod-like supramolecular structures, with an overall augmentation of PANI yield, hence further improved electrical performance. Compositional and microstructural analysis reveals such a PVAN/PANI bilayer with a thickness up to $\sim 2 \mu\text{m}$ on BC formed through a significant growth of PANI with rough surface morphology due to the insertion of PVAN, which has improved the functional properties of the BC nanocomposites. Successful impregnation of both layers onto BC fibrils was corroborated with systematic microstructural and chemical analysis. The solid-state electrical conductivity of such synthesised BC nanocomposites with PVAN interlayer reaches as high as $(4.5 \pm 2.8) \times 10^{-2} \text{ S.cm}^{-1}$ subject to the amounts of PVAN chemically embraced. Electrochemical examination evinces the switching in the electrochemical behaviour of BC/PVAN/PANI nanocomposites at $-0.70/0.74 \text{ V}$ (at 100 mV.s^{-1} scan rate) due to the existence of PANI, where the maximal electrical performance can be achieved at charge transfer resistance of as low as 21Ω and capacitance of as high as $39 \mu\text{F}$. Both electrochemical and mechanical properties can be tailored onto an incomplete BC dehydration, where a mathematical model is herein developed to predict BC water loss accordingly. BC/PVAN/PANI nanocomposites are thermally stable up to $200 \text{ }^\circ\text{C}$.

Furthermore, further improvement of the electrical conductivity has been achieved through grafting Carbon Nano Tubes (CNTs) into the BC/PVAN/PANI nanocomposites, where the interactions between PANI and CNTs present new electrochemical characteristics with enhanced capacity. PANI/CNTs coatings with a nanorod-like morphology can promote the efficient ions diffusion and charge transfer, resulting in the increased electrical conductivity up to $(1.0\pm 0.3)\times 10^{-1}$ S.cm⁻¹. An escalating amplification of the double charge capacity to ~54 mF of the CNTs grafted BC nanocomposites was also detected through electrochemical analysis. In addition, the thermal stability of CNTs grafted BC/PVAN/PANI nanocomposites are improved, and they become stable up to 234 °C.

Cytocompatibility tests conducted using two neuronal cell linages show non-cytotoxic effects for PC-12 Adh cells and SVZ neural stem cells, confirming cell viability that can be over 80 % and neuronal differentiation capability of the electrically functionalised BC-based nanocomposite membranes, which can induce neurites outgrowth up to 115 ± 24 μm long. These voltage-sensible nanocomposites can hence interact with neural cells, thereby significantly stimulate specialised response. These findings pave the path to the new tissue engineered neural interfaces which embraces electronic functions into the tissue regeneration, to enable full functional neural tissue recovery.

Acknowledgements

The author would like to acknowledge the PhD research studentship funded through a Loughborough University internally Mini-CDT scheme under the research topic of ‘Intelligent, adaptable electronics for healthcare and wellbeing’. The PhD research was also partially sponsored by a Marie Curie International Research Staff Exchange Scheme Project of the 7th European Community Framework Program (Grant No. PIRSES-GA-2010-559 269113), entitled “Micro-Multi-Material Manufacture to Enable Multifunctional Miniaturized Devices (M6)”. The outcomes of this research project resulted from joined efforts of solid international collaborations in the partnership with Huazhong University of Science and Technology (HUST) China, University of Applied Sciences of Kaiserslautern (FHKL) Germany, and National Institute of advanced Industrial Science and Technology (AIST) Japan. It was mainly performed at Wolfson School of Mechanical, Electrical and Manufacturing Engineering and at the Centre for Biological Engineering, Holywell Park, of Loughborough University (LU), and partially at Department of Biomedical Engineering of Huazhong University of Science and Technology (HUST), Wuhan, PR China and Departments of Biotechnology and of Microsystems and Technology of University of Applied Sciences of Kaiserslautern (FHKL), Zweibrücken, Germany.

This work would not have been possible without the generous and disinterested help of many people I had the pleasure to come across, who I believe they contribute to become the World a better place to live. Primarily, I would like to express my deepest gratitude to my beloved supervisors, Prof. Changqing Liu and Dr. Yang Liu, of Wolfson School of Mechanical, Electrical and Manufacturing Engineering of LU who gave me the opportunity to undertake this research. For all their guidance, efficient supervision and support throughout these four years, as well as for their valuable suggestions and constant encouragement, which endowed me to develop myself at both scientific, professional and personal levels to become a better person every day. To such inestimable persons, I am eternally grateful.

I would like to express my deepest gratitude for the generous financial support, assistance, comments and valuable suggestions of Prof. Guang Yang from the Department of Biomedical Engineering of HUST, Wuhan, PR China, and Prof. Dr.

med. Karl-Herbert Schäfer from Department of Biotechnology, and Prof. Dr. Monika Saumer from Department of Microsystems and Technology, of FHKL, Zweibrücken, Germany, who kindly welcome me with the opportunity to perform crucial and constructive research in their facilities over a five months period, which can be clearly recognised with the listed publications and submissions. These fruitful collaborations provided me with some of the most enriching experiences of my life I am greatly thankful. I also wish to express my appreciation to Prof. Andrew Archer from the Mathematical Department of LU who gently contributed to this work with his knowledge, comments, availability and warm character, that render one scientific publication.

Great deals to all my office and laboratory colleagues, as well as technical staff, based in UK, China and Germany, who provided me with a friendly and warm environment to work, with a continuous and constructive exchange knowledge and experience. In particular, I would like also to thank Dr. Xiuli Chen from HUST for her technical inputs and assistance for initial experimental procedures. To Dr. Lamboni Lallepak from HUST, who shared her knowledge and expertise with during my time in China, and also for her valuable comments, suggestions, and support. Mr. Irfan Massoud, PhD student of FHKL, that kindly supported me in my work in Germany, showing always willing to help with his irreplaceable experience and advices. Dr. Andrew McInnes from Department of Chemistry of LU for his generous and untiring assistance, with essential technical inputs. Dr. Jagdeep Sagu from Department of Chemistry of LU for the generous supply of single walled carbon nanotubes. Dr. Jing Wang from Department of Mechanical, Electrical and Manufacturing Engineering of LU, for his valuable technical inputs and experience in different knowledgeable areas.

To my beloved friends across UK, China and Germany who shared with me their happiness and character for a more enjoyable PhD life: Ana Barbosa, Ana Castanheira, Carlos Granja, Pedro Silva, Leandro Louro, Jing Wang, Lawrence, Luís Marques, Cristina Campos, Joana Macedo, Mattia Norrito, Irfan Massoud, Mohamed Alqahtani, but specially to Isabel Alves and Maria Varela for the amazing friends and people they are, who always supported me and helped me in everything. To the unconditional support and love of my family, who is always present when I most need, especially my mother, sister, and the most important person in my life, Miguel. Finally, to God who blessed me with this amazing journey and every single day of my life.

List of Publications

1. Rebelo A, Liu Y, Liu C, Schäfer K-H, Saumer M, Yang G. Poly(4-vinylaniline)/polyaniline bilayer functionalized bacterial cellulose membranes as bioelectronics interfaces. *Carbohydr Polym.* Elsevier; 2019 Jan 15; 204:190–201.
2. R. Rebelo A, Archer AJ, Chen X, Liu C, Yang G, Liu Y. Dehydration of bacterial cellulose and the water content effects on its viscoelastic and electrochemical properties. *Sci Technol Adv Mater.* Taylor & Francis; 2018 Dec 31; 19(1):203–11.
3. Rebelo A, Liu Y, Liu C, Saumer M, Schäfer K-H. Development Interfacing Technology for Implantable Neural Prosthetics/Bio-Electronics. The Proceedings of 4th International Conference in Advanced Manufacturing for Multifunctional Miniaturised Devices (ICAM3D) 2015, Loughborough, UK, June 2015, pp.101-102.
4. Rebelo A, Liu Y, Liu C, Schäfer K-H, Saumer M, Yang G. Carbon nanotubes-reinforced poly(4-vinylaniline)/polyaniline bi-layer grafted bacterial cellulose for bioelectronic applications. Accepted for publication in *Biomaterials Science & Engineering of American Chemical Society*, February 2019.
5. Rebelo A, Liu Y, Liu C, Schäfer K-H, Saumer M, Yang G. Flexible electrochemical poly(4-vinylaniline)/polyaniline bilayer functionalized bacterial cellulose biosensor. 2018 – To be submitted in March 2019.

Table of Contents

Keywords	I
Abstract.....	II
Acknowledgements.....	IV
List of Publications	VI
Table of Contents.....	VII
List of Figures	X
List of Tables	XX
List of Abbreviations	XXI
Chapter 1: Research Context and Introduction	1
1.1 Nervous System: Peripheral Nervous System	1
1.1.1 Functional Organisation	2
1.1.2 Anatomy	4
1.1.3 Cellular Components and Structure.....	4
1.1.4 Nerve Impulse	6
1.1.5 The Electrical Model of a Neuron	10
1.2 Peripheral Nerve Injuries.....	12
1.2.1 Physiological Events Post-Injury	13
1.3 Current Therapies	14
1.3.1 Surgical Procedures.....	14
1.3.2 Functional Rehabilitation	16
1.4 New Strategies.....	20
1.4.1 Nerve Tissue Engineering	20
1.4.2 Tissue-Engineered Neural Interfaces	22
1.5 Summary.....	23
1.6 Aims and Objectives.....	23
1.7 Structure of the Thesis	24
Chapter 2: Literature Review.....	27
2.1 Cellulose	27
2.1.1 Bacterial Cellulose	28
2.2 Chemical Modification of Bacterial Cellulose	33
2.3 Intrinsically Conducting Polymers	35
2.3.1 Polyaniline.....	36
2.4 Steric Stabilisation of Polyaniline.....	42
2.4.1 Poly(4-vinylaniline).....	46
2.5 Carbon Nanotubes	51
2.5.1 Chemical Structure.....	51
2.5.2 Electrical Properties	53
2.5.3 Synthesis.....	55
2.6 Carbon Nanotubes-based Composites	58
2.6.1 Carbon Nanotubes/Polyaniline.....	58

2.7	Summary and Implications	59
Chapter 3:	Research Methodology	61
3.1	Materials	62
3.1.1	BC Nanocomposites Production.....	62
3.1.2	Cell Viability	62
3.2	Production Methods.....	63
3.2.1	Synthesis of BC Membranes	63
3.2.2	Synthesis of BC/PVAN/PANI Nanocomposites	64
3.2.3	Carbon Nanotubes-Reinforcement of BC/PVAN/PANI Nanocomposites.....	70
3.3	Characterisation Methods	70
3.3.1	Surface Morphology.....	70
3.3.2	Chemical Composition	72
3.3.3	Grafting Yield.....	75
3.3.4	Dehydration and Modelling of BC Membranes	76
3.3.5	Viscoelastic Properties	77
3.3.6	Electrical Conductivity	78
3.3.7	Electrochemical Analysis	79
3.3.8	Thermogravimetric Analysis.....	83
3.3.9	Cytocompatibility Assays.....	84
Chapter 4:	Synthesis and Characterisation of BC Membranes	91
4.1	Results	92
4.1.1	Morphological Characterisation	92
4.1.2	Chemical characterisation	93
4.1.3	Thermogravimetric Analysis.....	95
4.1.4	Viscoelastic Properties	96
4.1.5	Electrochemical Properties.....	97
4.1.6	Dehydration and Numerical Modelling of Wet BC Membranes.....	99
4.2	Discussion.....	102
4.2.1	Water Loss Effects on BC Morphology	103
4.2.2	Effect of Water Content in the Viscoelastic Properties.....	104
4.2.3	Effect of Water Content in the Electrochemical Properties.....	106
4.2.4	Understanding the Water Loss Process	107
4.3	Conclusion.....	108
Chapter 5:	Development and Characterisation of BC/PVAN/PANI Nanocomposites	109
5.1	Results	110
5.1.1	Morphological Characterisation and Surface Composition.....	110
5.1.2	Chemical Characterisation.....	115
5.1.3	Grafting Yield.....	121
5.1.4	Thermogravimetric Analysis.....	122
5.1.5	Discussion	125
5.1.5	Understanding the PVAN/PANI Bilayer Functionalised BC System	126
5.2	Conclusion	128
Chapter 6:	Electrical Properties of BC/PVAN/PANI Nanocomposites	131
6.1	Results	132
6.1.1	Electrical Conductivity	132
6.1.2	Electrochemical Properties.....	136

6.2	Discussion.....	141
6.2.1	Factors Affecting the Electrical Conductivity of BC/PVAN/PANI.....	142
6.2.2	Influence of BC and PVAN Interlayer on the Electrical Conductivity of BC/PVAN/PANI.....	142
6.3	Conclusion.....	143
Chapter 7: CNTs-Reinforcement of BC/PVAN/PANI Nanocomposites.....		145
7.1	Results.....	146
7.1.1	Morphological Characterisation.....	146
7.1.2	Chemical Characterisation.....	149
7.1.3	Electrical Conductivity.....	152
7.1.4	Electrochemical Properties.....	153
7.1.5	Thermogravimetric Analysis.....	156
7.2	Discussion.....	158
7.3	Conclusion.....	160
Chapter 8: Biocompatibility of the Functionalised BC-based Nanocomposites.....		161
8.1	Results.....	162
8.1.1	Cytocompatibility with PC-12 Adh Cells.....	162
8.1.2	Cytocompatibility with SVZ Cells.....	168
8.2	Discussion.....	173
8.2.1	Different Cell Models for Cytocompatibility of BC-based Nanocomposites: PC-12 Adh <i>versus</i> SVZ.....	173
8.3	Conclusion.....	176
Chapter 9: Conclusions and Future Recommendations.....		177
9.1	Conclusions.....	177
9.2	Future Recommendations.....	179
9.2.1	Potential Applications.....	179
9.2.2	Improving the Biofunctional Performance.....	182
9.2.3	Towards Clinical Practice.....	Error! Bookmark not defined.
Bibliography.....		187
Appendices.....		217

List of Figures

Figure 1.1. Organisation of the NS consisting of CNS and PNS [5].	2
Figure 1.2. Functional organisation of the NS. CNS controls all bodily functions through close interaction with the PNS, to receive and transmit information. CNS can deliver impulses via efferent nerves of the PNS, which in turn induces responses to autonomic and somatic NSs. The autonomic NS transmits then the nerve impulses through the sympathetic and parasympathetic paths, while retrieving information to be transmitted to the CNS via afferent nerves.[8].	3
Figure 1.3. a) Schematic diagram of the anatomic structure of a peripheral nerve and b) a microscopic image of a sectional nerve. The external layer, epineurium, involves nerve fascicles, which in turn are surrounded by a perineurium layer. Each nerve fascicle has multiple nerve fibres (axons) [11].	4
Figure 1.4. a) Schematic structure of a neuron composed of a cell body, axon and dendrites. Neuronal axon is surrounded by myelin sheath which are multiple glial cells (Schwann cells in the PNS) regularly interspaced, forming the nodes of Ranvier. b) Axons can be surrounded by single (unmyelinated) or multiple folds (myelinated) of Schwann cells' membrane.(adapted from [12]).	5
Figure 1.5. Schematic diagram of the propagation of an action potential along the axon of a neuron with the depolarisation and repolarisation of the cell membrane (adapted from [16]).	7
Figure 1.6. a) Membrane potential of a neuron over time after triggered an action potential and b) respective events occurring in the cell membrane. (1) Membrane potential, initially at -70 mV (resting potential), increases up to -55 mV (depolarisation of the membrane), (2) an action potential is induced, which further rises the membrane potential which lasts about 1 ms. (3) After reaching the maximum amplitude, the membrane is repolarised to return to its basal conditions, (5) which becomes hyperpolarised during a refractory period just before (4) reestablishing its resting potential.[18].	8
Figure 1.7. Schematic diagram of A chemical and B electrical synapses established between a presynaptic and a postsynaptic neuron, and C neuromuscular junction between a neuron and muscle fibres [20].	9
Figure 1.8. Electrical cell model of a neuron. a) Neuron with ion channels (transmembrane proteins) imbedded within the cell membrane, allowing the passage of sodium (Na^+) and potassium (K^+) ions to inside or outside the cell. b) Representation of an electrical equivalent circuit model for the cell membrane at a resting potential. The natural impermeability of the phospholipid bilayer of the cell membrane allows the accumulation of ions inside, represented by an electrical capacitor (C_m). Ions can transpose this bilayer through the ion channels that have their corresponding electrical resistance, R_{Na^+} and	

R_{K^+} . The resting potential of -70 mV is achieved with ionic imbalance intra and extracellularly with more Na^+ ions inside and more K^+ ions outside. This can be represented by sodium and potassium batteries, V_{Na^+} and V_{K^+} , respectively. The resistance of the intracellular fluid can be described by an internal longitudinal resistance, R_i . c) The equivalent circuit of the whole membrane can be generically represented by the membrane capacitance, C_m , in parallel with a membrane battery, E_m , in series with the membrane resistance, R_m .(adapted from [24]). 11

Figure 1.9. Representation of Wallerian degeneration process of a neuron after an acute nerve injury. Phase I, increased cell population at the injury site; Phase II, axonal degeneration as result of the inflammatory and immune response – Wallerian degeneration. Phase III, beginning of axonal regeneration with subsequent remyelination. The result of the injury process can lead to a successful nerve regeneration or an incomplete reinnervation with disorganised axonal sprouts.[31]. 13

Figure 1.10. Examples of typical neural electrodes available commercially for interfacing with the PNS. Cuff electrode [44], flat nerve interface electrode (FINE, from MachineDesign), slowly penetrating interface nerve electrode (SPINE [45]), epineural electrode (from Finetech Implantable Drop Foot), helicoidal electrode (from Huntington Medical Research Institute), book electrode (from Finetech-brindley), transverse intrafascicular multichannel electrode (TIME, [46]), macro-sieve electrode (MSE, [44]), Utah slanted electrode array (USEA, from University of Utah and [47]). 17

Figure 1.11. Schematic diagram of an ideal tissue engineering nerve graft (TENG) with a sort range of physical, cellular and biomolecular cues. This TENG consists of a nerve conduit with different internal microstructures (internal channels or matrix) and porosity, with possible incorporation of cells and growth factors.[36]..... 21

Figure 1.12. Flow chart of the structure of the thesis..... 25

Figure 1.13. Chapters involved on the synthesis and characterisation of BC-based nanocomposites..... 25

Figure 2.1. Different sources from where cellulose can be extracted, including plants, cotton and bacteria. Microscopic morphology of cellulose fibres, microfibrils and nanofibrils, with their schematic representation at molecular level.[58]. 28

Figure 2.2. Chemical structure of (bacterial) cellulose. a) Molecular structure of cellulose repeating unit, cellobiose, showing the β -1,4 linkage between the two D-glucose units. b) Supramolecular structure with intra- and intermolecular hydrogen bonds established between adjacent cellobiose units and other cellulose chains, as well as within the repeating unit.[62]. 29

Figure 2.3. Illustration of the amorphous and crystalline domains of cellulose [65]. 30

Figure 2.4. Crystal form of cellulose type I found in BC, with a schematic representation of the coexisting allomorphisms, I_{α} and I_{β} crystal units, within the same microfibril. Disorganisation of the microfibrils can occur (amorphous area), as marked in the squared area (adapted from [66]).....	31
Figure 2.5. Scanning electron microscopic (SEM) images of bacteria colony synthesising cellulose as a metabolic product. Glucan chains are expelled in the form of fibres through tiny pores located in the cellular membrane.([67] that was adapted from [68]).	32
Figure 2.6. Electrical conductivity range of insulators, semiconductor and metals, represented in log-scale [83].	35
Figure 2.7. Different oxidation forms of PANI. The highest conductive form, emeraldine salt, can be reduced to leucoemeraldine salt that is non-conductive, or can be fully oxidised to pernigraniline that is less conductive than emeraldine. These three oxidation states can be further deprotonated into their respective base forms in a reversible manner.(adapted from [85]).	37
Figure 2.8. PANI in the emeraldine base structure. a) Polyconjugated system showing the alternating single and double bonds in the polymer backbone, formed by sigma (σ) and pi (π) bonds. b) Schematic representation of σ and π orbitals overlapping each other to form a double bond between two carbon atoms (adapted from [91]). σ -bonds gives the strength to the strain, while π -bonds ensure delocalisation of the electrons.	38
Figure 2.9. Doped and dedoped forms of emeraldine oxidation state of PANI, showing the polaron and bipolaron structures after protonation with HCl. The counterions from the dopant (Cl^{-} in the present example) compensate the charge carriers introduced after doping.[94].....	39
Figure 2.10. Oxidation of aniline and its products in function of the oxidation potential and the pH of the reaction medium during aniline polymerisation. pH over 3.5 and low oxidation potential result in the deprotonation of both aniline and polymer chain, which results in nonconducting oligomers being produced. pH under 2.5, produce protonated products, and thus conducting PANI. If $2.5 < pH < 3.5$, phenazine structures can result either in oligomerisation or polymerisation, depending on the initial conditions. This is determined by protonation constant of monomer pK_{An} and growing chain pK_{PANI} . [85].....	42
Figure 2.11. Examples of 3D and 1D supramolecular structures of PANI that can be obtained: a) Nanofibres, b) granular spheres (granules), c) plates, d) micro-sized granular agglomerates – commercial PANI – (adapted from [97]).	43
Figure 2.12. Schematic diagram of the self-assembling mechanism of PANI into 3D granular structures [98].	44
Figure 2.13. Examples of polymeric steric stabilisers in the form of a) block copolymers and b) graft copolymers, where A is the polymer with the	

anchor group and B is the polymer that provides the steric barrier [104].....	45
Figure 2.14. Schematic illustration of PANI brushes self-assembled onto a a) non-treated and b) pre-treated surface with a steric polymeric stabiliser, such as PVAN, and corresponding SEM images, showing PANI a) granules [85] and b) nanofibres/nanorods [105]. The presence of the polymeric stabiliser, in this case, PVAN, can stabilise phenazine interactions during aniline polymerisation, allowing the dispersion of PANI brushes, as shown in b), in contrast to what is observed when a) no polymeric stabiliser is used.....	46
Figure 2.15. Chemical structure of the repeating unit of PVAN that is the 4-vinylaniline (4-VAN) monomer.	47
Figure 2.16. Examples of possible molecular structures that can be synthesised with ATRP [114].....	49
Figure 2.17. Schematic illustration of the synthesis of grafted surfaces with ATRP following the ‘grafting-from’ (left) and ‘grafting-to’ (right) approaches. In the ‘grafting-from’, an initiator is attached to the substrate from which polymer chains can grow. In the ‘grafting-to’, a pre-synthesised macromolecule containing a reactive end group is attached to the substrate that had its surface previously activated.[117].	50
Figure 2.18. SEM [121] and optical [122] images of CNTs powders.	51
Figure 2.19. Electronic configuration of carbon atom at the ground state and the possible hybridisations, with the schematic illustration of their respective orbitals shape [124–126].....	52
Figure 2.20. Schematic representation of sp^2 hybridisation of the orbitals in carbon atom [127].	53
Figure 2.21. Molecular structure of a) a graphene sheet, b) SWCNTs and c) MWCNTs [130], and corresponding transmission electron microscopic (TEM) images on the top, showing the single (in SWCNTs) and the multiple walls (in MWCNTs) composing CNTs [131–133].....	53
Figure 2.22. Molecular representation of the possible atomic configurations of CNTs. a) representation of the vectors corresponding to b) armchair, c) zigzag, and d) chiral-based conformations [137].....	54
Figure 2.23. Examples of coexisting morphologies of MWCNTs: hallow tube, herringbone and bamboo (adapted from [138–140]).	55
Figure 2.24. Common methods used for CNTs synthesis.....	56
Figure 3.1. Schematic diagram of the processes involved in the production and characterisation of pristine BC and BC nanocomposites accordingly described in Chapter 3. a) Synthetic procedure of BC membranes followed by its functionalisation, and b-d) corresponding characterisation methods used.	61
Figure 3.2. BC membranes produced from <i>Gluconacetobacter hansenii</i> cultured in 6-well plates.....	64

Figure 3.3. Schematic mechanism of the ‘grafting-from’ approach on BC substrate initiated with BiBB.	65
Figure 3.4. Mechanism of metal complex-mediated ARGET ATRP.	65
Figure 3.5. Oxidation of aniline monomer with APS [100].	66
Figure 3.6. Mechanism of aniline polymerisation. I induction, II chain propagation and III chain termination [100].	67
Figure 3.7. Initialisation reaction of BC surface performed with BiBB kept under argon atmosphere.	68
Figure 3.8. ATRP reaction of VAN after inserting ASCA conducted under argon atmosphere. 1 , VAN, CuCl ₂ , PMEDTA and ASCA dissolved in DMF. 2 , BCi membranes in DMF. Solution 1 is being transferred to solution 2 through the double-tipped needle connecting both flasks.	69
Figure 3.9. COP of aniline performed on BC/PVAN membranes conducted in an ice-bath (~0-5 °C).	70
Figure 3.10. FIB/SEM images from different perspectives and magnifications illustrating the FIB lift-out process used to extract a thin film TEM sample from the bulk membrane sample.	72
Figure 3.11. Schematic representation of the XRD in a crystalline structure, according Bragg’s law. Incident X-rays (S ₁ and S ₂) reach the parallel planes of ions d-spaced, that are reflected at an angle θ , the same as the incident angle.	73
Figure 3.12. Jandel four-point probe set-up used to measure the sheet resistance of BC/PVAN/PANI membrane samples.	79
Figure 3.13. Schematic representation of a cyclic voltammogram from a single charge-transfer process. a) Applied cyclic excitation signal and b) corresponding response (cyclic voltammogram), showing one oxidation/reduction paired-peak when the potential is swept between V ₁ and V ₂ . i _{pa} and i _{pc} are the anodic and cathodic peak currents, respectively, and E _{pa} and E _{pc} are the corresponding peak potentials.	80
Figure 3.14. Illustrative set-up used for electrochemical measurements with a potentiostat. A BC/PVAN/PANI membrane clamped between two pieces of FTO glasses (1x2 cm ²).	81
Figure 3.15. a) Example of Nyquist plot with a diffusion line obtained from the equivalent Randles circuit shown in b). R _s , R _{ct} , C _{dl} and W stands for solution resistance, charge transfer resistance, double layer capacitance and Warburg impedance.	82
Figure 3.16. Illustrative TGA and 1st derivative TGA curves, showing the onset (T _{onset}), offset (T _{offset}) and peak temperatures (T _{peak}) extrapolated from the 1st derivative curve (adapted from [168]).	84
Figure 3.17. Schematic diagram of the cytocompatibility assays performed through cell cultures on pristine BC and BC-based nanocomposites with two neural cell models, PC-12 Adh and SVZ cells.	85

Figure 4.1. Schematic diagram illustrating BC membranes subjected to dehydration at 37 °C, with water loss modelling aiming the prediction of the viscoelastic and electrochemical properties of BC membranes.	92
Figure 4.2. Diagram of BC production displaying SEM images of both surfaces of a freeze-dried membrane, interfacing air and liquid respectively, and a cross section.	93
Figure 4.3. ATR-FTIR spectrum of BC with indication of the corresponding vibrational modes of the functional groups.	94
Figure 4.4. XRD pattern of BC.	95
Figure 4.5. Representative thermogravimetric curve of BC (black) and corresponding first derivative (red) from which the onset (T_{onset}), offset (T_{offset}) and peak (T_{peak}) temperatures were measured. Three main weight loss stages are identified: Stages I, II and III.	96
Figure 4.6. Storage (G') and loss (G'') moduli of BC membranes holding 100, 80 and 50 % water, measured as a function of strain (left) and frequency (right). The red dots indicate the interceptions between G' and G''	97
Figure 4.7. a) Randles circuit used for fitting the experimental data. b) Representative Nyquist plots of BC membranes with 100% (never-dried membrane), 80 % and 50 % water content. The solid lines (—) represent the respective fittings.	98
Figure 4.8. Experimental water loss (■) and respective modelling (—) of BC membranes 8 mm thick and 8 mm of diameter (T8D8), 8 mm thick and 5 mm of diameter (T8D5), 2 mm thick and 8 mm of diameter (T2D8) and 2 mm thick and 5 mm of diameter (T2D5). The water loss curves of each size/thickness correspond to an average of 5 samples and the error bars correspond to the respective standard deviations.	100
Figure 4.9. Schematic of the molecular structure of BC and their bound and free water.	103
Figure 4.10. Schematic representation of the effects of the water content on the morphological structure of BC membranes composed of multi-stacked layers with free and bound water in between (see also Figure 4.9).	104
Figure 5.1. Schematic synthesis of BC/PVAN/PANI nanocomposite membranes at a) macroscopic, b) microscopic and c) molecular levels. Step 1: Initiator (BiBB) immobilisation onto BC. Step 2: SI-ATRP of 4-VAN onto BC. Step 3: COP of aniline on BC/PVAN in the presence of HCl as doping agent, to form BC/PVAN/PANI.	110
Figure 5.2. Representative SEM images and respective magnifications of a) un-modified BC nanofibrous membrane, showing nanofibres with smooth surface, b-c) chemically modified BC membrane with its nanofibrils grafted with PVAN (BC/PVAN). BC nanofibres membrane treated with d) PANI (BC/PANI) and e-f) with PVAN/PANI coating bilayer in two consecutive grafting procedures with PVAN and PANI (BC/PVAN/PANI), illustrating an increase in the roughness of the BC nanofibrils surface in contrast to pristine BC	

and BC/PVAN nanocomposite membranes. b,e) and c,f) BC nanocomposite membranes were produced from molar BiBB:VAN ratios of 1:3 and 1:5, respectively. g-h) FIB/SEM images of the FIB lift-out process used to extract a thin film TEM sample from the bulk BC/PVAN/PANI (BiBB:VAN=1:5) membrane, showing the thickness of the upper PVAN/PANI layer of ~2 μm. Corresponding HRTEM images of the selected area in g,h) of i) BC matrix and j) of the PVAN/PANI bilayer. The red arrows in j) indicate pores of BC substrate.	111
Figure 5.3. Histogram of the diameter (relative frequency) of the fibres of a) BC, b) BC/PVAN, and c) BC/PVAN/PANI membranes, showing the respective cumulative frequencies (solid line –).....	112
Figure 5.4. a) STEM image showing the microstructure of PVAN/PANI-grafted BC at a cross sectional view, as illustrated in Figure 5.2g-h. b-f) corresponding EDX maps of the selected area in a).	114
Figure 5.5. TEM-EDX map sum spectra of BC/PVAN/PANI in three different regions/levels of the membrane indicated in a), which correspond to the area shown in Figure 5.2h. b-c) surface coatings of PVAN/PANI as represented in Figure 5.2hi and d) BC substrate as represented in Figure 5.2hj.	115
Figure 5.6. ATR-FTIR spectra of BC, BC-initiator (BC-BiBB), BC/PVAN and BC/PVAN/PANI.....	116
Figure 5.7. XRD spectra of pristine BC, and BC/PVAN and BC/PVAN/PANI grafted with molar BiBB:VAN ratios of 1:3 and 1:5.....	117
Figure 5.8. Typical wide scans of a.1) BC, b.1) BC-BiBB, c.1) BC/PVAN (BiBB:VAN=1:5) and d.1) BC/PVAN/PANI (BiBB:VAN=1:5). High resolution C1s scans of a.2) BC and b.2) BC-BiBB, and high resolution N1s scans of c.1) BC/PVAN (BiBB:VAN=1:5) and d.1) BC/PVAN/PANI (BiBB:VAN=1:5). Peaks were curve-fitted using Thermo Scientific™ Avantage Data System.	119
Figure 5.9. a) Thermogravimetric curves of BC, BC/PVAN and BC/PVAN/PANI nanocomposites with BiBB:VAN molar ratios of 1:3 and 1:5, measured from room temperature to 800 °C. Three main stages of weight loss identified: Stages I, II and III. b) Corresponding first derivative curves and magnification of the selected squared area. Different colours were used to better distinction of the curves.	123
Figure 5.10. Thermogravimetric curves of BC/PVAN/PANI 1:5 for different aniline polymerisation parameters. a) aniline concentration, b) oxidant to aniline molar ration, c) reaction time and d) acid concentration. Three main stages of weight loss identified: Stages I, II and III.	125
Figure 6.1. Schematic representation of the electrical and electrochemical conduction in PVAN/PANI coated BC nanofibrous membranes.....	132
Figure 6.2. Electrical conductivity of BC/PANI, and BC/PVAN/PANI membranes with different BC to VAN molar ratios, the embedded images show the morphology of the selected area.....	134

Figure 6.3. Differences on the electrical conductivity of BC/PVAN/PANI composites with variation of aniline polymerisation parameters: a) molar ratio APS:ANI, b) acid concentration, c) reaction time and d) aniline concentration.	136
Figure 6.4. Cyclic voltammogram curves of BC, BC/PVAN and BC/PVAN/PANI recorded at 50 and 100 mV.s ⁻¹ of scan rates, with the respective magnification of BC and BC/PVAN curves, showing the oxidation and reduction processes of PANI. Red and blue arrows point out to the peak currents corresponding to emeraldine (EM) measured at 50 and 100 mV.s ⁻¹ , respectively.	138
Figure 6.5. a) Randles equivalent circuit used to fit the impedance spectra shown in b-h. b-h) Nyquist plots of representative impedance data of BC/PVAN/PANI nanocomposites collected from different applied DC potentials upon superimposition of a sinusoidal AC potential of 10 mV. The solid lines (—) represent the fitting by the circuit in a).	141
Figure 7.1. Schematic diagram of step-by-step reaction of BC modification for synthesis of BC/PVAN/PANI/CNTs nanocomposites. a) SI-ATRP of 4-VAN onto BC, starting with the creation of initiating sites on OH-rich BC surface (BC _i) with BiBB. b) COP of ANI performed in an ice-bath in 1M HCl solution and APS as oxidant, to obtain BC/PVAN/PANI. c) Five-time dipping and drying process in SWCNTs dispersion for CNTs-reinforcement forming BC/PVAN/PANI composites.	146
Figure 7.2. Optical images of BC/PVAN/PANI membranes after dipping/drying process in CNTs solution continuously performed 5 times. The numeral index (1...5) indicates the dip times in CNTs.	147
Figure 7.3. SEM images of a) pristine BC, b) BC/PVAN, c) BC/PVAN/PANI and d) BC/PVAN/PANI/CNTs, membranes with e) and f) STEM images of a CNTs coating portion of BC/PVAN/PANI/CNTs accordingly identified. The pictures placed on the right corner in SEM images correspond to the respective nanocomposites. The circle area indicates PANI-nanorods.	148
Figure 7.4. SEM-EDX of BC/PVAN/PANI/CNTs membranes. a-d) X-ray maps of the selected area f) and e) respective sum map spectrum.	149
Figure 7.5. a) XRD spectra of BC, BC/PVAN, BC/PVAN/PANI and BC/PVAN/PANI/CNTs, b) with the corresponding magnification of the selected squared area. The curves were smoothened with FFT using Origin@2015 software.	150
Figure 7.6. Comparative XPS spectra of wide scans acquired for un-modified BC, and BC/PVAN, BC/PVAN/PANI and BC/PVAN/PANI/CNTs nanocomposite membranes. The double sized arrows point out to the contrasting peak intensities of C1s and O1s after the inclusion of the successive coatings onto BC, and the circular areas in BC/PVAN and BC/PVAN/PANI spectra identify the peaks ascribed to N1s.	151
Figure 7.7. High-resolution core-level spectra of C1s of BC, BC/PVAN, BC/PVAN/PANI and BC/PVAN/PANI/CNTs nanocomposites,	

extracted from XPS wide scans of Figure 7.6. Highlighted are the contributions of CNTs to BC/PVAN/PANI/CNTs nanocomposites.	152
Figure 7.8. Electrical conductivity of BC/PVAN/PANI nanocomposites before and after immersion in CNTs dispersion for one up to five times.....	153
Figure 7.9. a) Representative Nyquist plots of BC/PVAN/PANI and BC/PVAN/PANI/CNTs nanocomposite membranes BC/PVAN/PANI, with the respective b) equivalent Randles circuit used to fit the data. R_s stands for solution resistance, R_{ct} for charge transfer resistance, R_p for polarisation resistance, and CPE_1 and CPE_2 for constant phase element of the corresponding R_{ct} and R_p parameters. Square dots (■) represents the acquired experimental data and solid lines (—) for the fitting.....	155
Figure 7.10. Thermogravimetric curves of BC nanocomposites characterized by three weight loss stages accordingly marked as I, II and III. The differential thermal curve of BC/PVAN/PANI/CNTs (DTA) is also shown.	157
Figure 7.11. Schematic illustration of the possible interactions established between PANI and CNTs. 1 shows the pi-stacking interaction between the aromatic rings of both PANI and CNT and in 2, CNTs competes with chloride (Cl^-) to dope PANI and form a covalent C-N bond (adapted from [80]).	159
Figure 8.1. Schematic diagram of the possible cellular responses of PC-12 Adh and SVZ cells studied in this chapter after contact with the electrically conductive BC nanocomposites <i>in vitro</i> to conclude on their cytocompatibility: Cell proliferation and cell differentiation.	162
Figure 8.2. Cell activity of PC-12 Adh cells cultured on pristine BC, BC/PVAN (at 1:3 and 1:5) and BC/PVAN/PANI (at 1:3 and 1:5). The results are shown in terms of means±standard deviations of optical absorbance measured. * and # indicates statistical significance ($p<0.05$) compared to TCTP and BC, respectively, according to one-way ANOVA testing.....	163
Figure 8.3. SEM images showing the morphology of PC-12 Adh cells cultured on BC, BC/PVAN (BiBB:VAN=1:3 and 1:5) and BC/PVAN/PANI (BiBB:VAN=1:3 and 1:5) after 7 days of culture.....	164
Figure 8.4. Cell activity of PC-12 Adh cells cultured on pristine BC, BC/PVAN (at 1:3 and 1:5) and BC/PVAN/PANI (at 1:3 and 1:5). The results are shown in terms of means±standard deviations of optical absorbances measured. * indicates statistical significance ($p<0.05$) compared to TCTP and BC according to one-way ANOVA testing.	165
Figure 8.5. Fluorescence images of induced PC-12 Adh cells after 7 days incubated with NGF on TCTP, BC, and BC/PVAN and BC/PVAN/PANI prepared with different BiBB:VAN molar ratios. The nuclei are represented in blue (DAPI) and the cell projections are shown in green (Alexa Fluor® 488). The indexes 1:3 and 1:5 refer to BiBB:VAN molar ratios. Red arrows identify glial-type cell.....	166

Figure 8.6. a) Percentage of differentiated cells on pristine BC and BC nanocomposites relative to TCTP and b) Neurite length of cell projections on the different substrates. * and # indicates statistical significance ($p<0.05$) compared to TCTP and BC, respectively, according to one-way ANOVA testing.....	167
Figure 8.7. Live (green) and dead (red) stained SVZ cells, and corresponding merge images, using calcein-AM and propidium iodine, respectively, after 7 days of incubation with TCTP, BC, BC/PVAN, BC/PVAN/PANI and BC/PVAN/PANI/CNTs substrates.....	168
Figure 8.8. Viability of SVZ cells, as determined with LIVE/DEAD assay, after 7 days of culture with pristine BC and BC composites. a) Percentage of viable (live) cells and b) percentage of total number of cells relative to TCTP, with standard deviation error bars. Statistical significance between the different substrates (groups) tested is denoted as $*p<0.05$, according to one-way ANOVA testing.	169
Figure 8.9. Neural differentiation of SVZ cells on different substrates over time. a) Induced cells labelled with CFSE after 2 hours and 24 hours of harvesting on coverslip, BC, BC/PVAN, BC/PVAN/PANI and BC/PVAN/PANI/CNTs substrates. b) Differentiation degree (%) on the 7 th day of culture as determined differentiation on the different substrates. c) Neurite length evolution measured at different cultured periods (2 hours, 24 hours and 7 days). $*p<0.05$ denotes statistical significance compared to coverslip, according to one-way ANOVA testing.....	171
Figure 8.10. Immunofluorescent images of differentiated SVZ cells into neurons (GFP) and glia-like cells (RFP) cultured on BC, BC/PVAN, BC/PVAN/PANI, BC/PVAN/PANI/CNTs and coverslip for 7 days. Cell nuclei are stained in blue (DAPI) with merged pictures on the right.	172
Figure 9.1. Schematic representation of flexible electrically conductive BC/PVAN/PANI/CNTs nanocomposite membranes, biologically interfacing with neurons for efficient nerve impulse conduction.	180
Figure 9.2. Examples of other potential biomedical applications of the as-developed electrically conductive BC nanocomposites as drug-delivery systems, biosensors, wound dressings, tissue engineering scaffolds and pacemakers.	181

List of Tables

Table 1.1. Types of PNI electrodes, and general applications and status [43, 48–51].	18
Table 2.1. Commercial products based on BC and their applications (adapted from [61] and [70]).	33
Table 2.2. Principal technical characteristics of the typical methods used to produce CNTs, and respective advantages and disadvantages (adapted from [142–144]).	57
Table 4.1. Average values of solution resistance R_s , polarisation resistance R_p , constant phase element CPE, and N values of Randles circuit used to fit the experimental data of 6 never-dried BC membranes per BC water content (100, 80 and 50 %).	99
Table 4.2. Results obtained for the model expressed in equation 3.9 that gives the best agreement with the experimental data. Information related to surface area to volume ratio for each sample’s dimension.	101
Table 4.3. Influence of changes to the values of the rate constants in the model.....	Error! Bookmark not defined.
Table 5.1. Binding energies (eV) of C1s, O1s, Br3d, N1s and Cl2p detected by XPS on BC, BC-BiBB, BC/PVAN and BC/PVAN/PANI.	118
Table 5.2. Elemental composition (atomic percentage, at%) of BC, BC-BiBB, BC/PVAN and BC/PVAN/PANI composites extracted from XPS analysis, corresponding N/C atomic ratios.	120
Table 5.3. Elemental composition (atomic percentage, at%) of BC/PVAN/PANI 1:5 composites prepared using different aniline polymerisation conditions extracted from XPS analysis, with corresponding N/C ratios.	121
Table 5.4. Grafting yield (%) of PVAN and PANI on BC/PANI and BC/PVAN/PANI membranes.	122
Table 5.5. Onset, peak and offset temperatures extrapolated from the first derivative curves of TGA shown in Figure 5.9b.....	124
Table 6.1. Data extracted and calculated from the Nyquist plots shown in Figure 6.5.	139
Table 7.1. Values of the elements of the equivalent Randle circuit used to fit the data of Figure 7.9.	154
Table 7.2. Onset, peak and offset temperatures extrapolated from the first derivative curves of TGA shown in Figure 5.9b.....	158

List of Abbreviations

1D	One-Dimensional
2D	Two-Dimensional
3D	Three-Dimensional
4-VAN or VAN	4-Vinylaniline
β -ME	β -Mercaptoethanol
AC	Alternate Current
ACh	Acetylcholine
ANS	Autonomic Nervous System
ANI	Aniline
APS	Ammonium Persulfate
ARGET	Activators Regenerated by Electron Transfer
ATR-FTIR	Attenuated Total Reflectance Fourier Transform Infrared Spectroscopy
ATRP	Atom Transfer Radical Polymerisation
AS	Amplitude Sweep
ASCA	Ascorbic Acid
BC	Bacterial Cellulose
BC-BiBB	Bacterial Cellulose modified with 2-Bromoisobutyryl Bromide
BCi	Bacterial Cellulose Initiator
BC/PVAN	Bacterial Cellulose-graft-Poly(4-vinylaniline)
BC/PVAN/PANI	Bacterial Cellulose-graft-Poly(4-vinylaniline)-graft-Polyaniline
BE	Binding Energy

BiBB	2-Bromoisobutyryl Bromide
BSA	Bovine Serum Albumin
Calcein AM	Calcein acetoxymethyl ester
Cm	Capacitance of the cell membrane
CNS	Central Nervous System
CNTs	Carbon Nanotubes
COP	Chemical Oxidative Polymerisation
CPs	Conducting Polymers
CV	Cyclic Voltammetry
CVD	Chemical Vapour Deposition
DAPI	4',6-Diamidino-2-phenylindole
DC	Direct Current
DMAP	4-Dimethylaminopyridine
DMEM	Dulbecco's Modified Eagle's Medium
DMF	Dimethylformamide
DTA	Differential Thermal Analysis
ECM	Extracellular Matrix
EDX or EDS	Energy Dispersive X-ray Spectroscopy
Em	Electromotive force
EM	Emeraldine
ENS	Enteric Nervous System
EIS	Electrochemical Impedance Spectroscopy
ETA	Ethanol
FBS	Fetal Bovine Serum
FDA	Food and Drug Administration

FEI	Field Electron
FIB	Focused Ion Beam
FINE	Flat Interface Nerve Electrode
FS	Frequency Sweep
FTO	fluorine doped tin oxide
G'	Storage modulus
G''	Loss modulus
GA	Gluteraldehyde
GAG	Glycosaminoglycan
GFP	Green Fluorescence Protein
GSA	General Somatic Afferent
GSE	General Somatic Efferent
GY	Grafting Yield
HCl	Hydrochloric acid
HRTEM	High Resolution Transmission Electron Microscopy
HS	Horse Serum
LE	Leucoemeraldine
LIFE	Longitudinally Implanted Electrode
LVR	Linear Viscoelastic region
MSE	Macro-Sieve Electrode
NDS	Normal Donkey Serum
NHS	National Health Service
NGF	Nerve Growth Factor
NS	Nervous System
NTE	Nerve Tissue Engineering

PANI	Polyaniline
PBS	Phosphate Buffered Saline
PBST	Phosphate Buffered Saline Tween-20
PC-12 Adh	Pheochromocytoma of embryonic rat adrenal medulla
Pen/Strep	Penicillin/Streptomycin
PF	Paraformaldehyde
PGs	Proteoglycans
PG	Pernigraniline
PI	Propidium Iodine
PMEDTA	N,N,N',N'',N''-Pentamethyldiethylenetriamine
PNI _s	Peripheral Nerve Interfaces
PNS	Peripheral Nervous System
RA	Retinoic Acid
RFP	Red Fluorescence Protein
rhβFGF	Recombinant Human Fibroblast Growth Factor
rhEGF	recombinant Human Epidermal Growth Factor
R _m	Resistance of the Cell Membrane
SDBS	sodium dodecylbenzenesulfonate
SEM	Scanning Electron Microscopy
SPINE	Slowly Penetrating Interface Nerve Electrode
STEM	Scanning Transmission Electron microscopy
SVZ	Subventricular Zone
TCTP	Tissue Culture Treated Plastic
TE	Tissue Engineering
TEA	Triethylamine

TEM	Transmission Electron Microscopy
TENI	Tissue-Engineered Neural Interface
TENS	Transcutaneous Electrical Nerve Stimulation
TGA	Thermogravimetric Analysis
TIME	Transverse Intrafascicular Multichannel Electrode
UK	United Kingdom
US	United States
USEA	Utah Slant Electrode Array
XPS	X-Ray Spectroscopy
XRD	X-Ray Diffraction

Chapter 1: Research Context and Introduction

This chapter intends to contextualise the scope of this research study with relevant background information described accordingly in sections 1.1 to 1.4. Section 1.5 summarises the research context, highlighting the issues to be addressed with this project. Specific aims and objectives are then discriminated in section 1.6. Finally, section 1.7 includes an outline of the remaining chapters of the thesis.

1.1 NERVOUS SYSTEM: PERIPHERAL NERVOUS SYSTEM

The nervous system (NS, Figure 1.1) is one of the most complex and specialised systems of the human being. Simplistically subdivided into brain and spinal cord (central nervous system, CNS) and nerves (peripheral nervous system, PNS), CNS controls all the functions of the organism that can be reached through the nerves via deliverable electrochemical signals through synapses towards limbs and organs. It is consensually accepted that the number of synapses in brain is around 10^{14} , that results from 15 thousand connections per neuron for a total of 100 billion neurons – equivalent to a computer with 38 thousand trillion per second processor and 10-1000 terabytes storage capacity (memory). This represents only 0.002% of some of the world's most powerful supercomputers.

The accurate transmission of these electrochemical signals requires efficient pathways – the peripheral nerves of the PNS. The PNS receive external information (e.g. touching hot surfaces) and transmit it to the CNS, which in turn sends back appropriate actions to nerves towards the target organ via synapses to perform voluntary movements, feel sensations and keep the normal functions of vital organs. [1–3]. One of the major differences the CNS and the PNS is that PNS can undergo some self-repair, which is almost absent in the CNS.[4].

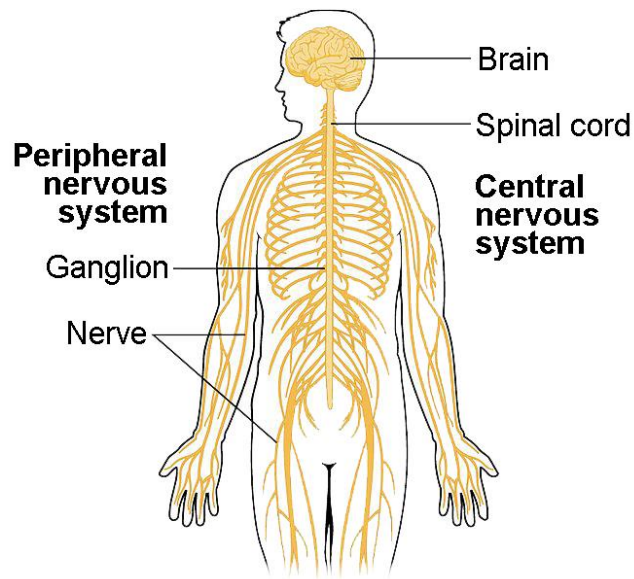


Figure 1.1. Organisation of the NS consisting of CNS and PNS [5].

1.1.1 Functional Organisation

The PNS is divided into somatic and autonomic nervous system, which controls the voluntary and involuntary bodily functions, respectively. The PNS has afferent (sensory) and efferent (motor) nerve fibres responsible for retrieving information from sensory organs and transmitting impulses from the CNS to limbs and organs (Figure 1.2).[6].

The somatic NS is subdivided into sensory and motor components, associated with the voluntary control of body movements, and with sensory reception of external stimuli (general somatic afferent fibres, GSA). There are distinct ways of gathering information from the body which includes the somatic senses, mechanoreception, thermoreception, and pain. Other special sensory routes involve senses such as vision, hearing, taste, smell, and equilibrium. The efferent nerve fibres (general somatic efferent fibres, GSE) of the somatic NS are responsible for stimulating muscle contraction, including all the neurons connected with skeletal muscles, skin, and sense organs.[7].

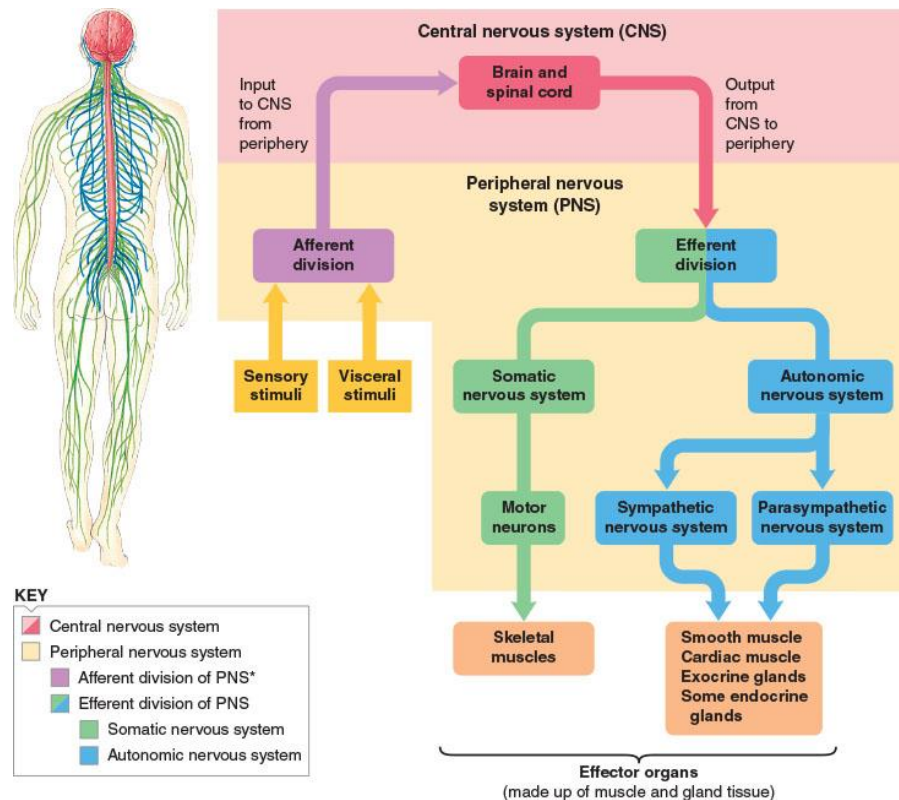


Figure 1.2. Functional organisation of the NS. CNS controls all bodily functions through close interaction with the PNS, to receive and transmit information. CNS can deliver impulses via efferent nerves of the PNS, which in turn induces responses to autonomic and somatic NSs. The autonomic NS transmits then the nerve impulses through the sympathetic and parasympathetic paths, while retrieving information to be transmitted to the CNS via afferent nerves.[8].

The autonomic NS integrates three anatomic structures that are sympathetic, parasympathetic, and enteric NSs, and it has an afferent limb, efferent limb and a central integrating system. This central integrating system regulates simple reflexes within the visceral organs, with both afferent and efferent limbs consisting of general visceral and special visceral, afferent and efferent fibres. The sympathetic and parasympathetic NSs constitute the motor pathways that usually have contrasting effects. Whereas the sympathetic NS is responsible for increasing the heart rate, blood pressure, breathing rate, and pupil size, the parasympathetic controls the bodily functions at rest by inducing opposite responses to those of sympathetic NS, with the enteric NS operating in the functions of the gastrointestinal system. Parasympathetic NS also stimulates digestion, activates various metabolic processes and contributes to relaxation.[9, 10].

1.1.2 Anatomy

In the PNS, motor and sensory axons are bundled together by connective tissue into an anatomically defined trunk (Figure 1.3). These bundles of axons are designated nerves (either spinal or cranial nerves), which also have blood vessels and capillaries within the nerves to supply nourishment to tissues. Three layers of fibrous connective tissue can be identified in a peripheral nerve structure. The inner layer, that loosely involves individual axons, is called endoneurium. Endoneurium consists predominantly of oriented collagen fibres supplied by Schwann cell sheaths. The intermediate layer, the perineurium, surrounds multiple axons to form the fascicles, which is composed of many layers of flattened cells (i.e. fibroblasts) and collagen. The outer layer, the epineurium binds individual nerve fascicles, involving them together with fibrocollagenous tissue to form a nerve trunk.[4].

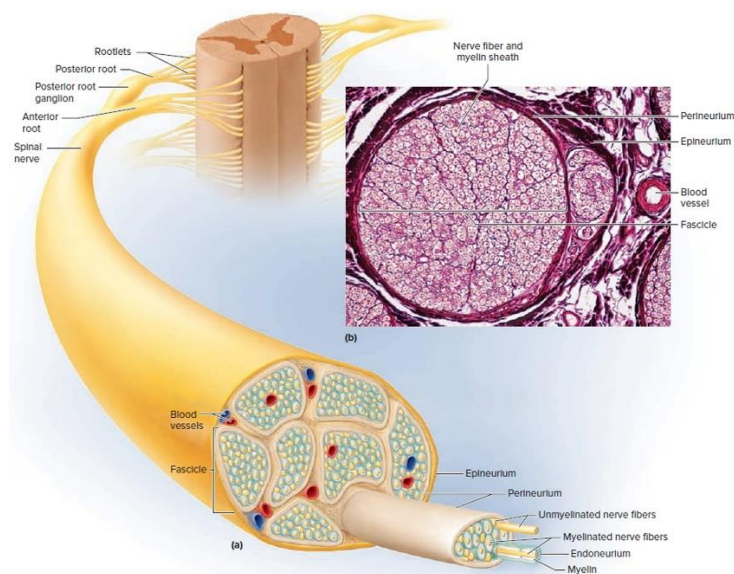


Figure 1.3. a) Schematic diagram of the anatomic structure of a peripheral nerve and b) a microscopic image of a sectional nerve. The external layer, epineurium, involves nerve fascicles, which in turn are surrounded by a perineurium layer. Each nerve fascicle has multiple nerve fibres (axons) [11].

1.1.3 Cellular Components and Structure

There are two types of cells present in the NS, neurons and neuroglia, which have different functions. Neurons are responsible for the basic structure and function of the NS and consist of a cell body (soma) and its extensions (axons and dendrites)

(Figure 1.4a). Neurons are electrically excitable cells that process and transmit information through electrical and chemical synapses. Their somas aggregate together to form the anatomic structure called ganglia. Glial cells, that are Schwann cells in the PNS, and astrocytes and oligodendrocytes in the CNS, exist in higher number than neurons and are responsible for supporting and assisting the functions of neurons. These cells have also the ability to undergo cell division.[4].

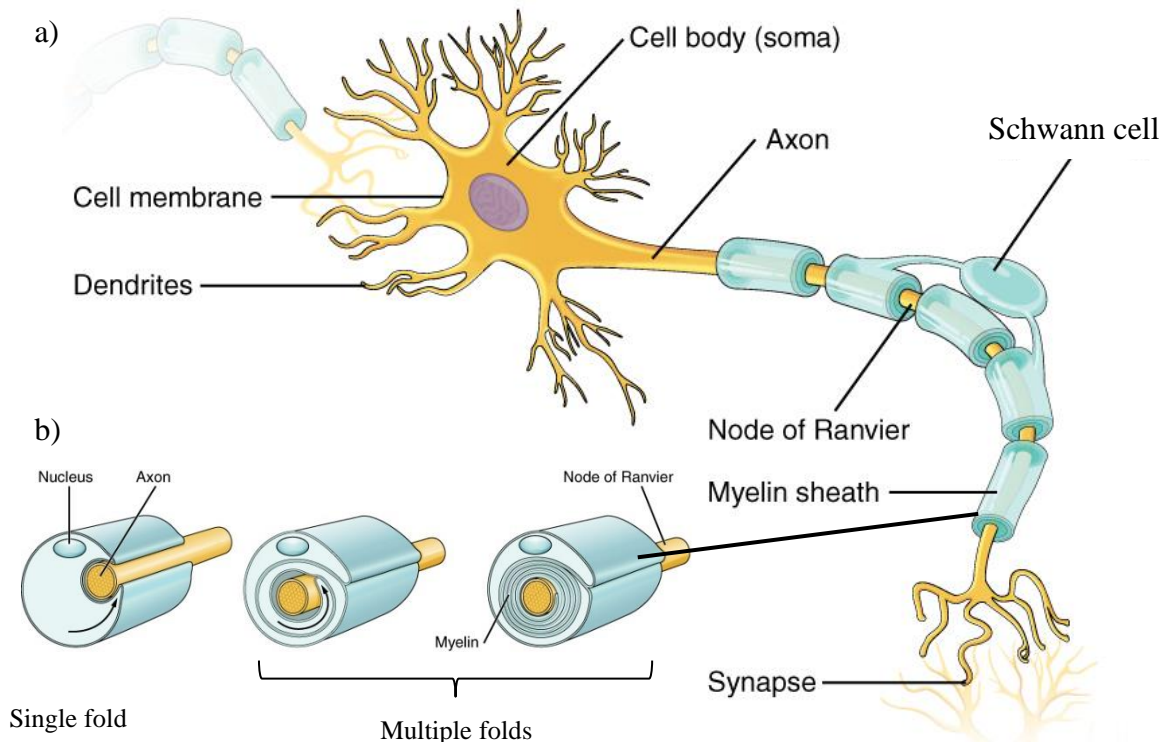


Figure 1.4. a) Schematic structure of a neuron composed of a cell body, axon and dendrites. Neuronal axon is surrounded by myelin sheath which are multiple glial cells (Schwann cells in the PNS) regularly interspaced, forming the nodes of Ranvier. b) Axons can be surrounded by single (unmyelinated) or multiple folds (myelinated) of Schwann cells' membrane.(adapted from [12]).

In the PNS, sheaths of living Schwann cells surround all axons with single or multiple folds of their membranes (Figure 1.4b). When the membrane involving axons have one single fold, they are called unmyelinated fibres, otherwise they are called myelinated fibres. Both types of fibres can be found in CNS and PNS. However, a basement membrane, the neurilemma, formed by the outer surface of the Schwann cell layer in the PNS, is not observed in the CNS. In contrast, axons in the CNS are involved by an insulating myelin sheath. This sheath is formed by dense layers of

successive wrappings of the cell membrane of Schwann cells (in the PNS) or oligodendrocytes (in the CNS). The sites along axons at which myelin sheath is interrupted by different cells are called Nodes of Ranvier (Figure 1.4a). The myelin sheaths and their regular gaps enable rapid and efficient saltatory propagation of action potentials, with a high level of spatial and temporal organisation. This is particularly important for those axons that are extended for long distances (up to 1 m).[4, 13].

Extracellular Matrix

The anatomic structures of the PNS are mainly composed of extracellular matrix (ECM), which provides essential physical scaffolding for the cellular constituents and also triggers crucial biochemical and biomechanical cues for tissue morphogenesis, differentiation and homeostasis. The ECM consists of proteoglycans (PGs), that are basically glycosaminoglycan (GAG) chains covalently linked to a specific protein core (with the exception of hyaluronic acid), and fibrous proteins, which are collagens, elastins, fibronectins and laminins. PGs occupies most of extracellular interstitial space in the form of a hydrated gel, which surrounds the fibrous proteins mainly constituted by collagens. While collagens yield tensile strength, regulate cell adhesion, support chemotaxis and migration, and direct tissue development, PGs furnish buffering, hydration, binding and force-resistance properties to ECM.[14].

1.1.4 Nerve Impulse

Neurons are electrically excitable cells and as such, they can propagate electrical signals through depolarisation and repolarisation of axon membrane, to transmit signals to motor cells, glands or another neuron via synapses occurring between the dendrites of the generator (neuron) and the axonal terminal of the receptor (neuron). The signal propagation along the axon is called action potential or nerve impulse, which occurs at the expenses of a polarity switch of the membrane (Figure 1.5).[15].

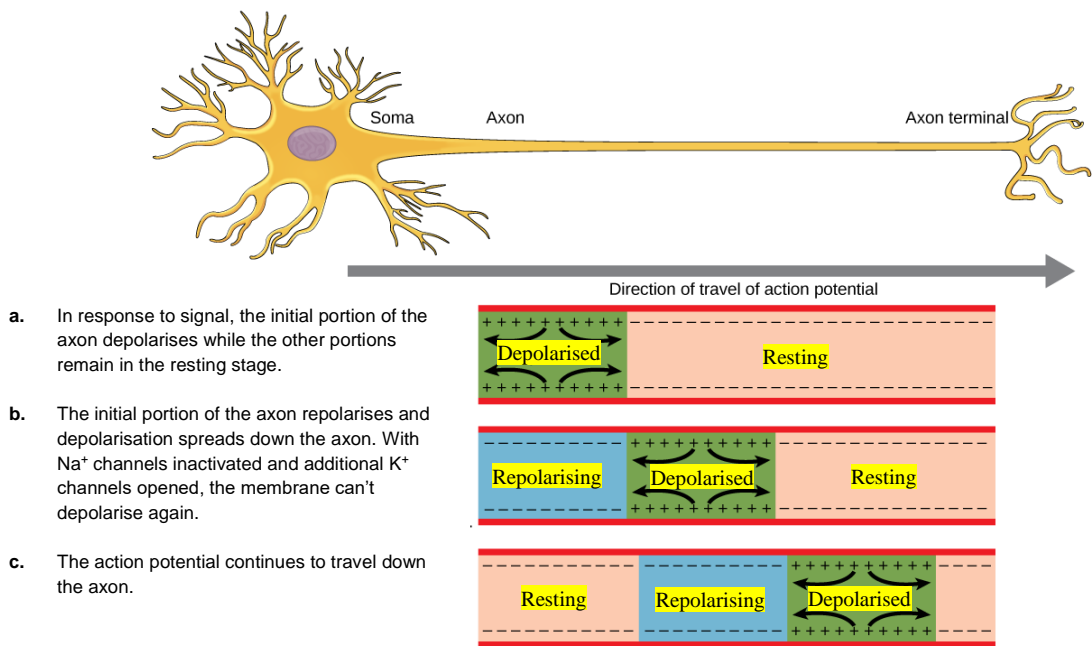


Figure 1.5. Schematic diagram of the propagation of an action potential along the axon of a neuron with the depolarisation and repolarisation of the cell membrane (Reproduced by permission from Science 25 Oct 2002:Vol. 298, Issue 5594, [16] copyright 2012).

The polarity of nerve cells is established with an ionic gradient of sodium (Na^+) and potassium (K^+), which maintains a certain potential difference (resting membrane potential), as illustrated in Figure 1.6. The membrane potential at rest is negatively charged (approximately -70 mV) due to the presence of a higher concentration of positive ions outside than inside, that is kept constant thanks to the multiple ion channels imbedded in the cell membrane. The ionic channels distributed across the membrane are voltage sensible. At basal conditions, these channels purge more Na^+ ions to outside of the membrane than inside, while impelling more K^+ ions to inside. Upon an action potential, the stimulus causes the membrane potential to rise (depolarise) and fall (repolarise) rapidly through a difference in the ionic concentration across the membrane, that becomes positively charged (depolarised) where the action potential is passing by while maintaining negatively charged (polarised) in the adjacent areas (Figure 1.5). This happens as the ionic channels start to open to allow an inward flow of Na^+ ions, which changes the electrochemical gradient. As the membrane potential further rises, more channels open, and thus, generating an electrical current (Figure 1.6). The impulse travels along the axon membrane with similar amplitude and

time course towards the axon terminals with successive depolarisation of the adjacent membrane region – propagation.[17].

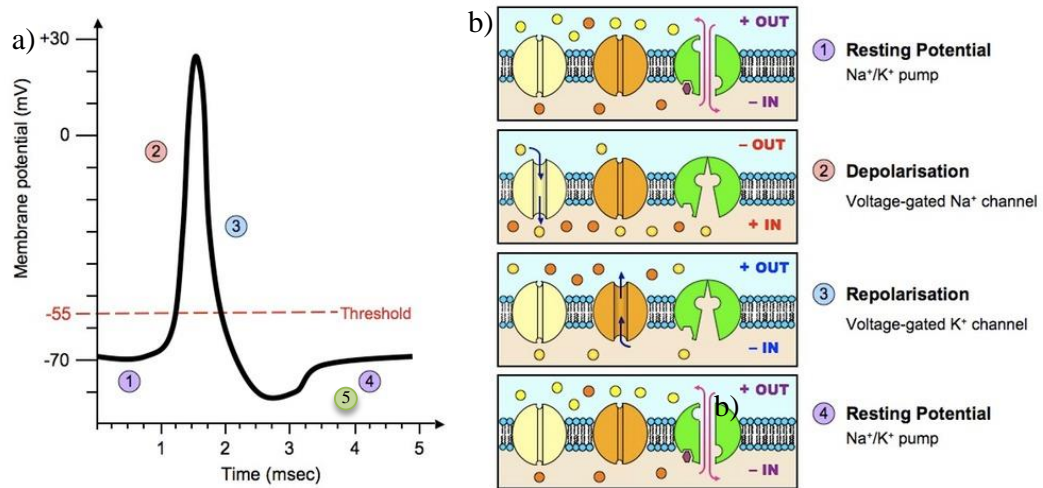


Figure 1.6. a) Membrane potential of a neuron over time after triggered an action potential and b) respective events occurring in the cell membrane. (1) Membrane potential, initially at -70 mV (resting potential), increases up to -55 mV (depolarisation of the membrane), (2) an action potential is induced, which further rises the membrane potential which lasts about 1 ms. (3) After reaching the maximum amplitude, the membrane is repolarised to return to its basal conditions, (5) which becomes hyperpolarised during a refractory period just before (4) reestablishing its resting potential.[18].

One single neuron can receive synapses from multiple neurons which can cause depolarisation or hyperpolarisation of the cell membrane. On average, each neuron can continuously emit 10 up to 100 action potentials per second. When the resting membrane potential is raised up to a certain level, an action potential is triggered. The minimum potential needed to cause depolarisation of the membrane and trigger an action potential is called threshold potential and is around -55 mV (Figure 1.6).

There are basically two ways that neurons transmit signals via synapses, chemical or electrically. The chemical synapses can be established with neurons or non-neuron cells, such as those of muscle tissue (neuromuscular junctions) and glands (Figure 1.7). In general, electrical synapses provide very fast transmission of the signals (nearly instantaneous) and are excitatory only, while in chemical synapses the transmission is much slower, but they can cause either excitatory and inhibitory responses. Additionally, there is some loss in the electrical transmission as it travels

towards the next cell, which diminishes the signal strength, while in the chemical synapses the message is transmitted without any loss in signal strength.[19].

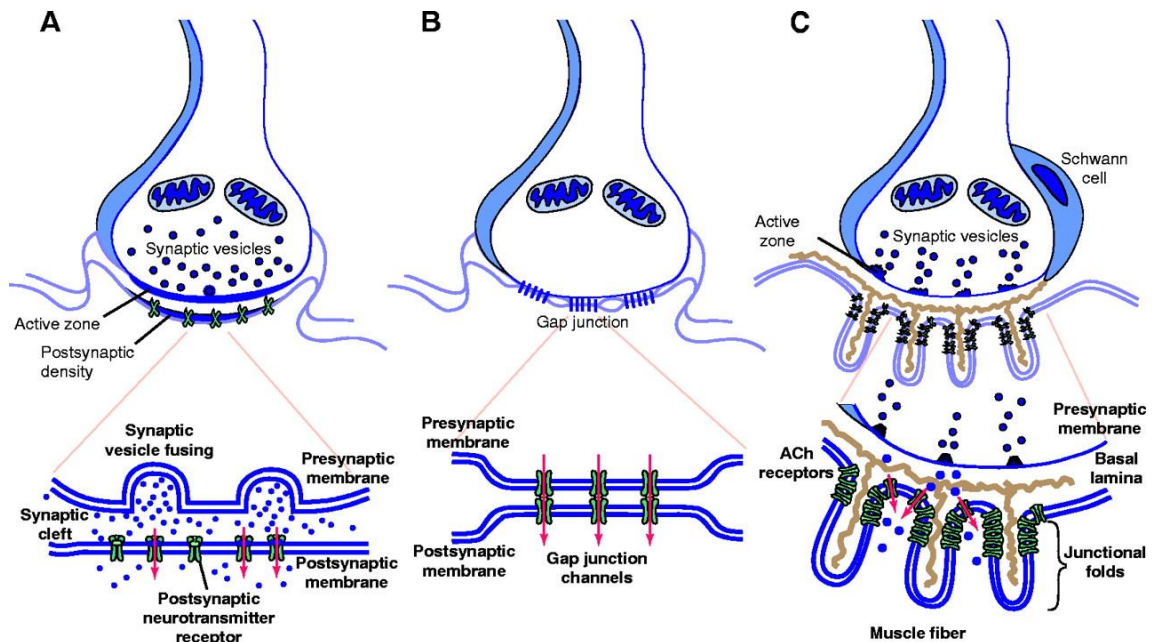


Figure 1.7. Schematic diagram of A chemical and B electrical synapses established between a presynaptic and a postsynaptic neuron, and C neuromuscular junction between a neuron and muscle fibres [20].

Chemical Synapses

In a chemical synapse (Figure 1.7A), the generated nerve impulse in the presynaptic neuron is converted to a chemical signal with the release of small molecules called neurotransmitters, at the synapse's junction. These neurotransmitters bind to receptors located in the plasma membrane of the dendrites of the postsynaptic cell. The process is initiated when an action potential passes by the terminal of the presynaptic neuron. The change in membrane potential causes a rapid influx of Ca^{2+} into the presynaptic terminal as the voltage-gated calcium channels open which results in a higher Ca^{2+} concentration in the cytoplasm. As consequence, synaptic vesicles containing neurotransmitters fuse with the plasma membrane of the presynaptic neuron to release the neurotransmitters into the synaptic cleft. There are many neurotransmitters studied, although acetylcholine released in the neuromuscular junctions is the most studied.[19, 21].

Electrical Synapses

In an electrical synapse (Figure 1.7B), the electrical current results from the action potential passing from the presynaptic to the postsynaptic neuron through the gap junctions, that are special channels connecting both neurons. These gap junctions originate a potential change of the presynaptic neuron which in turn causes a potential change in the postsynaptic cell. Compared to the chemical synapses, in the electrical ones the transference of signals from one cell to the next is much faster.[21].

Neuromuscular Junctions

Neuromuscular junctions (Figure 1.7C) are chemical synapses established between motor neurons and muscle fibres, which can cause muscle contraction or relaxation. The neurotransmitters (acetylcholine) bind to receptors located in the plasma membrane of the muscle fibre (nicotinic acetylcholine receptors), which can depolarise the muscle fibre, causing a cascade of events that result in muscle contraction.[19].

1.1.5 The Electrical Model of a Neuron

The way an action potential travels through a neuron in the form of a longitudinal ionic current has been compared with the way electrical current flows in wires of an electrical circuit. However, in neurons the current flow is a pure propagation phenomenon, in contrast to the conduction observed in wires. In living cells this current is carried by ions, which is different from those in the electrical circuits that is carried by electrons. The cell depolarisation can be achieved either by injection of positive ions into the cell with intraneural electrodes or under the cathode with extraneural electrodes.[22].

The cell membrane has an electrical capacitive behaviour that can be simplistically described with the equivalent circuit shown in Figure 1.8c. This membrane is composed of a molecular lipid bilayer of phospholipids that has hydrophobic tails hidden with the hydrophilic regions exposed to both intra- and extracellular media, along which are inserted proteins responsible for transposing materials across the cell membrane. This bilayer acts as an insulator separating the conducting internal and external media where ions are dispersed in, which constitute

an electrical capacitor where the two conducting plates are the ionic media and the membrane is the dielectric component.[23].

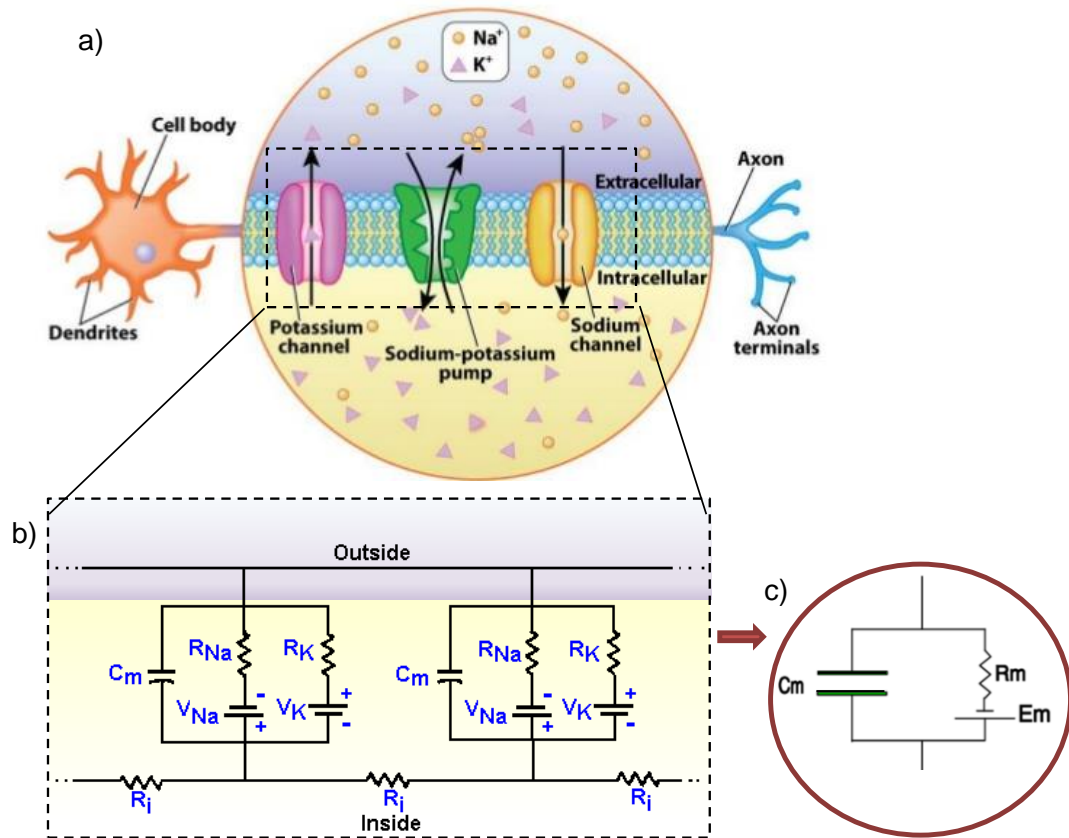


Figure 1.8. Electrical model of a cell membrane of a neuron. a) Neuron with ion channels (transmembrane proteins) imbedded within the cell membrane, allowing the passage of sodium (Na^+) and potassium (K^+) ions to inside or outside the cell. b) Representation of an electrical equivalent circuit model for the cell membrane at a resting potential. The natural impermeability of the phospholipid bilayer of the cell membrane allows the accumulation of ions inside, represented by an electrical capacitor (C_m). Ions can transverse this bilayer through the ion channels that have their corresponding electrical resistance, R_{Na^+} and R_{K^+} . The resting potential of -70 mV is achieved with ionic imbalance intra- and extracellularly with more Na^+ ions inside and more K^+ ions outside. This can be represented by sodium and potassium batteries, V_{Na^+} and V_{K^+} , respectively. The resistance of the intracellular fluid can be described by an internal longitudinal resistance, R_i . c) The equivalent circuit of the whole membrane can be generically represented by the membrane capacitance, C_m , in parallel with a membrane battery, E_m , in series with the membrane resistance, R_m .(adapted from [24]).

The lipid bilayer on its own is naturally impermeable to almost all ions. However, the selective permeability granted by the presence of the transmembrane

proteins accounts for the electrical conductance (reciprocal of resistance) of the membrane (R_m), as schematically illustrated in Figure 1.8a. The resting membrane potential that exists in the absence of stimulus or external electric field, can be represented by an electromotive force, E_m , calculated by the differential potential between the intra- and extracellular media (inside and outside the cell membrane, respectively – Figure 1.8c). This simplified electrical equivalent circuit describes the individual contributions of each sodium and potassium channels along the membrane (Figure 1.8b).[25].

1.2 PERIPHERAL NERVE INJURIES

If a certain degree of damage reaches the peripheral nerves, serious problems can arise which may need immediate actions to prevent further complications. Owing to the unique complexity of the NS, the restoration and replacement of the original functions in case of nerve injury either by trauma or disease – peripheral neuropathy – still faces uncountable challenges. Peripheral neuropathy can be caused by numerous conditions, such as alcoholism, autoimmune diseases, diabetes, exposure to poisons, medications, infections, inherited disorders, trauma or pressure on the nerve, tumours, vitamin deficiencies, bone marrow disorders and other disorders.[26]. According to the National Health Service (NHS, UK), diabetes is the most common cause of neuropathy in the UK, which affects around 50% of the diabetic patients [27]. Regardless the cause, nerve injuries can range from mild to severe and may end up with complete functionality loss if not properly and promptly treated. The consequences will be determined by the affected nerve and the extension of the damage, which can be reflected in actions involving voluntary motion and sensory feelings (somatic nervous system), or those controlling involuntary bodily functions, such as breath, heartbeat or digestion (automatic nervous system), that can seriously compromise the individual's health.[28]. Other possible complications associated with neuropathy are the formation of sores or ulcers stemmed from loss of sensation, which can become infected and progress into bone, resulting in amputation.[29]. It is thus critical to understand the physiology of the PNS before and after an injury to fully re-establish the damaged nerve and its functionality.

1.2.1 Physiological Events Post-Injury

In an unfortunate injury event, PNS can still self-regenerate under certain conditions, in contrast to what is witnessed in the CNS that has an inhibitory and abortive regenerative process [30]. However, in more severe nerve damage in PNS, axonal degeneration occurs in the distal portion of the injury to the proximal portion – Wallerian degeneration –, due to the protease activity and lack of metabolic resources, which can result in a complete or incomplete nerve repair (Figure 1.9).

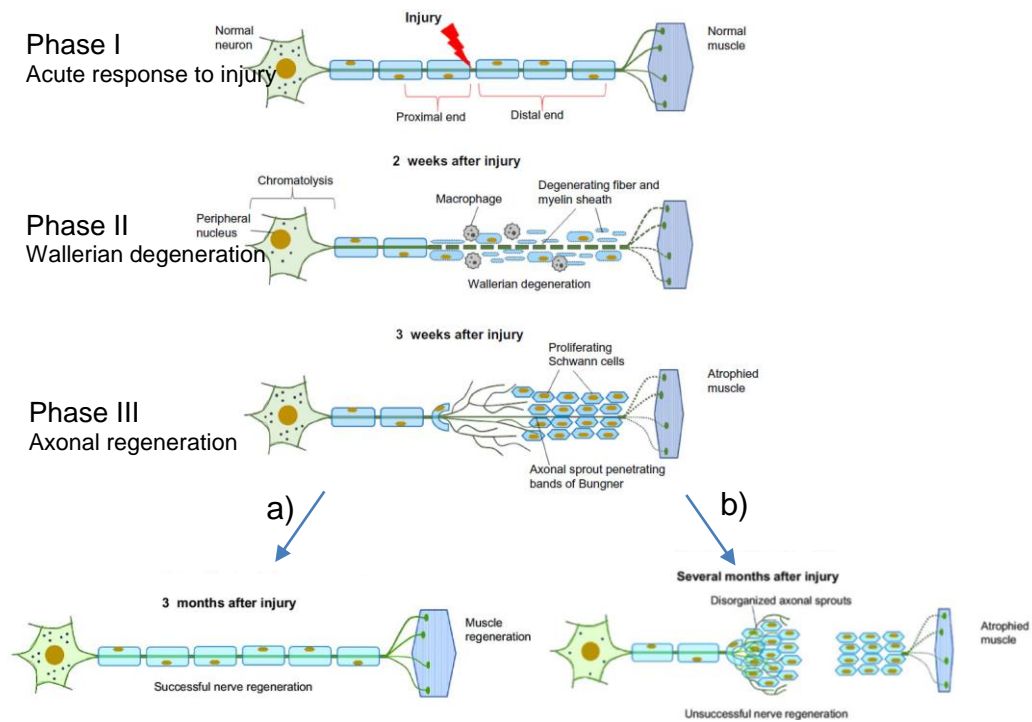


Figure 1.9. Representation of Wallerian degeneration process of a neuron after an acute nerve injury. Phase I, increased cell population at the injury site; Phase II, axonal degeneration as result of the inflammatory and immune response – Wallerian degeneration. Phase III, beginning of axonal regeneration with subsequent remyelination. The result of the injury process can lead to a successful nerve regeneration or an incomplete reinnervation with disorganised axonal sprouts.[31].

After an acute injury, the axonal skeleton disintegrates, and its membrane collapses (Figure 1.9, Phase I). With the degradation of the cytoskeleton and membrane, macrophages and monocytes are impelled to migrate into the nerve stumps to degrade the myelin sheaths and remove axon debris (Figure 1.9, Phase II), while Schwann cells proliferate to form bands of Büngner (Figure 1.9, Phase III). During this process, neurotrophic factors are released, and ECM molecules are secreted to

stimulate axonal regeneration (Figure 1.9, Phase III). This happens from the proximal stump and continues toward the distal stump. New axonal sprouts are emanated from the Nodes of Ranvier, with simultaneous axon remyelination performed by Schwann cells. When nerve fibres are successfully repaired, the regenerating axons grow until they reach their synaptic target and restore functional reinnervation (Figure 1.9, Phase IIIa), which occurs in a rate of about 2-5 mm per day in humans. Otherwise, disorganised axonal sprouts are formed, and the synaptic target is never reached (Figure 1.9, Phase IIIb).[32].

1.3 CURRENT THERAPIES

Despite the low neuroregeneration rate, PNS still shows certain degree of self-repair which leaves an open window for improvements in the regenerative mechanisms of the nerves. Depending on the nerve damage, injured axons may spontaneously grow to re-establish synaptic contacts with denervated targets. Treatments for peripheral neuropathy seeks the overall rehabilitation of the affected nerve, which is determined by degree of the damage, symptoms and location. The current therapies for nerve injuries can be divided into two stages, post-injury and long-term recovery, following mainly two different approaches according to the symptoms perceived: surgical procedures and functional rehabilitation. Those can be also complemented with administration of medicines and physiotherapy. Generally, according to NHS, nerve starts to heal three or four weeks after the initial treatments, and it grows on average one inch per month.[33, 34].

1.3.1 Surgical Procedures

Immediately after diagnosed nerve injury, palliative care is provided to prevent swelling and to reduce the risk of secondary injuries, which are followed by surgical procedures to reconnect the nerve ends, with/without aids of a nerve graft, typically an autograft – healthy nerve portion from the own patient [35]. Sutured nerves can remedy major damage, but the reconnection is often mismatched, causing the loss of the original nerve function. Furthermore, this approach is not suitable for long nerve gaps due to undesirable tension created in the nerve cable that inhibits nerve regeneration. To address this problem, clinicians have used a tissue graft to fill the nerve gap, which

can be provided from the own patient (autologous tissue grafts) or from other sources (non-autologous tissue grafts).[36].

Autologous Tissue Grafts

Autologous tissue grafts consist of portion of tissue isolated from another site of the body to fill in the impaired nerve, which can be nerve tissue or not. Common autografts are derived from cutaneous nerves, such as the sural or saphenous nerve. Muscle and vein have also been used in clinical practice but to a lesser extent. Current research has looked into other autologous grafts, such as epineurial sheaths, tendon grafts, muscle-vein grafts, inside-out vein grafts with incorporation of autologous Schwann cells.[37].

The use of this type of grafts covers the major drawbacks of the suturing approach and is 100% compatible (no rejection), but it is achieved at the expenses of the common loss of the nerve function at the donor site, to add the inconvenience of the multiple surgeries required [4]. Further, there is an eminent increased risk of infection at the donor site and failed reconnection with possible necrosis of the grafted tissue. Additionally, they are difficult to isolate, control the scale-up due to limited availability, there are limited number of locations that serve as a donor site and the regeneration is always incomplete.[4].

Non-Autologous Tissue Grafts

To prevent further damage to patient's nerves, non-autologous grafts, i.e. grafts from foreigner donors, have been considered. Donor tissues can be obtained from cadavers (allografts or homografts) or from animals (xenografts or heterografts). In contrast to autografts, there are no restrictions in terms of availability and dimensions, and do not inflict more damage to patients. However, there is the risk of transmission of pathogens and the possible immune response with consequent rejection. Attempts to cope with these issues include the administration of immunosuppressive drugs and the removal of cell-mediated immune components from the graft – acellular grafts. However, these purification processes still need to be improves to preserve the structure of the tissue, and have led most physicians to discard this practice and elect autografts as gold standard for nerve repair in gaps over 3 cm.[4].

1.3.2 Functional Rehabilitation

After the recovery from the surgical procedures, individuals may undertake long-term physiotherapeutic sessions and exercises to strengthen muscle, vital functions, and to reduce neuropathic pain, that can be supplemented with medication. Muscle function can also be assisted and improved with uses of braces or splints that hold the affected limb, fingers, hand or foot in the proper position [38]. In more acute symptoms of injured autonomic nerves, such as shorten breath or irregular heartbeat rate, pacing systems or other medical devices may have to be implanted immediately to reinstate the normal involuntary functions through electrical impulses sent at a specific pace determined by the body's needs [39]. These devices have also been explored to complement the rehabilitation process of mild nerve injuries. This includes nerve stimulation devices, with similar operation of pacing systems, that are used for pain relief and/or for restoring the motor and sensory functions through a deliverable small electrical current applied internally or externally near the impaired nerves. Examples of such devices are transcutaneous electrical nerve stimulation (TENS), vagus nerve stimulation devices, epineural and intraneural electrodes and cochlear implants. Although this clinical practice was initially used for regulating nerve functions and treating symptomatic chronic neuropathic pain, studies over the years have revealed evidence of improved regeneration of damage nerve tissues.[40]. However, despite the advances in the nerve repair, full recovery from the diverse array of neuropathic conditions has not been properly accomplished yet with the current therapies [41].

Traditional Peripheral Nerve Interfaces

Different types of peripheral nerve interfaces (PNIs) have been developed either to record or electrically stimulate individual fibres or the whole nerve (Figure 1.10). These devices can detect and covert ionic currents from nerves into a readable electrical signal of an electronic equipment, acting as a bridge between an external device and nerves – interface. This depends on the affected nerve, type of damage and symptoms. In general, PNIs consist of electrodes embodied into a non-metallic wafer, which can vary in geometry, complexity and invasiveness to meet the desired selectivity and spatial resolution. It can be a simple cuff electrode or a more robust Utah slant electrode array (USEA). When targeting individual nerve fibres or motor units, more invasive PNIs are used to reach specific nerve fibres. Good spatial

resolution and enhanced functionality can be simply achieved with increased number of electrodes.[42, 43].

The electrical principles behind stimulation and recording are fairly similar. However, when recording, the currents used are some orders of magnitude smaller and flow in opposite direction, in contrast to those in stimulation mode. During electrostimulation with a traditional PNI, an electrical current is purged towards the electrode, which creates a gradient of extracellular electrical potentials that may induce a nerve impulse; whereas, when recording, the variations occurring in the membrane potential generate a current that flows towards the electrode.[42, 43].

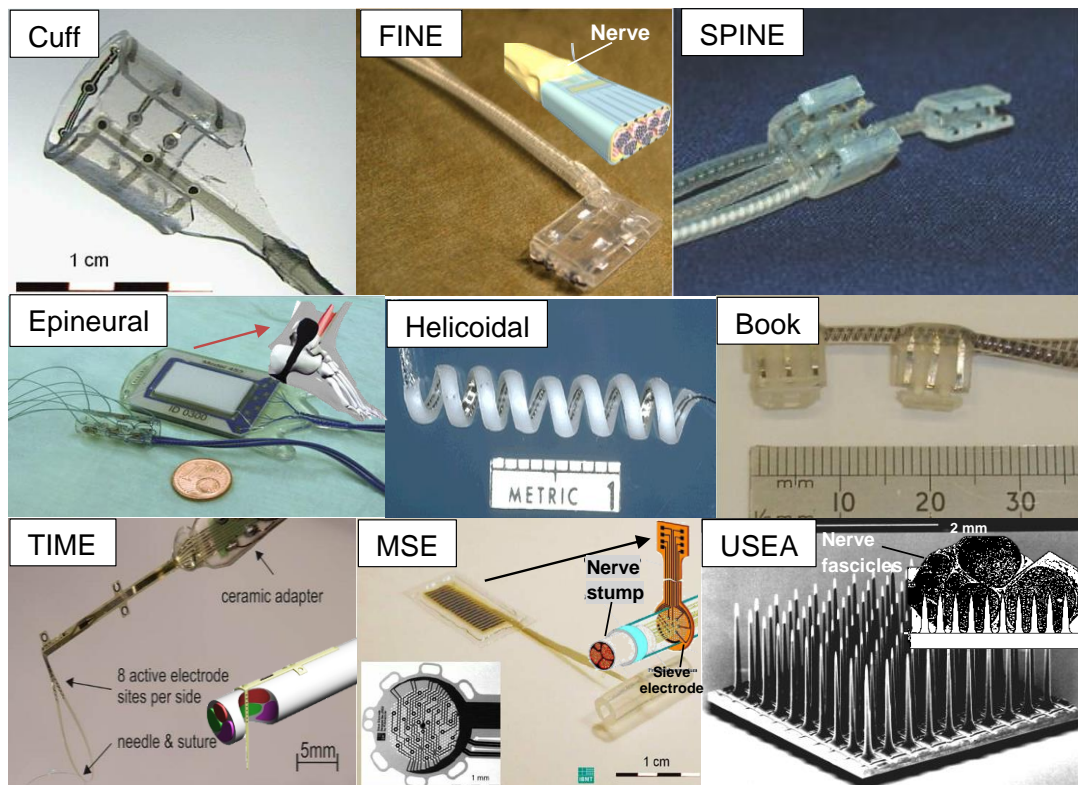


Figure 1.10. Examples of typical neural electrodes available commercially for interfacing with the PNS. Cuff electrode [44], flat nerve interface electrode (FINE, from MachineDesign), slowly penetrating interface nerve electrode (SPINE [45]), epineural electrode (from Finetech Implantable Drop Foot), helicoidal electrode (from Huntington Medical Research Institute), book electrode (from Finetech-brindley), transverse intrafascicular multichannel electrode (TIME, [46]), macro-sieve electrode (MSE, [44]), Utah slanted electrode array (Reproduced by permission from Annals of Biomedical Engineering, Spring Nature, Vol. 34, Issue 2 [47] Copyrights 2006, inset image [48]).

PNI with stimulation and recording modality have been developed to treat numerous neuropathic disorders (Table 1.1) and can be classified, according to their invasiveness, into extraneural and intraneural electrodes.

Table 1.1. Types of PNI electrodes, and general applications and status [43, 49–52].

Peripheral Nerve Interfaces				
	Type	Mode	Application	Status
Extraneural electrodes	Cuff	Recording/ Stimulation	Functional electrical stimulation control, chronic pain, loss of hearing.	Research/ Clinical practice
	Flat-interfaces	Recording/ Stimulation	Localized application of medication, chemical removal, limb motion measurements.	Research
	Interfascicular		Research on the function of the nervous system, treatment of neurological disorders, and motor control and sensory feedback signals.	Research/ Clinical practice
	Epineurial	Stimulation	Breathing, drop foot.	Clinical practice
	Helicoidal	Stimulation	Seizure suppression, sleep apnea.	Clinical practice
	Book	Stimulation	Bladder management. Retinal implant.	Research/ Clinical practice
Intraneural	Intrafascicular	Recording/ Stimulation	Artificial limb control.	Research
	Penetrating microelectrodes	Recording/ Stimulation	Measurement of multiunit peripheral nerve activity.	Research/ Clinical practice
	Regenerative	Recording/ Stimulation	Artificial limb control.	Research/ Clinical practice

The electrode contacts in extraneural electrodes are placed externally around the nerve surface, while in intraneural electrodes, these are pierced inside the nerve towards individual targeted fibres. Nowadays, there exist a sort range of PNIs, including cuff, flat-interfaces, interfascicular, epineural, helicoical, book,

intrafascicular, penetrating microelectrodes, and regenerative electrodes (see Figure 1.10 and Table 1.1).[53, 54].

Cuff and flat interface nerve (FINE) electrodes (see top row of Figure 1.10) represent some of the simplest and most affordable type of implantable PNI, which consists of a silicon tube with two or more electrode contacts on the inner surface which are positioned around the nerve. This allows a fair signal recording/stimulation with minimal invasiveness and hence, minor damage to the nerve tissue.

Other similar electrodes are the epineural and helicoidal (see middle row of Figure 1.10), that holds longitudinal strips of insulating material with two or more contact sites, and are sutured to the epineurium (epineurium electrode) or placed circumjacent the nerve in a helicoidal manner (helicoidal electrode). In book electrodes, a silicone rubber flap wraps the nerve in contact with platinum foil electrodes, which are connected through copper wires to an implantable control unit.

In contrast, intraneural electrodes, like longitudinally implanted (LIFE, intrafascicular electrode), transverse intrafascicular multichannel electrode (TIME) and USEA (microelectrode arrays – penetrating electrodes), and macro-sieve (MSE, regenerative electrode) show an excellent selectivity since the electrode probes are penetrated inside the nerve in direct contact with nerve fascicles or fibres. One of the major drawbacks of these PNIs is the high invasiveness, that can damage the nerve fibres and it raises questions for long-term implantation.

Other nerve interface electrodes, like slowly penetrating electrode (SPINE), have been also developed and can be categorised between cuff and intraneural electrodes, either in terms of performance, or invasiveness. They consist of a silicone tube with blunt elements extending radially into the lumen of the tube. SPINE belongs to the class of interfascicular electrodes, which brings together the simplicity of the extraneural electrodes with the axonal proximity contact and the selective stimulation of intrafascicular electrodes.[43, 49–52].

Overall, the current PNIs available offer an exceptional performance for a diverse range of neuronal disfunctions. However, the very harsh configuration and the composing materials of these electronic devices raise questions of biocompatibility and long-term use [55].

1.4 NEW STRATEGIES

The escalated advances in nanotechnology have enabled robust PNIs with outstanding functional performance being developed. The inappropriate connection with the biological tissues has, however, led to a mismatch in the performance from both engineering and biological sides, which ultimately limits its life span. With the emergence of Tissue Engineering (TE) as a research field, the biological interactions established with implantable medical products and devices, enlightened researchers in the field for the importance of building proper bioelectronic interfaces that can be accepted by the host environment, with usage of non-cytotoxic and 3D micro- and nanostructured materials, with suitable biochemical and physical cell guidance.[4, 54].

1.4.1 Nerve Tissue Engineering

TE strategies are attempting to create novel products that can enhance axonal regeneration, through physical or mechanical guidance cues, cellular components and biomolecular signals. The current strategies for nerve tissue engineering (NTE) focus on bridging the nerve gap and physically guiding axonal regeneration – nerve guides – with nerve conduits (nerve guidance conduit or nerve guidance channel, NGC) equipped with an internal microstructure to resemble the native anatomy and structure of the nerve trunk and fascicles. With this approach, the dispersion of regenerating axons within the NGC lumen and the polyinnervation of different targets can be significantly reduced. An ‘Ideal Neural Tissue Engineering Graft’ (Figure 1.11) requires proper materials’ selection, configuration and fabrication method, combined with appropriate physicochemical and biological cues.[36, 41].

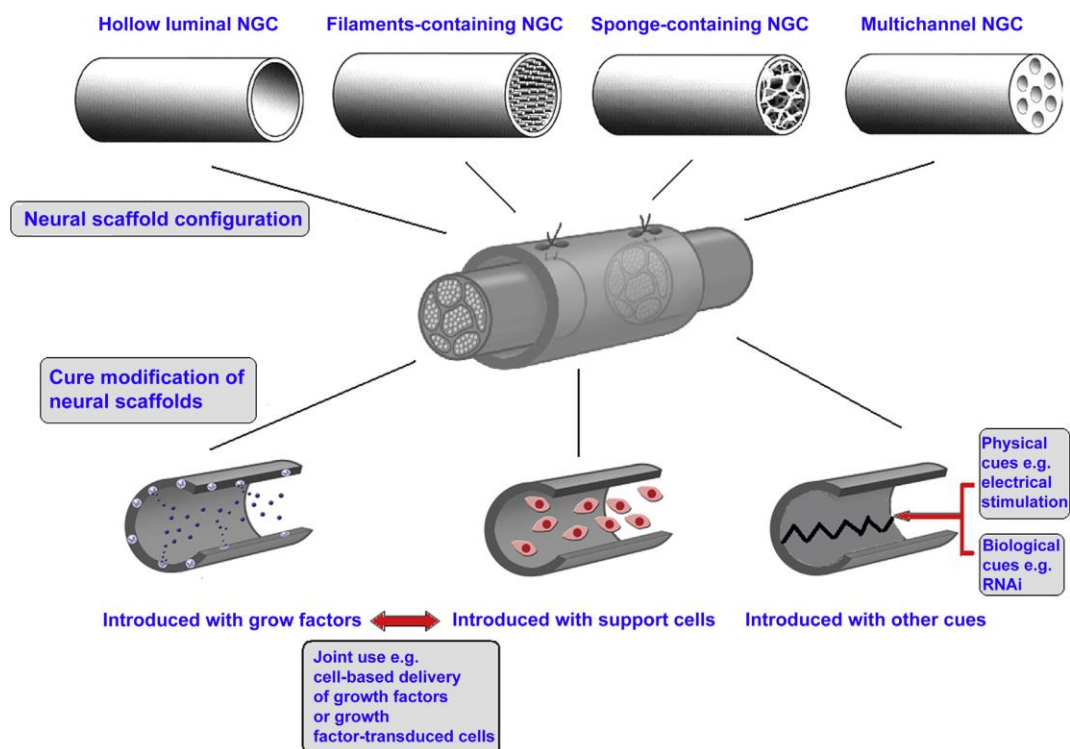


Figure 1.11. Schematic diagram of an ideal tissue engineering nerve graft (TENG) with a sort range of physical, cellular and biomolecular cues. This TENG consists of a nerve conduit with different internal microstructures (internal channels or matrix) and porosity, with possible incorporation of cells and growth factors (Reproduced by permission from Biomaterials, Elsevier, Vol. 35, Issue 24, [36] copyright 2014).

Different internal microarchitectures can be obtained with introduction of one or more intraluminal channels (multichannel NGCs), use of fillers, or the combination of both. While multichannel NGCs haven't shown visible benefits compared to single NGC, the incorporation of nanobiomaterial-based fillers in the form of gels, sponges, fibres or filaments, have been demonstrated to favour axonal regeneration, especially for longitudinally aligned along the NGC. This has been attributed to the similarities with ECM that enables guidance of Schwann cells, successful ingrowth of blood vessels, an adequate diffusion of nutrients and other molecules.[36, 37].

A wide range of materials, typically polymers, either natural or synthetic, have been used for the fabrication of these nerve guides. Natural-derived polymers obtained from ECM molecules, have been often used and already commercialised as nerve graft products, since those are naturally occurring in the nerve tissue. These include collagen, laminin, fibrin, fibronectin, and hyaluronan, and other polysaccharides,

including glycosaminoglycans, chitosan, alginate, agarose and proteins, like silk fibroin and keratin.[56].

Synthetic polymers have been increasingly investigated owing to their availability and non-immunogenicity, compared to majority of the natural polymers. Examples are silicone, poly(glycolic acid), poly(lactic acid)-based, poly(ϵ -caprolactone), polystyrene and poly(2-hydroxyethyl methacrylate-co-methyl methacrylate), which have shown satisfactory results to construct artificial ECM. Other materials, such as ceramic, carbon, metallic-based materials and electrically conducting polymers (e.g. polyaniline [PANI], polypyrrole [PPy]), have also been considered to reinforce the mechanical and electrical features of the established NGC. In particular, electrical stimulus relayed through electrical conductive composites have shown experimental evidences of inducing cellular differentiation, remyelination and neuritis extension upon electrical charges.[57]. However, the incorporation of these materials for NTE applications still needs to be extensively studied and as far as it is known, there is no commercialised nerve graft imparting electrical features up to now.

1.4.2 Tissue-Engineered Neural Interfaces

When interfacing with the PNS, it is critical to understand how the electrical activity of the nerves can be measured and accordingly stimulated. The proximity of muscles, tissue movement, and tissue compression have to be carefully considered when recording from nerves, as these elements can interfere with the nerve signals, lowering the signal-to-noise ratio. As seen in the previous section, nerves are formed by several fascicles with each fascicle consisting of multiple nerve fibres. These fibres have nodes of Ranvier, from which the largest electrical nerve activity is originated and detected. Those are regularly interspaced by 0.2 to 2 mm along the individual fibres, which create a 3D spatial distribution of nodes of Ranvier throughout each nerve. Depending on the size and location, an ideal neural interface demands also similar 3D nature, which is not exclusively limited to the geometric and structural aspects. For building an ideal PNI, physical and electrical symbiosis between the nerves and the interface should be encouraged, while allowing axonal growth near and along the electrode site. Bioelectronic interfaces to peripheral nerves must contend with the heterogeneity in nerve geometry, fascicular arrangement, and fibre composition.[54].

The future generation of PNIs seeks the usage of nanomaterials and nanotechnological tools available to engineer such devices with predetermined designs and soft materials inspired by the anatomic, structural and physiological aspects of the nerve tissue. These hybrid devices will have dual functionality: replace the nerve function via electrostimulation, while promoting axonal regeneration. The current state-of-the-art of NTE will allow a deeper understanding of the regenerative needs of the nerve tissue to attain a synergistic integration between the PNS and the developed PNI, at structural, physicochemical, biomolecular and cellular levels.

1.5 SUMMARY

Peripheral neuropathy represents a great fraction of the problems affecting the NS, which may cause failure of motor, sensory and vital functions. To date, the surgical procedures do not provide full functional recovery and the PNIs, used to restate some of these, show very harsh designs with non-biologically friendly components which compromise the biocompatibility, performance and long-term stability in a cascade of events. A comprehensive knowledge of the anatomy, structure and physiology of the PNS is underlying brand-new medical products, which is the blueprint of the more advanced alternatives offered by the current research field of TE. At the same time, NTE grafts commercially available lacks suitable electrically conductive properties that is overall accepted to benefit axonal regeneration and consequent reinnervation. The new generation of PNIs aims to bring together the nanotechnological advances of bioelectronics with the conceptual tools of TE to fully address the functional, morphological and regenerative issues of impaired nerves.

1.6 AIMS AND OBJECTIVES

Based on the present exposition, this thesis aims to develop a novel material formulation as a pathway towards a next generation of PNIs with enhanced functional and biocompatible capabilities, to eventually treat a wide span of neuropathic conditions – Tissue-Engineered Neural Interface (TENI). This novel product will result from cooperative efforts to break new ground of the traditional PNIs and combine them with the understandings provided by TE. A 3D electrically conductive composite material with nanoscale features may benefit a synergistic interaction with

the cellular and biomolecular components naturally occurring in the PNS, and thus providing a more biologically friendly environment when compared to the present-day neural electrodes.

An adequate choice of materials is of the highest importance. That being said, the main objectives of this thesis can be identified:

1. Produce electrically conductive bacterial cellulose (BC) nanocomposite membranes with nanoscale electroactive moieties;
2. Optimise the electrical properties and the overall synthesis process;
3. Evaluate the potentials of the developed nanocomposites for biomedical applications, and in particular for TENIs.

1.7 STRUCTURE OF THE THESIS

This thesis is structured into 9 chapters, schematically illustrated in the flow charts of Figure 1.12 and 1.13, which contains (1) Introduction, (2) Literature Review, (3) Research Methodology, (4 to 8) main Results and Discussion, and (9) final Conclusions and Future Recommendations.

In the following chapter, Chapter 2 – Literature Review –, a systematic technical literature review of the current uses of BC in the medical field and possible routes to electrically modify BC with polyvinylaniline (PVAN), polyaniline (PANI) and carbon nanotubes (CNTs) to match the requirements of a TENI are discussed.

All materials and methods used to develop and characterise this BC-based TENI are described in Chapter 3 – Research Methodology. Essential information on the procedures adopted are carefully discriminated, with some methodological fundamentals to allow well-founded discussions in the following chapters.

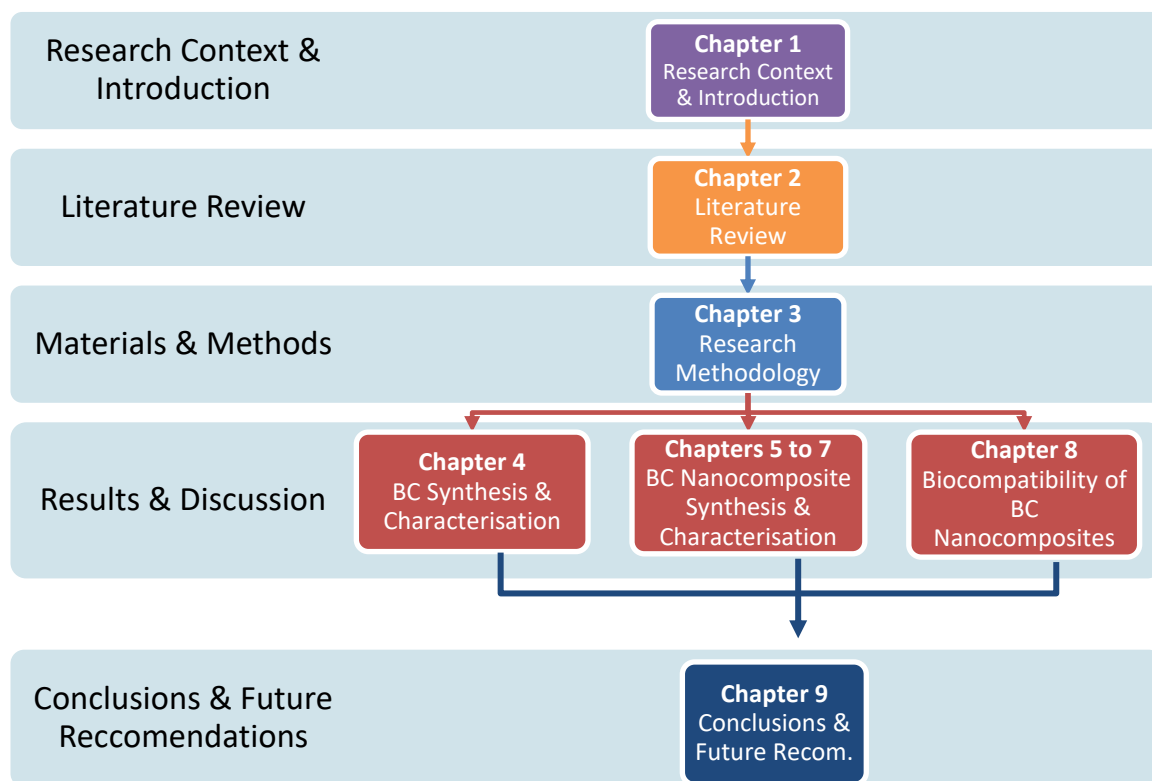


Figure 1.12. Flow chart of the structure of the thesis.

Chapters 4 to 8 embody the main results of this research, with chapter 4 related with BC synthesis, chapters 5 to 7 with the development of the electrically conductive BC-based nanocomposites (Figure 1.13) and chapter 8 with the biological characterisation of the materials produced in chapters 4 to 7.

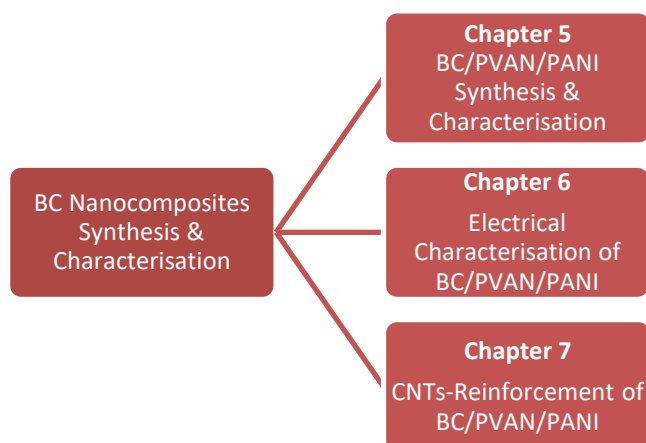


Figure 1.13. Chapters involved on the synthesis and characterisation of BC-based nanocomposites.

Finally, Chapter 9 – Conclusions and Future Recommendations – summarises the main findings and conclusions of this research, with recommended potential biomedical applications. Further work is also suggested for improved biofunctional performance for possible introduction into clinical practice as a medical device/product.

Chapter 2: Literature Review

This chapter intends to give an overview of the current status and methods to produce electrically conductive BC nanocomposites and reviews literature on the following topics: cellulose and its relevant properties for biomedical applications, with particular focus on BC (section 2.1); present strategies to chemically modified BC in order to acquire additional functional properties for targeting specific applications (section 2.2) and in particular with PANI, which is an intrinsically conducting polymer (section 2.3); section 2.4 reviews possible synthetic routes to obtain different PANI products, especially as regards steric stabilisation using PVAN; section 2.5 briefs the most important features of CNTs, with their electrochemical interactions with PANI in composite materials (section 2.6). Finally, section 2.7 highlights the implications from the literature and develops the conceptual framework for the study.

2.1 CELLULOSE

The urgent development of scalable devices from biosources has led researchers to embrace cellulose with extensive investigations on its properties and physicochemical modifications to tailor relevant applications, in particular in the biomedical field.

Cellulose is the most abundant available biomass on Earth and as such, it has gained immense interest as an industrial material for numerous applications. It can be found in plant cell walls, such as in wood, plant leaves and stalks, some fungi like algae, cotton fibres and it can be also synthesised by certain bacteria strains (Figure 2.1). In general, this polysaccharide has a microfibrillar structure endowed by high tensile strength, high water absorption associated with outrageous hydrophilic nature, superior thermal stability and crystallinity.

Cellulose has been recognised for many industrial applications, such as paper products (paper, paperboard, cardboard, packages), textile fibres, inactive fillers in drug tablets, additives in manufactured foods and laboratory consumables. With the emergence of TE, cellulose has been also exploited for a wide range of tissue grafts,

wound dressings and other medical devices. For most of the applications, cellulose is extracted from wood-pulp or cotton, which often requires extensive processing to remove undesirable components which are present naturally in plant-derived cellulose, in particular hemicellulose, lignin and pectin. Therefore, the research focus is on cellulose-based materials has moved towards microbial cellulose that, not only presents a much higher purity and yield, but it has also shown overall superior properties, such as higher mechanical strength, crystallinity, thermal stability and more interesting structural characteristics.[58].

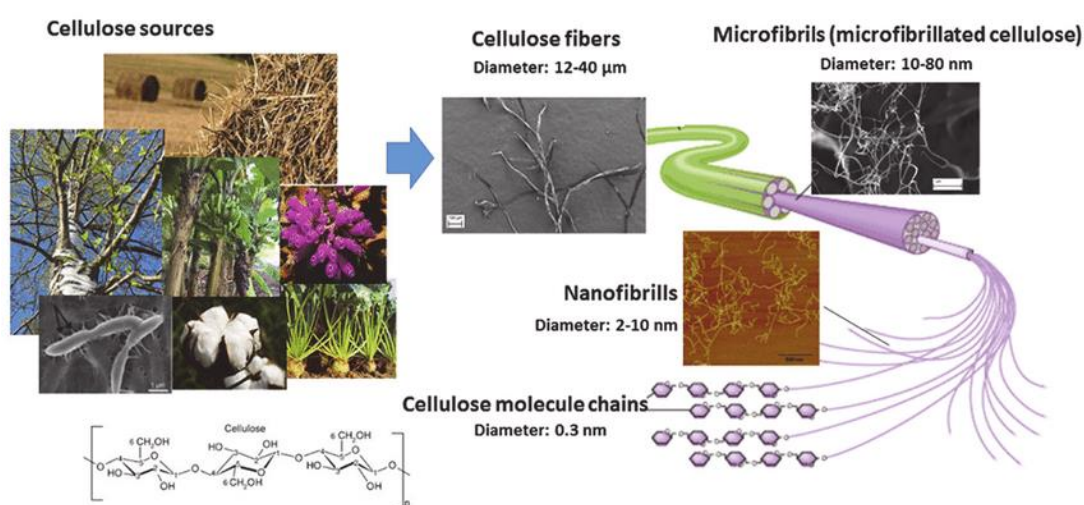


Figure 2.1. Different sources from where cellulose can be extracted, including plants, cotton and bacteria. Microscopic morphology of cellulose fibres, microfibrils and nanofibrils, with their schematic representation at molecular level (from alvenotes.com and [59]).

2.1.1 Bacterial Cellulose

Microbial cellulose or bacterial cellulose (BC) was first described by Anselme Payen in 1838 with *Acetobacterium Xylium* and later recognised by A.J. Brown in 1886. But it was only from the 20th century that sufficient attention started driving scientists into deeper investigations on this type of cellulose. BC is synthesised by growing certain species of bacteria in a proper culture medium containing a high-carbon source, such as glucose and fructose. Despite the similar molecular structure, BC possesses quite distinct properties, which is different from those of cellulose plant-based.[60].

The as-obtained BC is a film with a 3D nanofibrillar network, in which all nanofibres are surrounded by large amounts of water which constitutes nearly 99% of its total weight. The absence of impurities along with the demonstrated biological affinity attributed to the peculiar microstructure, has rendered its approval by the US Food and Drug Administration (US FDA) as a material for various biomedical applications, including wound dressings, artificial skin, hemostatic materials, artificial vessels and electronic platforms (see Table 2.1 and section 2.2).[61]

Chemical Structure

Chemically, BC as other kinds of cellulose, is formed by a long-chain of D-glucose repeating units that are linked together through β -D (or β -1,4)-glucosidic bonds between the carbon C1 of one glucose unit and the C4 of the adjacent unit (Figure 2.2a). Owing to the hydrogen bonds established between the multiple hydroxyl groups (OH) and the oxygens (O) within the same and with neighbouring chains, BC adopts a supramolecular structure with a stiff rod-like conformation (Figure 2.2b). This relatively compact and OH-rich molecular structure is responsible for some of its most remarkable properties.[62]

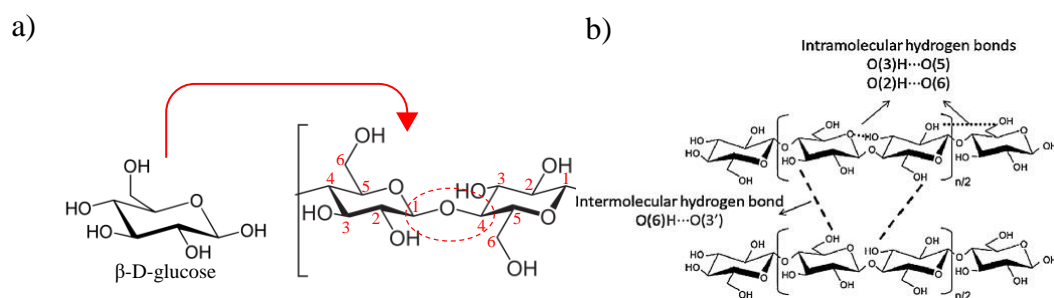


Figure 2.2. Chemical structure of (bacterial) cellulose. a) Molecular structure of cellulose repeating unit, cellobiose, showing the β -1,4 linkage between the two D-glucose units. b) Supramolecular structure with intra- and intermolecular hydrogen bonds established between adjacent cellobiose units and other cellulose chains, as well as within the repeating unit (Reproduced by permission from Carbohydr Polym, Elsevier, Vol. 133, [63] Copyrights 2015)

Crystal Structure

Both plant-cellulose and BC have their crystalline and amorphous domains alternately disposed. However, in BC, the number of crystalline regions are significantly superior when compared to those found in plant-cellulose (Figure 2.3), and hence, it is observed a higher crystalline degree with consequent enhancement of the tensile strength.[64]. The high crystallinity along with the high purity, are also responsible for the elevated thermal stability and biocompatibility, which can act as a thermal stabiliser and it is attractive for building thermally stable medical devices. This upraised thermal stability presents also advantages in the sterilisation process that can be performed easily and inexpensively using temperatures over 100 °C (e.g. autoclaving) while preserving their physicochemical properties [65].

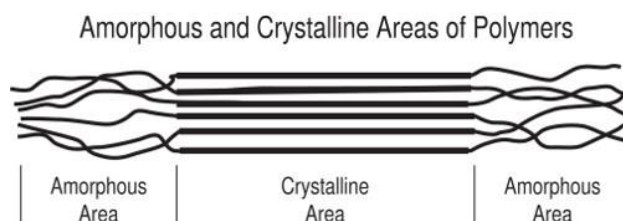


Figure 2.3. Illustration of the amorphous and crystalline domains of cellulose [66].

BC possesses a crystallographic structure type I (Cellulose I) that is further subdivided into I_α and I_β , showing prevalence of the I_α type. Both dimorphisms I_α and I_β share similar chain conformation, except their longitudinal stacking, in which I_α adopts a triclinic crystallographic symmetry with a square-like shape, whereas I_β shows a monoclinic symmetry with a parallelogram-like shape. I_α unit cell includes one cellulose chain in a P1 (crystallographic) space group and I_β unit cell is composed of two cellulose chains that belongs to the P21 space group. The crystallographic structures and the respective unit cell parameters are present in Figure 2.4.[63].

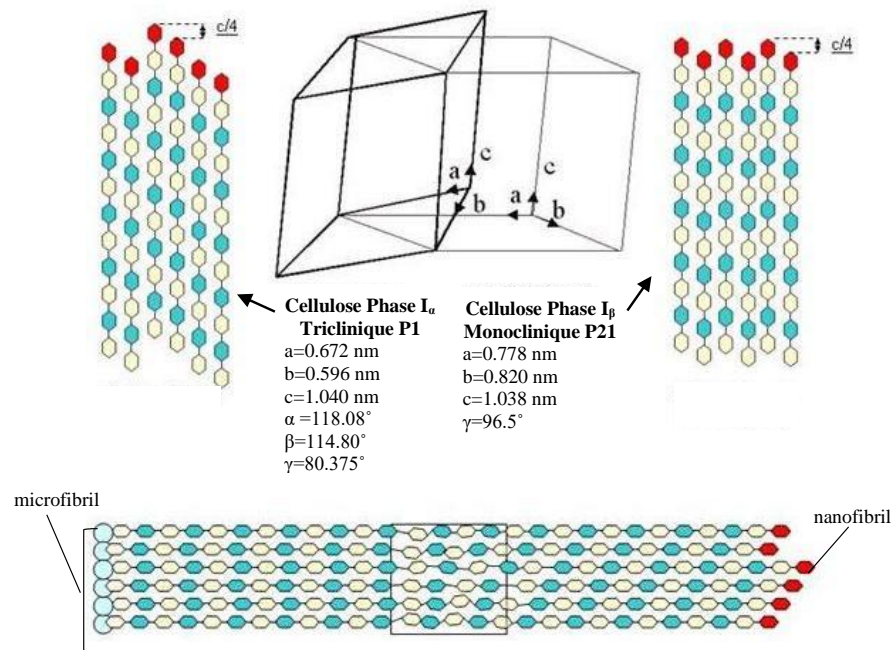


Figure 2.4. Crystal form of cellulose type I found in BC, with a schematic representation of the coexisting allomorphisms, I_α and I_β crystal units, within the same microfibril. Disorganisation of the microfibrils can occur (amorphous area), as marked in the squared area (adapted from [67]).

Biosynthesis

BC is synthesised extracellularly as a fibrous material by gram-negative bacteria, such as *Gluconacetobacter*, *Acetobacter*, *Agrobacterium*, *Achromobacter*, *Aerobacter*, *Sarcina*, *Azobacter*, *Rhizobium*, *Pseudomonas*, *Salmonella* and *Alcaligenes*. A thin pellicle is initially formed, that acts a protective barrier preventing the invasion of foreigner organisms, drying and radiation. Over the culture period, this pellicle increases in thickness as bacteria expel cellulose downwards deeper in the culture medium. Under static conditions, the obtained membranes have uneven fibres density across the thickness, different from agitating culture which produces membranes with more uniform fibres distribution.[62].

From a mechanistic point of view, BC synthesis starts with the production of uridine diphosphoglucose (UDPGlc) with subsequent formation of linear-chains of β-1,4-glycosidic via glucose polymerisation. This process occurs inside bacteria and then the polymeric chains are extruded as secondary metabolite through the small pores located in the envelope of the cell membrane (Figure 2.5).

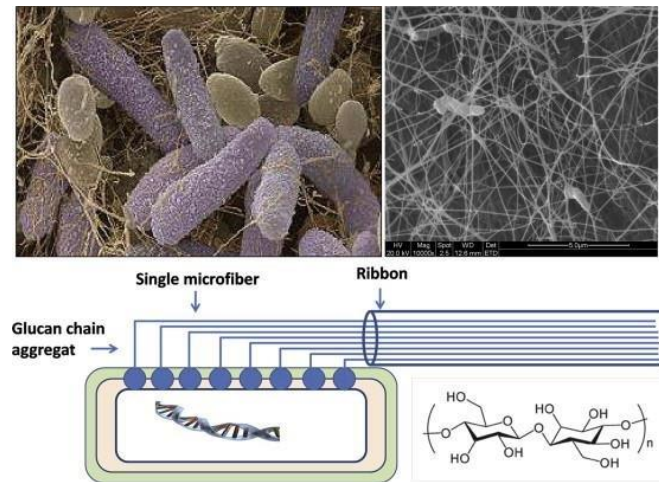


Figure 2.5. Scanning electron microscopic (SEM) images of bacteria colony synthesising cellulose as a metabolic product. Glucan chains are expelled in the form of fibres through tiny pores located in the cellular membrane (Reproduced by permission from Food Hydrocoll, Elsevier, Vol. 35 [68], copyright 2014).

The as-expelled glucose chains bundle together to form branched-chains of nanofibres 3–8 nm width and ribbons with diameters of 40-60 nm, that are arranged in a three-dimensional (3D) web-like network with large open space. Despite BC synthesis is a microbial process, the resulting membranes can have their thickness, shape and microstructure controlled with reasonable consistency.[69].

Commercial Uses

Since its first reported synthesis, BC has been the focus of a large number of biomedical applications with ongoing research in the field. The peculiar features found in the as-synthesised BC, in particular the large surface area of the interspaced nanofibrils with high water content, have inspired scientists to test it for skin-related applications. With US FDA certification, several medical products have been developed and commercialised as tissue grafts and skin replacements, such as biofill®, bionext® and gengiflex® (Table 2.1). Other applications include supporting proteins, cell culture and microorganisms.[62, 70].

Table 2.1. Commercial products based on BC and their applications (adapted from [62] and [70]).

Brand	Product type	Application
Biofill [®]	Temporary skin substitute	Ulcers, burns
Bioprocess [®]	Wound dressing	Ulcers, burns, lacerations
Dermafill [®]	Wound dressing	Ulcers, burns, lacerations, grafts
Gengiflex [®]	Dental implants, grafting material	Recovery of periodontal tissues
Bionext [®]	Wound dressing	Ulcers, burns, lacerations
Membracell [®]	Temporary skin substitute	Ulcers, burns, lacerations
Xcell [®]	Wound dressing	Venous ulcer wounds

2.2 CHEMICAL MODIFICATION OF BACTERIAL CELLULOSE

Despite the multiple uses of BC-based materials, chemical, physical or physicochemical modifications are often recommended in order to fully exploit the potential functionalities of BC targeting specific applications. Electrical functionalisation is required for a wide range of biomedical applications, such as electrostimulated drug delivery systems [71], biosensors [72], bioelectronics [73] and tissue regeneration [74]. The development of BC-based composites containing electrically conductive materials can be a possible route to address the above-mentioned applications.

By definition, a composite is a material that is constituted of a matrix, often polymeric, that supplies a homogeneous and monolithic physical phase, in which a reinforcing agent is imbedded to boost the likelihood of a specific response or behaviour, such as mechanical, thermal, chemical and electrical.[75]. BC can be chemically modified following *in situ* or *ex situ* strategies, i.e. via incorporation of exogenous molecules during or after BC synthesis, respectively. Both approaches can successfully introduce new functionalities to BC, however showing significant different characteristics. In the *in situ* polymerisation, the introduced molecules affect the intrinsic properties of BC upon chemical interactions, creating new interconnected

hydrogen bridges. On the other hand, in the *ex situ* approach, the as-synthesised and purified pristine BC is subjected to chemical functionalisation, that usually consists of direct immersion of BC matrix into a solution containing the modifier-substance.[65]. In contrast to the *in situ* methodology, with *ex situ* polymerisation the original BC structure remains practically intact and only nanosized materials would be able to impregnate the nanostructure through diffusional mechanisms. Moreover, the *ex situ* polymerisation can assume a variety of forms on the account of the large surface area of network membranes with a hydroxyl-rich backbone. Thus, monomeric, reactive and potentially polymerisable chemical species can be accommodated into BC matrix interstices, essentially by occupying its void volume and/or interacting with chain segments or pendant moieties of the host hydrogel to produce blends or grafted composites. These characteristics make BC hydrogel an excellent candidate for materials functionalisation.[73].

A vast number of electroactive compounds, such as intrinsically electroconductive polymers (ICPs), CNTs, graphene and metal nanoparticles (e.g. gold, silver) have been successfully impregnated within BC network.[73]. Among these, ICPs and in particular PANI, and carbon nanostructures, have been extensively studied for many electronic related applications. While PANI can permit a fine control over electrical and optical properties [76], CNTs can upgrade the electrical and mechanical properties with their outstanding electrical conduction up to 10^5 S.cm^{-1} , excellent specific capacitance and high tensile strength.[77, 78]. However, both neat PANI and CNTs are usually obtained as intractable and brittle powders with poor processability (see sections 2.4 and 2.5) and therefore, their incorporation into fibrous and absorbent substrates like BC, can potentially overcome these issues through grafting, surface coating technologies or with simple preparation of blends, with no meaningful changes needed to the manufacturing procedures.[79].

PANI has been successfully synthesised by oxidative polymerisation of aniline directly onto BC membranes, via either chemical or electrochemical methods and CNTs have also been efficiently incorporated within BC network with a simple immersion procedure [72, 74]. The dual combination of PANI with CNTs has shown new and superior electrical functionalities that are being investigated in the current literature, presenting unprecedented features for some applications, including bioelectronics. Published work have revealed increased electrical conductivity of

pristine BC from 10^{-4} S.cm⁻¹ to a wide range conductivity values of 10^{-3} - 10^0 S.cm⁻¹ after modification with PANI and/or CNTs, which falls into the category of semiconductive materials (10^{-4} - 10^0 S.cm⁻¹).[72, 73, 80]. In addition, PANI and CNTs can be strongly tethered to BC nanofibrillar structure, different from PANI and CNTs coatings typically employed in electronic devices that show the eminent disadvantage of poor adhesive properties to most of the substrates, typically on metals or other semiconductive materials such as silicon, leading ultimately to the failure of the devices.[81].

Despite the scarce number of studies, the formulation of these composites and especially for BC/PANI/CNTs, would be promising for a broad range of biomedical applications that demand suitable electroactive characteristics and mechanical flexibility (bendable and stretchable). This can be particularly valuable for bioelectronic interface devices that, in addition to the electrical properties, also requires soft materials for perfect match with the soft tissues, question that is being neglected in the current implantable medical devices.[82].

2.3 INTRINSICALLY CONDUCTING POLYMERS

ICPs are polymers which possess inherent electrically conductive characteristics in the semiconductive range that arises from a conjugated electron system in their structure, with high electron affinity and low ionisation potential (Figure 2.6) [76]. Several ICPs have been studied, such as polyacetylene, PANI, PPy, poly(3,4-ethylenedioxythiophene) (PEDOT), polythiophene (PDMBT), poly(p-phenylenevinylene) [PPV] and poly(p-phenylene) [PPP].

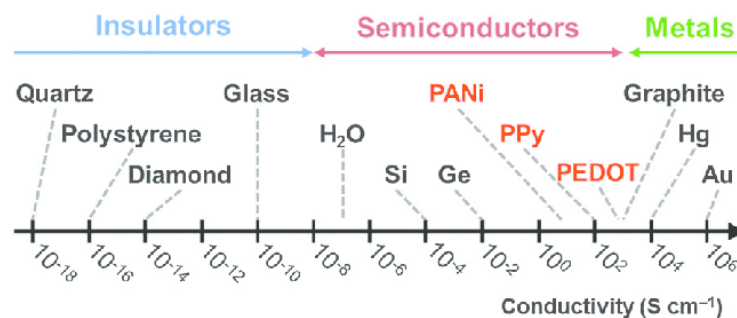


Figure 2.6. Electrical conductivity range of insulators, semiconductor and metals, represented in log-scale [83].

With their semiconducting nature, ICPs have been largely used in a wide range of applications, such as actuators, sensors, artificial receptors, pH-responsive films, electrochromic display devices, energy storage devices and organic electrode coatings. ICPs have also expanded their potential applications into the biomedical field aiming to overcome some of the major drawbacks of metallic biomaterials, especially the poor biointegration, inflammation, mechanical instability with poor flexibility, tissue infections and eventual necrosis, and associated prolonged patient care, pain and loss of tissue function.[84].

Comparable to inorganic semiconductors, ICPs can vary some of its intrinsic characteristics when externally stimulated, including the conductivity, colour, density, magnetic properties, hydrophilicity/hydrophobicity, and permeability to gases and liquids [85]. For instances, the electrical conductivity can be easily controlled by switching the redox states, doping/dedoping process and the supramolecular structures under certain conditions [86]. This versatility explains such broad spectrum of possible applications of ICPs, which may replace the ‘gold-standard’ of metal-based materials used in electrical devices.

2.3.1 Polyaniline

PANI is one of the most studied and used ICPs due to facile synthesis and chemistry, good ion-exchange properties, low-cost production, high capacitance, specific surface area, and environmental and thermal stability, compared to its counterparts.[87]. Other interesting properties of PANI include electro- and solvatochromism, non-linear optical properties and paramagnetism.[85]. Considering these unique properties, PANI has been found to be effective when being used as electrical conductors, batteries, sensors, actuators, electromagnetic shielding, antistatic coatings, corrosion protection, and electro-optic and electrochromic devices.[74].

PANI has a highly organised nanostructure system at molecular and supramolecular levels, responsible for its properties and in particular the conductivity, which can be controlled during the process of synthesis. There is a diverse array of coexisting supramolecular structures of PANI. These can be one-dimensional, 1D, (nanofibres, nanorods and nanotubes), planar two-dimensional, 2D, (e.g. ribbons, nanobelts and nanoplates) and three-dimensional, 3D, particles (microspheres,

nanospheres and granules), that can be further combined into more complex architectures. For applications in nanotechnology that requires reasonably good conductivity with high surface to aspect ratio, one-dimensional (1D) structures are more attractive as high homogeneity, unique surface properties and high charge carrier mobility can be achieved. Comprehending the molecular mechanisms underlying PANI synthesis and their nanostructures is thus, of the highest importance.[88].

Chemical Structure

PANI comprises two types of repeating units, the reduced and the oxidised, each one consisting of two para-substituted aniline units linked together in a ‘head-to-tail’ manner. This regular arrangement of the monomeric units builds a polyconjugated system with a zig-zag configuration lay on a single plane. The number of reduced and oxidised units determines its oxidation level, described with the variable x (between 0 and 1), as shown in Figure 2.7.

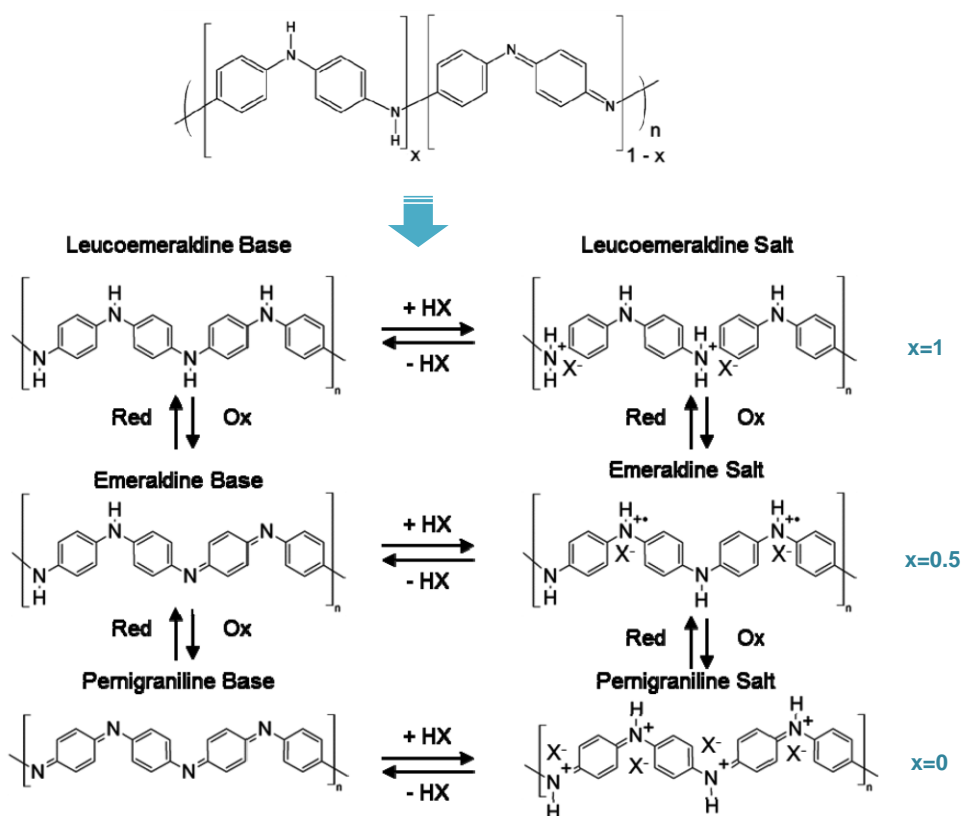


Figure 2.7. Different oxidation forms of PANI. The highest conductive form, emeraldine salt, can be reduced to leucoemeraldine salt that is non-conductive, or can be fully oxidised to pernigraniline that is less conductive than emeraldine. These three oxidation states can be further deprotonated into their respective base forms in a reversible manner (adapted from [85]).

Accordingly, PANI coexists mainly in three different forms: the fully reduced leucoemeraldine ($x=1$), the half oxidised emeraldine ($x=0.5$) and completely oxidised pernigraniline ($x=0$), and each one can be protonated or deprotonated. Virtually, PANI can assume continuum oxidation states ranging from a completely reduced to a completely oxidised form. However, the most chemically stable state is emeraldine, which is also the most conductive.[88].

Electrical Properties

The outstanding electrically conductive properties of PANI arises from the peculiar organisation of the monomeric units, which embodies a mix of electronic and protonic conductivity produced during the protonation of the imine nitrogen atoms resulting in positive charges which are compensated by negatively charged counterions (charge carrier mobility).[89]. The alternating double and single bonds between the monomeric units of the polymer chain forms the polyconjugated system, in which pi (π) orbitals in the series of π -bonds overlap each other, causing the delocalisation of the electrons that can readily circulate (Figure 2.8).[90].

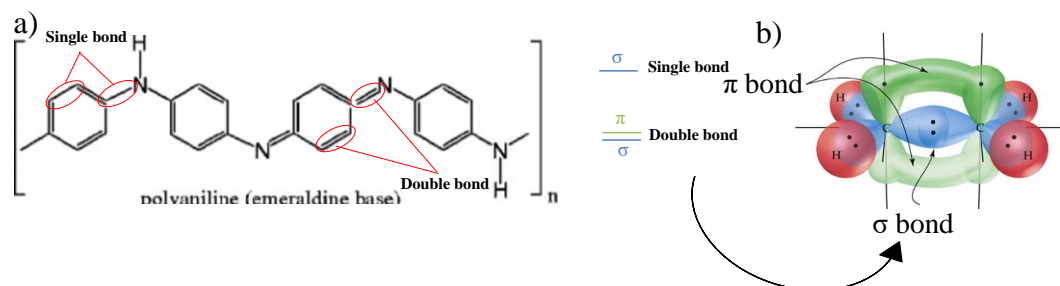


Figure 2.8. PANI in the emeraldine base structure. a) Polyconjugated system showing the alternating single and double bonds in the polymer backbone, formed by sigma (σ) and pi (π) bonds. b) Schematic representation of σ and π orbitals overlapping each other to form a double bond between two carbon atoms (adapted from [91]). σ -bonds gives the strength to the strain, while π -bonds ensure delocalisation of the electrons.

This polyconjugated system can be further elongated upon protonation of the chains with doping agents, as such the p-orbital system is extended through which electrons can more freely circulate. The doping process (or protonation) stabilise and

neutralise the backbone, while introducing charge carriers either by removing or adding electrons from/to the polymer chain.[87]. This results in the relocation of the charges in the polymer chain into polaron and bipolaron structures (Figure 2.9), i.e. a localised state with the present loosely held but confined electron surrounded by a crystal lattice distortion.

Some studies have suggested that the formation of (bi)polarons during protonation results from the interaction between protons (H^+) in aqueous acidic solution and the nitrogen of the imine segment ($C=N$) of EM base chain, followed by the diffusion of protons (H^+) and counterions (e.g. Cl^- from HCl) into PANI. With an applied electrical potential, the heretofore stable backbone is disrupted as dopants start moving across the chain, generating a current in the form of the above-mentioned polarons and bipolarons.[92, 93].

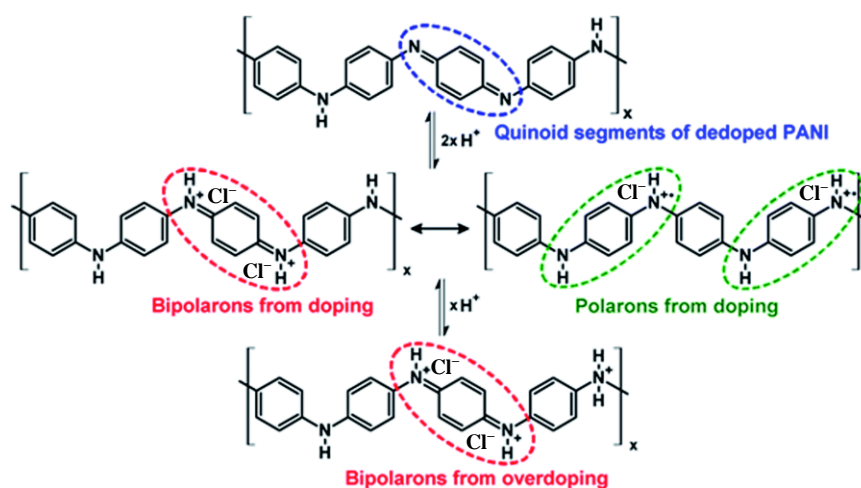


Figure 2.9. Doped and dedoped forms of emeraldine oxidation state of PANI, showing the polaron and bipolaron structures after protonation with HCl. The counterions from the dopant (Cl^- in the present example) compensate the charge carriers introduced after doping.[94].

Strong acids are usually used for PANI synthesis and as doping agent, as they can stabilise the polaron formation during oxidation and further supply PANI with protonic conductivity. Protonation of the chains occurs in the oxidative centres, i.e. imine group, but also amine nitrogen atoms. The nitrogen atoms can capture protons from acid to generate radical cations (NH^+ or NH_2^+).[95]. The degree of protonation

of PANI is determined by its oxidation state, as well as the pH of the solution in which it is immersed.

In total, PANI can be found in six different forms according to the oxidation state and the doping level, as seen previously with Figure 2.7. This results in PANI products with very distinct properties that can only be controlled during the polymerisation process. Defects introduced to this regular structure can be detrimental to the electrical conductivity, as charge carriers are generated during polymer growth. Incorrect addition of monomeric units at different positions (ortho- or meta-), and chemical modifications, such as copolymerisation with other monomers, are examples of some possible defects that can take place. Good electrical, optical and magnetic properties imply thus the development of polymeric chains with proper charge carrier paths. This can be accomplished providing that there is a perfect understanding of the synthesis mechanisms to successfully guide the self-assembling of regular polymer chains at molecular and supramolecular levels.[96].

PANI can reversibly switch between its different oxidation and protonation states. Both emeraldine and pernigraniline are conducting forms of PANI, whereas the fully reduced leucoemeraldine is non-conductive (Figure 2.7). Under typical conditions, protonated emeraldine shows conductivity in the range of 10^0 - 10^1 S.cm⁻¹. Continuous oxidation over a certain level with an oxidising agent (e.g. ammonium persulfate, APS, or electrical potential) causes emeraldine to be transformed into pernigraniline with concomitant decrease of the conductivity below 10^{-2} S.cm⁻¹. The conducting forms can be reversibly converted into leucoemeraldine either by adding an electron to reduce the nitrogen atom (through an applied electrical potential) or by removing the polaron-stabilising acid using a reducing agent (e.g. ascorbic acid, ASCA). This causes the disappearance of polyconjugation and consequent decrease in the electrical conductivity of about eight orders of magnitude to 10^{-8} - 10^{-10} S.cm⁻¹.

Protonated forms of PANI have the acid linked to the main chain via ionic interactions. Deprotonation of the different oxidation states of PANI is achieved by neutralisation of acid with a base, which may lower the conductivity up to 10 orders of magnitude. Owing to the reversibility of the redox reactions, reprotonation/deprotonation cycles can be infinitely performed without losses of PANI properties.[85].

PANI Synthesis

PANI synthesis results from the oxidation of aniline monomer in a chain-reaction with the nitrogen atoms acting as oxidation centres. As a chain-reaction, the polymerisation occurs basically in three steps: the initialisation characterised by an induction stage, propagation when polymer chains grow and termination, when at least one of the reactants is fully consumed. During the polymerisation, the nitrogen atoms from both aniline monomer and the growing chain (oligomer) undergo oxidation. The polymer chains grow with monomer addition to the oligomer in a chain-reaction via electrophilic substitution – the attacking species are oxidised and act as electrophilic agents, transforming π bonds into σ bonds. However, the oxidation of aniline not always result in PANI with a polyconjugated system. Other oxidation products with disordered molecular structure can be obtained in a process called oligomerisation. Whether the oxidation of aniline lead to polymerisation or oligomerisation, strongly depends on the initial reaction conditions as such a polyconjugated system can be efficiently formed.

In general, successful aniline polymerisation occurs in low pH medium and under action of an oxidising agent, that can be a chemical compound (oxidant) or an applied electrical potential. In both cases, a certain oxidation potential has to be exceeded to ensure the oxidation of both aniline monomer and oligomer, that is dependent on the different dissociation constants of aniline monomer ($pK=3.5$) and the imine groups of the propagating chains ($pK=2.5$), as shown in Figure 2.10.

Low pH medium ensures adequate protonation of aniline monomer and its oxidation products and thus, well-organised polymer chains with a conjugated system can be formed. In contrast, alkaline and weakly acidic medium can't protonate all the existing species, resulting in different molecular mechanisms and consequently, products with different molecular structures, morphologies and properties.

With strong acids, a minimum oxidation potential of +1.05 V is required to be overcome. Several oxidants, ranged from weak (~ 1 V) to strong (~ 2 V), have been tested for PANI synthesis and they are crucial for the polymer structure obtained. Those can be APS, silver nitrate, hydrogen peroxide and iron(III) chloride, although APS is often used due to its high oxidising potential of 2.5 V that is able to oxidise all monomer and oligomer species.[85].

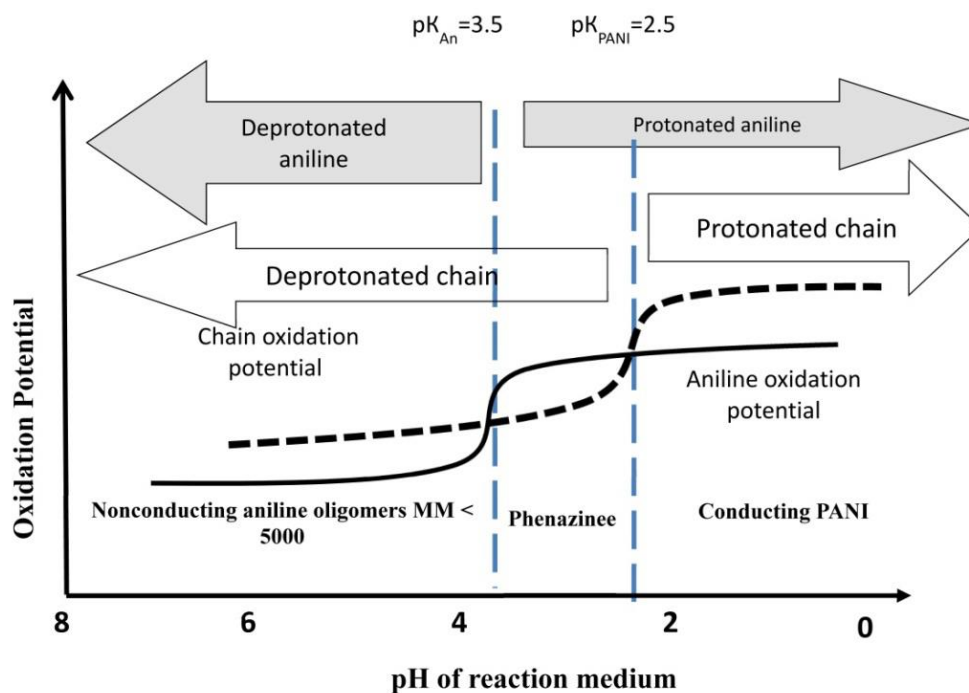


Figure 2.10. Oxidation of aniline and its products in function of the oxidation potential and the pH of the reaction medium during aniline polymerisation. pH over 3.5 and low oxidation potential result in the deprotonation of both aniline and polymer chain, which results in nonconducting oligomers being produced. pH under 2.5, produce protonated products, and thus conducting PANI. If $2.5 < \text{pH} < 3.5$, phenazine structures can result either in oligomerisation or polymerisation, depending on the initial conditions. This is determined by protonation constant of monomer pK_{An} and growing chain pK_{PANI} . [85].

2.4 STERIC STABILISATION OF POLYANILINE

PANI can assume a wide range of different nanostructures, the as-called supramolecular structures, which strongly depends on the synthetic route adopted. The resultant product in a typical chemical oxidative polymerisation (COP) of aniline is a precipitate that has an infusible and insoluble character, with brittle nature (intractable powders).

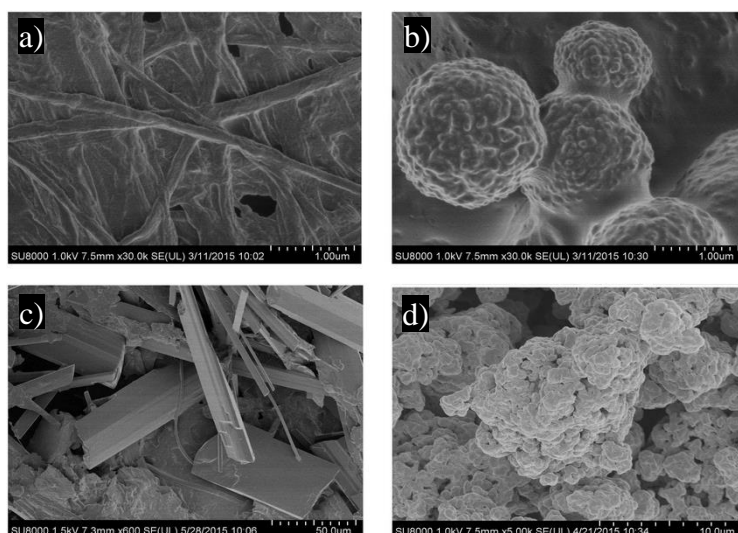


Figure 2.11. Examples of 3D and 1D supramolecular structures of PANI that can be obtained: a) Nanofibres, b) granular spheres (granules), c) plates, d) micro-sized granular agglomerates – commercial PANI – (adapted from [97]).

With increased knowledge of the self-assembling molecular mechanism of PANI, several approaches have been followed aiming to obtain more processable products with more organised 1D nanostructures and an elongated polyconjugated system. Slight adjustments in the procedure, such as using two immiscible solvents (interfacial polymerisation), surfactants, templates, have been tested. Depending on the reaction conditions, the type of self-organisation of PANI structures can take the shape of 1D, 2D and 3D nanostructures.

In general, oxidation of aniline at pH 2.5-3.5 results in aniline oligomers having cyclic phenazine structure, which are aromatic rings with π -electron density. Phenazines tend to stack together via π - π interactions between the aromatic rings. Regular self-assembling of these stacked phenazines may result in well-defined PANI nanostructures. However, chaotic spherical agglomeration occurs more often with the common precipitation method, leading to the formation of big PANI aggregates (Figure 2.12).

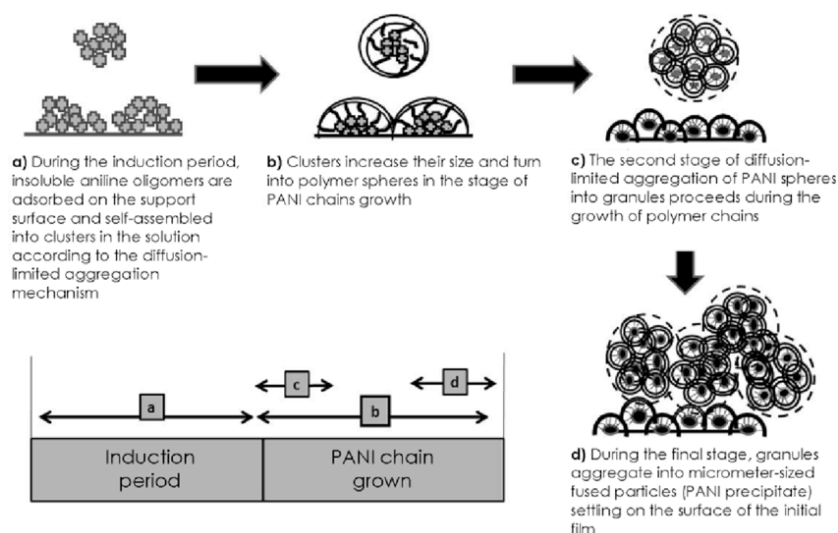


Figure 2.12. Schematic diagram of the self-assembling mechanism of PANI into 3D granular structures [98].

The aniline monomer has an amphiphilic nature owing to its hydrophobic benzene and the hydrophilic amine group, which is anticipated to form micelle-like structures of aniline monomers – phenazine clusters – just before the polymerisation is started. Upon addition of the oxidant, the reaction initiates and PANI chains grow at the micelle/liquid interface according to the principles of aniline polymerisation and elongation.[99]. Under typical reaction conditions, phenazine clusters will keep growing following the diffusion-limited aggregation to form particle resembling blackberry that occurs during the propagation step. This is thought to be caused by changes in surface properties of the initial cluster and, hence, its interactions with medium, that forms insoluble microgranular particles.[100].

The introduction of templates and surfactants can stabilise the interactions between phenazine clusters, and control the crystal nucleation and growth during PANI synthesis with consequent change of the morphology [101]. Molecular components in solution, such as phenazines, may also well-perform as templates for the formation of 1D PANI structures. It is assumed that during the propagation step those structures grow at the expenses of new nucleates generated directly on the surface of the template, which leads to lengthen the fibres, tubes or rods. The well-organised polymer chains may also interact to each other with adjacent chains via hydrogen bonds, and then thickening the fibres.[88].

Surfactants introduced in the reaction are often recommended to obtain well-dispersed colloids, but they can also serve as soft-templates to develop coatings with 1D PANI structures endowed with additional strong, stable electrical and chemical functionalisation. Polymeric surfactants impart excellent particle stability via steric stabilisation, by reducing the interfacial tension. In contrast to monomeric surfactants, polymer chains can better prevent coalescence and agglomeration owing to the larger repulsive barriers. Moreover, the multiple anchoring points of polymeric surfactants provide superior interaction between surfactant and substrate.[102]. As such, steric polymeric stabilisers are expected to benefit the formation of highly regular structures at both molecular and supramolecular levels.[86].

Water-soluble polymers or polymers with water-loving groups, such as poly(vinyl alcohol), polyvinylpyrrolidone, cellulose, and chitosan, have been used as steric stabilisers for aniline polymerisation in dispersed media [103]. As a rule, the best steric stabilisers are those containing amphiphilic 2-block or graft copolymers, in which a polymer A acts as bridge between the substrate surface and the (co)polymer B. In such instances, A has to have demonstrated affinity to the substrate surface while providing anchoring sites to bound (co)polymer B (Figure 2.13).[104].

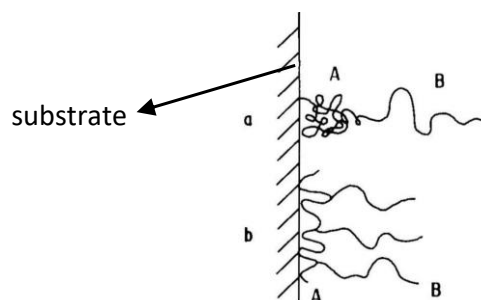


Figure 2.13. Examples of polymeric steric stabilisers in the form of a) block copolymers and b) graft copolymers, where A is the polymer with the anchor group and B is the polymer that provides the steric barrier [104].

Polymeric surfactants with a free amine group, like PVAN, can serve as steric stabilisers, while participating actively in the oxidative polymerisation of aniline from which PANI chains can grow. Therefore, amine-containing surfactants, not only are

able to stabilise phenazine interactions, but also can act as a soft-template for aniline polymerisation, as schematically illustrated in Figure 2.14.[99].

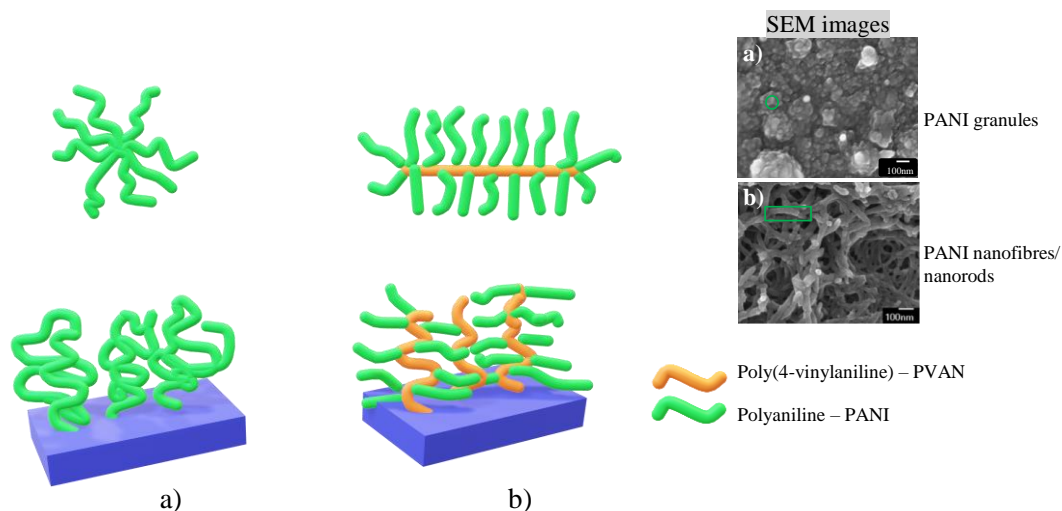


Figure 2.14. Schematic illustration of PANI brushes self-assembled onto a a) non-treated and b) pre-treated surface with a steric polymeric stabiliser, such as PVAN, and corresponding SEM images, showing PANI a) granules [85] and b) nanofibres/nanorods [105]. The presence of the polymeric stabiliser, in this case, PVAN, can stabilise phenazine interactions during aniline polymerisation, allowing the dispersion of PANI brushes, as shown in b), in contrast to what is observed when a) no polymeric stabiliser is used.

2.4.1 Poly(4-vinylaniline)

PVAN is a primary amine surfactant and steric stabiliser with versatile synthesis, and chemical and environmental stability, that can be used to lower the interfacial tension of a diverse range of materials [106]. For that reason, it has been found applications in paints as stabilisers, but also as ionic conductive materials, photo induced electron transfer materials, organic semiconductors and fluorescent dyes [107].

A variety of substrates have been successfully treated with PVAN to allow PANI functionalisation. Yuan *et al* [108] produced anti-corrosive coatings for stainless steel based on PVAN/PANI dual coating. Poly(tetrafluoroethylene) (PTFE) have been efficiently grafted with PANI by means of a PVAN primer coating layer before aniline polymerisation [109]. Fu *et al* [110] were able to produce electrically conductive

hollow spheres through grafting PVAN/PANI polymers on silica particles, which are later removed with UV light. In all these studies, it was demonstrated PANI was strongly tethered to the substrates attributed to the presence of PVAN interlayer. Furthermore, it was also revealed that higher yields of grafted PVAN improved the efficiency of PANI grafting, and increased conductivity.

Chemical Structure

PVAN, also called poly(4-aminostyrene), shares similar molecular structure with polystyrene but it possesses an extra secondary amine as pending moiety, as shown in Figure 2.15. It is formed by a long hydrocarbon chain to which phenylamine groups are alternately attached. PVAN has an amphiphilic nature, with hydrophobic and hydrophilic segments. The pending amine moiety is responsible for the hydrophilic character of PVAN and at the same time can serve as anchoring sites for PANI growth. Despite similar monomer structure, PVAN and PANI repeating units are significantly different.[86].

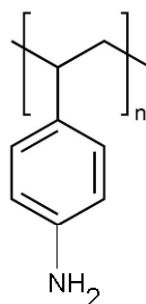


Figure 2.15. Chemical structure of the repeating unit of PVAN that is the 4-vinylaniline (4-VAN) monomer.

Synthesis

PVAN is originated from a vinyl-type monomer and synthesised by monomer addition in a chain-growth polymerisation. The unsaturated C=C double bond of each monomer is broken to form a linear carbon chain (single C–C bonds). Monomers with unsaturated carbon bonds can be easily polymerisable with radical polymerisation, following chain initiation, propagation and termination.

Radicals are generated from the broken π -bonds of the vinyl group, which are transferred from the initiator molecules to the monomer units – initiation. The radical initiator containing the monomer unit attacks the π -bond of another monomer and converts it into a σ -bond in between. This releases an electron of the second carbon of the monomer and transforms the whole molecule into a radical ready to attack the next monomeric unit – chain propagation. Chain will continue to propagate with consecutive monomer addition until complete consumption of monomer or until termination occurs, which can be either by combination of two chain ends or radical deprotonation.[111].

Atom Transfer Radical Polymerisation (ATRP)

The recent advances in controlled/living radical polymerisation and in particular ATRP, has prompted great progresses in the synthesis of polymeric surfactants in terms of flexibility, diversity and functionality. ATRP, and living polymerisations in general, is a chain-growth polymerisation mediated by a metal catalyst system that proceeds without chain transfer events and chain termination. It can be operated with a diverse array of monomers, typically vinyl monomers, such as styrene, vinyl alcohol, methyl methacrylate and inclusively, 4-vinyaniline.[112, 113]. ATRP reaction proceeds with radically (co)polymerisable monomers at the expenses of a dynamic equilibrium established between dormant ($P_n\text{-X}$) and activating species (P_n^*), that are continuously activated and deactivated at constant rates k_{act} and k_{deact} , respectively, according to the equation 2.1. During this process, a radical atom or group (X) is transferred from the ‘initiator’ to the transition metal complex of the lower oxidation state (Mt^n/L) to form an active propagating polymer chain (P_n^*) that can accept one or more monomers. P_n^* species are then deactivated via reverse transfer of the atom or group to reform the dormant species ($P_n\text{-X}$) or to form new initiator species. But the concentration of the growing radicals P_n^* , which propagate at a propagation constant rate k_p , can be increased such that radical-radical termination may occur at a termination constant rate k_t . However, the amount of radicals is normally sufficiently low to prevent this and hence, well-defined polymers with low polydispersities can be successfully obtained.[114].

bactericidal/fungicidal, anti-corrosive, biocompatibility, adhesion and adsorption properties, as well as to change the melting point. There are currently two different approaches to attach polymers onto solid surfaces by ATRP: ‘grafting-from’ and ‘grafting-to’ (Figure 2.17). The ‘grafting from’ method consists of a macromolecule substrate onto its surface initiating sites are added to allow the subsequent growth of polymer chains. While in the ‘grafting-to’, a polymer chain with a reactive end-group is attached to the backbone of other polymer and thus, polymer chains have to diffuse to the surface.[113, 116]. The choice for one of the routes not only depends on the polymer that is intended to graft or be grafted, but also on the type of architecture desired. ‘Grafting to’ can be employed for the preparation of star molecules and loosely grafted copolymers, whereas for densely grafted surfaces and end-functionalisation, ‘grafting from’ via surface-initiated ATRP (SI-ARTP) is often preferred since it is more efficient.[117].

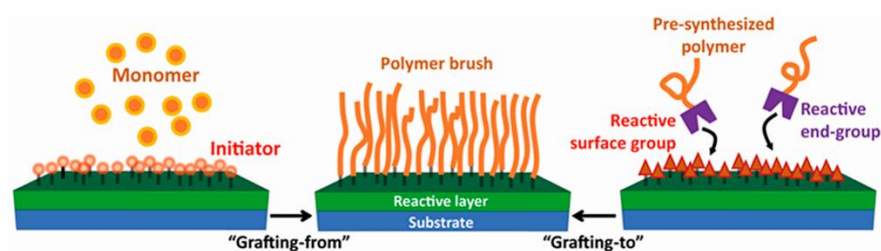


Figure 2.17. Schematic illustration of the synthesis of grafted surfaces with ATRP following the ‘grafting-from’ (left) and ‘grafting-to’ (right) approaches. In the ‘grafting-from’, an initiator is attached to the substrate from which polymer chains can grow. In the ‘grafting-to’, a pre-synthesised macromolecule containing a reactive end group is attached to the substrate that had its surface previously activated.[117].

The versatility of ATRP for producing graft copolymers can be extended to cellulose substrates. An appropriate initiator has to be immobilised onto the solid surface that can be accomplished either by chemical, radiation, photochemical, plasma-induced or enzymatic grafting techniques [118]. On cellulose substrates, the richness of hydroxyl groups makes the chemical means the easiest route for ‘grafting from’ by simply attaching R-bromoesters, which are exceptional initiators for ATRP. Some examples include 2-bromopropanitrile (BPN), α -bromoisotutyryl bromide (BiBB), ethyl 2-bromoisobutyrate (EBriB), ethyl 2-bromopropionate (EBriP) and

methyl 2-bromopropionate (MBriP). The structure of the initiator dictates the rate of activation, which ideally should be at least as fast as the propagation rate, so that low polydispersities and high initiation efficiency are obtained.[119].

2.5 CARBON NANOTUBES

CNTs have emerged rapidly as new nanostructured materials for uncountable industrial applications, especially for microelectronics/nanoelectronics, such as energy storage, conversion and optical devices, as well as transistors, owing to their outstanding electrical conductivity, optical properties, excellent chemical, electrochemical and thermal stability, high surface to area ratio within their small dimensions at nanoscale. Such characteristics have found particular usefulness in miniaturised devices in the biomedical field, as for example bioelectronic (neural) interfaces that requires nanosized materials for adequate signal transduction with elevated sensitivity, while possibly favouring tissue integration thanks to its softer texture when compared to metals.[120].

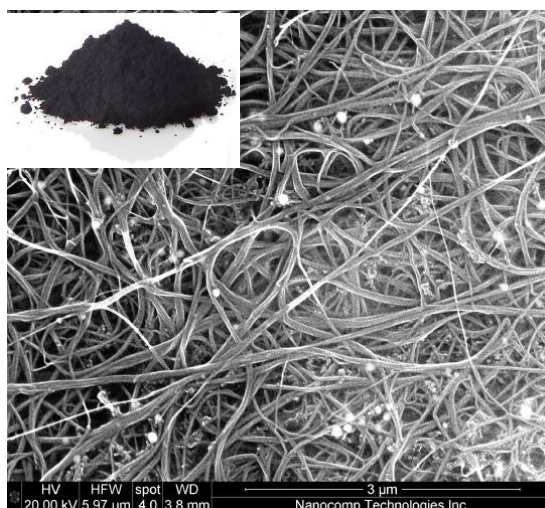


Figure 2.18. SEM [121] and optical [122] images of CNTs powders.

2.5.1 Chemical Structure

The carbon atom possesses 6 electrons – two core electrons with four valence electrons – that are distributed within three orbitals (1s, 2s and p) with electronic

configuration $1s^2 2s^2 2p^2$ in the ground state, as shown in Figure 2.19. Electronic orbitals $1s$ and $2s$ are spherical, whereas $2p$ orbitals show lobular shape perpendicular to each other according to the axis planes. When two or more carbon atoms are close to each other, one of the electrons in the $2s$ orbital can be pulled into the p orbital of higher energy and hybridisation occurs, resulting in sp^2 orbitals belonging to the trigonal plane, i.e. the three orbitals lie on the same plane rotated by 120° . [123].

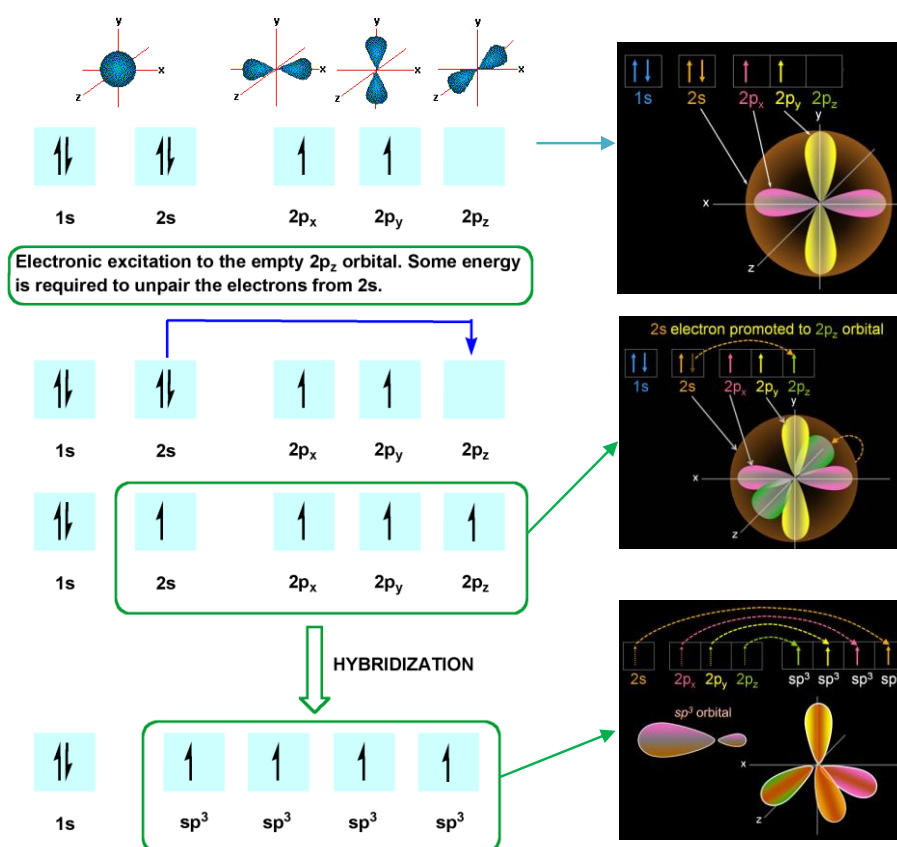


Figure 2.19. Electronic configuration of carbon atom at the ground state and the possible hybridisations, with the schematic illustration of their respective orbitals' shape [124–126].

The carbon atom then bonds to other three carbons located in its vicinity to form a hexagonal lattice – graphene sheet –, via sp^2 hybridisation with sigma (σ) and pi (π) bonds. The electron located in the p_z orbital further forms a delocalised π -band structure with all other p_z orbitals, and this is responsible for the electronic conduction in CNTs (Figure 2.20).

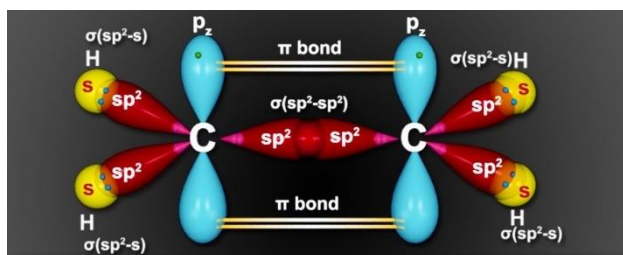


Figure 2.20. Schematic representation of sp^2 hybridisation of the orbitals in carbon atom [127].

Graphene sheets of sp^2 bonded carbon atoms roll up to assemble CNTs with cylindrical shape, consisting of either a single sheet (single-walled carbon nanotubes, SWCNTs) of 0.4-2 nm diameter or multiple sheets (multi-walled carbon nanotubes, MWCNTs) of larger diameters, ranging between 2-100 nm and interspaced by 0.34 nm. CNTs can have lengths from hundreds of nanometres up to several hundreds of millimetres.[128, 129].

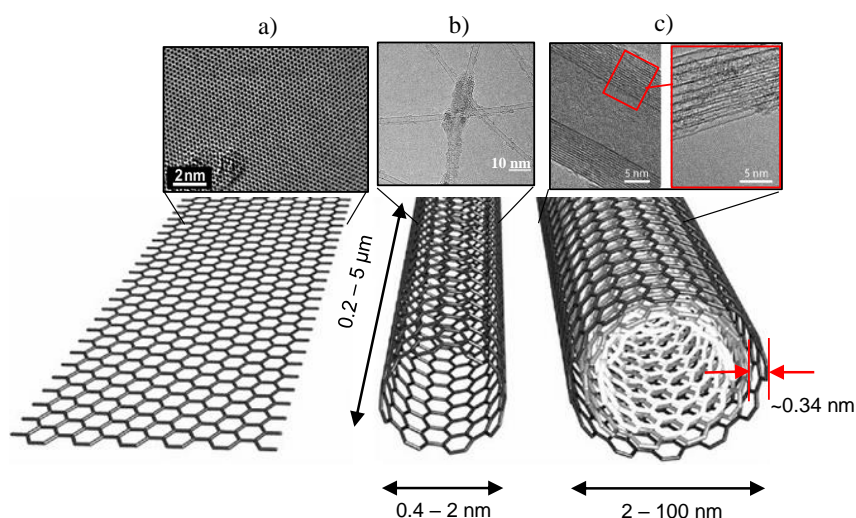


Figure 2.21. Molecular structure of a) a graphene sheet, b) SWCNTs and c) MWCNTs [130], and corresponding transmission electron microscopic (TEM) images on the top, showing the single (in SWCNTs) and the multiple walls (in MWCNTs) composing CNTs [131–133].

2.5.2 Electrical Properties

CNTs demonstrate different electrical properties according to their chirality, morphology, size and nanotube diameter. The atomic arrangement of the carbon atoms of a nanotube can be used to describe the electronic band structure of CNTs. The angle

at which the graphene sheets roll up, i.e. the alignment of the p orbitals, determines the chirality of CNTs and are described in terms of the chiral vector (n,m) , where n and m are the (integer) numbers of hexagons traversed in the two unit-vector directions, a_1 and a_2 of the graphene lattice, as shown in Figure 2.22a.

In general, there are three possible atomic structural arrangements of CNTs based on the chirality, that are armchair, zigzag and chiral (Figure 2.22 b, c and d, respectively). SWCNTs can adopt metallic ($n-m=3q$, with q an integer or zero) or semiconducting properties ($n-m \neq 3q$), depending on its chirality. Interestingly, MWCNTs that are composed of several coaxial SWCNTs, show predominantly metallic electronic properties similar to the metallic conduction in SWCNTs.[134–136]. Also, in MWCNTs, the current flows through the outer most nanotube, that most likely arises from multiple contributions of individual interactions between adjacent coaxial tubes (inter-tube coupling). The overall electronic characteristics of MWCNTs will depend on the metallic or semiconductive properties of the constituent carbon tubes, which can raise very complex situations in terms of electronic conduction. These peculiarities make MWCNTs with a much richer and versatile electronic band structure when compared to SWCNT.

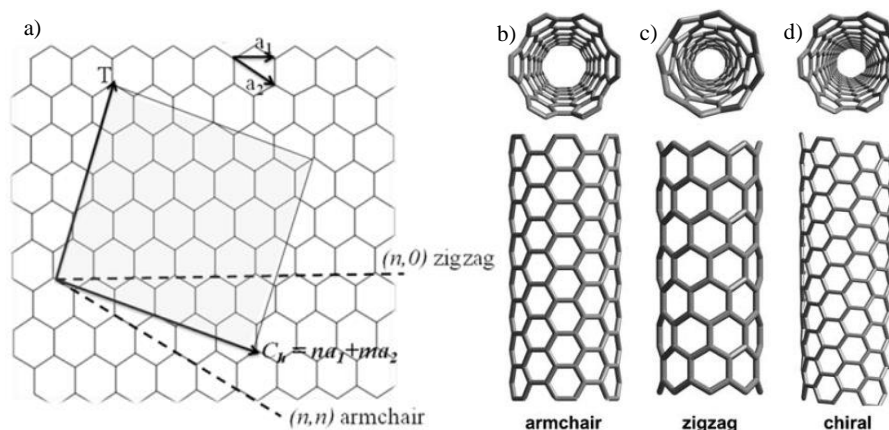


Figure 2.22. Molecular representation of the possible atomic configurations of CNTs. a) representation of the vectors corresponding to b) armchair, c) zigzag, and d) chiral-based conformations [137].

MWCNTs can further exist in miscellaneous morphologies, such as hollow tube, herringbone and bamboo, as illustrated in Figure 2.23 [134]. The morphology of the

MWCNTs can be controlled by the preparation method, although ‘hollow tube’ is the most common and well-known, in which the axis of the graphene plane is parallel to the tube axis (Figure 2.21c and Figure 2.23a). In ‘herringbone’, graphene sheets form also a hollow tube but their planes are at angle with the tube axis, resulting in a cone shaped of graphene sheets; whereas in the ‘bamboo’ type morphology, multiple cones along the nanotube are stacked together periodically, forming compartments inside.[138].

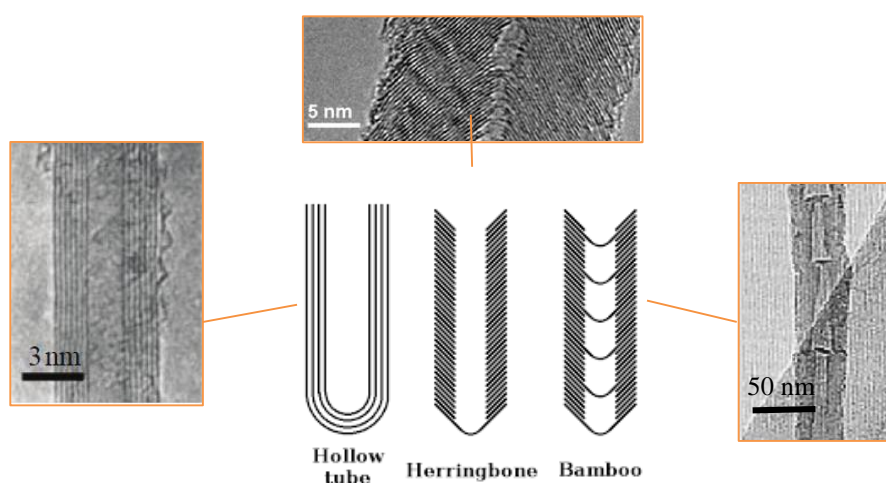


Figure 2.23. Examples of coexisting morphologies of MWCNTs: hollow tube, herringbone and bamboo (adapted from [138–140]).

Despite the structural differences, both own 1D electrical characteristics responsible for the ballistic electronic conduction [130]. This allows CNTs to transport currents with very low electrical resistivity of about 10^{-8} - 10^{-7} $\Omega\cdot\text{m}$, i.e. conductivity up to 10^6 - 10^7 $\text{S}\cdot\text{m}^{-1}$, with negligible heating and scattering over long lengths. Also, the ballistic conduction of CNTs combined with a high surface aspect ratio of about 120-500 $\text{m}^2\cdot\text{g}^{-1}$, renders excellent specific capacitance that can range from 2 $\text{F}\cdot\text{g}^{-1}$ to 200 $\text{F}\cdot\text{g}^{-1}$. [77, 141].

2.5.3 Synthesis

There are currently several routes for preparing CNTs, but the most common are arc discharge, laser ablation and chemical vapor deposition (CVD) techniques (Figure

2.24). The product is obtained as a stable solid that can be either in the form of powders or films, showing relatively high yield rate of over 75% in all techniques.[142]. Table 2.2 summarises the key characteristics of each technique, and the respective advantages and drawbacks.

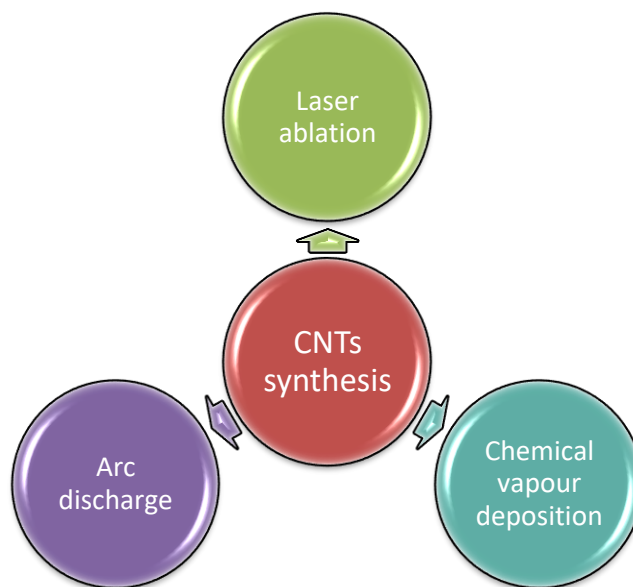


Figure 2.24. Common methods used for CNTs synthesis.

Arc discharge and laser ablation employ high temperature and were used to synthesise CNTs in the early stages of its discovery, but currently, these techniques have been replaced by techniques that use lower temperature which comprise chemical vapor deposition (CVD) methods. The latter have gained considerable attention as both SWCNTs and MWCNTs can be obtained with high quality and quantity in a relatively simple process. CVD allow the preparation of CNTs with an accurate control over the nanotube length, diameter, alignment, purity, density, and orientation.

Regardless the method used, purification of the obtained product is required and involves essentially the removal of large graphite particles and aggregations with filtration, dissolution of catalyst particles and fullerenes in appropriate solvents, as well as size separation and removal of amorphous carbon clusters through microfiltrations and chromatography. Depending on the desired requirements, additional processability can be performed with the dispersion of CNTs in colloidal suspensions with aids of ultrasounds and materials that can prevent aggregation, such as surfactants, polymers, or other colloidal particles.[142].

Table 2.2. Principal technical characteristics of the typical methods used to produce CNTs, and respective advantages and disadvantages (adapted from [142–144]).

	Characteristics	Advantages	Disadvantages
Arc discharge	<ul style="list-style-type: none"> ✓ >1700 °C; ✓ Helium atmosphere; ✓ Low pressure; ✓ DC arc discharge between two graphite electrodes. 	Simple, low cost, high-quality nanotubes with low structural defects.	High temperature, exhaustive purification, tangled nanotubes.
Laser ablation	<ul style="list-style-type: none"> ✓ >1200 °C; ✓ Argon atmosphere; ✓ Low pressure; ✓ Laser hits a graphite pellet reinforced with catalysts, such as Ni or Co, to vaporise carbon. 	Relatively high purity.	High temperature, lab-scale limited, crude product obtained.
Chemical vapour deposition	<ul style="list-style-type: none"> ✓ <800 °C; ✓ Vacuum ✓ Sub- to atmospheric pressure; ✓ Dissociation and/or chemical reactions of gaseous reactants in an activated (heat, light, plasma) environment. 	Simple, low temperature, high purity, large-scale production, aligned structures possible.	Synthesised CNTs are usually MWNTs, some defects.

2.6 CARBON NANOTUBES-BASED COMPOSITES

The chemical inert nature and product form of CNTs limit their use to most of the applications. For this reason, CNTs are often combined with other materials in order to improve their processability, practicability, or to include additional functionality, which will ultimately be determined by the necessary requisites. This can be done in different ways, either by coupling sidewall functional groups; doping and filling with atoms, molecules, nanoparticles and nanowires into the carbon structure, and blending with various nanoparticles and organic compounds.[138].

CNTs can be efficiently blended with CPs for producing composite organic films aiming to enhance the electronic performance of several electronic devices. This has shown to be particularly relevant to modify some bioelectronic electrode devices as such a larger and softer contact interface can be provided and hence, the common limitations of the state-of-the-art electrodes can be addressed, amongst which can be highlighted low charge injection limits, mechanical mismatch and foreign body response.[145].

2.6.1 Carbon Nanotubes/Polyaniline

Despite the electrical excellency of CNTs, these can be further enhanced and/or complemented with other conductive materials. As-developed PANI/CNTs composites typically show transitional electrical, thermal and mechanical properties between those of pure PANI and CNTs, which can be controlled with the content ratio. However, it has been demonstrated that the individual electrochemical properties are exceeded upon their dual combination, raising new and unique pseudocapacitance behaviour with superior electrochemical stability. This is conjectured of resulting from the decreased electrochemical impedance and optimal intra- and interstructure porosity that promotes ion diffusion in the active sites of PANI.[146]. The unique interactions established between CNTs and aromatic amines of the planar PANI chain, can form a strong π - π conjugated system [147]. The possible bidirectional flow of charges between CNTs and the imine group of aniline, which is a good electron donor, forms a charge-transfer complex that culminates in π -stacking interactions. Moreover, prior modification of CNTs with carboxyl acids may have a dopant effect in PANI and thus,

an increase in the electrical conductivity of PANI/CNTs system may be expected.[147].

2.7 SUMMARY AND IMPLICATIONS

Electrically functionalised BC-based nanocomposite membranes have successfully been synthesised with varied electrically conductive moieties. In particular, PANI and CNTs have shown to considerably enhance the electrical properties of pristine BC, with BC providing a substrate for the intractable powders of neat PANI and CNTs. The large PANI aggregates typically formed has prevented the optimisation of electrical properties, which are intrinsically related with the nanostructures formed during synthesis. Optimisation of the synthetic routes with the inclusion of surfactants during aniline polymerisation, such as PVAN, may promote highly organised 1D supramolecular PANI structures, that are expected to increase the electrical conductivity of PANI grafted onto BC. This PANI coating can be strongly tethered, in contrast to those found in bioelectronic devices. Further augmentation of the electrical properties can be achieved with CNTs-reinforcement, which has outstanding electrical properties with superior thermal stability and mechanical strength.

Chapter 3: Research Methodology

This chapter describes the design and methodology adopted in this research to achieve the aims and objectives stated in section 1.6. It lists all materials (Section 3.1) and the methods (section 3.2) used to conduct this research project, with an outline of the procedure implemented for the development of the BC nanocomposites and their comprehensive characterisation (section 3.3). Sufficient details on the methods used were carefully discriminated to allow an understanding of the overall processes followed, so that this work can be reproducible by interested researchers in the field.

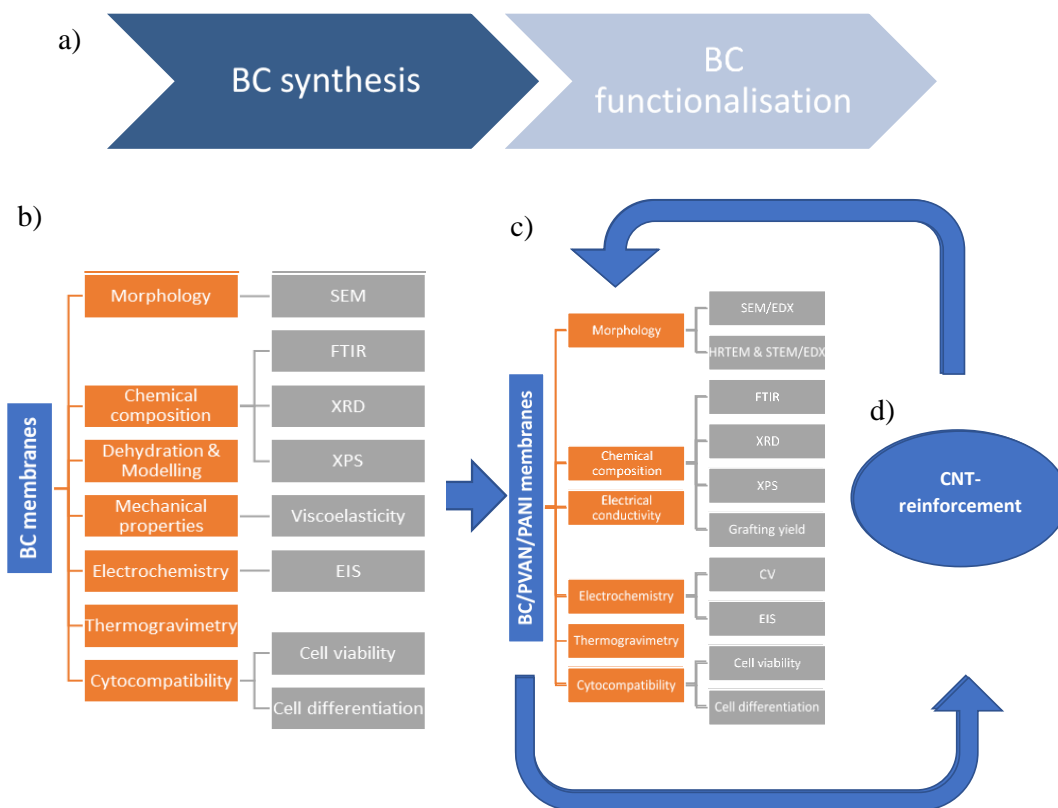


Figure 3.1. Schematic diagram of the processes involved in the production and characterisation of pristine BC and BC nanocomposites accordingly described in Chapter 3. a) Synthetic procedure of BC membranes followed by their functionalisation, and b-d) corresponding characterisation methods used.

The characterisation techniques and methods employed to assess the several features at various levels of the as-developed BC nanocomposites are also described,

including those to examine the surface and internal microstructures, chemical composition, dehydration modelling, viscoelastic properties, electrical conductivity and electrochemistry, thermogravimetry and ultimately, cytocompatibility (Figure 3.1). Fundamental concepts on the synthetic methods, such as ATRP and COP, as well as those of some characterisation methods, are briefly reviewed for a reliable and accurate interpretation of the results accordingly presented and discussed in the following chapters (4 to 8).

3.1 MATERIALS

3.1.1 BC Nanocomposites Production

Disodium hydrogen phosphate dodecahydrate, tryptone (Oxoid™ – Thermofisher Scientific), yeast extract (Oxoid™ – Thermofisher Scientific), citric acid, glucose, sodium hydroxide (sigma Aldrich), dimethylformamide (DMF, Sigma Aldrich), dry-dimethylformamide (dry-DMF, Fisher Scientific), triethylamine (TEA, Sigma Aldrich), 4-dimethylaminopyridine (DMAP, Sigma Aldrich), 2-bromoisobutryl bromide (BiBB, Sigma Aldrich), 4-vinylaniline (97%, 4-VAN, Sigma Aldrich), N,N,N',N'',N''-pentamethyldiethylenetriamine (PMEDTA, Fisher Scientific), copper(II) chloride (CuCl₂, Sigma Aldrich), ascorbic acid (ASCA, Fisher Scientific), aniline (ANI, Sigma Aldrich), hydrochloric acid (HCl), ammonium persulfate ((NH₄)₂S₂O₈, APS, Sigma Aldrich), 100 % ethanol (ETA, Sigma Aldrich), SWCNTs, sodium dodecylbenzenesulfonate (SDBS). All chemicals were used straightaway with no further purification.

3.1.2 Cell Viability

Dulbecco's Modified Eagle's Medium (DMEM, high glucose, no phenol red, Gibco™, Life Technologies – Thermofisher Scientific), DMEM/Nutrient Mixture F-12, supplemented with GlutaMAX™ (DMEM/F-12, GlutaMAX™ supplement, Gibco™, Life Technologies – Thermofisher Scientific), fetal bovine serum (FBS, qualified, EU-approved, South America origin, Gibco™, Life Technologies – Thermofisher Scientific), horse serum (HS, heat inactivated, New Zealand origin, Gibco™, Life Technologies – Thermofisher Scientific), phosphate buffered solution (X1 PBS, Lonza), PBST (phosphate buffered saline tween-20), penicillin/streptomycin

(pen/strep 10,000 U.mL⁻¹, Life Technologies – Thermofisher Scientific), Presto Blue® cell viability reagent (Life Technologies – Thermofisher Scientific), nerve growth factor 2.5S native mouse protein (NGF 2.5S, Invitrogen – Thermofisher Scientific), bovine serum albumin (BSA, Sigma Aldrich), neural cell culture supplement β-27 with and without retinoic acid (β-27 w/ and w/o RA, Gibco™, Life Technologies – Thermofisher Scientific), β-mercaptoethanol (50 mM β-ME, Gibco™, Invitrogen – Thermofisher Scientific), recombinant human fibroblast growth factor (rhβFGF 10 μg.mL⁻¹,), recombinant human epidermal growth factor (rhEGF, Invitrogen, Life Technologies – Thermofisher Scientific), extracellular matrix gel (ECM Laminin Mouse Protein, Natural, Gibco™ – Thermofisher Scientific) paraformaldehyde (PF, Sigma Aldrich), gluteraldehyde (GA, Sigma Aldrich), 0.1% and 0.5 % Triton X-100 (Invitrogen – Thermofisher Scientific), normal donkey serum (NDS, Sigma Aldrich), 4',6-diamidino-2-phenylindole (DAPI, Life Technologies– Thermofisher Scientific), Alexa Fluor™ 488 Phalloidin (Molecular Probes, Life Technologies – Thermofisher Scientific), calcein acetoxymethyl ester (calcein AM, (Invitrogen – Thermofisher Scientific), propidium iodine (PI, Invitrogen – Molecular Probes, Life Technologies – Thermofisher Scientific), CellTrace™ CFSE Cell Proliferation Kit (Invitrogen – Thermofisher Scientific), anti-rabbit β-tubulin III (Invitrogen – Thermofisher Scientific), anti-mouse α-gial fibrillary acidic protein (α-GFAP, Thermofisher Scientific), donkey anti-mouse IgG (H+L) highly cross-absorbed secondary antibody, Alexa Fluor® 488 (DAM-488, Invitrogen – Thermofisher Scientific), donkey anti-rabbit IgG (H+L) highly cross-absorbed secondary antibody, Alexa Fluor® 594 (DAR-594, Invitrogen – Thermofisher Scientific).

3.2 PRODUCTION METHODS

3.2.1 Synthesis of BC Membranes

BC membranes were produced from fermentation of *Gluconacetobacter hansenii* (ATCC® 53582TM) inoculated at 10% V/V, harvested in 6-well plates (3.5 cm) and kept in a sterile environment under static conditions for 4 days at 30 °C. The culture medium was prepared in pure water containing 6.8 g.L⁻¹ disodium hydrogen phosphate dodecahydrate, 5 g.L⁻¹ peptone, 5 g.L⁻¹ yeast extract, 1.5 g.L⁻¹ citric acid, 20 g.L⁻¹ glucose. The obtained BC membranes were soaked with pure water for 2-3

days, prior to boiling with 4 g.L⁻¹ sodium hydroxide solution for 40 min to remove medium and any adsorbed bacteria. The full protocol on BC synthesis can be seen in the Appendix A. The as-prepared BC hydrogels 3.2±0.5 mm thick were dried in an oven under the ambient conditions for overnight at 60 °C.



Figure 3.2. BC membranes produced from *Gluconacetobacter hansenii* cultured in 6-well plates.

3.2.2 Synthesis of BC/PVAN/PANI Nanocomposites

BC coated with PANI was prepared with two consecutive polymerisation processes. First, BC membranes were covalently grafted with PVAN (BC-g-PVAN) by activators regenerated by electron transfer surface initiated-atom transfer radical polymerisation (ARGET SI-ATRP) following a ‘grafting-from’ approach. Then, BC-g-PVAN membranes were further functionalised with conductive PANI through *in situ* chemical oxidative polymerisation (COP).

Fundamentals of Activators Regenerated by Electron Transfer Surface-Initiated Atom Transfer Radical Polymerisation

Solid surfaces, like BC, can be modified with polymers with ATRP through a ‘grafting-from’ approach, which consists on the pre-incorporation of an initiator to enable the growing of polymeric chains from the solid surface – surface initiated. BC substrate can be easily initiated with R-bromoesters (e.g. BiBB) from its hydroxyl groups in an esterification reaction. This preformed macromolecule with distributed initiating functionality (BC-BiBB), can then be subjected to ATRP of VAN for proper surface modification.[113].

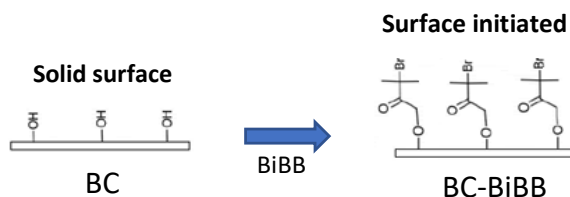


Figure 3.3. Schematic mechanism of the ‘grafting-from’ approach on BC substrate initiated with BiBB.

As exemplified in Figure 3.4, ATRP is processed by establishing an equilibrium between propagating radicals and dormant chains, that is strongly shifted towards the dormant species. The transition metal complex (M_t^n/L) reacts with an alkyl halide (P_n-X) to generate active species or radicals (P_n^\bullet) that propagate at a propagation rate k_p . The M_t^n/L undergoes one-electron oxidation to $n+1$, with simultaneous transference of a (pseudo)halogen atom, X, from dormant species, P_n-X . These are reversibly formed at activation and deactivation constant rates (k_{act} and k_{deact} , respectively). Thus, P_n^\bullet can propagate with a vinyl monomer, M (VAN), be deactivated in the equilibrium by $M_t^n X/L$, or terminate by either coupling or disproportionation with another P_n^\bullet . Reducing agents, like ascorbic acid (ASCA), can rapidly reduce deactivated species by electron transfer (ARGET). In the present study, the catalytic system used was Cu-based, complexing ligand with PMDETA, which was continuously regenerated by ASCA.[148].

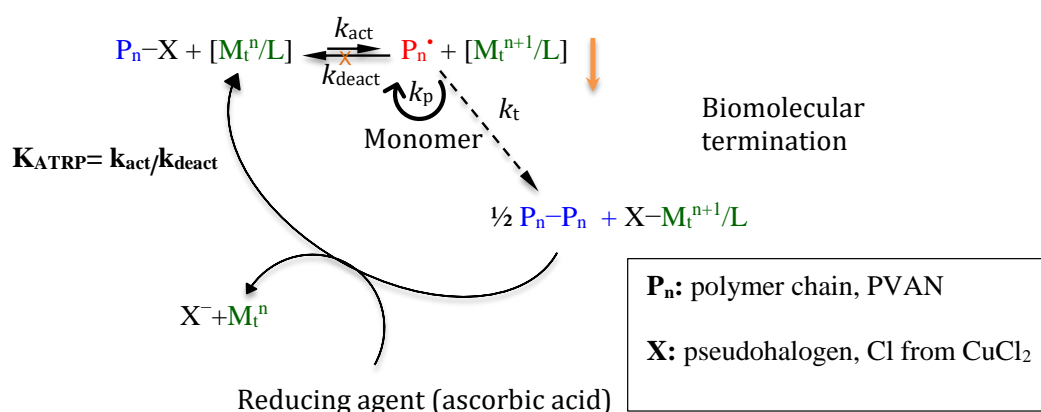


Figure 3.4. Mechanism of metal complex-mediated ARGET ATRP.

The polymerisation rate, R_p , equation 3.1 often follows a first-order kinetics, and thus, monomer conversion increases linearly with time in a semilogarithmic scale [115].

$$R_p = k_p[M][P_n^*] = k_p[M]k_{ATRTP}[P_n - X] \frac{[Cu^I/PMDETA]}{[Cu^{II}X/PMDETA]} \quad (3.1)$$



$$R_p = k_p[VAN][PVAN^*] = k_p[VAN]k_{ATRTP}[PVAN - Cl] \frac{[Cu^I/PMDETA]}{[Cu^{II}Cl/PMDETA]}$$

Fundamentals of Chemical Oxidative Polymerisation

In COP of ANI, the reaction starts with the oxidation of ANI with aids of an oxidising agent (initiator) in acidic medium to form cation and cation radical sites with subsequent loss of two protons, leading to the formation of covalent bonds between monomer units (chain reaction) [85]. In this study, APS was used as oxidant for having a high oxidation potential (+2.1V) that is able to overcome the activation energy of chain propagation (+1.05 V in acidic medium), while HCl provides a reaction medium with very low pH to ensure sufficient protonation of ANI oxidation products. During the polymerisation, the hydrogen atoms abstracted from ANI monomer upon its oxidation are released as protons, and thus, the pH always lowers in the course of the reaction, in the form of sulphuric acid as a by-product (Figure 3.5).[149].

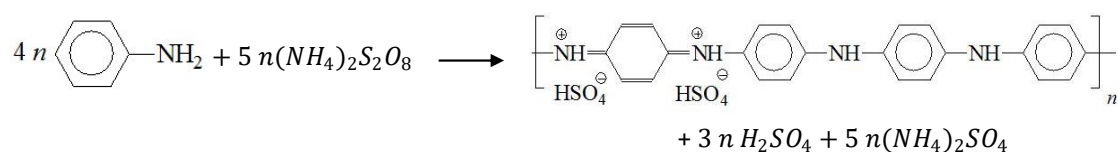


Figure 3.5. Oxidation of aniline monomer with APS [100].

From a mechanistic point of view (Figure 3.6), polymer chains grow by addition of ANI monomer (A_{nm}) to the activated dormant polymer chain (A_{nm}^*) with increased size and molecular mass (A_{nm+1}) [100]. ANI is first oxidised to nitrenium cation (cation radical) with subsequent formation of the dimer p-aminodiphenylamine (PADPA),

and/or benzidine and N,N-diphenylhydrazine, depending on the pH conditions – induction period. PADPA (growing chain) is then reduced with the concomitant oxidation of ANI in a redox process, which culminates with addition of a monomer to the chain end. The chain propagates via electrophilic substitution in a chain-reaction polymerisation (addition). Polymer chains will continue to grow in the protonated pernigraniline (PG) form, while the oxidation potentials of both growing chain and monomer have not been equilibrated. Termination takes place when either the monomer or the oxidant is fully consumed, or if the degrees of oxidation and/or the protonation of the chains are not high enough to ensure chain propagation, which happens when the emeraldine (EM) is formed.[85, 149].

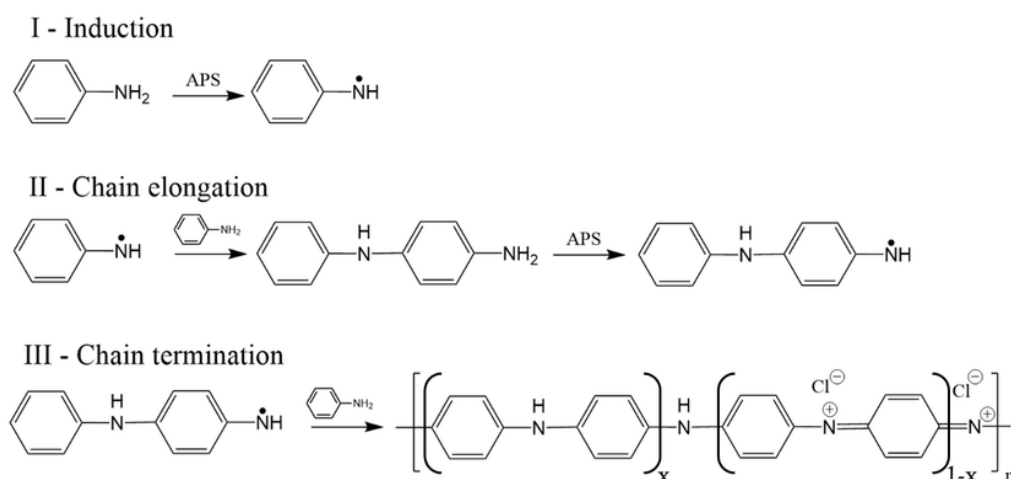


Figure 3.6. Mechanism of aniline polymerisation. I induction, II chain propagation and III chain termination [100].

The degree of oxidation of the final polymer is determined by the strength of the oxidant and by the oxidant-to-monomer ratio. The ANI polymerisation follows a first-order kinetics with respect to monomer, according to the equation:

$$-\frac{d[\text{ANI}]}{dt} = k_1[\text{ANI}][\text{OX}] + k_2\sigma[\text{ANI}][\text{P}] = k_1[\text{ANI}][\text{OX}] + k_2'[\text{ANI}][\text{P}], \quad (3.2)$$

where [ANI] is the molar concentration of ANI, [OX] is the molar concentration of the oxidant that in this case is APS, P is the equivalent concentration of polymer, σ is the

surface factor (total available surfaces/[P]), k_1 is the rate constant for the initial step and k_2 is the rate constant for the chain propagation.[85].

Procedure

BC-g-PVAN (or BC/PVAN) synthesis was completed in two steps with the ‘grafting-from’ approach, starting with the creation sites on BC membranes to generate BC-initiator, which was followed subsequently of 4-VAN on BC-initiator membranes by ARGET ATRP. Thereafter, BC/PVAN were subjected to COP of aniline. Full details of the experimental procedure can be checked in Appendix B.

2-Bromoisobutryl Bromide Immobilisation onto BC

Oven-dried BC membranes were subjected to solvent exchange from water to dry DMF by immersion into an excess amount of DMF (30-50 mL) for 2 days, which was replaced up to 3 times per day. Then, BC membranes were mixed with DMAP, dry-DMF (about 30 mL) and TEA under stirring, to which BiBB was added dropwise in an ice-bath. The feeding molar ratio used was BiBB:TEA:DMAP=1:2:2. The reaction was kept under inert atmosphere with protective argon gas and left at room temperature for 24 hours . The resultant BC-initiator (BCi) membranes were then soaked in DMF for 2 days as purification step, prior to PVAN grafting.



Figure 3.7. Initialisation reaction of BC surface performed with BiBB kept under argon atmosphere.

Activators Regenerated by Electron Transfer Surface-Initiated Atom Transfer Radical Polymerisation of 4-Vinylaniline

ATRP was carried out with dissolution of VAN monomer in DMF (about 30 mL), together with CuCl_2 and PMEDTA under argon atmosphere, before injecting ASCA dropwise. BCi membranes were later inserted to the reaction (Figure 3.8). ATRP was left running for 24 hours at room temperature, after which the grafted BC (referred to as BC-g-PVAN or BC/PVAN) was thoroughly washed with DMF and left in an excess amount of DMF overnight to ensure the removal of any physically adsorbed PVAN homopolymer. The molar ratio used for the reaction were $\text{CuCl}_2:\text{PMDETA}:\text{ASCA}:\text{VAN}=1:2:5:500$ and two different VAN monomer ratios (BC:VAN=1:3 and 1:5) were used in this study.

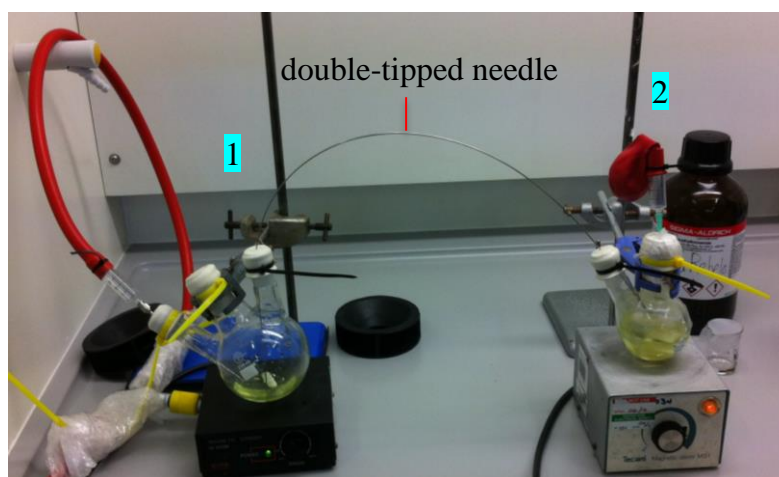


Figure 3.8. ATRP reaction of VAN after inserting ASCA conducted under argon atmosphere. **1**, VAN, CuCl_2 , PMEDTA and ASCA dissolved in DMF. **2**, BCi membranes in DMF. Solution 1 is being transferred to solution 2 through the double-tipped needle connecting both flasks.

Chemical Oxidative Polymerisation of Aniline

Conductive PANI layer was grafted on BC/PVAN composites (referred to as BC-g-PVAN-g-PANI or BC/PVAN/PANI) via COP of ANI on BC-g-PVAN. BC/PVAN was first dipped into a 10 mL aqueous solution of 1 M HCl containing 0.25 M of APS. Then, 0.20 M of ANI was added dropwise to the reaction that was left for 6 hours in an ice-bath (at 0-5 °C). These were designated as standard conditions. Purification of the ready-grafted BC/PVAN/PANI membranes was done with thorough washes with ETA and distilled water, and oven-dried overnight at 60 °C. The

thickness of dried samples measured between 0.03-0.05 cm. Adjustments to ANI polymerisation parameters, including acid concentration (0.5 M, 1 M), molar ratio of oxidant to monomer (1:1, 1:1.25, 1:1.5), monomer concentration (0.2 M, 0.5 M, 0.7 M) and polymerisation time (3 hours, 6 hours, 18 hours), were performed to investigate the effects of each individual parameter. BC/PANI membranes were also prepared from pre-oven dried BC membranes under standard COP conditions for comparison in terms of morphological and electrical characteristics of the nanocomposites.

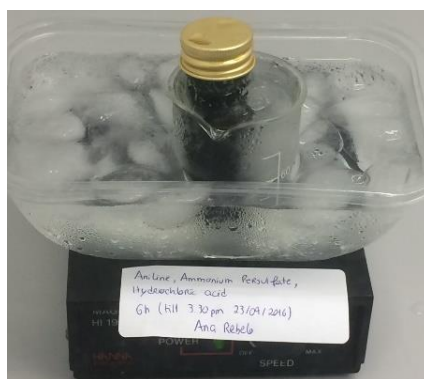


Figure 3.9. COP of aniline performed on BC/PVAN membranes conducted in an ice-bath ($\sim 0-5^{\circ}\text{C}$).

3.2.3 Carbon Nanotubes-Reinforcement of BC/PVAN/PANI Nanocomposites

Procedure

CNTs were blended thereafter with BC/PVAN/PANI, achieved following a procedure described elsewhere [150] by repeatedly dipping the nanocomposites in a CNT suspension composed of $1.6\text{ mg}\cdot\text{mL}^{-1}$ SWCNTs ink dispersed in $10\text{ mg}\cdot\text{mL}^{-1}$ SDBS surfactant with an ultrasonic bath. The samples were subsequently oven-dried at 120°C for 10 min and immersed again in the suspension. This process was repeated for 4 times. The thickness of dried samples measured between 0.03-0.05 cm.

3.3 CHARACTERISATION METHODS

3.3.1 Surface Morphology

The surface morphology of the un-modified and grafted BC membranes was analysed via scanning electron microscopy (SEM) and transmission electron

microscopy (TEM), for overall perception of the surface modification of BC nanofibres and closer inspection of PANI and CNTs coating at micro- and nanoscale.

Scanning Electron Microscopy

SEM uses a focused beam of high-energy electrons to build a high-resolution image of the material's surface after appropriate signal processing methods (magnification ranging from 20X to approximately 30,000X, spatial resolution of 50 to 100 nm). These electro-sample interactions enable the analysis of surface topographies, including external morphology (texture) and orientation of materials. Punctual analysis on the specimen's surface of the semi-quantitative chemical compositions can be also performed with SEM coupled with energy dispersive X-ray spectroscopy (EDX).[151].

The samples were assembled on carbon tape and sputtered with 0.1 nm thick gold/palladium for 60 seconds with a rotatory-pumped coating system (Q150R S, Quorum Technologies, UK) prior to SEM and TEM observation (GeminiSEM, Zeiss). SEM-EDX elemental maps were recorded on the surface of BC nanocomposite membranes. The diameter of the fibres was calculated based on the average of 50 fibres' diameters using ImageJ software.

High-Resolution Transmission Electron Microscopy

In contrast to SEM that focuses on the sample's surface from scattered electrons, TEM provides the details about internal composition from transmitted electrons and has a much higher resolution. Physical behaviour of many nanostructured materials can be perceived with HRTEM, as the atomic structure of interfaces and defects can be determined reliably and with very high positional accuracy. As such, it can provide very useful information of the surface coatings of BC, in particular PANI and CNTs. EDX analysis can be also coupled with TEM for insights on the chemical compositions of such nanostructured materials.[152].

To acquire spatially resolved microstructural and compositional information of the membranes, conventional and high-resolution TEM (C-/HR-TEM) were performed using a FEI (Field Electron) Tecnai F20 operating at 200 kV. The EDX elemental maps were acquired in the scanning TEM (STEM) mode, using long dwell

time to minimise beam drift during data collection. The TEM samples were attached to copper grids using a standard lift-out method on a FEI Nova SEM/FIB dual-beam microscope (FIB – Focused Ion Beam), fitted with a liquid Ga ion source and operating at 30 kV accelerating voltage (Figure 3.10). Ion-beam Pt was applied on site to minimise any ion milling artefact.

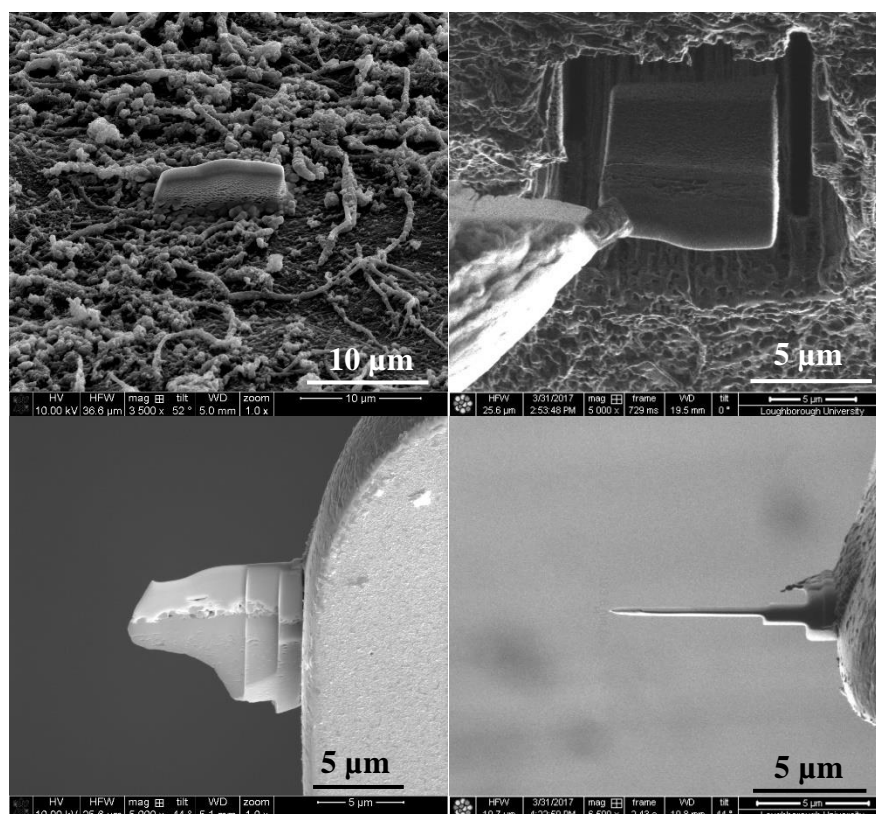


Figure 3.10 . FIB/SEM images from different perspectives and magnifications illustrating the FIB lift-out process used to extract a thin film TEM sample from the bulk membrane sample.

3.3.2 Chemical Composition

The chemical composition of BC, BC/PVAN and BC/PVAN/PANI membranes, and PVAN and PANI powders was assessed by attenuated total reflectance Fourier transform infrared spectroscopy (ATR-FTIR), X-Ray diffraction (XRD) and X-ray photoelectron spectroscopy (XPS).

Fourier Transform Infrared Spectroscopy

ATR-FTIR identifies chemical bounds established between atoms that compose a certain material detectable on the surface. It is a suitable tool for confirming the components of a chemical system by detecting its characteristic vibrations. ATR-FTIR was performed on dried BC, BC-BiBB, BC/PVAN and BC/PVAN/PANI membranes dried at 60 °C. The spectra were acquired in the 4000-600 cm⁻¹ wavenumber range, using a Shimadzu FTIR-8400S spectrophotometer (USA) equipped or not with an Attenuated Reflectance attachment.

X-Ray Diffraction

A crystalline material causes a beam of X-rays to diffract into different and specified directions (Figure 3.11). With XRD technique, the angles and corresponding intensities of these diffracted beams produces an X-ray diffractogram that has information of electrons distribution within the structure. With this, the crystal unit cell of a crystalline compound can be determined, as well as their chemical bonds and their crystallographic disorder. In a crystalline compound intense and narrow peaks are produced. According to Bragg's law, wavelength (λ), crystal plane separation (d) and diffraction angle (θ , also called Bragg's angle) are correlated as follows [153]:

$$n\lambda = 2d \sin \theta \quad (3.3)$$

with n the number of crystallographic planes.

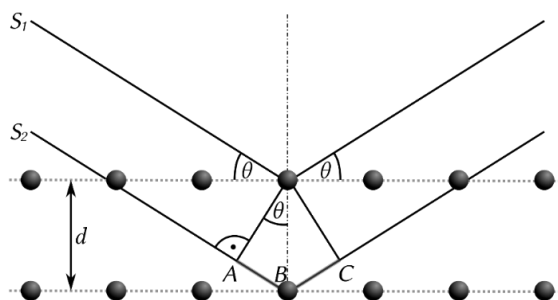


Figure 3.11. Schematic representation of the XRD in a crystalline structure, according Bragg's law. Incident X-rays (S_1 and S_2) reach the parallel planes of ions d -spaced, that are reflected at an angle θ , the same as the incident angle.

The degree of crystallinity can be estimated from the relationship between the total area of crystalline peaks and the total area of all peaks in the XRD spectrum, as follows [154]:

$$\% \text{ Crystallinity} = \frac{\text{total area of the crystalline peak}}{\text{total area of all peaks}} \times 100\%. \quad (3.4)$$

The crystallite size can be calculated with the information extracted from the diffractogram and Bragg angle (θ), using Scherrer equation [155]:

$$\tau = -\frac{K\lambda}{\beta \cos \theta} \quad (3.5)$$

where τ is the mean size of the ordered (crystalline) domains (i.e. crystallite size), K is a dimensionless shape factor (close to unit), λ is the X-ray wavelength, β is the line broadening at half the maximum intensity (FWHM) (in radians) and θ is the Bragg angle.

XRD was performed on BC and BC nanocomposites to ascertain about the crystallographic arrangement, as well as their chemical bonds. The diffractograms were acquired with a bench-top X-ray diffractometer (D2 PHASER, Bruker) using Cu radiation (30 kV, 10 mA, $K\alpha$ radiation ($\lambda = 1.542 \text{ \AA}$) measured between 2θ of 0° and 40° in steps of 0.02° .

X-Ray Photoelectron Spectroscopy

XPS is a spectroscopic technique that consists of irradiating a material with a beam of X-rays while measuring the kinetic energy and number of electrons that escape from the material under study up to 10 nm deep from the surface. XPS can measure the elemental composition empirical formula, chemical state and electronic state of the elements of a material.[156].

XPS was performed to assess the chemical compositions of BC, BC/PVAN, BC/PVAN/PANI and BC/PVAN/PANI/CNTs membrane samples using a

spectrometer from Thermo Scientific™ equipped with an Al K-Alpha™ source. Survey and selective high-resolution spectra were collected using 1 and 0.1 eV pass energy. Samples were mounted on double sided adhesive tape and the analyser chamber was degasified, keeping the pressure as low as 108 Torr. The data was collected on three different sites randomly chosen from a total covered area of 6 mm per 4.5 mm. Spectral analysis was carried out using the Thermo Scientific™ Avantage Data System for quantification and peak fitting. Quantification was based on peak areas calculated from the high-resolution spectra. All spectra shown were charge-balanced with dual beam source (source gun A: X-Ray004 150 μm - FG ON (150 μm) and source gun B: shutdown (0 μm)).

Degree of Substitution of 2-Bromoisobutryl Bromide

The degree of substitution (DS) of BiBB onto BC can be inferred from the content of the C1s associated to the ester bond (O-C=O) from the following equation [157]:

$$DS = \frac{-\%C(O-C=O) \times M_{AGU}}{\%C(O-C=O) \times M_{grafts} - M_C}, \quad (3.6)$$

where %C(O-C=O) is the atomic percentage of C1s of the ester group, M_{AGU} is the mass of the anhydro-glucose unit ($162 \text{ g} \cdot \text{mol}^{-1}$), M_{grafts} is the mass of the graft moiety and M_C is the mass of carbon.

3.3.3 Grafting Yield

The grafting yield (GY) of PVAN and PANI on BC surface, defined as the relative amount of PVAN and PANI attached to the initialised BC (BC-BiBB), was estimated using the following equation [158],

$$GY = \frac{m_{after} - m_{before}}{m_{before}} \times 100\% \quad (3.7)$$

where m_{after} is the mass of the composite and m_{before} is the mass before the grafting.

3.3.4 Dehydration and Modelling of BC Membranes

Five ready-made BC membranes per thickness (8 ± 0.5 mm and 2 ± 0.2 mm) and per size (8 and 5 mm diameter obtained using standard biopsy punches) were placed into plastic petri dishes (without lid) and kept in an incubator until complete dehydration (Sanyo MCO-18AIC CO₂) at 37 °C and 5 % CO₂. At different time points, the samples were weighted using a high precision scale electronic balance (Adventurer® Pro). Before weighting for the first time, the excess of water on the surface of the ready-made samples was carefully removed by tapping onto paper towels. For weights in the following time points, the petri dishes were cover with lid to prevent further water evaporation. The term TxDy is used to designate the geometry of samples, i.e. membranes with thickness Tx (x=2 or 8 mm) and diameter Dy (y=5 or 8 mm).

In order to model the BC water loss via water evaporation, a simple model is proposed based on the hypothesis that the water in the system assumes one of the three following states: bound (B), free (F), or evaporated (E). Rate equations were used to describe the transitions between the three different states, as shown hereunder:



where k_1 is the rate coefficient for bound water becoming free, k_2 the rate coefficient for free water becoming bound, and k_3 the rate coefficient for free water evaporating.

Considering that, from experimental observation, the process involved in the conversion of bound water to free water is reversible and that the conversion of free water to evaporated is irreversible (i.e. we assume there is no condensation of water from the atmosphere into the BC), differential equations may be written for calculating the amount of bound water and free water as a function of time ($B(t)$ and $F(t)$, respectively), following the thermodynamic laws.

$$\frac{d}{dt}B(t) = k_2F(t) - k_1B(t) \text{ and } \frac{d}{dt}F(t) = -k_1B(t) + k_2F(t) - k_3F(t). \quad (3.9)$$

It is then straightforward to solve these coupled linear differential equations; herein the Maple computer algebra package was used. The total mass of the system equals the sum of the individual masses of both bound and free water, along with that of the net mass of cellulose membrane. Considering that only 2 % of the total mass of BC is that of the cellulose, the total mass fraction is given by the sum:

$$M = B + F + 0.02. \quad (3.10)$$

Origin®2015 software was used to determine the parameters k_1 , k_2 and k_3 recurring to the damped least-squares. The difference between the observed and estimated value (Residuals or R) and the respective coefficient of determination (R-squared or R^2) of the best fitting obtained were calculated and discussed accordingly.

3.3.5 Viscoelastic Properties

Oscillatory rheology was used to study the dynamic mechanical properties of hydrogels under shear, including the viscoelasticity of solid hydrogels. It characterises the amount of shear energy that is stored in entropic distortion of the network or lost due to relaxations during a specific timescale.

The deformation energy that is stored in entropic distortions of the network is quantified by the storage modulus (G'), while the loss modulus (G'') quantifies the deformation energy that is dissipated due to relaxations that occur in the sollicitation timescale (τ_{exp}), which can be expressed with the following equation:

$$G^* = G' + iG'' \quad (3.11)$$

Oscillatory strain sweeps (amplitude sweep mode) can detect variations in the storage and loss moduli with the magnitude of the oscillation (strain) at a constant frequency, whereas oscillatory frequency sweeps (frequency sweep mode) can detect

those variations with frequency of the oscillation at a constant magnitude strain located in the *plateau* region.[159].

Procedure

The viscoelastic properties of BC membranes with 100, 80 and 50% of initial water content, which corresponds to 98, 78.4 and 49 % of BC total weight respectively, were assessed with a parallel plate rheometer (Physica MCR, Anton Paar). Three BC membrane samples per each water content levels were cut into squares of 2.5x2.5 cm² and placed on the rheometer plate at 37 °C, to simulate the human body temperature. Based on the weight loss curves, the samples with 80 and 50% water content were obtained by placing fully swollen BC membranes in the incubator at 37 °C for the different time periods required to allow loss of 20% and 50% of their initial weight, respectively. Never-dried fully swollen membranes measured 2.3±0.4 mm of thickness. The tests were performed in amplitude and frequency sweep modes and G' and G'' moduli as function of strain (ε) and angular frequency (ω) were obtained.

3.3.6 Electrical Conductivity

The sheet resistance (R) of 5 samples was measured on both sides of the membranes at three different sites with a Jandel four-point probe (Model HM20) at room temperature in dry state (Figure 3.12). As the thickness (t) of the samples was much smaller than the probe spacing (S) (t/S<<5), the electrical conductivity (S.cm⁻¹) was derived from the reciprocal of the bulk resistivity (ρ) according to the following equation [160]:

$$\sigma = \frac{1}{\rho} = \frac{\ln 2}{\pi} \frac{1}{tR} . \quad (3.12)$$

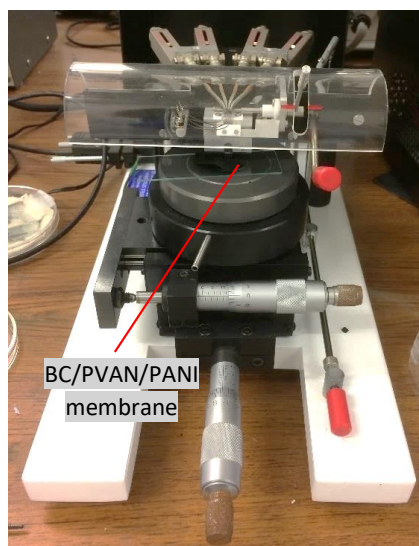


Figure 3.12. Jandel four-point probe set-up used to measure the sheet resistance of BC/PVAN/PANI membrane samples.

3.3.7 Electrochemical Analysis

Electrochemistry is a powerful tool to study the electron transfer triggered by chemical reactions, which is often the result of simultaneous oxidation and reduction (redox) of two different elements. Owing to the redox properties of PANI that can easily switch between its three oxidation states, it is reasonable to have an insight on the electrochemical properties of the as-prepared BC/PVAN/PANI nanocomposites and to understand the contributions of BC substrate and PVAN coating layer. As such, cyclic voltammetry (CV) and electrochemical impedance spectroscopy (EIS) were performed on pristine and nanocomposite BC membranes.

Fundamentals of Cyclic Voltammetry

CV allows a qualitative study of the reduction and oxidation processes of molecular species, which can give useful information about the reversibility of the reaction, possible formation of redox intermediates, electron stoichiometry of a system, the diffusion coefficient of a sample and the concentration of an unknown solution (through Nernstian system) [161].

In a typical CV set-up, the potential of the material under study (working electrode) is measured against a reference electrode (e.g. Ag/AgCl) which has a known electrode potential and is kept constant upon an applied excitation signal (cyclic

voltage). The current is then measured at the working electrode, which is converted to voltage – voltammogram. The applied voltage induces an excitation signal that goes from a lower potential V_1 to a greater potential V_2 , which is swept back to V_1 at a fixed rate (cyclic) [Figure 3.13a].

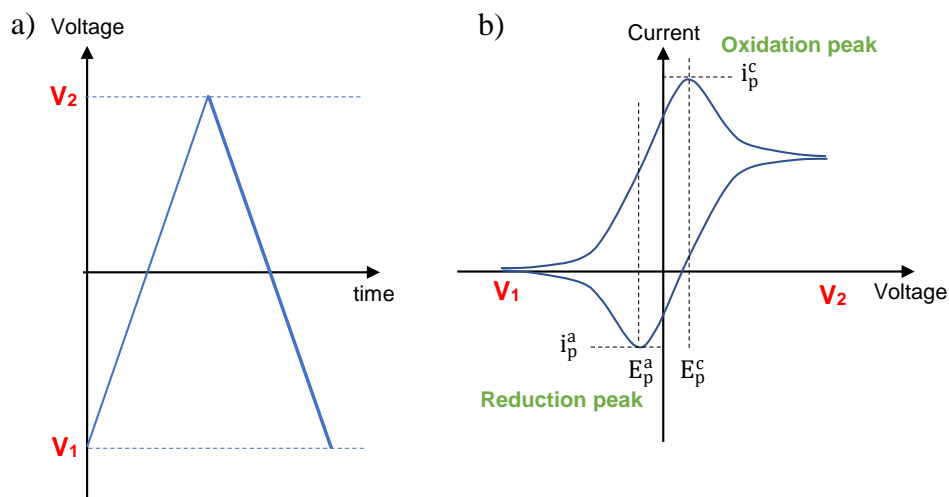


Figure 3.13. Schematic representation of a cyclic voltammogram from a single charge-transfer process. a) Applied cyclic excitation signal and b) corresponding response (cyclic voltammogram), showing one oxidation/reduction paired-peak when the potential is swept between V_1 and V_2 . i_p^a and i_p^c are the anodic and cathodic peak currents, respectively, and E_p^a and E_p^c are the corresponding peak potentials.

At V_2 potential, the surface of the analyte becomes sufficiently charged, either positively or negatively, and undergoes oxidation or reduction, respectively. The resulting response is exemplified in Figure 3.13b. An electrolyte solution is commonly used to facilitate ions diffusion between the two electrodes. [162].

Procedure

CV was performed in solid-state on oven-dried BC membranes (pristine and nanocomposites) using a Galvanostat/Potentiostat (Eco Chemie microAutolab type III). The membranes (either BC/PVAN/PANI or BC/PVAN/PANI/CNTs) were previously dipped into a sulphuric acid solution (1 M H_2SO_4) prior to any measurement and placed between two pieces of fluorine doped tin oxide (FTO) glasses ($1 \times 2 \text{ cm}^2$), acting as working and counter electrodes (two electrode mode), as shown in Figure 3.14. CV was recorded for different scan rates (50 and 100 mV).

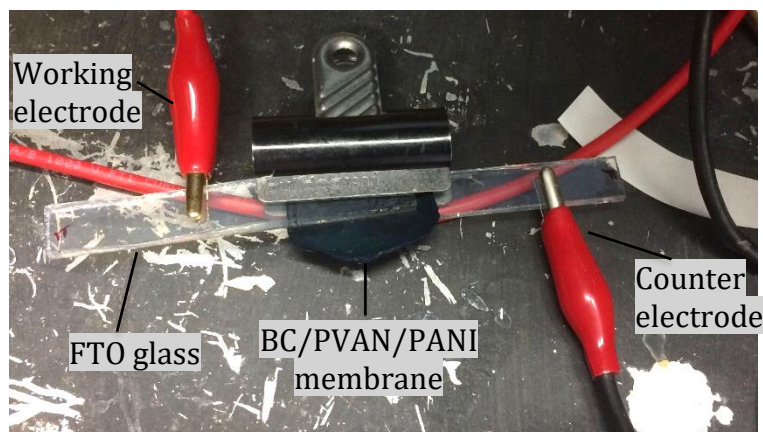


Figure 3.14. Illustrative set-up used for electrochemical measurements with a potentiostat. A BC/PVAN/PANI membrane clamped between two pieces of FTO glasses (1 cm per 2 cm).

Fundamentals of Electrochemical Impedance Spectroscopy

The analysis of complex electrical systems is often performed with EIS, which can easily detect diverse surface phenomena, changes in bulk properties, corrosion mechanisms, charge transport across membranes and membrane/solution interfaces [163]. The electrical resistance, as defined by means of Ohm's law ($R=V/I$), states a linear relationship between an applied potential (V) and the measured current (I), considering an ideal resistor. However, most of the real systems do not follow Ohm's law, showing much more complex behaviours. As such, the impedance, Z , is often used to describe the ability of a circuit to resist the flow of the electrical current, which is not limited to the simplified assumptions of Ohm's law [164].

Z can be efficiently measured with EIS by applying an AC voltage to an electrochemical cell with the measure of the resulting AC current. A small sinusoidal perturbation ensures a pseudo-linear response (similar to Ohm's law). The data is often represented in the complex space in Nyquist plots, which enables the characterisation of surfaces, layers or membranes, as well as exchange and diffusion processes. In Nyquist plots, low Z_{real} -values have information acquired at high frequencies, while high Z_{real} -values have information at low frequencies.

Equivalent circuits are used to describe the experimental data and to understand the contributions of the individual components of the material under study [165]. These electrical circuits consist of ohmic resistances, capacitances/constant phase elements, inductances, and Warburg elements, that can be arranged in parallel or in series.

The Randles circuit is used when an electrode is in contact with an electrolyte, which often serves as basis for building more complex circuits. This is consisted of a solution resistance, R_s , charge transfer resistance R_{ct} , double layer capacitance C_{dl} , which can include or not a Warburg impedance, W (Figure 3.15b). The impedance representation of a Randles circuit is a semicircle in the complex space, due to limited range of frequencies during data acquisition (Figure 3.15a). Two or more of these circuits in series result in two or more semicircles, respectively. Warburg impedance accounts for a diffusional process, which can be seen as straight 45° line raising from the interception of the semicircle with the real axis at higher values (Figure 3.15a). However, its contribution is often omitted when the interfacial or bulk impedance is dominant.[164].

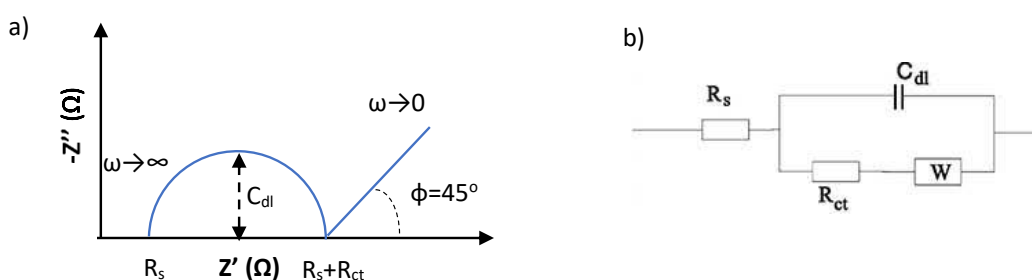


Figure 3.15. a) Example of Nyquist plot with a diffusion line obtained from the equivalent Randles circuit shown in b). R_s , R_{ct} , C_{dl} and W stands for solution resistance, charge transfer resistance, double layer capacitance and Warburg impedance.

Procedure

Electrochemical properties of pristine BC and BC nanocomposite membranes were assessed through EIS in solid-state. The spectra were acquired using a Galvanostat/Potentiostat (Eco Chemie microAutolab type III). The data were recorded for 0 V of DC potential and on superimposition of a sinusoidal AC potential of 10 mV, over the frequency range of 9997 Hz to 0.1 Hz. All samples were placed between two pieces of fluorine doped tin oxide (FTO) glasses with size 1 cm per 2 cm, which acted as working and counter electrodes (two electrode mode) [Figure 3.14].

Initial testing was performed on never-dried (100% water content) and partially dried (80% and 50% water content) BC membranes. The samples used were roughly 8 ± 0.5 mm thick in their never-dried state with 8 mm of diameter (obtained using a

standard biopsy punch). For the oven-dried membranes, the spectra were recorded for pristine BC, BC/PVAN and BC/PVAN/PANI, that were previously soaked in 1 M sulphuric acid (H_2SO_4) solution used as electrolyte. EIS of BC/PVAN/PANI was further obtained with different applied DC bias of 0, 0.5, 1, 1.5, -0.5, -1 and -1.5 V.

3.3.8 Thermogravimetric Analysis

Thermogravimetry (TG) is the study of the variations in the mass of a material when heated within a specific temperature range. TG is particularly useful for analysing the thermal stability of a material and can also draw conclusions on the reaction mechanisms of thermal (catalytic or non-catalytic) decomposition involved in the pyrolysis and combustion processes of different materials. It provides information on different matters, such as phase transitions, absorption and desorption, chemisorptions, thermal decomposition, and solid-gas reactions (e.g. oxidation or reduction).[166].

Thermogravimetric analysis (TGA) of the samples was evaluated within the temperature range 30-800 °C, using a thermogravimetric analyser (TGA, SDT Q600 V20.9 Build 20, TA Instruments). TGA testing was performed under an inert atmosphere of nitrogen and in open alumina pans heated at 10 °C.min⁻¹. From the TGA curve and its first derivative, the following parameters can be extrapolated: the onset (T_{onset}) and the offset (T_{offset}) temperatures, ascribed to the start and the end temperatures of a process, respectively. The peak temperature (T_{peak}) can be also extrapolated and marks the point of greatest rate of change in the weight loss, commonly associated to the melting point of a material. Figure 3.16 shows a representative TGA curve and its first derivative, illustrating how the aforementioned parameters can be obtained from the graphic.[167].

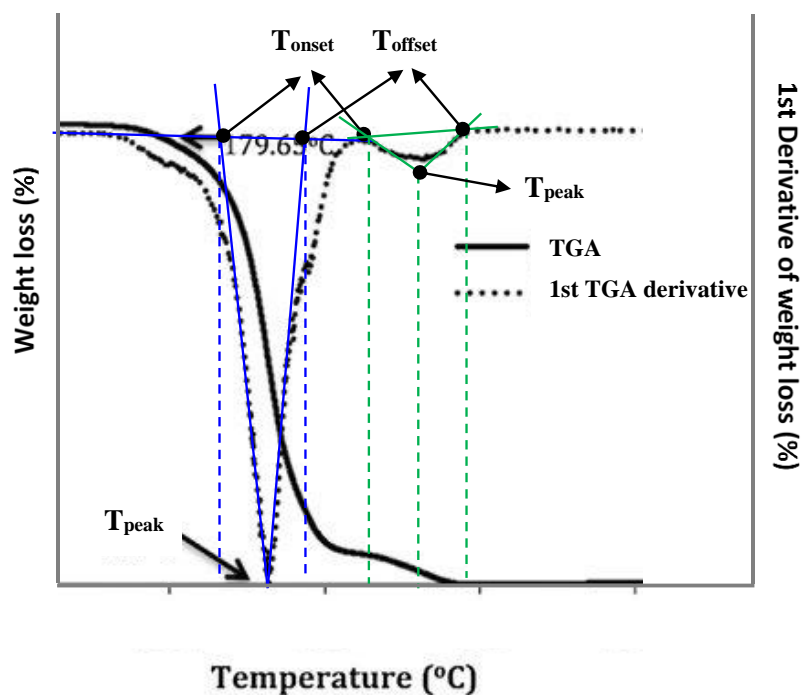


Figure 3.16. Illustrative TGA and 1st derivative TGA curves, showing the onset (T_{onset}), offset (T_{offset}) and peak temperatures (T_{peak}) extrapolated from the first derivative curve (adapted from [168]).

3.3.9 Cytocompatibility Assays

To verify the cytocompatibility of the newly developed functionalised BC-based nanocomposites, PC-12 Adh cells and neural stem cells isolated from the subventricular zone (SVZ) of postnatal mice were incubated with the grafted BC membranes for 7 days, as such their responses were evaluated and compared with that of pristine BC and tissue culture treated plastic (TCTP), which was used as a control. Cell viability and differentiation tests were performed for both cell types, as schematically illustrated in Figure 3.17.

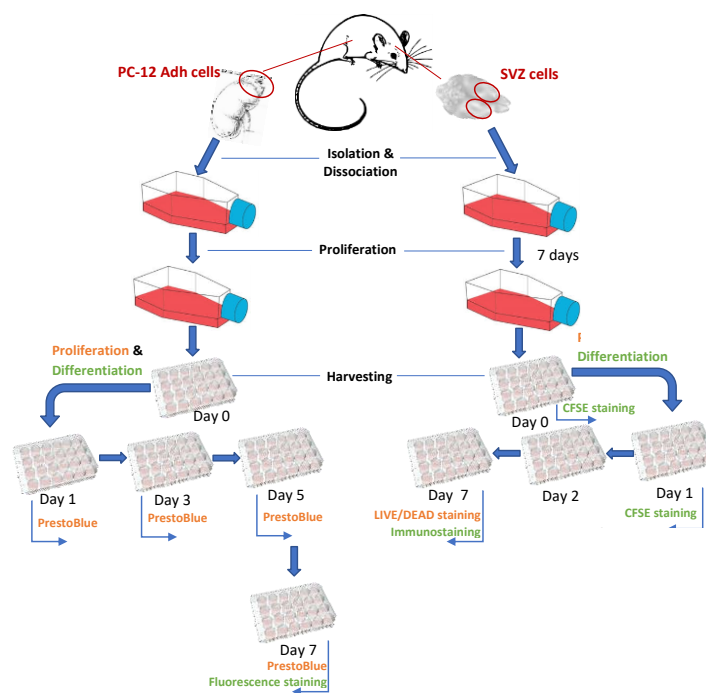


Figure 3.17. Schematic diagram of the cytocompatibility assays performed through cell cultures on pristine BC and BC-based nanocomposites with two neural cell models, PC-12 Adh and SVZ cells.

Cytocompatibility with PC-12 Adh Cells

Cell Culture

PC-12 Adh cells (Rattus norvegicus adrenal gland, ATCC[®] CRL-1721.1[™]) were cultured for 7 days in proliferation medium consisted of DMEM medium supplemented with 15% HS, 10% FBS and 1% pen/strep, which was kept in a sterile environment at 37 °C and 5% CO₂ atmosphere with medium replenished every 2 days. Cells were then passaged with a scrapper before being used for further analysis. See Appendix C for more details.

Cell Viability with Presto Blue Assay

PC-12 Adh cells were seeded on BC-based membranes and tissue culture treated plastic (TCTP) in 24-well plates at a density of 1×10^4 cells.cm⁻² and kept in culture for 7 days in proliferation medium. To assess the viability of the cells, metabolic testing was performed using Presto Blue[®] reagent added at 10% V/V and incubated for 2 hours, before measuring the optical absorbance with a microplate reader (FLUOstar Omega, BMG LABTECH) at 570 nm and 600 nm, as described in the supplier's protocol (see more details in Appendix C). The absorbance was measured

24 hours after seeding and every 2 days until the end of the culture period. The absorbance measured at 570 nm was normalised to that at 600 nm, and the contributions from the medium and Presto Blue (blank) were subtracted. The results were compared with that of TCTP, which served as cell control. Cells were fixed with 2.5% GA for morphological observation with SEM. Pristine BC and BC nanocomposite membranes were soaked in proliferation medium 2 hours before seeding for improved cell adhesion.

Cell Differentiation

PC-12 Adh cells were induced to differentiate in the presence of NGF-supplemented medium for 7 days. In summary, cells were harvested at 1×10^4 cells.cm⁻² in proliferation medium, which was exchanged in the following day (24 hours) by differentiation medium containing DMEM, 1% HS, 1% pen/strep and 100 ng.mL⁻¹ of NGF. Differentiation medium was replenished every 2 days up to 7 days. In the end of the culture period, PC-12 Adh cells were fixed with 4% PFA solution (1 mL) and stained with DAPI and Alexa Fluor® 488 Phalloidin, as described in the supplier's protocol (just the enough to cover the surface). Briefly, samples were first permeabilised with 0.1% Triton X-100 in PBS for 15 min and washed for at least two times with PBS. Then, fixed cells on the samples were incubated with 1% BSA in PBS solution for 30 min to prevent non-specific staining. Diluted Alexa Fluor® 488 Phalloidin stock solution (5 µl per 200 µl of PBS) was added to each well, just enough to cover the surface. Cells were incubated at room temperature for 30 min and washed thoroughly with PBS for at least 3 times. As phalloidin conjugates stains F-actin, a protein present in cell processes, any cell projections, including those from neurons or glia, will be interchangeably stained as green. After that, 300 nM of diluted DAPI stock solution was added to each well (just enough to cover the surface) for 30 min at room temperature and then, washed with PBS for at least 3 times. Stained cells were protected from the light during the whole staining procedure. The samples were mounted in glass slides using mounting media before visualisation of the induced cells with fluorescence microscopy (Nikon, Eclipse Ti).

Statistical and Data Analysis

Cell viability results performed with Presto Blue assay was represented in terms of average values (AV) of 3 samples and corresponding standard deviation (SD) of the normalised optical absorbance measured on all substrates (TCTP, BC, BC/PVAN, BC/PVAN/PANI and BC/PVAN/PANI/CNTs), for different set time points. According to supplier's specifications, the metabolic activity as detected by resazurin conversion is nearly directly proportional to the number of the existing cells. It is then defined 'cell adhesion' as the number of cells that were present after 24 hours of harvesting, and 'cell proliferation' as the evolution in the cell number throughout the culture period.

The differentiation degree of the induced PC-12 Adh cells was calculated based on the total number of cells that underwent differentiation on BC and BC nanocomposites seen in the fluorescence images, in relation to those on TCTP. It is understood by 'differentiated cells' as those cells that showed any signs of projections arising from the soma which were extended to further away. The average number of 20 neurites (with corresponding SD) of the induced cells were measured with ImageJ software from each fluorescence image (for a total of 3 per sample) to determine the neurite length in the end of the culture period. The length of each neurite was considered to be the maximum distance of any cell body projection or to the end of the longest branch, in the case of branched neurites.

Statistical significance ($p < 0.05$) between the several substrates for each set time point and/or over the culture period on both assays was determined with two-sample t-test or one-way ANOVA, accordingly, using Origin®2015 software.

Cytocompatibility with SVZ Cells

Cell Isolation and Culture

Primary SVZ cells were isolated from subventricular zones of 1–5 days old postnatal BALB/c mice (P1-P5), following German local regulations for animal welfare. After appropriate cell purification and digestion procedures, cells were grown in proliferation medium consisting of DMEM/F12 GlutaMAX supplemented with 1% pen/strep, 1% BSA, 2% β -27 w/o RA, 2% β -ME, 0.2% rh β FGF and 0.1% rhEGF. The culture was kept in the incubator for 5 days at 37 °C and 5% CO₂ atmosphere with

medium replenished every 2 days, followed by dissociation. See Appendix C for more details.

Cell Viability with LIVE/DEAD Assay

SVZ cells were further incubated with BC scaffolds at 1×10^4 cells per cm^{-2} and kept for 7 days in proliferation medium under the atmospheric conditions described above. Cell suspensions were collected at day 7 and live and dead assay was performed to verify cell cytotoxicity. The staining solution was prepared in PBS containing 1% calcein AM and 1% PI. 200 μl of dual fluorescence calcein AM/PI solution were added into each well and incubated for 20 min at 37 °C. Four images per well were taken using a fluorescence microscope (Olympus, IX71, Japan), which were used to calculate the average number of live and dead cells on each well. Live cells were stained green and dead cells were stained red. See Appendix C for more details.

Cell Differentiation

Neural differentiation of SVZ cells was assessed *in vitro* with BC nanocomposites and compared with those seeded on glass coverslip, used as cell differentiation control. 5×10^4 cells. cm^{-2} were harvested on substrates, that were previously steam sterilized at 120 °C for 30 min and coated with extracellular matrix gel (ECM, 1:200 in DMEM-F-12 medium) to facilitate cell adhesion. Differentiation was induced for 7 days in differentiation medium (DM), containing DMEM-F-12 GlutaMAX medium supplemented with 1% pen/strep, 1% BSA, 2% β -27 with RA and 2% β -ME. CellTrace™ CFSE staining was used for labelling SVZ cells, conform is described in the supplier's protocol for cell tracking, and observed with fluorescence microscopy in green fluorescence mode throughout the culture period and at specific check point times (2 hours, 24 hours and 7 days). The induced cells were fixed at 4% PF and stained with DAPI, green and red fluorescence proteins (GFP and RFP, respectively) for observation of cell nuclei (blue), neurons (green) and glia (red), correspondently. Briefly, cell membranes were initially permeabilised with 0.5 % Triton X-100 for 10 min, followed by 1 hour of incubation with 1% NDS for blocking unspecific binding. The excess of NDS solution was removed with washes in PBST (once) and PBS (three times). Primary (1:200 anti-rabbit β -tubulin III for neurons + 1:500 anti-mouse α -GFAP for glial cells) and secondary (1:1000 DAM-488 for β -

tubulin III + 1:1000 DAR-594 for α -GFAP) antibody solutions were consecutively added thereafter and incubated for 1 hour each, followed by triple washes in PBS. Lastly, DAPI was added for 10 min and the residual amount removed with triple washes in pure water. All solutions were added with an amount just the enough to cover the surface.

Statistical and Data Analysis

Cell viability was calculated for each condition based on the average of 3 replicates using the following equation:

$$\text{Cell viability (\%)} = \frac{\text{live cells}}{\text{total number of cells}} \times 100\%, \quad (3.13)$$

where the total number of cells correspond to the sum of live and dead cells.

The differentiation degree of SVZ cells on BC nanocomposites and glass coverslip substrates was estimated with the ratio of the number of cells showing processes to the total number of cells displayed in immunostained images on the 7th day, using the average of three pictures. Neurite length over time (2 hours, 24 hours and 7 days) was quantified by measuring the length of 10 neurites from the average number of three CFSE labelled-cell images per replica and per condition, using ImageJ software. All results were expressed in terms of $AV \pm SD$ and statistical significance between the different groups of substrates was hypothesised for $p < 0.05$ using two-sample t-test or one-way ANOVA, accordingly, using Origin®2015 software.

Chapter 4: Synthesis and Characterisation of BC Membranes

The content of this chapter is included in the published scientific article “R. Rebelo A, Archer AJ, Chen X, Liu C, Yang G, Liu Y. Dehydration of bacterial cellulose and the water content effects on its viscoelastic and electrochemical properties. *Sci Technol Adv Mater*. Taylor & Francis; 2018 Dec 31; 19(1):203–11”.

This chapter is dedicated to the preparation and characterisation of BC membranes that were used as a substrate for further modification and functionalisation (Chapters 5 to 7). Although extensively studied in the last few years, the properties of BC are far from being completely understood, in particular how the content of bounded and unbounded water would be reduced during the dehydration process and its corresponding effects on its viscoelastic and electrochemical properties. This chapter intends to elucidate some of these aspects to potentially optimise the electrochemical and viscoelastic properties of BC-based materials relying on the water content. Morphological, chemical and mechanical analysis was performed to assist this study, and a mathematical model was also proposed for analysis and eventual predication of the water loss of BC membranes at 37 °C, with a determined thickness and surface area (Figure 4.1). This analysis will be important for targeting specific applications, inclusively those out of the scope of this research.

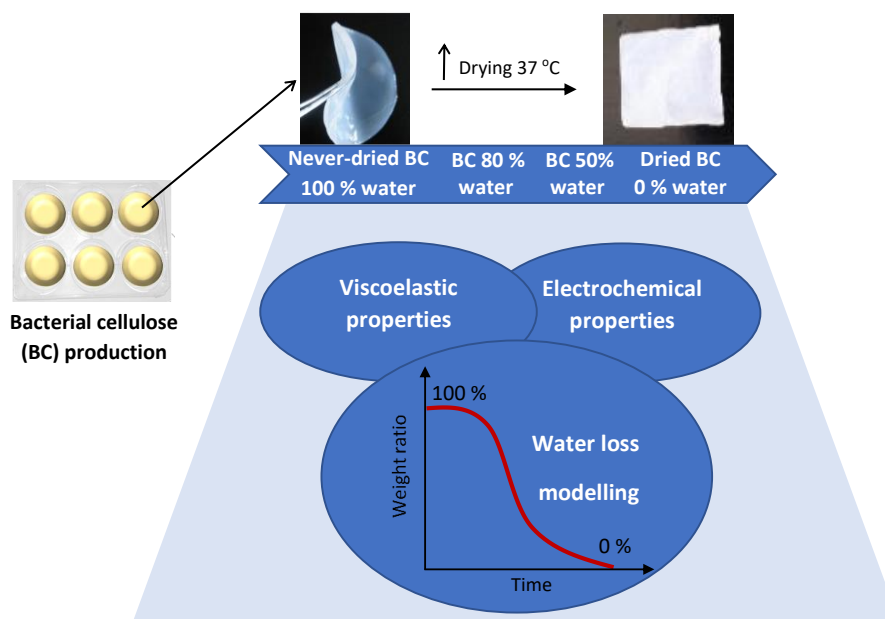


Figure 4.1. Schematic diagram illustrating BC membranes subjected to dehydration at 37 °C, with water loss modelling aiming the prediction of the viscoelastic and electrochemical properties of BC membranes.

4.1 RESULTS

4.1.1 Morphological Characterisation

Figure 4.2 shows a scheme of BC production with representative SEM images of a freeze-dried membrane with sides interfacing air or liquid, as well as the internal structure exemplified in a vertical cross section. A stratified structure could be observed with multiple nanofibrous layers. At the air interface, high conglomerate of nanofibres formed a dense and compact layer, while at the liquid interface, large pores were observed.

Bacterial cellulose production

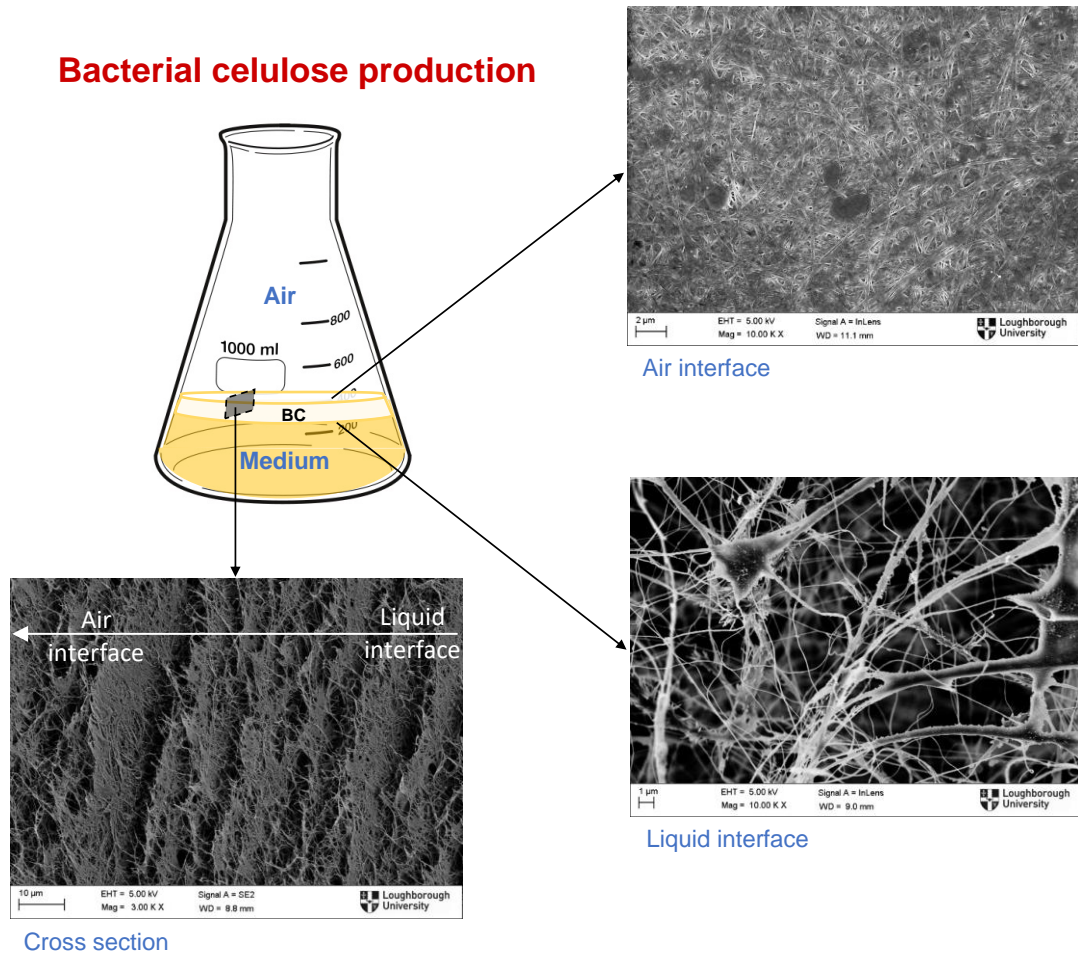


Figure 4.2. Diagram of BC production displaying SEM images of both surfaces of a freeze-dried membrane, interfacing air and liquid respectively, and a cross section [169].

4.1.2 Chemical characterisation

Fourier infrared spectroscopy

ATR-FTIR spectrum of BC is represented in Figure 4.3. The strong absorption band at $3600\text{--}3100\text{ cm}^{-1}$ was assigned to the stretching of -OH groups in BC. O-H bending was also observed at 1641 cm^{-1} . CH stretching and symmetric bending of CH_2 was identified at 2887 cm^{-1} and 1425 cm^{-1} , respectively. The peak at 1359 cm^{-1} could be attributed to CC and CO cellulose skeletal vibrations, while that at 1313 cm^{-1} corresponded to stretching and bending modes of hydrocarbons. The absorption peaks at 1161 cm^{-1} and 893 cm^{-1} were ascribed to COC stretching of $\beta\text{-(1-4)}$ linkages. Pronounced peaks at around 1105 cm^{-1} and 1026 cm^{-1} were attributed to vibrational modes of CO stretching groups.[170, 171].

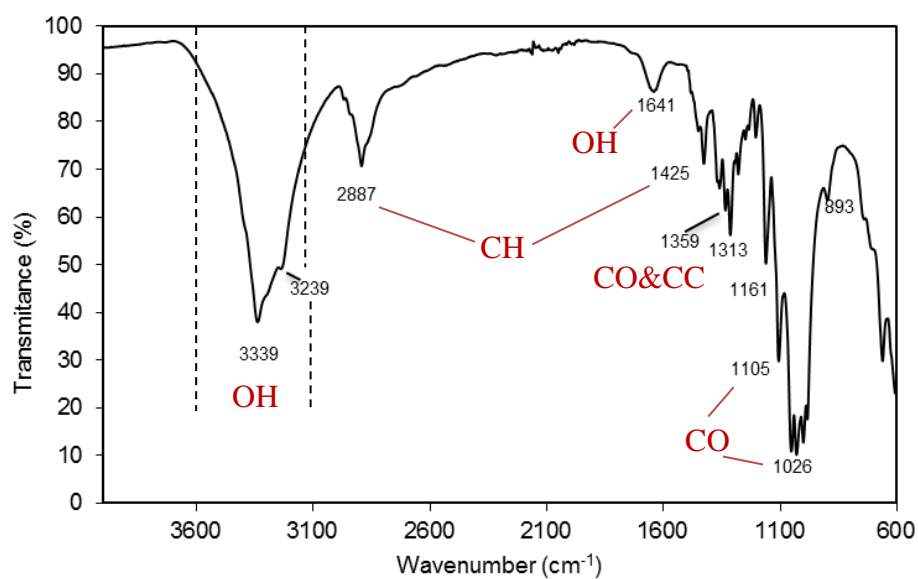


Figure 4.3. Representative ATR-FTIR spectrum of BC with indication of the corresponding vibrational modes of the functional groups [169].

X-Ray Diffraction

BC has a highly crystalline structure, as displayed in XRD spectrum of Figure 4.4. Two diffraction peaks at 14.5° and 22.7° were identified and ascribed to various crystal plane of unit cell structure of I_α and I_β crystal cellulose. The first diffraction peak is associated to 100_{I_α} , 110_{I_β} and 010_{I_β} plans and the second, to 110_{I_α} and 200_{I_β} [172]. According to the data obtained and using the Scherrer equation 3.4 and 3.5, BC crystallinity is as high as 90.5 % and with a crystallite size of approximately 50.4 nm, similar to what has been found in literature for microbial cellulose [173].

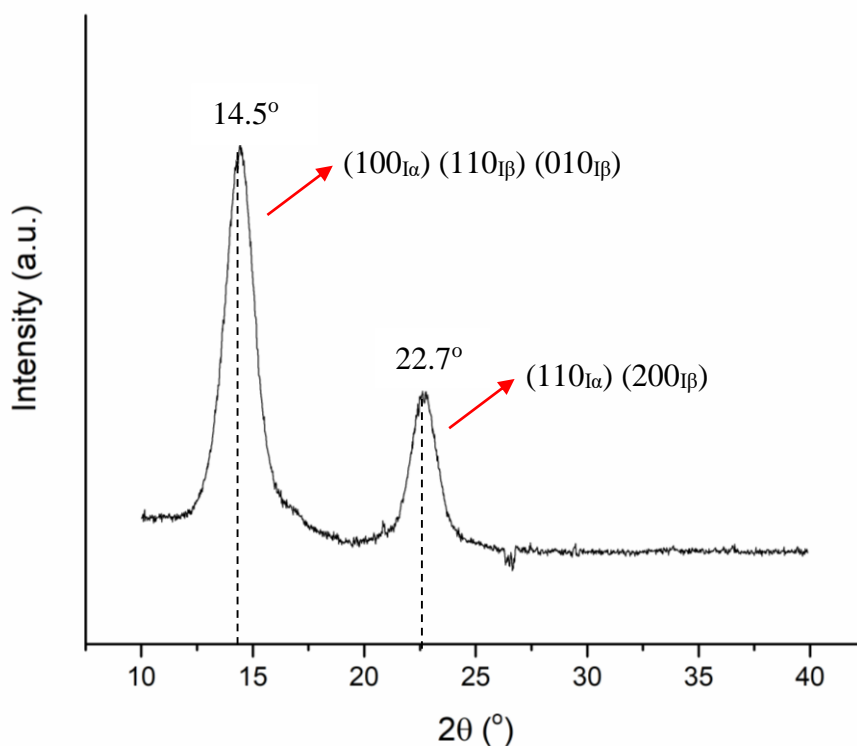


Figure 4.4. Representative XRD pattern of BC.

4.1.3 Thermogravimetric Analysis

The thermal stability of BC was inferred from TGA curve measured in the range of 25-800 °C, from which the first derivative curve could be obtained to estimate the onset (T_{onset}), offset (T_{offset}) and peak (T_{peak}) temperatures (Figure 4.5). There are three weight loss stages which were marked by two main thermic transitions. The initial and tiny mass loss (of about 5 %) observed below 200 °C could be attributed to the evaporation of the remaining water confined within BC (see stage I in Figure 4.5). From about 325 °C to 375 °C (stage II in Figure 4.5), most of the BC was lost occurred, showing the highest degradation rate at 362 °C (T_{peak}), corresponding to the temperature at which BC lost half of its weight (50%). This stage was associated to the main chain decomposition of crystalline and amorphous regions of BC into D-glucopyranose monomer and free radicals (pyrolysis). The final degradation stage, from about 375 °C onwards (stage III), was attributed to the residual main chain decomposition with a final residual weight of 20 %.[174].

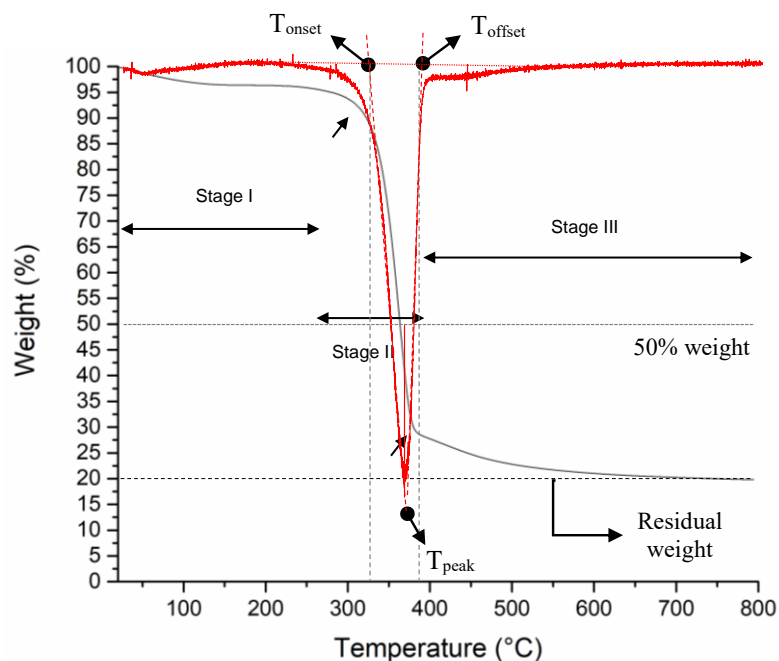


Figure 4.5. Representative thermogravimetric curve of 5 BC samples (black) and corresponding first derivative (red) from which the onset (T_{onset}), offset (T_{offset}) and peak (T_{peak}) temperatures were measured. Three main weight loss stages are identified: Stages I, II and III.

4.1.4 Viscoelastic Properties

Figure 4.6 displays representative data of the viscoelastic properties of BC membranes (2.3 ± 0.4) mm thick and with different water contents. The viscoelastic properties followed the same pattern for the varied water contents, with higher storage modulus magnitude than that of loss modulus over angular frequency and nearly all the strain range measured. It is also clear that all moduli became higher with lower water contents in BC membranes.

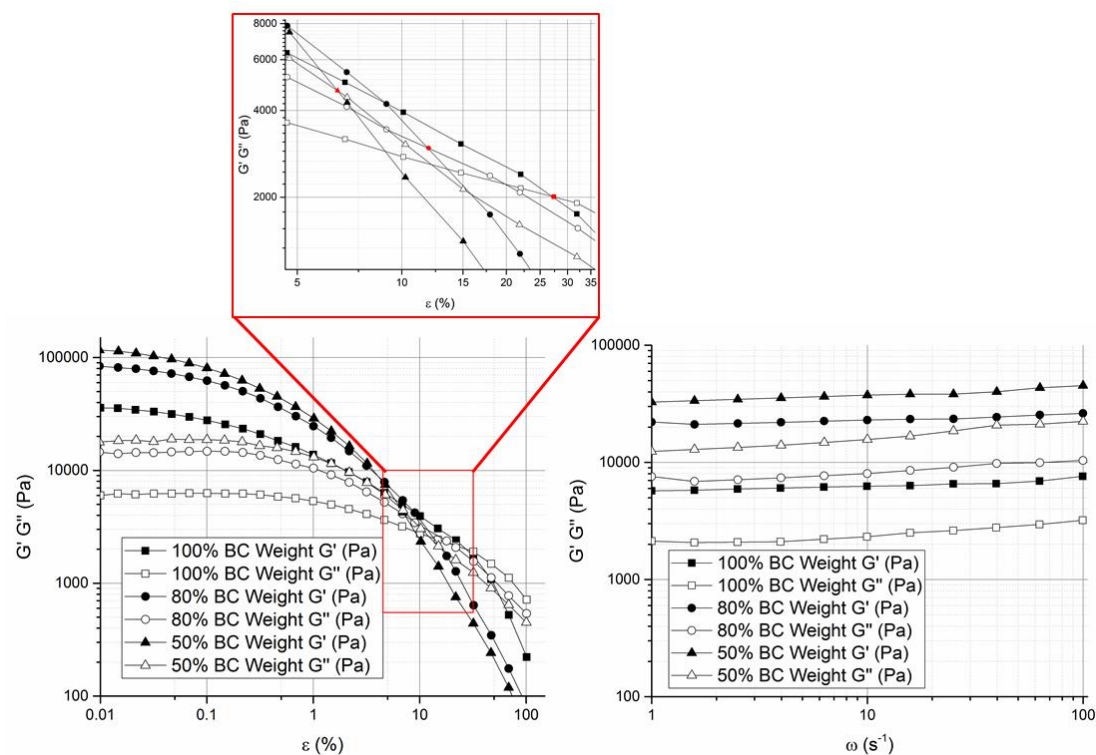


Figure 4.6. Representative curves of storage (G') and loss (G'') moduli of BC membranes holding 100, 80 and 50 % water, measured as a function of strain (left) and frequency (right). The red dots indicate the interceptions between G' and G'' . [169].

Over the applied strain, the storage and loss moduli remained reasonably constant up to 0.1 % and 1 % strain, respectively - Linear Viscoelastic Region -, and then they started decreasing gradually until the loss modulus G'' intersected the storage modulus G' . With reduction of water content in BC membranes, both moduli were increased and the intersection between G' and G'' occurred at lower strain values. Establishing a steady-strain at the limit of the *plateau* region (1 %) led to a slight but almost insignificant increase in the moduli (storage and loss) could be measured in the frequency range of 1-100 $\text{rad}\cdot\text{s}^{-1}$.

4.1.5 Electrochemical Properties

Figure 4.7 illustrates the Nyquist plots of BC membranes holding 100, 80 and 50 % water content, evincing a semicircle shape that could be fitted into a Randles circuit as shown in Figure 4.7a. This circuit comprises a resistance, R_s (solution resistance), in series with other resistance, R_p (polarisation or charge-transfer resistance), which in turn is in parallel with a constant phase element (CPE). These

three parameters can be easily deduced from the Nyquist plots. R_s is obtained from the first intercept of the semicircle with the real axis at higher frequencies and is a measure of the electrolyte resistance. R_p is deduced by the second intercept of the semicircle with the X axis (Z') at low frequencies that refers to R_s+R_p , which counts for the resistance of charge transfer between the electrode and the electrolyte. Finally, the CPE quantifies the ability of the material (BC) to store electrical charges (capacitance) and can be inferred from the maximum point of the semicircle. The closer the N factor is to the unit ($N=1$), the closer the element's behaviour is from that of an ideal capacitor, which is the case under study. Table 4.1 summarises the corresponding information of the equivalent circuit elements R_s , R_p and CPE.

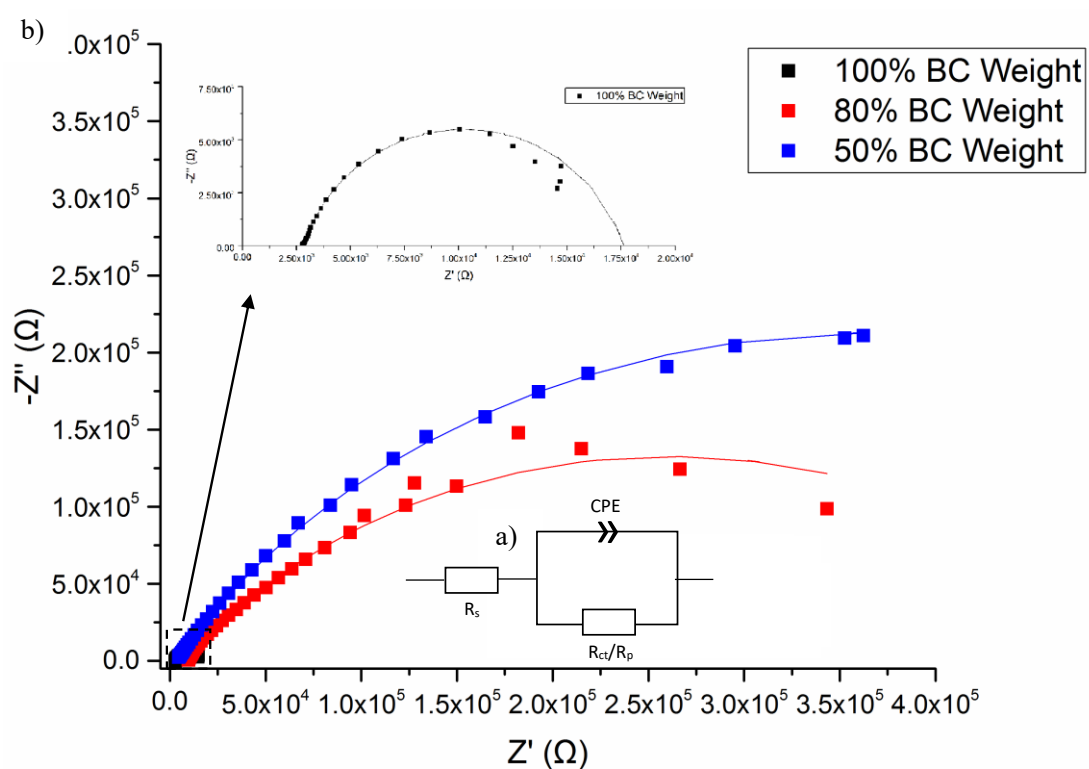


Figure 4.7. a) Randles circuit used for fitting the experimental data. b) Representative Nyquist plots of BC membranes with 100% (never-dried membrane), 80 % and 50 % water content. The solid lines (—) represent the respective fittings.[169].

Table 4.1. Average values of solution resistance R_s , polarisation resistance R_p , constant phase element CPE, and N values of Randles circuit used to fit the experimental data of 6 never-dried BC membranes per BC water content (100, 80 and 50 %) [169].

BC water content	R_s (k Ω)	R_p (k Ω)	CPE (μ F)	N
100 %	3.34 \pm 0.64	15.9 \pm 0.8	6.24 \pm 0.49	\sim 1
80 %	5.80 \pm 2.96	371 \pm 81	1.60 \pm 0.57	\sim 1
50 %	3.86 \pm 1.30	1400 \pm 910	1.09 \pm 0.76	\sim 1

By visual inspection of R_s , R_p and CPE values, obvious changes induced by the water content of BC could be observed. The capacitance, CPE, decreased almost 6 times when BC membranes lost half of the water content, whereas R_p increased about one order of magnitude per 20-30 % of water loss from 15.9 \pm 0.8 k Ω up to 1.40 \pm 9.10 M Ω . In the case of the solution resistance, R_s , the highest value was measured for 80 % of water content (almost 6 k Ω), while for 100 % and 50 %, lower resistances were observed (below 4 k Ω). Overall, R_p seemed to be the most affected parameter by changes in membrane water content, having risen to around 1000 times when BC lost half of its water content, whereas R_s was the least affected and CPE revealed just a slight tendency to change.

4.1.6 Dehydration and Numerical Modelling of Wet BC Membranes

Water evaporation of BC membranes with varied thickness and diameter were analysed after drying in the incubator. The water loss profiles over time and their respective predictions by the model equation system 2 are shown in Figure 4.8 in terms of weight percentage. For all samples, the final weight of the remaining materials after complete water loss was on average 2 % of BC initial weight, corresponding to dry cellulose fibres. All profiles displayed the same trend, decreasing over time with distinguishable three phases of water loss in each profile, namely, a slow but short beginning, followed by a fast and sustained water loss, and a very slow evaporation rate in the final step. This distribution was mostly observed in the 8 mm thick-samples, which generally required longer time for complete water loss comparing with the 2 mm thick-samples, as expected. Likewise, increasing the diameter from 5 to 8 mm

caused slower water evaporation. For instances, the thickest membranes with 8 mm of diameter required roughly 11 hours for complete water evaporation, while those with 2 mm of diameter required 9 hours.

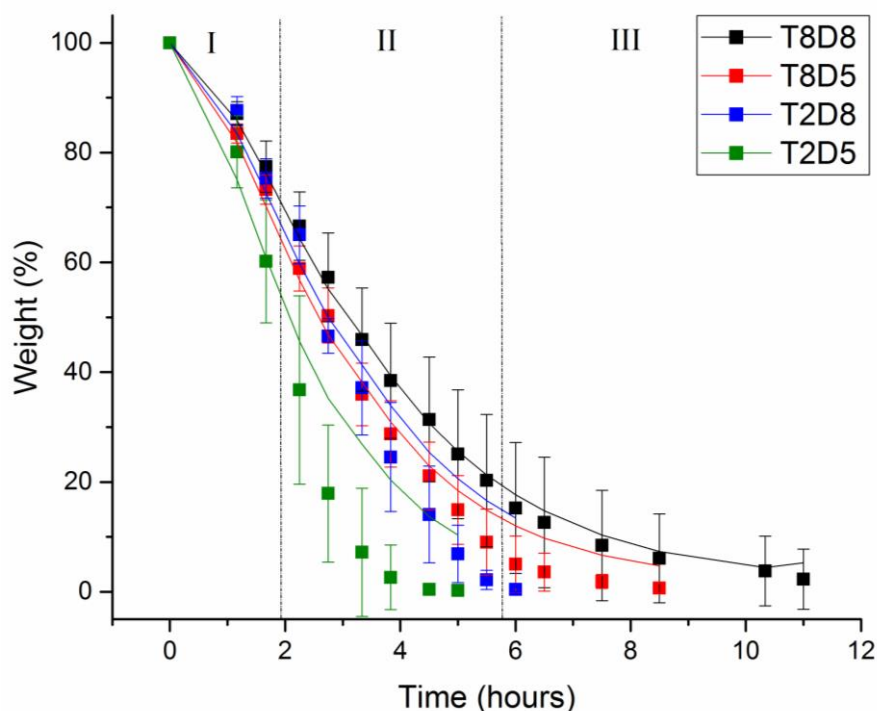


Figure 4.8. Experimental water loss (■) and respective modelling (—) of BC membranes 8 mm thick and 8 mm of diameter (T8D8), 8 mm thick and 5 mm of diameter (T8D5), 2 mm thick and 8 mm of diameter (T2D8) and 2 mm thick and 5 mm of diameter (T2D5). The water loss curves of each size/thickness correspond to an average of 5 samples and the error bars correspond to the respective standard deviations.[169].

The curve-fitted water loss was obtained by using Levenberg–Marquardt algorithm that determined the three parameters values of the system (k_1 , k_2 and k_3) that minimized the difference between the predicted and the experimentally observed total mass $M(t)$ over time (Table 4.2). The initial proportions for bound and free water were considered based on that only 0.3 % of the 98 % of water in BC corresponds to free water and the remaining 97.7 % is bound water [175]. Thus, at $t=0$, $B(0)=0.977$ and $F(0)=0.003$. In general, the model allows for a very good fitting, with R-squared up to ~ 1 (Table 4.2). The best fitting was observed for the largest membranes, with increased deviation from the model as samples were reduced in size ($R^2 > 0.93$). Calculation of

the statistical residuals (Figure D.1 in Appendix) corroborated that, for T8D8 membranes, the theoretical adjustment could be mathematically accepted, and for other samples dimensions, the model needed to be finely tuned. Nevertheless, notable conclusions can still be drawn. Table 4.2 gives the sets of parameter values and respective ratios, calculated by OriginLab software that best fits the experimental data, for each size of membranes.

Table 4.2. Results obtained for the model expressed in equation 3.9 that gives the best agreement with the experimental data. Information related to surface area to volume ratio for each sample's dimension. [169].

	k_1 (hours ⁻¹)	k_2 (hours ⁻¹)	k_3 (hours ⁻¹)	R^2	Surface area/Volume (SA/V) (mm ⁻¹)
T8D8	0.56	11.8×10^{-8}	0.55	1.00	0.6
T8D5	0.68	1.0×10^{-8}	0.68	0.99	0.9
T2D8	0.70	65.6×10^{-8}	0.70	0.95	1.0
T2D5	1.02	20.5×10^{-8}	1.02	0.93	1.3

From Table 4.2, it is clear that k_1 and k_3 is much higher than k_2 . On average, the un-binding (k_1) and evaporated constant rates (k_3) are about the same regardless the size of the samples, that are meaningfully higher than the binding constant rate (k_2).

According to the model, a reduction in the diameter led to an increase of k_1 and k_3 of the thicker membranes in 22 % (T8D8→T8D5), and in 47 % (T2D8→T2D5) of the thinner ones. In contrast, k_2 decreased in 1000 % and 221 %, respectively¹. Decreasing the thickness of the membranes from 8 to 2 mm led to an increase of the constant rates. In particular, k_1 and k_3 increased by 25 % (T8D8→T2D8) and 50 % (T8D5→T2D5), while k_2 increased in 82 % and 95 %, respectively².

¹ Percentages calculated based on the expression $\frac{k_{D=5mm} - k_{D=8mm}}{k_{D=5mm}} \times 100 \%$

² Percentages calculated based on the expression $\frac{k_{T=2mm} - k_{T=8mm}}{k_{T=8mm}} \times 100 \%$

Because k_2 is very small and it is insignificant as compared to the rate constants k_1 and k_3 , variations in k_2 caused by changes in diameter and thickness of the samples, were not considered to be relevant. Overall, the parameters tended to decrease identically with both diameter and thickness, although thickness was apparently the factor that reflected bigger changes. In addition, k_1 and k_3 are proportional to the surface area to volume ratio (SA/V), which means higher SA/V ratios lead to higher un-binding and evaporation rates.

Non-dimensionalising the model (equation 3.9) showed that the behaviour depends on the rate constant ratios (Table 4.2). It is worth to notice that setting other k_1 , k_2 and k_3 values can give similar fittings to the experiments herein presented, by keeping equal ratios to those shown.

To study the effect of the parameters on the shape of the water loss curves, different k_1 , k_2 and k_3 from the optimal solution were tested and the water loss curves inspected using the Maple software. Increasing k_2 resulted in a gradual slope, whilst higher k_1 or k_3 resulted in a steeper slope, and vice-versa (Figure 4.8).

Decreasing k_2 to zero did not change the overall trend in the graph preventing that k_2/k_1 and k_3/k_1 are below 1. However, when k_2 increased by more than one order of magnitude the curve no longer fitted the experimental data for any other combination of k_1 and k_3 . Moreover, only small fractional changes in k_1 and k_3 could lead to significant modifications in the fitting.

4.2 DISCUSSION

BC has a very complex molecular structure that is bounded to water through hydrogen bonding. BC fibrils are formed by linear chains of successive glucan units linked through β -1,4 glycosidic bonds (Figure 4.9). Inter- and intra-molecular hydrogen bonds are established between glucan chains, which gives BC a rigid molecular structure but it is still mechanically flexible [176]. The understanding of the dynamic of the water loss process would allow further engineering of the BC hydration level to tailor various requirements on mechanical and electrochemical properties of BC membrane. Mathematically modelling the water loss can assist the process for reaching such requirements and can guide to a closer perception of the strong correlation between BC network and water. Accordingly, this information may be

useful for future manufacturing and optimisation of some biomedical applications including electrically conductive hydrogels and papers with different conductive range [73].

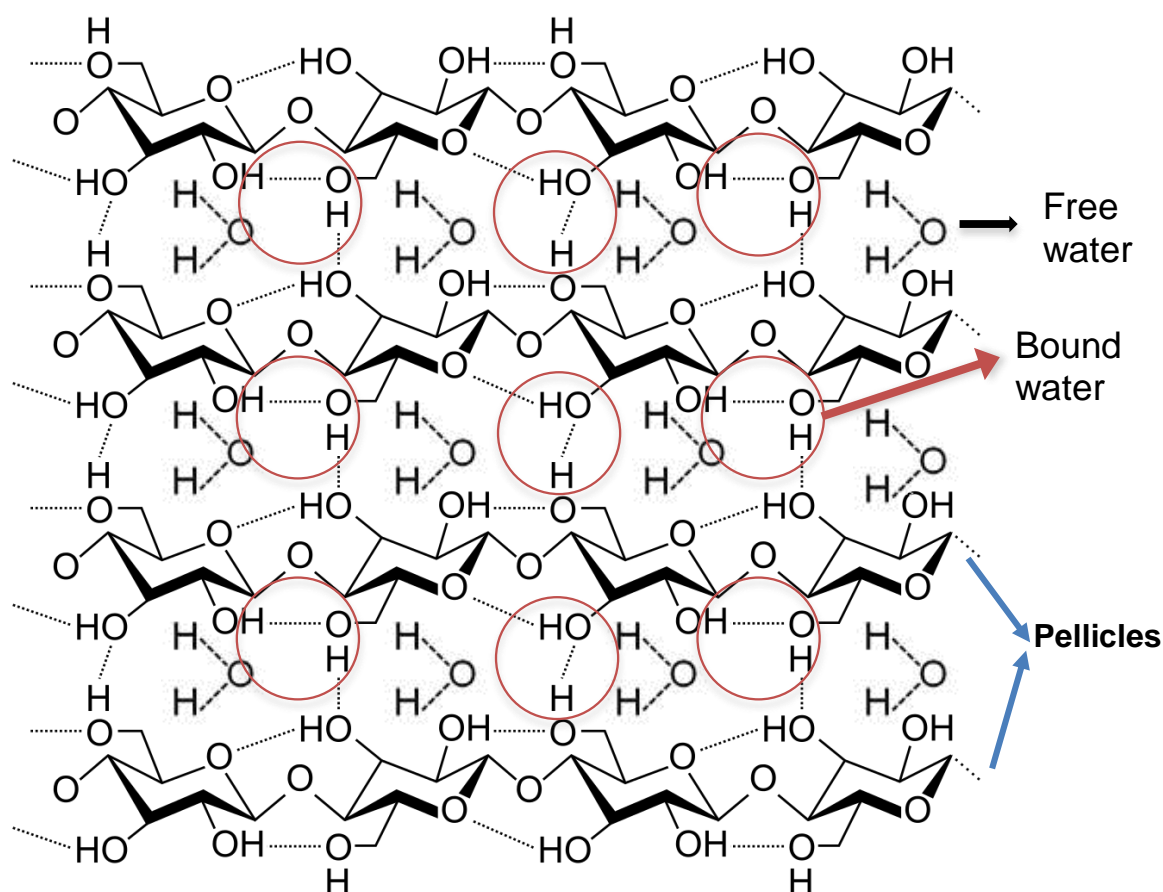


Figure 4.9. Schematic of the molecular structure of BC and their bound and free water [169].

4.2.1 Water Loss Effects on BC Morphology

Under static conditions, BC membranes result in a complex stratified structure that is controlled by the air supply from the medium surface, while the yield is regulated by the carbon source [58]. It starts with the formation of a thin layer called pellicle. During the process, cellulose is synthesised downwards into the medium interface and multiple pellicles are linked through interfibrillar hydrogen bonds, forming opened-spaces in between [177]. However, SEM images of both top and bottom surfaces demonstrated structural differences according to the side of the membrane that interface air or medium (Figure 4.2). Similar results have been reported already and it was attributed to a lesser availability of oxygen as bacteria travel deeper

into the medium upon bacteria proliferation and cellulose secretion. Therefore, larger number of microorganisms are present at the air interface, creating a denser layer that forms an additional nutrient barrier.[177–179]. These structural differences contribute to the mechanical and electrochemical properties of BC, that will be discussed in the next sections. From the TGA analysis, the temperature at which the chemical decomposition of BC starts is as high as 323 °C (T_{onset}) and thus, the drying process at 37 °C is not expected to affect its chemical and crystalline structure. However, morphological changes occur in BC membranes as the multiple layers pack together during the dehydration (Figure 4.10).

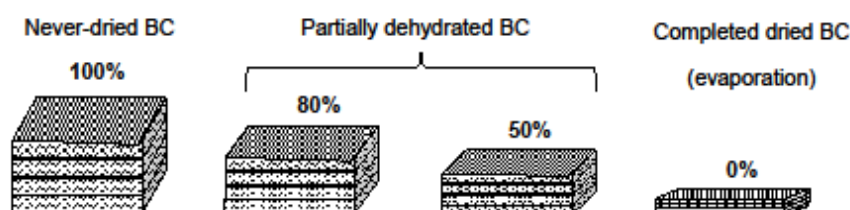


Figure 4.10. Schematic representation of the effects of the water content on the morphological structure of BC membranes composed of multi-stacked layers with free and bound water in between (see also Figure 4.9).

4.2.2 Effect of Water Content in the Viscoelastic Properties

Storage (G') and loss (G'') moduli indicate the elastic and viscous responses of BC membranes under compression and shear, allowing for prediction of its mechanical behaviours when used as biomaterials. Experimentally, G' modulus quantifies the material's ability to store energy elastically in entropic distortions of the fibril network of BC membranes; whilst G'' modulus quantifies the energy that is dissipated.

Depending on the strain and frequency, response of components of BC network, including free and bounded water and BC fibril interaction to shear stress at the interface [180], can be detected via oscillatory rheology. The water content in BC does not dramatically alter the shape of the profiles of both amplitude and frequency sweeps representative of G' and G'' . The elastic component dominates in the lower strain range, depending on the water content, which leads to the conclusion that BC behaves more like an elastic solid than a viscous liquid at lower strain level. Ideally, a *plateau*

region or Linear Viscoelastic region (LVR) should be observed below 1 % strain, where the amount of energy (G') stored and damped (G'') would be nearly steady and independent on the applied strain.

The LVR of BC could be considered up to 1 % strain at which the structure is barely affected and can be fully recovered elastically from the deformation imposed. Thus, 1 % strain would be the maximum deformation for reversible structure damage of the fibril network. Stored and lost energies decreased gradually after the *plateau* region, which could be due to junction disruptions, that partially and irreversibly damaged to the network. However, BC still responded mechanically more like an elastic material ($G' > G''$). Moreover, the storage and loss moduli got closer with increased strain, which also evinced some loss of the mechanical stability over strain and increased viscous behaviour.

Much of the inherent network properties can be scrutinised during frequency sweep at a given small oscillatory strain close to the *plateau* region observed in the Amplitude Sweep mode (1 % strain) because at this level, membranes store energy elastically between two network points as entropic springs (polymeric segments or strands). This allows a better understanding of the mechanical behaviour of BC with shear deformation. As expected in the LVR, BC fibril in the network structure showed a solid-like response ($G' > G''$) practically independent on the frequency, as evidenced by that storage and loss moduli reasonably constant throughout the frequency range measured and below the critical strain [181]. The tiny frequency hardening observed could be ascribed to some water loss during testing, although the possibility of frequency dependency could not be totally excluded, in particularly considering the power law dependence of storage modulus $G'(w) \sim w^{0.068}$ reported by Clasen C *et.al.*[182].

When BC was partially dehydrated, fibres aggregated together as result of the evaporation process, leading to some loss of elasticity (or increased rigidity) of more compact and cohesive membranes [182]. This slight mechanical property shift could be witnessed at a first glance in an increase in storage and loss moduli in both sweep modes; but also in a decrease in 'gel breaking strain' and in G'/G'' ratio in the LVR of the frequency sweep ($G'_{100\%}/G''_{100\%} \approx 2.69$; $G'_{80\%}/G''_{80\%} \approx 2.51$; $G'_{50\%}/G''_{50\%} \approx 2.00$). Though BC membranes behaved always more like a viscoelastic solid ($G'/G'' > 1$), the lesser the water content the closer the properties are to those of a pure solid, and vice-

versa, which is consistent with the increased stiffness. The storage modulus can be expressed in terms of the density of the polymeric segments:

$$G_p^0 = \frac{n}{V} K_B T, \quad (4.1)$$

where n is the absolute number of segments in the total volume V , K_B is the Boltzmann constant and T is the temperature [182]. In the LVR, with either water loss or swelling, it is anticipated no structural change in the network occurs and the number of segments n should not be affected, but the volume V would be altered. Consequently, according to equation 4.1, BC network with less water content and lower total volume would have an increase of the storage modulus. Lowering the water content below 50 %, it would lead to a dramatic loss of the rheological behaviour with a boost of the storage modulus.

4.2.3 Effect of Water Content in the Electrochemical Properties

EIS is a very useful tool that allows the characterisation of the electrical properties driven by chemical reactions in non-linear systems, i.e. in systems that do not follow the Ohm's law ($R=V/I$). In EIS, the impedance, Z , is used to describe the 'resistance' of the material instead. Studying the electrochemical properties of BC via EIS might be useful for understanding its contribution to the overall electrical properties of electrically conductive BC composites and the water content effects. The observed conductive properties extracted from EIS were probably originated from multiple current paths, including cellulose itself, although the protonic conductivity on hydrated surface of BC was most likely the major contributing source, due to the formation of protonic carrier by hydration of the surface of BC nanofibril [183]. Further, it is known that hydrogen bonding, as that present in BC, is a common feature of the majority proton conductors, as such interaction provides a proton transfer path, while also acting as a limiting step of the overall protonic conductivity [184].

The Randles equivalent circuit used to fit the experimental data showed a reasonable fitting. According to its definition (see Figure 4.7a), R_s is related to the bulk resistance of the system, which accounts for the resistance of the solution or electrolyte inside the material, the material between the electrodes and between the counter- and working-electrodes [185]. In this study, R_s is the part contributed from the water

resistance and the BC network, and remains the same regardless the water content as we observed here. The slight fluctuations observed in the average R_s values could be ascribed to the change of the conformation of the BC network with the dehydration. To a lesser extent, the resistance resulted from the contacts of the working-electrode and counter-electrode may also account for R_s . [73]. In this study, it was also observed that increased R_p with reduced water content in BC, which might be related with the correspondent lower amount of proton carriers in BC molecular structure, as well as decreased porosity and pore size of BC network after the dehydration ($R \propto 1/S A_{BC\ fibrils}$ [186]). Hence, the increased resistivity would be expected with R_p representing an indirect measurement of the network resistance. Considering that CPE was reduced after the dehydration process, it can be concluded that water contributed to the higher capacitance of BC. BC is formed by multiple stratified layers in which each set of two can be seen as a double layer capacitor with water within it as electrolyte. Eventually, a decrease of the protonic carrier and the distance between those stratified layers followed partial water loss might also contributed to lowering its capacitance ($C \propto Area$ [187]).

4.2.4 Understanding the Water Loss Process

The mathematical model for analysing the water loss profile within BC carried out at 37 °C matched reasonably well whole experimental data. The interdependency of k_1 , k_2 and k_3 suggests that it is the balance of the different processes that determines the water loss in the same time frame. The drying process can be considered as a two-step reaction, in which a series of chemical and physical processes take place concurrently. Water evaporation from surfaces, like in an open tank, is a physical process that depends on the temperature, humidity, and velocity of the air above the water surface. In our model, this process is easily described by the evaporated constant rate, k_3 , which accounts for water that is lost from BC membranes per unit of time. But the un-binding constant rate, k_1 , accounts also for the fact that there is a certain amount of water per unit of time that becomes free within the structure, due to the breaking of hydrogen bonds between cellulose and water; while the binding constant rate k_2 , accounts for water per unit of time that re-establishes those hydrogen bonds. Therefore, k_1 and k_3 are the constant rates that contribute to speed up water evaporation, whereas k_2 is responsible for slowing it down.

Hence, based on the model herein proposed, the following mechanism underlining water evaporation from BC can be adopted, which involves both the water that is bound to the cellulose molecule via hydrogen bounds, and the water freely circulating within the network (Figure 4.9). When the temperature is raised up to 37 °C, the constant rates of the system change according to Arrhenius equation ($k = Ae^{\frac{E_a}{RT}}$), causing changes in the chemical equilibrium. ‘The first’ water molecules which evaporate are the free ones located on the surface of the membrane. At the same time, as consequence of heat transfer, hydrogen bonds between water and BC start breaking, freeing water molecules. As free water travels within BC towards its surface, the amount of water that evaporates increases. The binding constant rate is very low but may not be zero due to possible air saturation which may lead to re-conversion of yet to be evaporated free water (remaining in the BC) into bound water. Furthermore, SA/V ratio of thicker membranes (0.6 and 0.9 mm⁻¹) is inferior compared to that of thinner ones (1.0 and 1.3 mm⁻¹). Hence, higher evaporation rates (K) are for samples with higher SA/V ratios and lower, for lower SA/V ratios. Although a simple model was presented, it is believed this model could be further improved to include other factors influencing the evaporation-drying process of BC membranes, such as the morphological heterogeneity of BC fibril network and its swelling capacity, considering for instances the evaporation through multiple layers.

4.3 CONCLUSION

Water comprises about 98 % of the BC structure, and slight changes to its content can lead to significant modifications in the overall properties. Along with the structural changes, the water content was shown not only to be responsible for BC’s viscoelastic characteristics, but also for the electrochemical behaviour found, while retaining the molecular and crystalline structure. Lower water contents like 80 and 50 % caused increased stiffness, while BC resistance to electron transfer became higher and with lower electron capacity. Therefore, BC mechanical and electrochemical properties could be tailored to different biomedical applications by simply varying the water content that may be controlled with the proposed model for the drying process of BC.

Chapter 5: Development and Characterisation of BC/PVAN/PANI Nanocomposites

The content of this chapter is partially included in the published scientific article “Rebelo A, Liu Y, Liu C, Schäfer K-H, Saumer M, Yang G. Poly(4-vinylaniline)/polyaniline bilayer functionalized bacterial cellulose membranes as bioelectronics interfaces. *Carbohydr Polym.* Elsevier; 2019 Jan 15; 204:190–201”.

This chapter is concerned with the production and overall characterisation of BC nanocomposite. On this wise, BC/PVAN/PANI nanocomposites membranes were produced in a three-step reaction. Oven-dried BC membranes were first modified with PVAN via ATRP for subsequent COP of aniline (Figure 5.1). This PVAN/PANI bilayer is electrically conductive and strongly tethered to BC. The presence of PVAN adds extra initiating sites within the BC/PANI interface, which is expected to increase the grafting PANI yield and to promote better PANI distribution on BC fibres with easier doping access. This can lead to an enhancement of the overall electrical properties, that will be discussed later in Chapter 6. The morphological, chemical and thermogravimetric analysis were performed and disclosed here to assess carefully the changes caused to the BC nanocomposites in the presence of PVAN. The results found in this study suggests prospective developments in cellulosic-based bioelectronic devices.

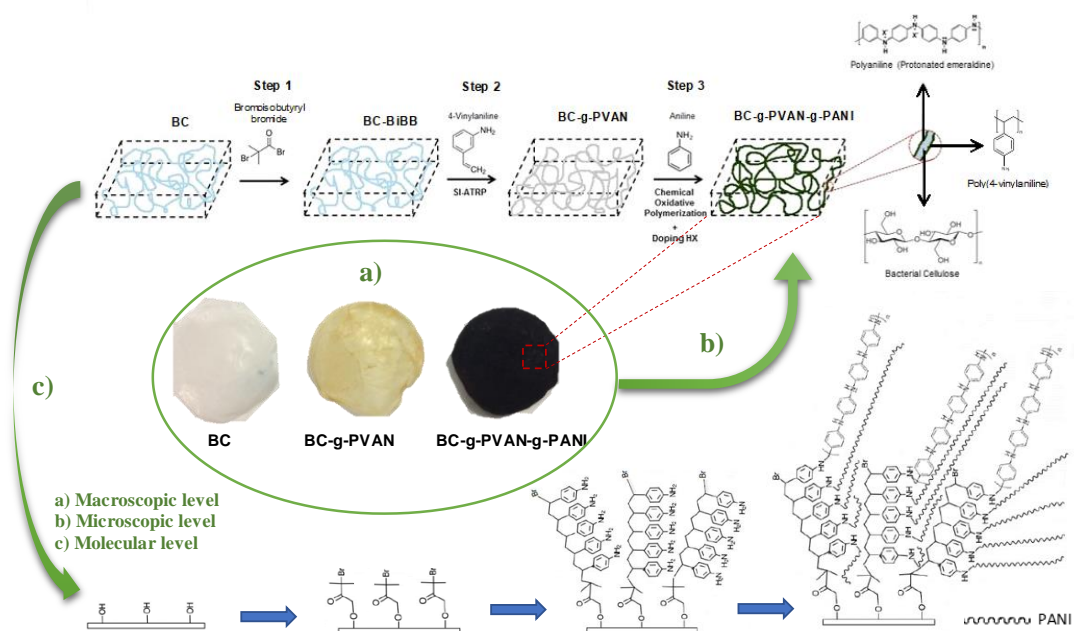


Figure 5.1. Schematic synthesis of BC/PVAN/PANI nanocomposite membranes at a) macroscopic, b) microscopic and c) molecular levels. Step 1: Initiator (BiBB) immobilisation onto BC. Step 2: SI-ATRP of 4-VAN onto BC. Step 3: COP of aniline on BC/PVAN in the presence of HCl as doping agent, to form BC/PVAN/PANI. (Reproduced by permission from Carbohydr Polym, Elsevier, [188] copyright 2019).

5.1 RESULTS

5.1.1 Morphological Characterisation and Surface Composition

As schematically shown in Figure 5.1, synthesis of BC/PVAN/PANI nanocomposite membranes has been achieved through the BC grafting chemical processes. The SEM and HRTEM morphology of these as-prepared nanocomposites (Figure 5.2) indicates that PANI functional coatings can cause immediate changes of texture and roughness to the original BC substrate as it has been observed elsewhere. Accordingly, the type of PANI supramolecular structures (Figure 5.2d-f) is closely correlated with the polymerisation conditions and the adopted synthetic procedure. Under highly acidic media with strong oxidants, PANI usually exhibits a granular morphology as observed in both BC/PANI and BC/PVAN/PANI membranes with BiBB:VAN=1:3 monomer content (Figure 5.2d,e), which has been reported for BC/PANI grafted membranes, as also present in Figure 5.2d.[189]. This is regarded as the result of random aggregation of high concentrations of aniline nucleates, which were produced during the short induction period [88]. These hydrophobic nucleates

are continuously formed and agglomerate together while PANI chains grow. Under magnetic stirring, heterogeneous nucleation takes place and new initiating sites appear on the surface of preformed particles, leading to a granular morphology [190]. However, it has been found in the present study that a lower ratio BiBB to VAN can cause the formation of both granules and nanofibers, providing also a more uniform PANI coverage on the BC nanofibres (Figure 5.2f).

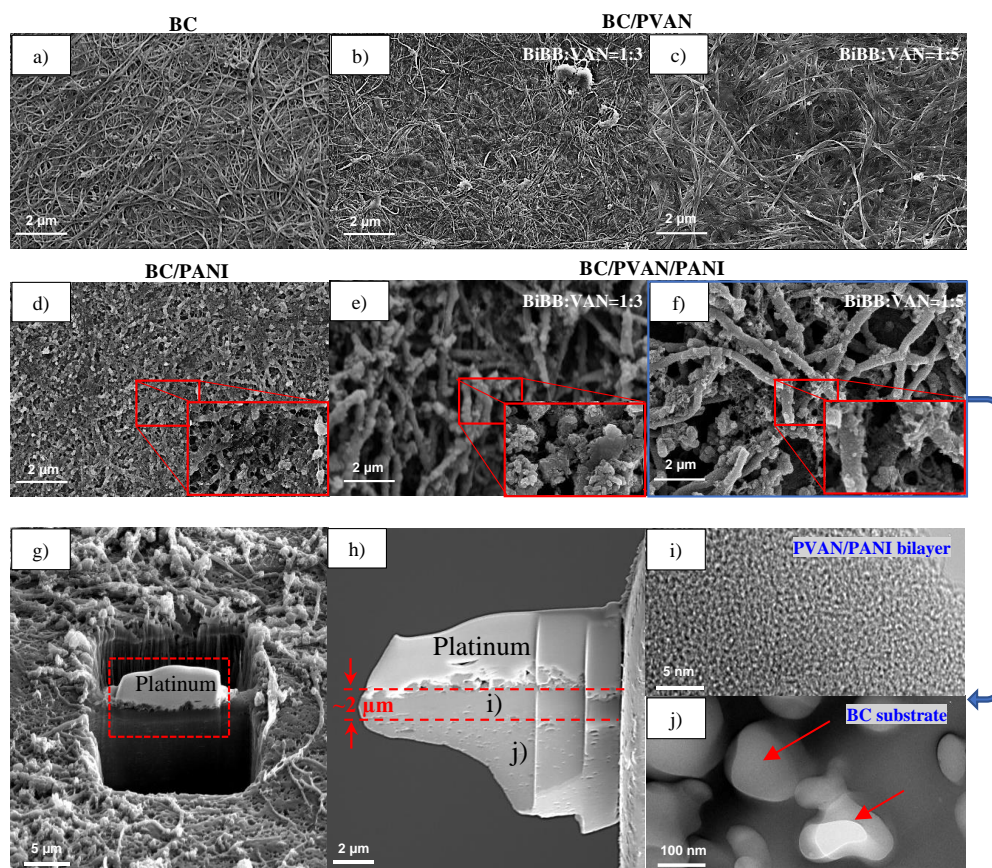


Figure 5.2. Representative SEM images and respective magnifications of a) un-modified BC nanofibrous membrane, showing nanofibres with smooth surface, b-c) chemically modified BC membrane with its nanofibrils grafted with PVAN (BC/PVAN). BC nanofibres membrane treated with d) PANI (BC/PANI) and e-f) with PVAN/PANI coating bilayer in two consecutive grafting procedures with PVAN and PANI (BC/PVAN/PANI), illustrating an increase in the roughness of the BC nanofibrils surface in contrast to pristine BC and BC/PVAN nanocomposite membranes. b,e) and c,f) BC nanocomposite membranes were produced from molar BiBB:VAN ratios of 1:3 and 1:5, respectively. g-h) FIB/SEM images of the FIB lift-out process used to extract a thin film TEM sample from the bulk BC/PVAN/PANI (BiBB:VAN=1:5) membrane, showing the thickness of the upper PVAN/PANI layer of $\sim 2 \mu\text{m}$. Corresponding HRTEM images of the selected area in g,h) of i) BC matrix and j) of the PVAN/PANI bilayer. The red arrows in j) indicate pores of BC substrate (Reproduced by permission from Carbohydr Polym, Elsevier, [188] copyright 2019).

PVAN on BC in such instance acts as a soft template that can induce preferential PANI growth, while stabilising interactions between phenazine-containing structures probably owing to its surfactant properties (i.e. primary amine surfactant) [191]. Under such conditions, homogeneous nucleation may take place with the suppression of secondary nucleates, which has been observed as a key factor for synthesis of this type of supramolecular structure [192]. Denser PVAN brushes implies more initiating sites for nucleation that may induce the continuous growth of PANI nanofibers in their vicinity [193]. Thus, different supramolecular PANI structures can be obtained subject to different PVAN grafting degrees.

The diameter of the fibres of BC before and after modification was also measured for BiBB:VAN=1:5 feeding ratio, accordingly displayed in Figure 5.3, with the respective histograms and cumulative frequencies (—). BC provides a nanofibrillar base structure suitable for subsequent chemical modification [194], with approximately 90 % of the fibres measuring below 40 nm in diameter (Figure 5.3a).

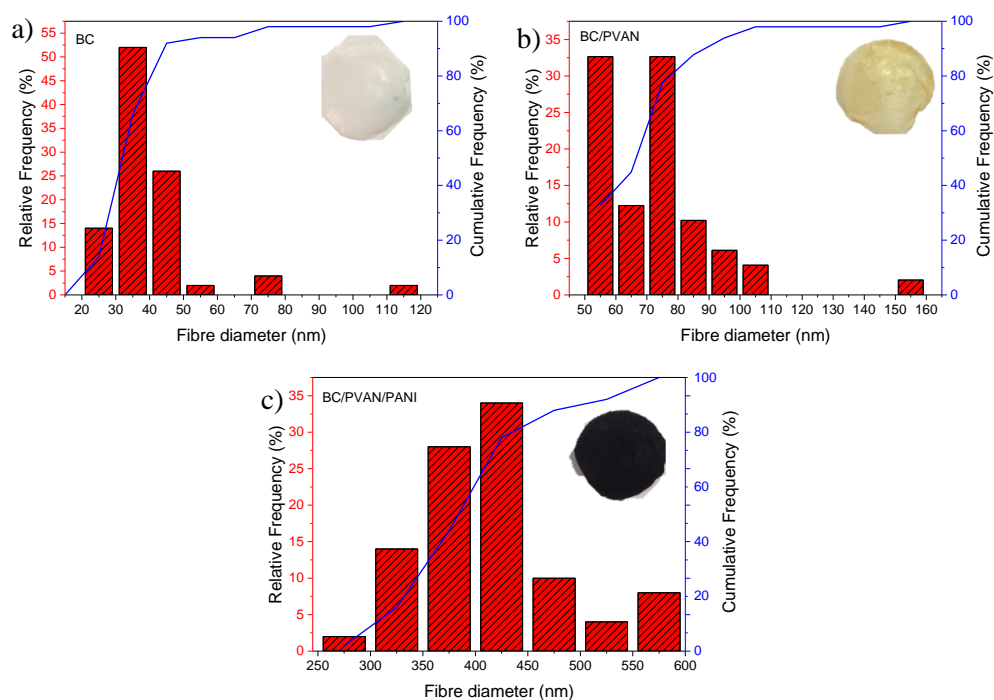


Figure 5.3. Histogram of the diameter (relative frequency) of the fibres of a) BC, b) BC/PVAN, and c) BC/PVAN/PANI membranes, showing the respective cumulative frequencies (solid line —).

After surface functionalisation with PVAN, the diameters of almost 90 % of the fibres increased up to 80 nm (Figure 5.3b). The heterogeneity of frequency of diameters measuring 50-60, 60-70 and 70-80 nm, might be related with fusion of some fibres. It has been found both pristine BC and BC/PVAN consist of smooth nanofibres, which entails a uniform PVAN coating successfully deposited, as shown in Figure 5.2b,c. After aniline polymerisation, however, an uneven surface is adopted, as just concluded, with diameters up to 600 nm and a nanorod-like arrangement spread all over the BC networks.

The microstructural analysis cross micro- to nanoscale of PVAN/PANI functionalised BC was further examined in detail with FIB/SEM (Figure 5.2g,h), which has yielded the high resolution TEM (HRTEM) images in the regions of PVAN/PANI coating and BC matrix (Figure 5.2i,j). As clearly shown, the porous BC substrate (Figure 5.2h,j) was covered with a uniform and homogenous PVAN/PANI coating of ca. 2 μm thick (Figure 5.2h,j). Further examination of microstructural characteristics of the PVAN/PANI bilayer (Figure 5.2i), confirms the formation of an intact coating well-adhered to BC substrate with no signs of visible defects. However, as expected the pores still remained in the substrate of BC network, with variable pore size of up to few hundred of nanometres, as seen in Figure 5.2j.[195]. This can potentially result in some remarkable properties, for instance, high mechanical strength, and biocompatibility, as well as high water holding capacity that can accommodate ionic solutions for improved conductivity [196]. The slightly higher density of interconnected pores compared to never-dried pristine BC is likely attributed to the deposition of PVAN/PANI inside of the oven-dried BC structure, thus densified the BC matrix.

The TEM X-ray elemental mapping at the interface between PVAN/PANI and BC substrate (Figure 5.4a) showed a N-enriched coating on the nanocomposite surface (Figure 5.4e). The general elevation of N concentration in the surface region implies the presence of the PVAN/PANI coating bilayer, that are nitrogen-containing compounds, as schematically shown in Figure 5.1c. It is however difficult to distinguish the PVAN/PANI interfaces because PANI is cross-linked with PVAN through -NH- bonds, resulting in a homogenous and gradual N change at the interface. Carbon (C) and oxygen (O) are also uniformly distributed across the section in the selected area. Br is also present which indicated the successful impregnation of the

initiator associated to PVAN synthesis. Residual amounts of Cl^- from HCl were detected mainly on the surface, which confirmed the existence of PANI in that region.

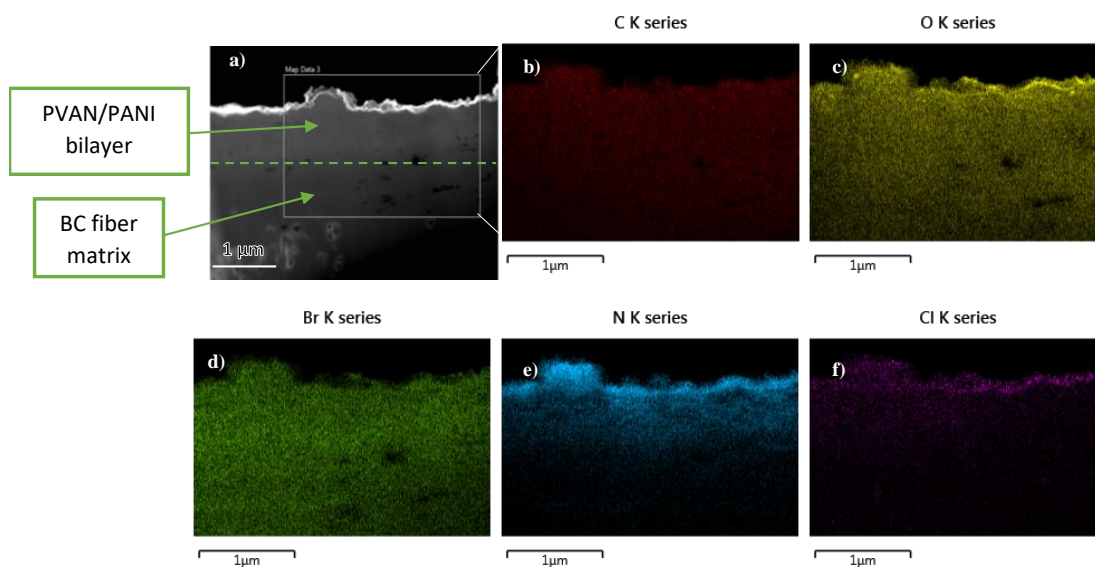


Figure 5.4. a) STEM image showing the microstructure of PVAN/PANI-grafted BC at a cross sectional view, as illustrated in Figure 5.2g-h. b-f) corresponding EDX maps of the selected area in a) (Reproduced by permission from Carbohydr Polym, Elsevier, [188] copyright 2019).

Different at. %N composition is present in the different regions of BC/PVAN/PANI membranes (Figure 5.5). Larger amounts were detected (6.6 ± 0.2 %) on the very surface (high Y-values) of the selected area (spectrum of Figure 5.5b) with decreased content (to 3.5 ± 0.2 %, Figure 5.5c, and to nil, Figure 5.5d) as we go deeper in the layer (low Y-values) to 3.5 ± 0.2 %. The spectrum of Figure 5.5d confirms that region corresponds to BC, as no N was measured. On the other hand, Br was mostly detected deeper in the membrane (lower Y-values) rather than on the surface (higher Y-values), which is coherent with the initial BC modification (BC-BiBB).

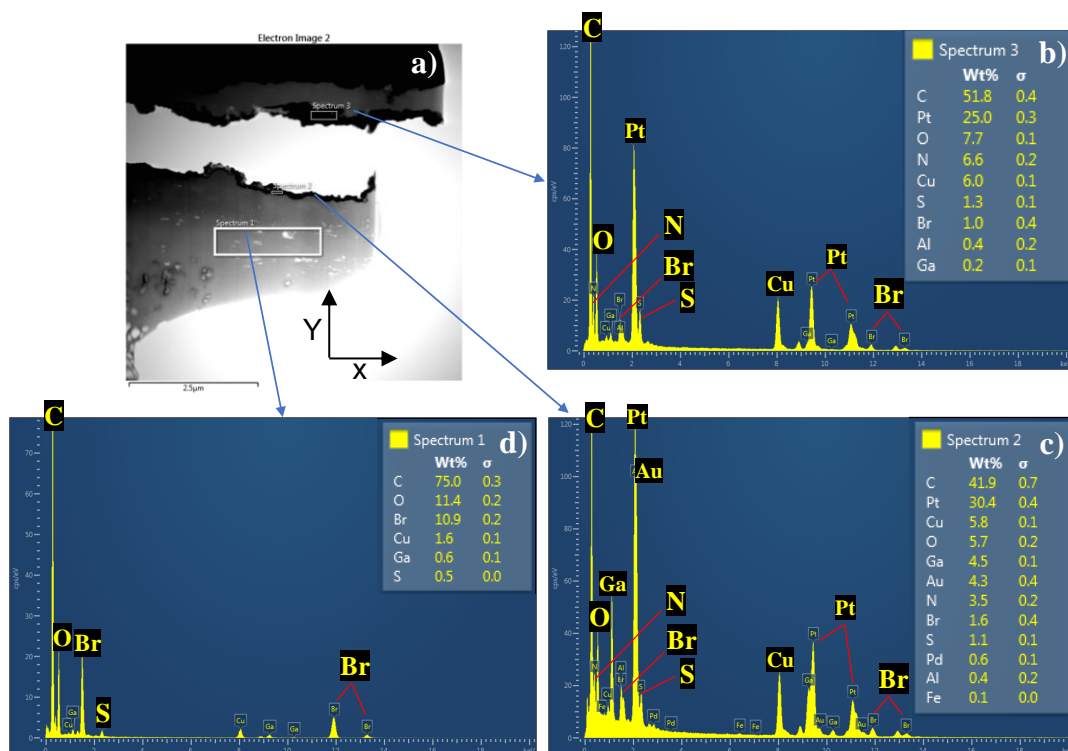


Figure 5.5. TEM-EDX map sum spectra of BC/PVAN/PANI in three different regions/levels of the membrane indicated in a), which correspond to the area shown in Figure 5.2h. b-c) surface coatings of PVAN/PANI as represented in Figure 5.2hi and d) BC substrate as represented in Figure 5.2hj.

5.1.2 Chemical Characterisation

Fourier Transform Infrared Spectroscopy

Figure 5.6 illustrates the ATR-FTIR spectra of BC, BC-BiBB, BC-g-PVAN and BC-g-PVAN-g-PANI membranes. In BC-BiBB spectrum, a new peak at 1721 cm^{-1} can be seen, which could be attributed to the O-C=O group of the initiator BiBB [197]. This was accompanied by a slight decrease in the relative intensity of the vibrations ascribed to the bending O-H at 1641 cm^{-1} observed in unmodified BC [198]. A progressive decrease in the relative intensity of the peaks at 3343 , 2893 and 1641 cm^{-1} was also witnessed after successive grafting with PVAN and PANI. The peak at 1518 cm^{-1} in BC/PVAN spectrum can be assigned to the C=C stretching mode characteristic of aromatic rings [199]. In BC/PVAN/PANI, C-N stretching vibrations of the quinoid (Q) and benzenoid (B) rings from PANI can be observed at 1557 (N=Q=N) and 1483 cm^{-1} (N-B-N) [200], while the CN stretching vibrations of the benzenoid ring were found at 1290 (C-N of secondary amine), 1249 (N-B-N) and 1133 cm^{-1} (N=Q=N).[79].

Polaron formation of the quinonoid structure ($Q=N^+H-B$ or $B-N^+H-B$) due to doping were identified at 1118 cm^{-1} [201]. Peaks at 1033 and 785 cm^{-1} were ascribed to aromatic C-H in plane and out-of-plane bending vibration of p-disubstituted benzene ring, respectively [79].

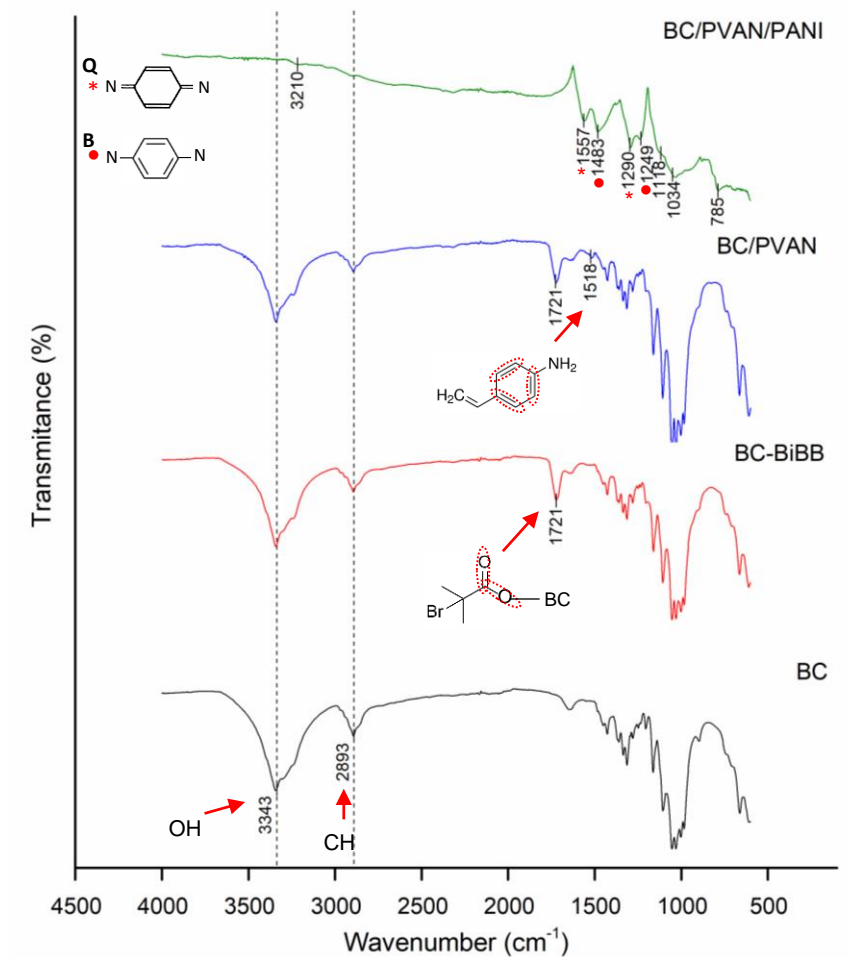


Figure 5.6. ATR-FTIR spectra of BC, BC-initiator (BC-BiBB), BC/PVAN and BC/PVAN/PANI.

X-Ray Diffraction

XRD, as shown in Figure 5.7, was performed to assess the changes in the crystalline structure of BC upon grafting with PVAN/PANI bilayer. Two main diffraction peaks at 14.5° and 22.7° were ascribed to the multiple crystal planes of unit cell structure I_α and I_β of the crystalline forms of BC (Chapter 4) [173], which revealed a progressive decrease as well as broadening with PVAN and PVAN/PANI bilayer coatings. This effect was particularly obvious in BC/PVAN/PANI membranes with

higher VAN content. The broadened spectrum observed is likely correlated to the amorphous structure of PANI that has largely hindered the crystalline structure of the backbone BC, confirming the presence of a thick PANI layer as observed in SEM images (Figure 5.7) [202]. In addition, the premise that higher GY_{PVAN} promoted a higher GY_{PANI} could be herein demonstrated. The slight shift in the main diffraction peaks can also endorse the enrichment in PVAN and PANI content of the functionalised BC nanocomposites [203].

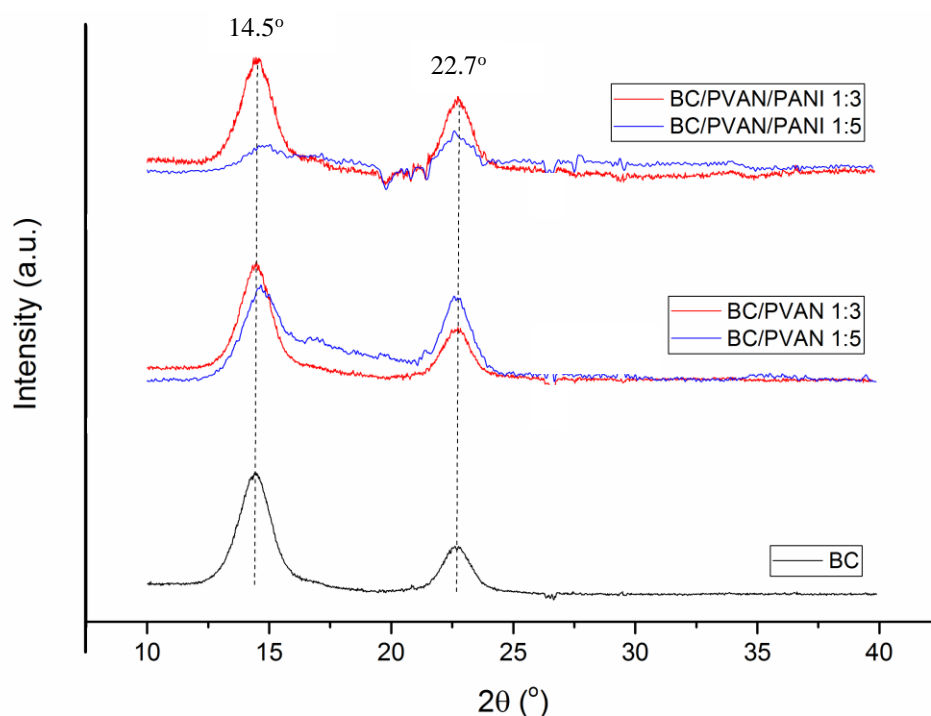


Figure 5.7. XRD spectra of pristine BC, and BC/PVAN and BC/PVAN/PANI grafted with molar BiBB:VAN ratios of 1:3 and 1:5.

X-Ray Photoelectron Spectroscopy

The chemical composition of pristine BC and the as-prepared BC composites was also investigated by XPS. Table 5.1 summarises the associated binding energies (BE) obtained for the different membranes. The wide scan of pristine BC shows BE of carbon 1s (C1s) and oxygen 1s (O1s) derived from BC backbone. The core-level spectrum of C1s in BC can be deconvoluted into BE at 285.0 eV (C-C/C-H), 286.6 eV (C-O) and 288.1 eV (O-C-O) typical from pristine BC (Figure 5.11a.2) [37]. SI-ATRP is strongly dependent on the efficient esterification of BC OH groups with BiBB [36].

The successful immobilisation of the initiator could be testified from the new peak emerged at 71 eV (Figure 5.11b.1) assigned to bromide 3d (Br3d) core shell level and from the new deconvoluted C1s peak (Figure 5.11b.2) attributed to the O-C=O bond (at 289.4 eV) proceeded from BC esterification [38]. C-Br bond may have also contributed to the intensity read at 285.0 eV [39].

Table 5.1. Binding energies (eV) of C1s, O1s, Br3d, N1s and Cl2p detected by XPS on BC, BC-BiBB, BC/PVAN and BC/PVAN/PANI (Reproduced by permission from Carbohydr Polym, Elsevier, [188] copyright 2019).

	C1s/eV	O1s/eV	Br3d/eV	N1s/eV	Cl2p/eV
BC	286.9	533.1	-	-	-
BC-BiBB	287.0	533.2	71.0	-	-
BC/PVAN	285.9	533.1	71.0	400.1	-
BC/PVAN/PANI	284.8	531.5	67.8	399.4	197.8

The degree of substitution (DS) of BC-BiBB as determined from equation 3.6 was 77 %, which means about 77 % of BC growing sites were readily available for PVAN grafting which shows a good agreement with the reported literature [204]. Moreover, it would be very unlikely that every hydroxyl group was equally accessible for modification as consequence, among others, of BC drying process prior to BiBB immobilisation.

The resultant spectra in Figure 5.8c,d confirmed PVAN and PANI successfully grafted onto BC membranes evidenced by the presence of BE corresponding to nitrogen 1s (N1s) and higher relative peak intensities of C1s, reflecting the enrichment in carbon content from the aromatic rings that composes both PVAN and PANI (Figure 5.1c). The N1s core-level of BC/PVAN could be curved-fitted into two individual peaks at 399.8 eV and 401.7 eV, ascribed to the neutral (-NH-) and positively charged (-NH₂⁺) amine group, respectively. Further functionalisation with PANI led to an expected increase in N1s content, that can be de-convoluted into four peaks representing four components with BE corresponding to the quinoid imine (=N-) at

398.0 eV, benzenoid amine (=N=) at 399.3 eV, and positively charged nitrogen atoms at 400.1 eV and 401.9 eV (=NH⁺= and -NH₂⁺, respectively).[205].

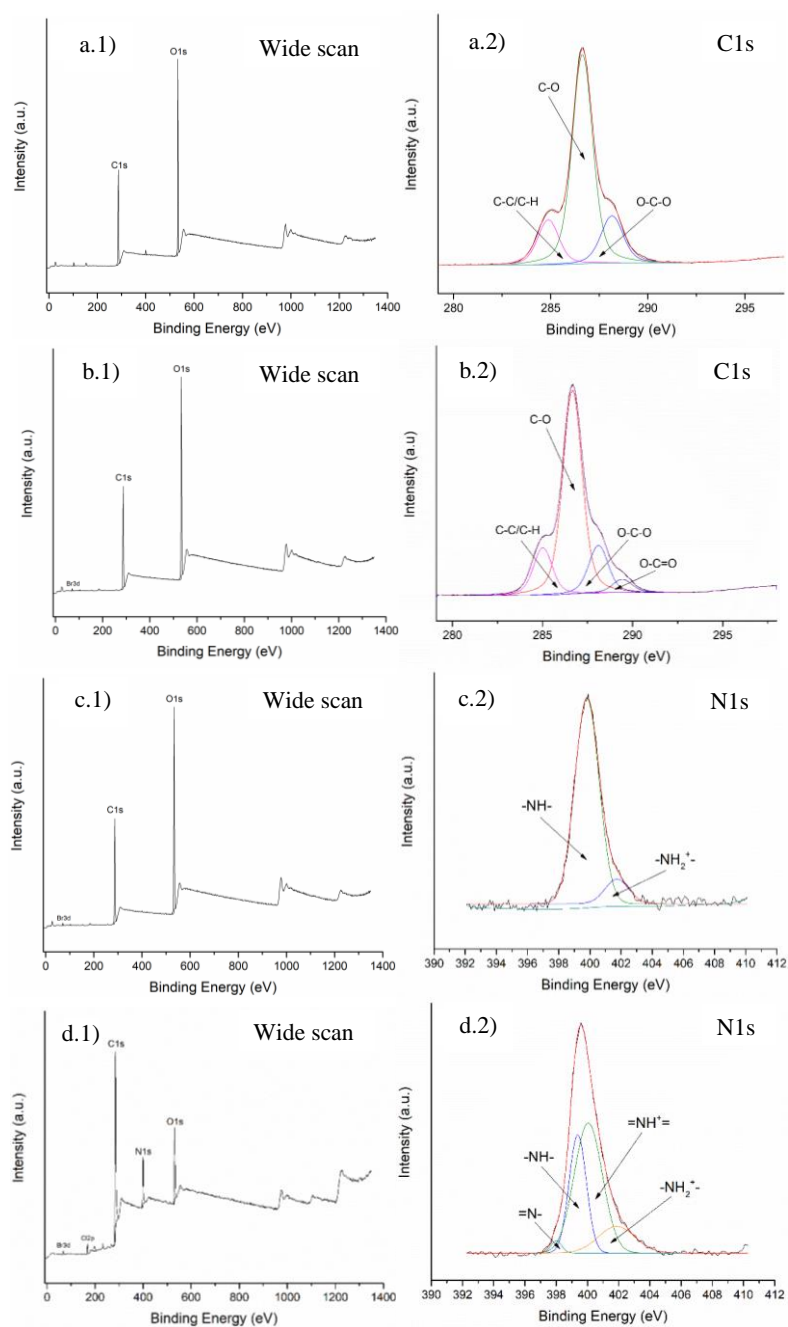


Figure 5.8. Typical wide scans of a.1) BC, b.1) BC-BiBB, c.1) BC/PVAN (BiBB:VAN=1:5) and d.1) BC/PVAN/PANI (BiBB:VAN=1:5). High resolution C1s scans of a.2) BC and b.2) BC-BiBB, and high resolution N1s scans of c.1) BC/PVAN (BiBB:VAN=1:5) and d.1) BC/PVAN/PANI (BiBB:VAN=1:5). Peaks were curve-fitted using Thermo Scientific™ Avantage Data System. (Reproduced by permission from Carbohydr Polym, Elsevier, [188] copyright 2019).

The doping level of PANI can be estimated from the fractional areas of protonated nitrogen atoms. The fractional areas of these four peaks were estimated to be 0.02, 0.30, 0.54 and 0.14, which indicates the doping level can reach as high as 68 % [206].

The relative amount of both PVAN and PANI on BC surface could be inferred from the N1s/C1s ratio (Table 5.2). As anticipated, higher N1s/C1s intensity was perceivable with higher VAN feeding ratio. After aniline polymerisation, N1s/C1s ratio doubled from 0.07 to 0.15 for BiBB:VAN=1:5 membranes. Interestingly, when lower VAN monomer contents were used, N1s/C1s ratio decreased, which implies that higher VAN amounts promote higher PANI yields.

Table 5.2. Elemental composition (atomic percentage, at%) of BC, BC-BiBB, BC/PVAN and BC/PVAN/PANI composites extracted from XPS analysis, corresponding N/C atomic ratios.

		%C1s	%O1s	%Br3d	%N1s	N1s/C1s
BC	-	58.3	38.0	-	-	-
BC-BiBB	-	59.8	39.3	0.4	-	-
BC/PVAN	BiBB:VAN=1:3	69.4	25.6	-	4.3	0.06
	BiBB:VAN=1:5	68.8	23.1	2.3	4.8	0.07
BC/PVAN/PANI	BiBB:VAN=1:3	79.5	15.4	-	3.6	0.04
	BiBB:VAN=1:5	73.7	12.0	0.5	11.1	0.15

Different relative amounts of N were obtained after adjusting ANI polymerisation parameters, indicating the yield is also influenced by reaction conditions (Table 5.4). N/C ratio seemed to have reached the maximum ratio of 0.157 when prolonging the reaction up to 18 hours, suggesting that there was still ANI monomer to be consumed. It was also found that for higher APS:ANI feeding ratios (N/C=0.138), N/C increased, which indicates a possible higher PANI grafting yield, as APS:ANI>1.25 ensures efficient oxidation of all ANI monomer. Other variations from the standard conditions like, monomer concentration, lower oxidant:monomer ratio, lower reaction time and acid concentrations, caused a decrease in the following order: T=18h > standard > APS:ANI=1.5 > Time=3h > APS:ANI=1 > [HCl]=0.5 M >

[ANI]=0.5 M > [ANI]=0.7 M. For instances, the lowest N/C was achieved for higher [ANI] may be due to the large amounts of ANI that could not be properly oxidised by APS. On the other hand, lower [HCl] was not sufficient to properly protonate ANI monomers and products and hence, lowering slightly the amount of PANI grafted.

Table 5.3. Elemental composition (atomic percentage, at%) of BC/PVAN/PANI 1:5 composites prepared using different aniline polymerisation conditions extracted from XPS analysis, with corresponding N/C ratios.

Atomic weight	%C1s	%N1s	N1s/C1s
[ANI]=0.5 M	73.1	8.1	0.111
[ANI]=0.7 M	73.6	8.2	0.111
[HCl]=0.5 M	77.8	8.8	0.113
18 hours	72.2	11.3	0.157
3 hours	79.0	9.9	0.125
APS:ANI=1	76.6	8.9	0.116
APS:ANI=1.5	75.5	10.4	0.138

5.1.3 Grafting Yield

The GY on the initialised BC surface membrane was determined through weight gain after functionalisation with PVAN and PANI (equation 3.7). The results, discriminated in

Table 5.4, corroborate the previous findings obtained from XPS with N/C ratios (Table 5.2). The molar BiBB:VAN ratio seemed to have affected the GY of both PVAN and PANI. After 24 hours of reaction, around 29% of PVAN was grafted on BC when BiBB:VAN=1:3 was used, whereas about 43% was grafted after increasing VAN feeding ratio. Furthermore, the GY of PANI also tended to improve with greater amounts of VAN from 46% to 53%. Comparable results have been reported for BC/PANI, which is in agreement with PANI synthesis kinetics [170, 207]. This confirms PVAN may act as catalyst for PANI growth. As previously mentioned, the chain propagation rate of PANI is also controlled by the surface area available for

synthesis (k_2' of equation 3.2). As such, with increased initiating sites for chain propagation, i.e. larger surface area, exponential PANI growth may occur within the same time scale and thus, leading to an increase of the GY.

Table 5.4. Grafting yield (%) of PVAN and PANI on BC/PANI and BC/PVAN/PANI membranes.

Grafting Yield			
BC/PVAN/PANI	GY_{PVAN}	BiBB:VAN=1:3	29 %
		BiBB:VAN=1:5	43 %
	GY_{PANI}	BiBB:VAN=1:3	46 %
		BiBB:VAN=1:5	53 %
BC/PANI	GY_{PANI}		39 %

5.1.4 Thermogravimetric Analysis

Thermogravimetric analysis (TGA) was performed from room temperature up to 800 °C on pure BC and the PVAN/PANI functionalised composite BC membranes to assess their thermal stability (Figure 5.9). As measured through weight loss, the thermal decomposition of these membranes after thermal loading follows a similar trend with the temperature increase, consisting of three main stages, as observed earlier for pristine BC in Chapter 4. In the first stage, the initial weight loss of BC and BC/PVAN membranes took place from room temperature to ~150 °C, but the degradation occurred from room temperature to 100 °C for BC/PVAN/PANI membranes. This is concerned with some moisture remaining inside the membranes, in the form of either water and/or dopant HCl as has been reported elsewhere [208]. In the second stage, a drastic weight reduction in the pure BC membranes was found between 250 and 375 °C, whereas in BC/PVAN and BC/PVAN/PANI membranes the temperature range for the abrupt weight loss has started earlier, i.e. 200-350 °C and 175-250 °C, respectively. This can be associated with the main chain decomposition of crystalline and amorphous regions of BC into D-glucopyranose monomer and further into free radicals, as seen in Chapter 4 [79]. On functionalised BC nanocomposites, this degradation stage could be further subdivided into two, as seen with the two peaks of the respective first derivative curves – mass-loss peaks –, which may indicate components of BC composites with different thermal stability [209]. This

might be due to the presence of smaller chain oligomers [210]. In the third and final degradation stage as can be identified from about 390, 350 and 250 °C in BC, BC/PVAN and BC/PVAN/PANI membranes respectively, the weight loss was insignificant and gradually reaching a relative steady level owing to the residual main chain decomposition [174].

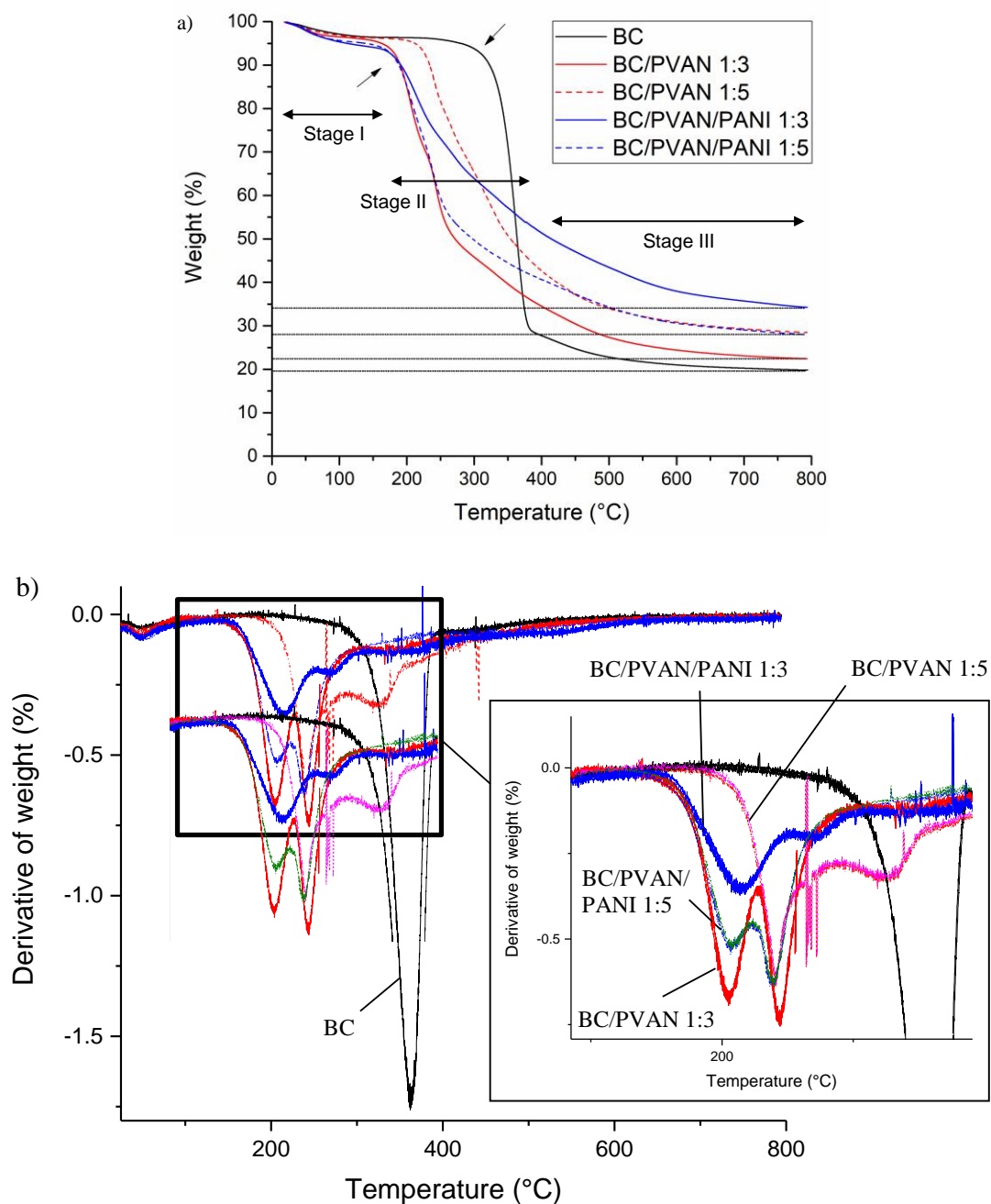


Figure 5.9. a) Thermogravimetric curves of BC, BC/PVAN and BC/PVAN/PANI nanocomposites with BiBB:VAN molar ratios of 1:3 and 1:5, measured from room temperature to 800 °C. Three main stages

of weight loss identified: Stages I, II and III. b) Corresponding first derivative curves and magnification of the selected squared area. Different colours were used to better distinction of the curves.

Table 5.5 lists the onset, offset and peak temperatures extracted from first derivative of TGA curves of BC and BC-based composites, shown in Figure 5.9, at the varied degradation stages. As seen, the onset temperature 1 of stage II (T_{onset1}) varied more from 323 °C in BC to 175-223 °C in BC/PVAN and 159-171 °C in BC/PVAN/PANI membranes, showing the highest degradation rate at 362 °C, 203-242 °C and 202-213 °C, respectively. The secondary weight loss within stage II of coated BC membranes, as observed in Figure 5.9, started in the temperature range of 202-234 °C (T_{onset2}). Despite the narrower degradation temperature interval after coating BC with PVAN and PANI, it seems higher PVAN loading amounts tend to increase the thermal stability of the composites. Noticeably, the remaining mass of both BC/PVAN and BC/PVAN/PANI composite membranes was approximately 30%, which is greater than that of 20% found in pure BC membranes.

Table 5.5. Onset, peak and offset temperatures extrapolated from the first derivative curves of TGA shown in Figure 5.9b.

	$T_{\text{onset1}}/^{\circ}\text{C}$	$T_{\text{peak1}}/^{\circ}\text{C}$	$T_{\text{offset1}}/^{\circ}\text{C}$	$T_{\text{onset2}}/^{\circ}\text{C}$	$T_{\text{peak2}}/^{\circ}\text{C}$	$T_{\text{offset2}}/^{\circ}\text{C}$
BC	323	362	390	-	-	-
BC/PVAN 1:3	175	203	245	220	247	270
BC/PVAN 1:5	223	242	251	202	324	377
BC/PVAN/PANI 1:3	159	213	289	234	267	328
BC/PVAN/PANI 1:5	171	202	296	213	241	267

In general, different BiBB:VAN molar ratio (Figure 5.9) and aniline polymerisation conditions (Figure 5.10) seemed not to have significant effects on the TGA profiles, although a more pronounced weight loss occurred at lower temperatures could be observed in the composites containing lower VAN:BiBB feeding ratios. In particular, BC/PVAN 1:3 membranes showed a residual weight of about 25 %, most probably due to a lower grafting degree that was redeemed after PANI coating. The residual weight of grafted membranes in the remaining cases, increased from 20 % in BC to about 35 %, which indicates that both PVAN and PANI conferred a protective

layer against BC substrate degradation. Different aniline polymerisation parameters did not considerably change the weight loss profile of BC/PVAN/PANI composites, although slightly slower degradation rate and higher residual weight could be noticed after 18 hours of reaction time (Figure 5.10c), attributed to higher PANI grafting yields.

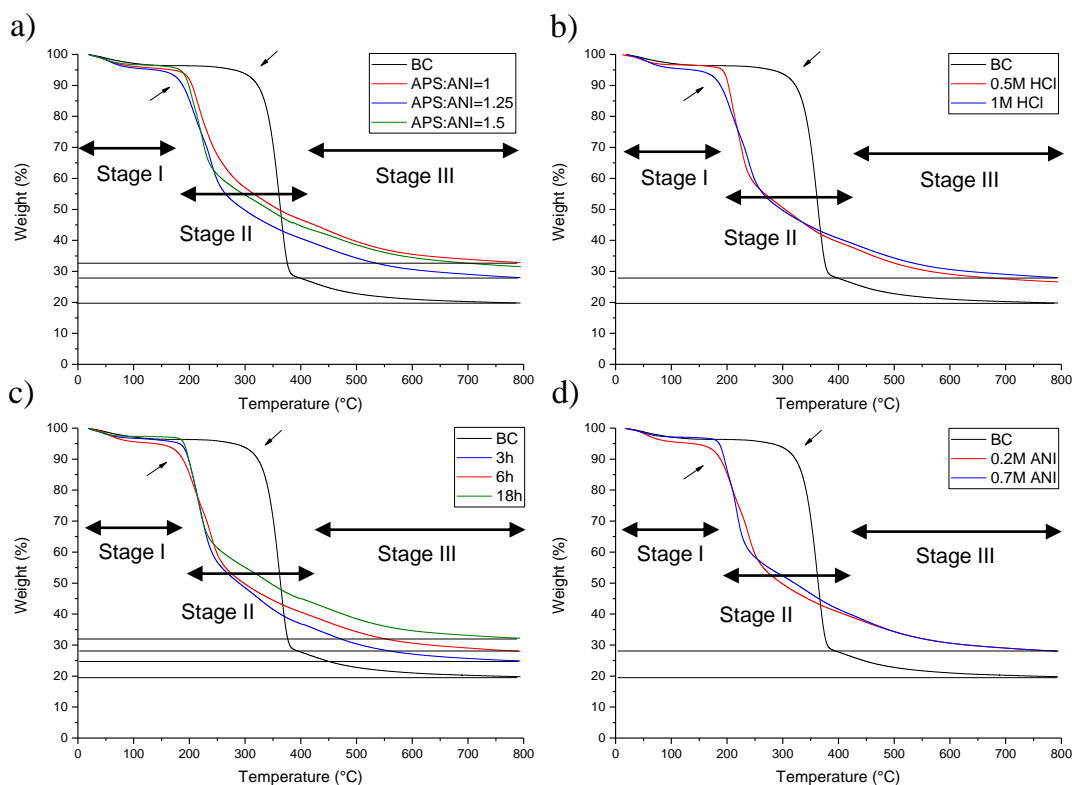


Figure 5.10. Thermogravimetric curves of BC/PVAN/PANI 1:5 for different aniline polymerisation parameters. a) aniline concentration, b) oxidant to aniline molar ratio, c) reaction time and d) acid concentration. Three main stages of weight loss identified: Stages I, II and III.

5.1. DISCUSSION

Flexible and functional BC/PVAN/PANI membranes were successfully synthesised following a novel three-step approach. BC was first grafted-from with PVAN via ARGET SI-ATRP, furnishing BC with a primary stabiliser coating layer rich in amine groups that acted as anchors for subsequent aniline polymerisation. This process allowed the predominant synthesis of 1D nanostructured PANI, the as-called supramolecular structures, known to provide superior electrical conductive and mechanical properties [88, 100]. PANI grows as a thick dark green layer corresponding

to the EM oxidation state that is overall accepted as the highest conductive form of PANI, and thus of interest for applications requiring electrically conductive properties.

The chemical characterisation confirmed the successful grafting of PVAN and PANI, with HRTEM further showing a good interfacial integrity between BC, PVAN and PANI layers, that is important to preserve the cohesion of the coatings and general materials stability, and thus, ensuring durability of the material's performance [211]. The inclusion of higher yields of grafted-PVAN, accomplished with lower BiBB:VAN feeding (molar) ratios, could be detected mainly by XPS and weight gain, which was responsible for an increased PANI grafting yield. Furthermore, PVAN/PANI bilayer does not considerably affect the outstanding thermal stability profile of pristine BC, as seen with TGA analysis, and further reckon this bilayer may provide a protective coating for preventing early thermal decomposition of BC substrate, that is critical for numerous applications, especially for bioelectronic devices [212]. The thermal degradation of BC composites occurred at slightly lower temperatures may be related with the decreased crystallinity when compared to unmodified BC. This is most likely because PVAN and PANI coatings are not as crystalline as BC, and thus they are not so thermally stable as BC is. However, higher PVAN grafting yield seemed to have led to an increase of the thermal stability of PANI-coated BC composites with a detectable higher residual weight when compared to pristine BC. In contrast, variations to aniline polymerisation did not influence visibly, probably because such variations did not cause significant changes to PANI yield that could cause deviations to the thermal stability profiles. This suggests also that the different PANI nanostructures do not play a pivotal role in the thermal stability of PANI-coated composites.

Understanding the functionalisation process of BC with this bilayer is thus crucial to enable a deeper comprehension of the chemical and molecular processes behind, especially as regards PANI synthesis, so that BC coating properties can be efficiently tailored to the targeted applications with an optimised synthetic process.

5.1.5 Understanding the PVAN/PANI Bilayer Functionalised BC System

Immobilisation of the Initiator

The functionalisation of BC membranes was initiated with the creation of suitable propagating sites on the OH-rich surface. This step is of special importance to

ensure PVAN germination and propagation, which is achieved through the immobilisation of an ‘initiator’ onto BC, commonly alkyl halides. Alkyl bromides, like BiBB, are versatile initiators in a variety of substrates, including BC, on which these are particularly effective. BiBB can covalently bound to cellulose backbone through ester linkages, while providing a fast initiating process which is decisive for PVAN chain propagation.[213]. Low initiator concentrations can compromise the control over the radical polymerisation, which may result in low density of polymer brushes grafted [214]. Thus, the amount used was overestimated to 100 % coverage of the three OH groups (Figure 5.1) of each repeating cellulosic unit, as this is a very unlike event. Nevertheless, the %DSS showed that sufficient BiBB was successfully immobilised onto BC backbone for ensuing ARGET ATRP.

Activators Regenerator by Electron Transfer Atom Transfer Radical Polymerisation of 4-VAN

BC/PVAN was synthesised via ARGET SI-ATRP, performed with $\text{CuCl}_2/\text{PMDETA}$ as the catalytic system that was continuously regenerated between its two oxidation states (Cu(I) and Cu(II)), using ASCA as the regenerator agent. VAN monomer carries a vinyl functional group that is able to stabilise the propagating radicals originated from the catalytic system. PVAN grows by successive monomer addition via C-C single bonds.[215]. Molar ratios of catalyst to monomer, ligand and regenerator, were kept constant and their quantities adjusted with different BiBB:VAN molar ratios to allow different grafting degrees. Molar ratios below 1 implies an increase in the number of anchoring sites (aniline moieties of VAN, see Figure 5.1c) for PANI germination, which might have caused an enlargement of the surface area available for COP reaction.[100].

The chemical characterisation performed confirmed the successful grafting of PVAN. The molar ratios of BiBB:VAN herein used, 1:3 and 1:5, were expected to append ideally 3 and 5 times more initiating sites respectively, in contrast to the nongrafted BC. Although the theoretically GY can be hardly achieved, higher amounts of VAN monomer undeniably resulted in higher GY_{PVAN} , as expected. With prolonged reaction times, raised temperature [216] and previous washes of BC membranes with NaOH, it is anticipated an improvement in the GY_{PVAN} [217].

Chemical Oxidative Polymerisation of ANI

COP of aniline was performed on BC/PVAN nanocomposites using different polymerisation parameters that are known to influence directly or indirectly the kinetics of aniline polymerisation. Besides the ‘aniline pending moiety’ of PVAN not actively participating in aniline polymerisation, it may serve as a germinator and stabiliser of the reaction. Standard conditions (0.2 M aniline, 0.25 M APS and 1 M HCl for 6 hours of reaction time) were established based on stoichiometric amounts of the reaction (Figure 3.7, Chapter 3) that would theoretically maximise the GY_{PANI} assuming a complete reaction.[100]. Larger GY_{PVAN} was also shown to increase GY_{PANI} , that might have resulted from a faster COP rate provided by the aforementioned increased surface area when compared to the common *in situ* COP performed strictly on BC sites [88].

Different PANI supramolecular structures were formed on BC/PVAN according to PVAN content used, which confirmed PVAN had an important role in PANI self-organisation. Favourable aggregation and film irregularity were reached for lower PVAN grafting yields, where only PANI clusters sprouted on BC/PVAN surface. However, higher GY_{PVAN} guided PANI to a more uniform distribution on the BC fibres’ surface, with clusters being progressively replaced by PANI nanorods. This anticipates that PVAN acted as a soft-template for the growth of more well-defined and organised structures in nanorods-like shape and with all individual objects of similar dimensions, i.e. every single nanorod that cover BC/PVAN nanofibres have identical sizes. Such PANI nanostructures are very attractive to boost the electrical, mechanical and thermal stability properties for numerous applications.[218].

5.2 CONCLUSION

Functionalised BC nanocomposite membranes with PVAN/PANI were successfully synthesised through consecutive ARGET SI-ATRP and COP reactions. The grafted PVAN/PANI bilayer on BC was confirmed with their chemical compositions by FTIR, XRD and XPS analysis. When an intermediate functional PVAN layer was inserted between PANI and BC, a higher PANI integrating yield was acquired together with a homogeneous distribution of its structural units as observed in SEM and TEM images in the form of nanorods-like shape. Denser PVAN brushes

promoted further this effect, which opens a window for future studies on PVAN usage for BC functionalisation. BC nanocomposites are proven to be thermally stable up to approximately 200 °C. Despite no significant changes have been revealed in the nanocomposite's properties using different aniline polymerisation parameters, higher PVAN grafting yield tended to improve the thermal stability of the BC nanocomposites. Furthermore, these polymerisation conditions are anticipated to have a major role in the final electrical and electrochemical properties of the as-developed BC nanocomposites that are closely related with the supramolecular PANI structures produced during the chemical reaction (Chapter 6).

Chapter 6: Electrical Properties of BC/PVAN/PANI Nanocomposites

The content of this chapter is partially included in the published scientific article entitled “Rebelo A, Liu Y, Liu C, Schäfer K-H, Saumer M, Yang G. Poly(4-vinylaniline)/polyaniline bilayer functionalized bacterial cellulose membranes as bioelectronics interfaces. *Carbohydr Polym.* Elsevier; 2019 Jan 15; 204:190–201”.

PANI endows BC/PVAN/PANI nanocomposites with electrical and electrochemical characteristics that can be exploited for different applications, including bioelectronic devices which demands both electrical conductivity and biocompatibility. Synthetic parameters are strongly associated to the final electrically conductive properties of PANI [100]. It is well-established that its conductive form is dependent on the oxidation state and protonation degree (doping level) that can be easily obtained under low pH conditions along with uses of strong oxidants [219]. The present chapter will be devoted to the systematic study of the conductivity and electrochemistry of the as-developed BC/PVAN/PANI nanocomposites (Chapter 5), showing the effects of the reaction conditions for attainable optimisation. In particular, it is demonstrated the role of the PVAN intermediate layer. As such, the conductive features will be carefully examined and discussed with a 4-point probe method, CV and EIS, as schematically represented in Figure 6.1.

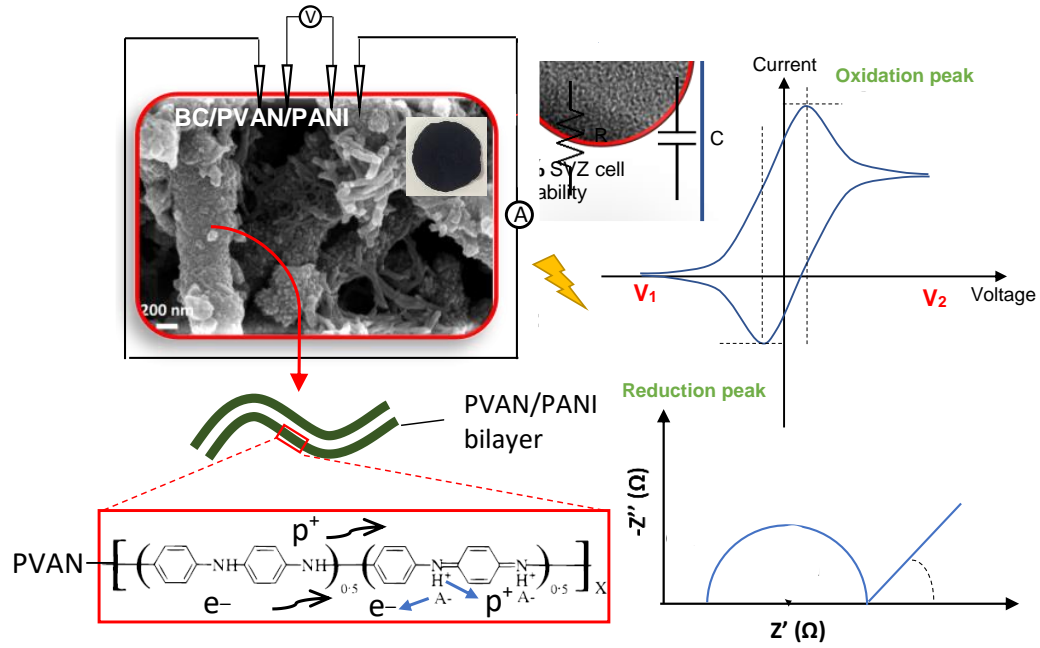


Figure 6.1. Schematic representation of the electrical and electrochemical conduction in PVAN/PANI coated BC nanofibrous membranes.

6.1 RESULTS

6.1.1 Electrical Conductivity

As an estimation of the intrinsic electrical properties of the nanocomposites, the conductivity was calculated from sheet resistance measured from a common 4-point probe set-up, considering the probes spacing and the composite's thickness, which is accordingly represented in Figure 6.2 and 6.3. The conductivity of PANI-based membranes showed a trend to increase with nanofibers density (dense side), PVAN grafting yield, as well as with some COP parameters, achieving values as high as $\sigma = (4.5 \pm 2.8) \times 10^{-2} \text{ S.cm}^{-1}$.

The kinetic of PANI synthesis determines the overall conducting properties, which depend on several parameters according to equation 3.2 ($k_1[\text{ANI}][\text{OX}] + k_2'[\text{ANI}][\text{P}]$) in which k_1 accounts for the induction period, while k_2 reflects the contribution of both acid concentration and surface area. It is worthwhile to mention that an increased polymerisation rate, and hence PANI yield, does not always lead to the formation of highly conductive structures, although it may indirectly have

contribution under certain conditions, providing that suitable electronic band structures are created [88].

Effect of BC Porosity and Grafting Yield of PVAN

The intrinsic PANI conductivity can be attributed to the long-range of delocalized charge carriers system arising from the oxidation of nitrogen atoms that serve as oxidation centres [220]. Variations of parameters in the polymerisation had a definitive effect on the PANI size and shape, which induced some changes in this delocalized system [100]. In spite of the widely recognised electrically insulating properties, BC not merely provides a substrate for allocating PVAN/PANI bilayer as a cohesive and uniform coating, but also acts as a catalyst of aniline polymerisation once it increases its growth rate. In addition, it furnishes an appropriate 3D porous system as a path for efficient charge carrier flow. In Figure 6.2, PVAN treated membranes showed a comprehensive higher value of conductivity up to one order of magnitude than those non-treated BC/PANI. The measurements from all samples revealed a trend of a comparable difference in the conductivity on both sides of the membrane that is correlated with the asymmetry seen in BC network, as seen in Chapter 4, that is related with BC synthesis procedure. Assuming a uniform PANI coating was formed, the side of BC membranes with a compact packing of BC fibres would reflect in a larger area covered by PANI as a continuous film and thus, resulting in a higher conductivity in comparison with the side with a more porous structure of BC fibres (Figure 6.2). Different surface areas with simultaneous changes on COP parameters are expected to reflect additional modifications in PANI properties, as such this leads to a multiplicity of PANI synthetic rates [100]. Similar to BC, PVAN is not inherently conductive as PANI [87]. However, the incorporation of PVAN and subsequent increase of its content led to an augmented conductivity up to one order of magnitude. For instances, on the compact side of the membrane it increased from $(3.7 \pm 0.5) \times 10^{-3}$ (BC/PANI) to $(5.2 \pm 0.9) \times 10^{-3}$ (BiBB:VAN = 1:3) and then to $(2.2 \pm 0.6) \times 10^{-2}$ S cm⁻¹ (BiBB:VAN = 1:5), respectively. This increased conductivity might have been resulted from the formation of more organised PANI structures that, among others, elongated the polyconjugated system by enhancing the charge carrier mobility as that of the doping agent (HCl) [86].

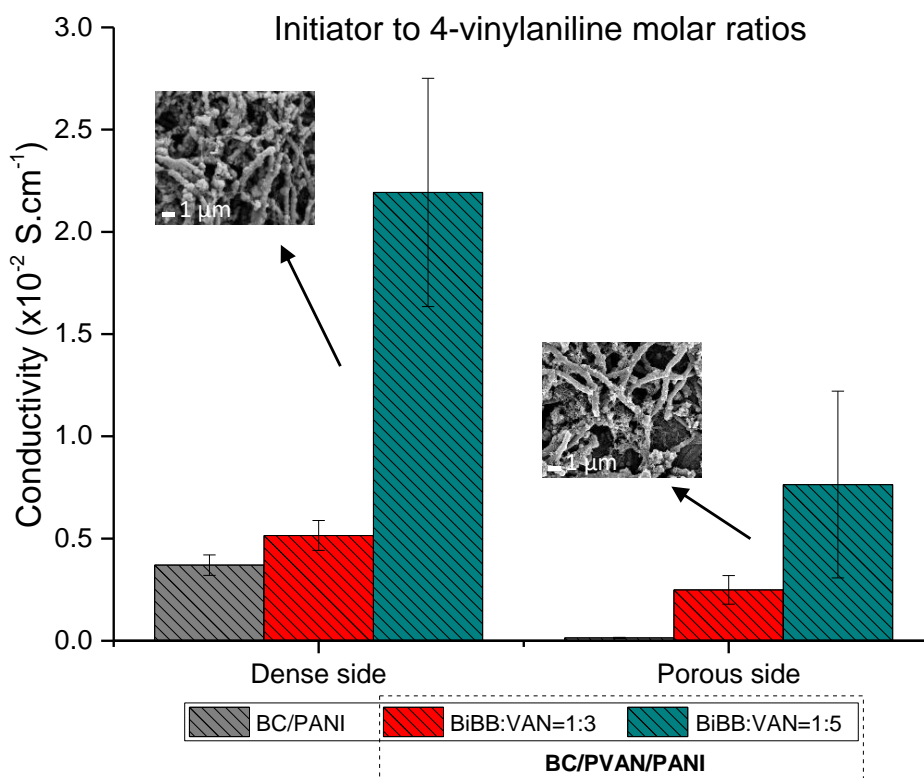


Figure 6.2. Electrical conductivity of BC/PANI, and BC/PVAN/PANI membranes with different BC to VAN molar ratios, the embedded images show the morphology of the selected area. (Reproduced by permission from Carbohydr Polym, Elsevier, [188] copyright 2019).

Effect of Aniline Polymerisation Parameters

The effect of COP parameters on the electrical conductivity of the PVAN/PANI functionalised BC composites is summarised and presented in Figure 6.3. Studies reported in the literature up to now on PANI synthesis have suggested that the strong acidic media (pH below 2.5) promotes highly conductive PANI structures, i.e. in the emeraldine oxidation form [149]. Herein, higher conductivity was also observed with the samples prepared in the solutions containing 1 M HCl in comparison with those prepared in 0.5 M HCl (Figure 6.3a). This was likely to be related to a higher degree of protonation products of aniline oxidation and may also be correlated with an increase of the crystallite size together with a decrease in d-spacing and interchain separation of PANI [100]. Slightly higher conductivity at 0.5 M on the porous side can be observed, probably related with a balanced effect of the surface area. The conductivity under both conditions fell, however, into the same range due to the slightly increase of pH value of the media from 0 to 0.3 when decreasing the

concentration of acid from 1 M to 0.5 M. The variation of molar ratio of APS (oxidant) to aniline (monomer) also influenced the final conductivity of the synthesised membranes. APS is characterised as a strong oxidising agent, which is able to oxidise both aniline monomer and the growing chain during polymerisation. According to aniline oxidation reaction with APS (see Figure 3.5, Chapter 3) $[APS]:[ANI]=1.25$ is the stoichiometric ratio that reflects the minimum oxidant amount to be used for complete monomer oxidation, which is expected to yield more conductive structures. However, the highest conductivity was obtained when using the lowest molar APS:ANI feeding ratio (APS:ANI=1) (Figure 6.3b), this is likely associated with the over-oxidation of aniline that enabled the formation of fully oxidised pernigraniline with low conductivity, instead of the partially oxidised emeraldine with high conductivity [221]. This effect has been reported in the literature for oxidant to monomer ratios over 1.15, which is comparable with the results herein obtained [222]. Extending the polymerisation time, e.g. from 3 hours to 6 hours, the conductivity of the PVAN/PANI functionalised BC membranes increased from $(1.0\pm 0.6)\times 10^{-2}$ S.cm⁻¹ up to $(2.2\pm 0.6)\times 10^{-2}$ S.cm⁻¹ accordingly (Figure 6.3c). However, further prolonged polymerisation time hardly showed any significant improvements in their conductivity because higher PANI molecular weight induced the formation of certain defects that caused modification of the delocalised system which ultimately reduced the conductivity [223]. In contrast, on the porous side there is an apparent trend to increase, ascribed to a slower PANI loading process with appropriate band structure that may be able to increase for longer reaction times.

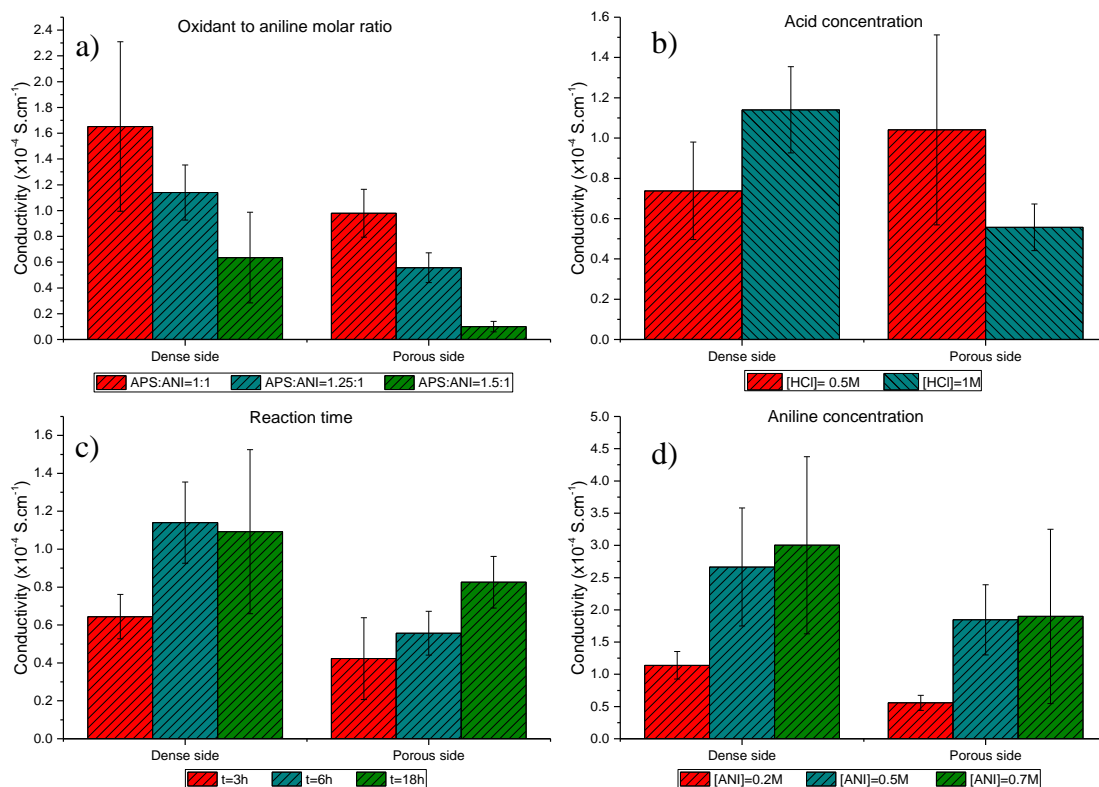


Figure 6.3. Differences on the electrical conductivity of BC/PVAN/PANI composites with variation of aniline polymerisation parameters: a) molar ratio APS:ANI, b) acid concentration, c) reaction time and d) aniline concentration (Reproduced by permission from Carbohydr Polym, Elsevier, [188] copyright 2019).

Greater conductive values were also found to be associated with larger monomer concentration (Figure 6.3d). From $[ANI]=0.2\text{ M}$ to 0.7 M , the conductivity of the BC composites increased significantly, at which the highest value of $(4.5\pm 2.8)\times 10^{-2}\text{ S.cm}^{-1}$ was achieved. Increasing monomer concentration led to an increased yield, and thus ultimately increased BC/PVAN nucleation sites for continuous PANI growth of proper band structure [224].

6.1.2 Electrochemical Properties

Cyclic Voltammetry

CV (Figure 6.4) was performed on composite membranes to understand the redox processes undergone during potentiodynamic cycling in acidic media. Structural

changes due to the oxidation were detected via current peaks upon doping or dedoping of protons and anions [225]. Pure BC and BC/PVAN are inherently insulators, thus, their respective cyclic voltammograms appear to be linear (grey line in Figure 6.4) when plotted with the PANI treated BC [226]. However, the enlarged view of the selected area reveals a trend for a capacitive-like response of BC and BC/PVAN [227]. Upon incorporation of PANI coating, BC/PVAN membranes acquire redox activity as shown in Figure 6.4. PANI is usually oxidised in two step-reaction according to its three different oxidation states: leucoemeraldine (LE), emeraldine (EM) and pernigraniline (PG) [228]. A single pair of redox peaks is observed at two selected scan rates, as indicated with arrows in Figure 6.4. The oxidation potential at 100 m.Vs^{-1} scan rate appeared approximately at +0.74 V and -0.70 V in the forward and reversible scans, respectively, corresponding to the conversion of LE into EM form [73]. During this process, benzoid and quinoid rings (EM) give place mostly to quinoid structures (PG). At lower scan rate (50 m.Vs^{-1}), the redox peak couple slightly shifted in the potential axis to 0.57 V and -0.56 V, in the positive and reverse scans, respectively. This is likely due to the lower flux of charge-carriers towards the electrode at slow scan rates (that is proportional to current) [229]. Other redox peaks associated with the fully oxidised and reduced form of PANI (PG and LE, respectively) were not herein detected, probably related to the type of acid used, the scan rate that was not sufficiently low to enable complete oxidation/reduction of PANI intermediates or because those transitions were not thermodynamically stable under these conditions [230]. Nevertheless, the oxidation of EM into PG occurred between +0.7 V and +1.5 V with the further reduction of EM into LE between -1.5 V and -0.7 V [229], that is associated to the release of radical cations compensated by imine ions from the electrolyte and to the formation of quinoid moieties, respectively [73].

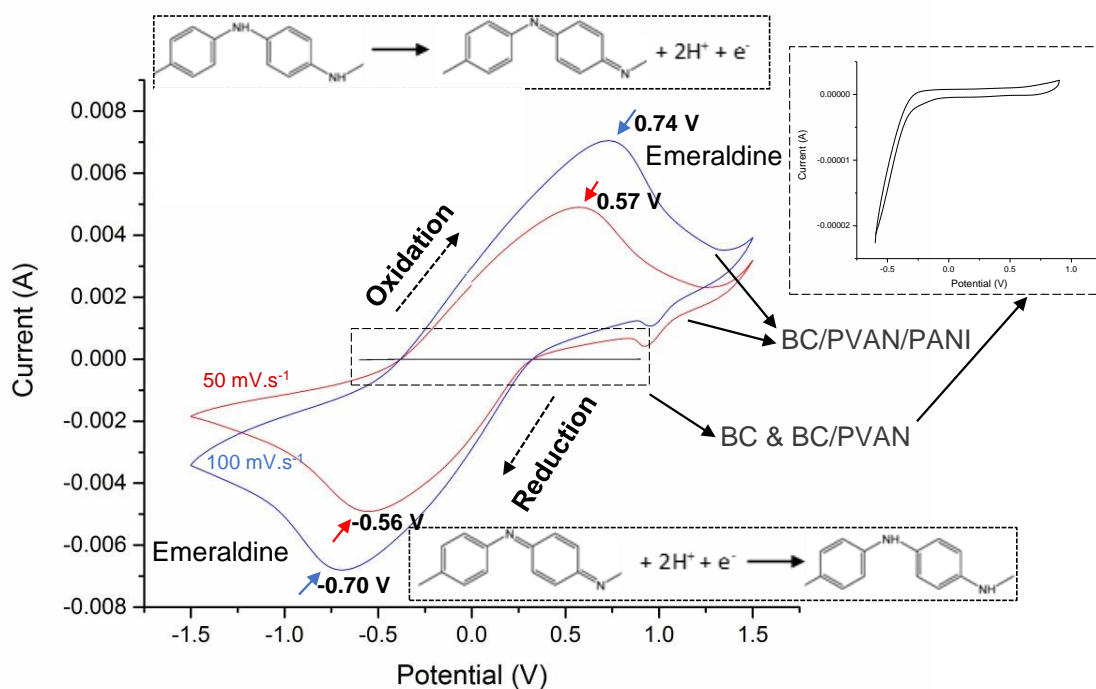


Figure 6.4. Cyclic voltammogram curves of BC, BC/PVAN and BC/PVAN/PANI recorded at 50 and 100 $\text{mV}\cdot\text{s}^{-1}$ of scan rates, with the respective magnification of BC and BC/PVAN curves, showing the oxidation and reduction processes of PANI. Red and blue arrows point out to the peak currents corresponding to emeraldine (EM) measured at 50 and 100 $\text{mV}\cdot\text{s}^{-1}$, respectively.

Electrochemical Impedance Spectroscopy

The electrochemical impedance response of BC/PVAN/PANI was analysed at different applied voltages that fall into the oxidation/reduction potentials of those corresponding to the oxidation states of PANI described in CV analysis of the previous section. Figure 6.5 shows representative EIS data recorded for BC/PVAN/PANI nanocomposites at different voltage bias which were subsequently curve-fitted into two semi-circles using an equivalent circuit shown in Figure 6.5a. The corresponding fitted values of the parameters are accordingly listed in Table 6.1. The solution resistance (R_s) marks the beginning of the first semicircle at higher frequencies that comprises a parallel combination of a charge transfer resistance (R_{ct}) with the respective double layer capacitance described as constant phase element (CPE_1) [231]. R_s accounts for the uncompensated resistance of the electrolyte H_2SO_4 [232] and the resistance between the contact electrodes to some extent [73]. R_{ct} can be ascribed to the electrode/electrolyte resistance concerning the charge transfer between the electrode and the electrolyte and ionic diffusion, whereas CPE_1 can be assigned to a

faradic capacitance (or pseudocapacitance) due to accumulation of charges from PANI redox processes [233]. At lower frequencies, the data could be extrapolated into a second semicircle formed by a polarisation resistance (R_p) in parallel with a static double layer capacitance (CPE_2) attributed to the separation and accumulation of charges at the respective electrodes [234]. The partial absence of the low frequency semicircle has been pointed out as resulting from high ionic conductivity at the electrode/electrolyte interface [235]. CPE accounts for the non-ideal capacitor behaviour (depressed semicircle) of the nanocomposites and the deviation of the diffusion line from the 45° slope (Warburg element) at low frequencies [236].

Table 6.1. Data extracted and calculated from the Nyquist plots shown in Figure 6.5.

V_{bias} (V)	R_s (Ω)	R_{ct} (Ω)	CPE_1 (F)	R_p (Ω)	CPE_2 (F)
0	51.3 \pm 5.3	21.2 \pm 5.1	(26.7 \pm 5.8) $\times 10^{-6}$	(1.1 \pm 0.05) $\times 10^{12}$	(1.5 \pm 0.2) $\times 10^{-6}$
0.5	51.3 \pm 2.8	20.7 \pm 1.48	(39.0 \pm 7.3) $\times 10^{-6}$	(1.1 \pm 0.03) $\times 10^{12}$	(6.4 \pm 0.1) $\times 10^{-7}$
1	53.3 \pm 6.7	291 \pm 40	(43.3 \pm 8.2) $\times 10^{-6}$	(1.1 \pm 0.02) $\times 10^{12}$	(1.5 \pm 3.4) $\times 10^{-6}$
1.5	55.7 \pm 12	500 \pm 101	(18.0 \pm 2.4) $\times 10^{-6}$	(1.1 \pm 0.05) $\times 10^{12}$	(1.6 \pm 0.8) $\times 10^{-6}$
-0.5	47.3 \pm 3.2	35 \pm 7	(24.1 \pm 4.7) $\times 10^{-6}$	(1.1 \pm 0.04) $\times 10^{12}$	(2.1 \pm 0.4) $\times 10^{-7}$
-1	49 \pm 4.1	532 \pm 67	(26.2 \pm 4.2) $\times 10^{-6}$	(1.1 \pm 0.06) $\times 10^{12}$	(9.6 \pm 0.8) $\times 10^{-7}$
-1.5	49.8 \pm 4.9	2350 \pm 89	(19.5 \pm 3.9) $\times 10^{-6}$	(1.1 \pm 0.03) $\times 10^{12}$	(1.3 \pm 0.2) $\times 10^{-7}$

R_s , arising mainly from electrolyte resistance, is largely independent on the applied DC bias (V_{DC}) as it can be expected. The parameters herein used to describe

the semicircle at low frequencies (R_p , CPE_2) also showed not to be significantly affected by the potential, indicating that the diffusion limited electron transport and the charge accumulation was purely of a double layer charging on BC/PVAN/PANI surface [237], suggesting also the low frequency electrochemical semicircle may be related with the electrical behaviour of hydrated BC, as discussed in Chapter 4. In such instances, proton conductivity may be the most contributor source for the higher resistance and lower capacitance observed, regardless the applied voltage owing to the reduced proton mobility within the network.

However, notorious variations on R_{ct} can be observed, which reflects the redox properties of the composite. According to the cyclic voltammogram (Figure 6.4), +0.7 V sets the potential at which LE is transformed into EM, which is the highest conductive form of PANI. At +0.5 V, EM oxidation state is nearly entirely reached and thus, R_{ct} is lower than at +0.7 V. From +0.5 to +1.5 V, R_{ct} continuously increased up to 500 Ω owing to the conversion of EM into PG. This confirms that PG oxidation potential should take place above +0.7 V as stated before in the CV analysis. When –0.5 V potential is applied, PANI is converted back to EM salt form as R_{ct} goes down again. However, decreasing the potential down to –1.5 V, the resistance increased to 2350 Ω , which corresponds to the conversion of EM to the fully reduced and also the least conductive form (LE). Contrarily, the capacitance CPE_1 increased up to 43.3 μF at +1 V and reached the lowest value of 18 μF at +1.5 V related with the accumulation of charges from the charge-transfer in faradaic processes. These results corroborate those obtained from CV and also show that EM is the most conductive form of PANI with higher capacitive properties. Accordingly, it can be stated that the optimised PVAN/PANI is responsible for the electrical switching responses at different potentials, whereas BC grants a protonic conduction path on its hydrated surface (Chapter 4) through the nanofibrillar network that embodies the PVAN/PANI bilayer. Deviations measured in R_{ct} and CPE_1 for symmetrical potential couple (e.g. –0.5 V *versus* +0.5 V) might be related with the heterogeneities of the membranes and with the slight displacement of the oxidation/reduction peak pair potential of PANI into its half-oxidised form (EM salt).

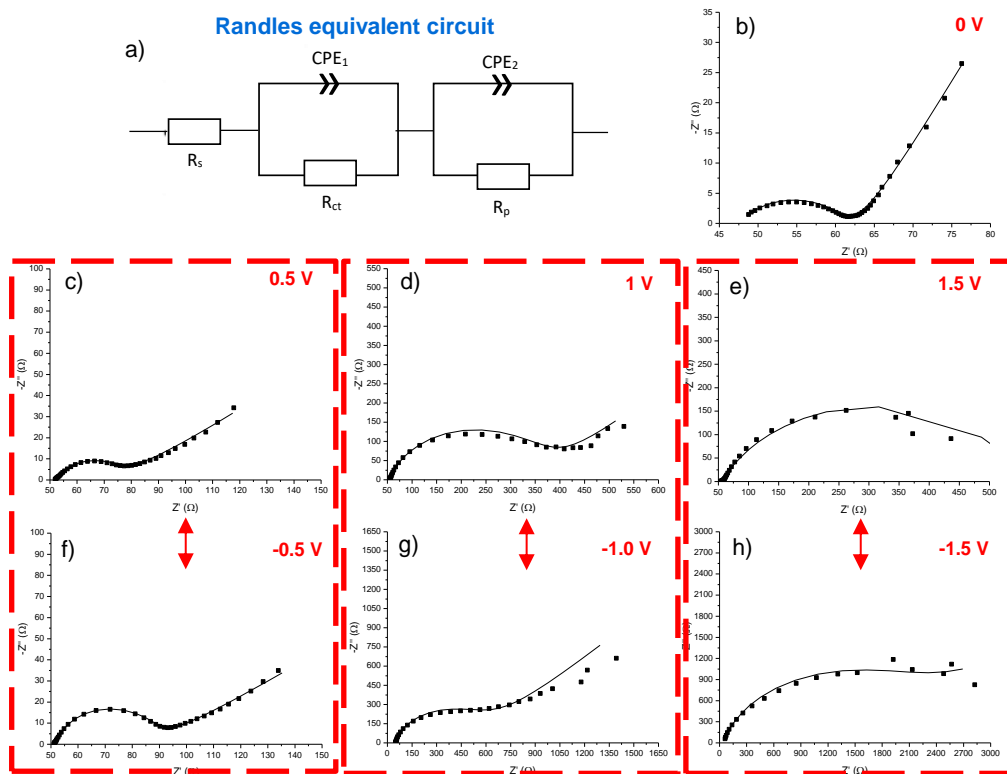


Figure 6.5. a) Randles equivalent circuit used to fit the impedance spectra shown in b-h. b-h) Nyquist plots of representative impedance data of BC/PVAN/PANI nanocomposites collected from different applied DC potentials upon superimposition of a sinusoidal AC potential of 10 mV. The solid lines (—) represent the fitting by the circuit in a).

6.2 DISCUSSION

PANI is the main responsible for the electrical variations of BC/PVAN/PANI nanocomposites and is an ideal candidate for countless applications demanding outstanding electrical conductivity, particularly owing to the ease and ‘smart’ switch of its electrical properties [238]. PANI chains possess both electronic and protonic conductivity that are raised from the charge carriers formed in the course of aniline oxidation during synthesis. PANI can be found in six different oxidation states in which EM salt is the most capable of electrical conduction, showing also the greatest stability.[100]. The grafted PVAN/PANI bilayer imparted the peculiar electrical and electrochemical behaviour of BC/PVAN/PANI nanocomposites shown, with BC conferring good support for selective ions transport. The electrical conductive properties of the as-synthesised PANI film on BC/PVAN/PANI membranes were

determined by regular polymer chains grown, driven by numerous reaction parameters that could modify the polyconjugated system, doping agent accessibility, as well as the protonation degree [86].

6.2.1 Factors Affecting the Electrical Conductivity of BC/PVAN/PANI

Favourable environment for successful synthesis of electrically conductive PANI (EM) is often obtained under extremely acidic medium with strong oxidising agents, that is able to stabilise polaron formation during oxidation [239] and easily oxidise all PANI intermediates over the synthesis process [100], respectively. Straightforward optimisation of the electrical properties of BC/PVAN/PANI nanocomposites can be achieved provided that suitable adjustments are made to the reaction conditions [240]. It is well-established that monomer and acid concentrations, polymerisation time, monomer:oxidant ratio, as well as the surface area available for the reaction, are key important factors that can greatly affect and guide the self-organisation of this complex polyconjugated system [241]. In this study, optimal parameters for maximised electrical conductivity were achieved with higher VAN monomer contents (BC:VAN=1:5), 1 M HCl concentration, stoichiometric amounts of oxidant to aniline, and 0.7 M aniline concentration for over 6 hours of reaction time. Additional optimisation may be achieved using other synthetic methods and additive manufacturing.

The presence of an elongated polyconjugate system with high conductivity can be accomplished with specific supramolecular PANI structures [86, 88]. Nanostructured PANI encounters high homogeneity with unique surface properties and high charge carrier mobility at nanoscale [242]. Regular one-dimensional (1D) nanostructures, including nanowires, nanotubes, nanorods and nanofibers, are preferred for electronic applications for several reasons, but specially for the superior electrical and optical properties at nanoscale [100].

6.2.2 Influence of BC and PVAN Interlayer on the Electrical Conductivity of BC/PVAN/PANI

The enhanced conductivity of the nanocomposites with grafted-PVAN could be explained by changes induced on PANI at molecular level. The growth of 1D PANI

nanostructures were developed at higher PVAN amounts, in contrast to the typical random aggregation of 3D PANI spherical particles obtained for lower GY_{PVAN} , as seen in SEM and TEM images of the previous chapter (Chapter 5). The formation of such supramolecular structures was attributed to the surfactant properties of PVAN [243] and the higher surface area [88], which might be capable of decreasing carrier scattering [244], while facilitating the doping process through a high charge carrier mobility. The increase from 3 to 5 times more VAN moles, double the GY_{PVAN} and further improved PANI grafting. The nanorod-like PANI coating uniformly distributed on BC/PVAN/PANI nanocomposites observed for higher amounts of PVAN, might have led to the development of a more elongated polyconjugated system with improved electrical conduction.[100]. In addition, it was found that a higher conglomerate of BC nanofibres (densest side of the membrane) contributed in part for the elevated conductivity measured, ascribed to the larger surface area for COP reaction.

The electrochemical analysis revealed the capacitive-like behaviour of PVAN that may have contributed to the overall electrochemistry of BC/PVAN/PANI, besides the apparent non-electroactivity of PVAN. The electrochemical activity of PVAN/PANI layer resulted mainly from a mix of protonic and electronic conduction upon redox reactions induced by the electrolyte and/or the applied potential [245], while proton conductivity was most likely the major contributor in BC conduction, in a synergetic network/electrolyte interaction [169]. Such results show prospective developments in PVAN functionalised substrates for enhanced electrically conductive and electroactive responses, which may be useful for several applications, inclusively to build highly advanced medical devices that can interface with nervous system by detecting and/or stimulating electrical signals.

6.3 CONCLUSION

The electroactivity of BC/PVAN/PANI nanocomposites was successfully analysed via four-point probe and electrochemical methods. Overall, BC/PVAN/PANI nanocomposites revealed reasonably good conductivity up to $(4.5 \pm 2.8) \times 10^{-2} \text{ S.cm}^{-1}$, improved by means of PVAN incorporation and appropriate adjustments of COP parameters. The boosted formation of nanorod-like PANI supramolecular structures

caused by PVAN intermediate layer (Chapter 5) were responsible for the enhancement of the electrical performance detected, as hypothesised. The different density of BC nanofibres seen (Chapter 4) was responsible for the contrasting conductivity values measured on both sides of the membrane due to disparate PANI grafting yields. This nanocomposite responded to the applied voltage via charge-transfer redox reactions taken place on PVAN/PANI surface, with charge carriers able to travel through BC network. The electrochemical switch of PANI occurred with oxidation or reduction to EM salt that, in CV, was observed as a redox peak couple at about $-0.70/0.74$ V (at $100 \text{ mV}\cdot\text{s}^{-1}$ scan rate in sulphuric acid). Close to this oxidation state ($+0.5$ V), PANI showed the minimum charge-transfer resistance of 21Ω with the corresponding capacitance as high as $39 \mu\text{F}$. This unique electrochemical activity can render BC/PVAN/PANI nanocomposites as an amplification mechanism for analysis and detection of electrochemical signals or molecules in numerous bioelectronic applications.

Chapter 7: CNTs-Reinforcement of BC/PVAN/PANI Nanocomposites

The content of this chapter is partially included in the accepted manuscript for publication “Rebelo A, Liu Y, Liu C, Schäfer K-H, Saumer M, Yang G. Carbon nanotubes-reinforced poly(4-vinylaniline)/polyaniline bi-layer grafted bacterial cellulose for bioelectronic applications. *Biomaterials Science & Engineering of American Chemical Society*, February 2019”.

Microbial cellulose treated with PANI/CNTs can be attractive as potential neural interfaces in terms of further improvements of the electrical conductivity, capacity and thermal resistance. The interactions between PANI and CNTs exhibited new electrochemical features with efficient ionic diffusion and charge-transfer, and thereby increasing the electrical conductivity and capacity. In this chapter, the formerly developed PVAN/PANI-grafted BC (BC/PVAN/PANI) nanocomposite substrate (Chapters 5 and 6, Figure 7.1a,b) was further reinforced with SWCNTs (referred to as CNT or CNTs from this point) with a dipping/drying process, as schematically exemplified in Figure 7.1cd. It is a primary concern to have a representative perspective of the changes raised from CNTs impregnation, especially as regards the electrical properties. As such, the as-prepared BC/PVAN/PANI/CNTs nanocomposites were morphologically analysed with SEM-EDX and HR-TEM, the electrical conductivity was measured with a four-probe method and the electrochemical properties were investigated with EIS, and the thermal stability was assessed via TGA.

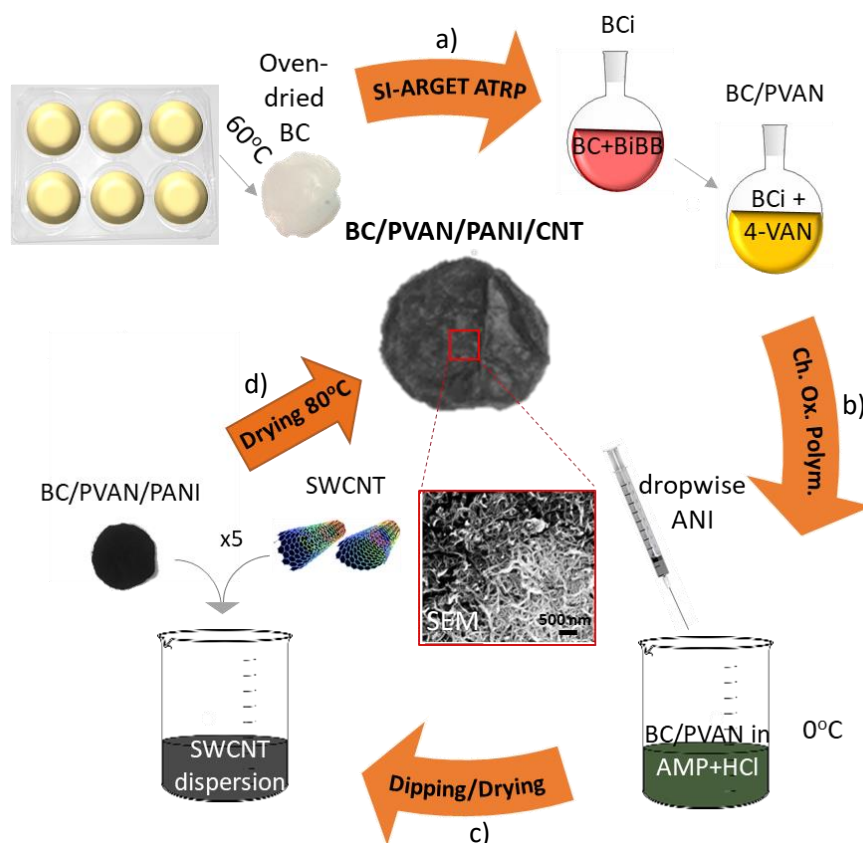


Figure 7.1. Schematic diagram of step-by-step reaction of BC modification for synthesis of BC/PVAN/PANI/CNTs nanocomposites. a) SI-ARGET ATRP of 4-VAN onto BC, starting with the creation of initiating sites on OH-rich BC surface (BCi) with BiBB. b) COP of ANI performed in an ice-bath in 1M HCl solution and APS as oxidant, to obtain BC/PVAN/PANI. c) Five-time dipping and drying process in SWCNTs dispersion for CNTs-reinforcement forming BC/PVAN/PANI composites.

7.1 RESULTS

7.1.1 Morphological Characterisation

BC/PVAN/PANI/CNTs nanocomposites were successfully synthesized following a multiple-step reaction, as schematically exemplified in Figure 7.1. The colour changes of BC membranes visible in Figure 7.2 gives a preliminary indication of the successful BC chemical modification. In Chapter 5, it was seen that upon SI-ARGET ATRP, BC membrane changed from white to light yellow colouring with no significant morphological effects on pristine BC, which became dark green with an uneven surface after COP, typical of PANI in the highest conductive form (emeraldine salt), as it is also shown in SEM images of Figure 7.3 [246]. PANI nanorod-like structures raised to fully coverage PVAN-treated BC nanofibres in the course of COP

(Chapter 5), may act as a suitable substrate for accommodation of CNTs through π - π interactions [247].

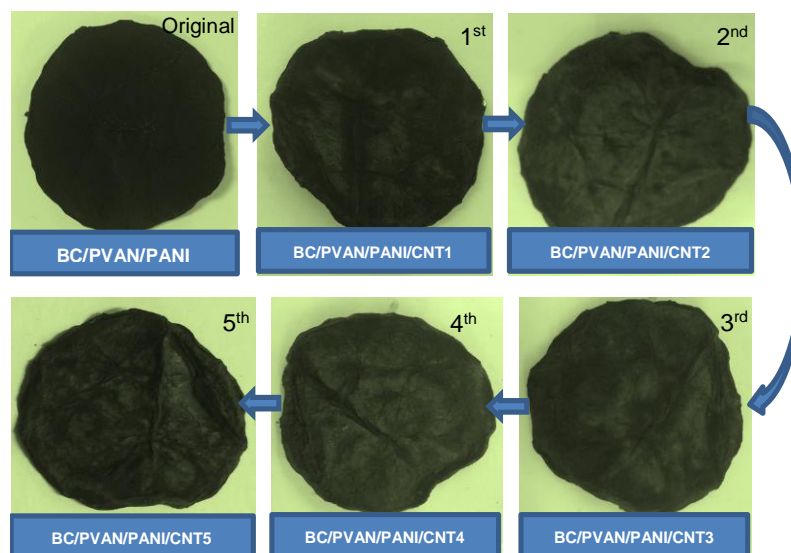


Figure 7.2. Optical images of BC/PVAN/PANI membranes after dipping/drying process in CNTs solution continuously performed 5 times. The numeral index (1...5) indicates the dip times in CNTs.

The interconnected porosity of BC network with large specific surface area is extensively reported in literature and is responsible for the exceptional absorption of CNTs, besides the additional presence of PVAN/PANI bilayer [248]. The successful impregnation of CNTs can be testified at a first glance by a slight shifting from dark green to dark grey colour (Figure 7.3). CNTs is prompted with a thin nanofibrillar-like network [249] coating on BC/PVAN/PANI surface, as it is seen in the SEM image of Figure 7.3, covering the as-recognised PANI morphology. A closer look to the functionalised-CNTs composite membranes, as representatively illustrated in HRTEM image of Figure 7.3b, demonstrates the nanotubular features of CNTs in a nanofibrillar arrangement, self-assembled into an interpenetrated and nanoporous structure [250] (Figure 7.3a,b), that is reasonably well distributed throughout the selected area.

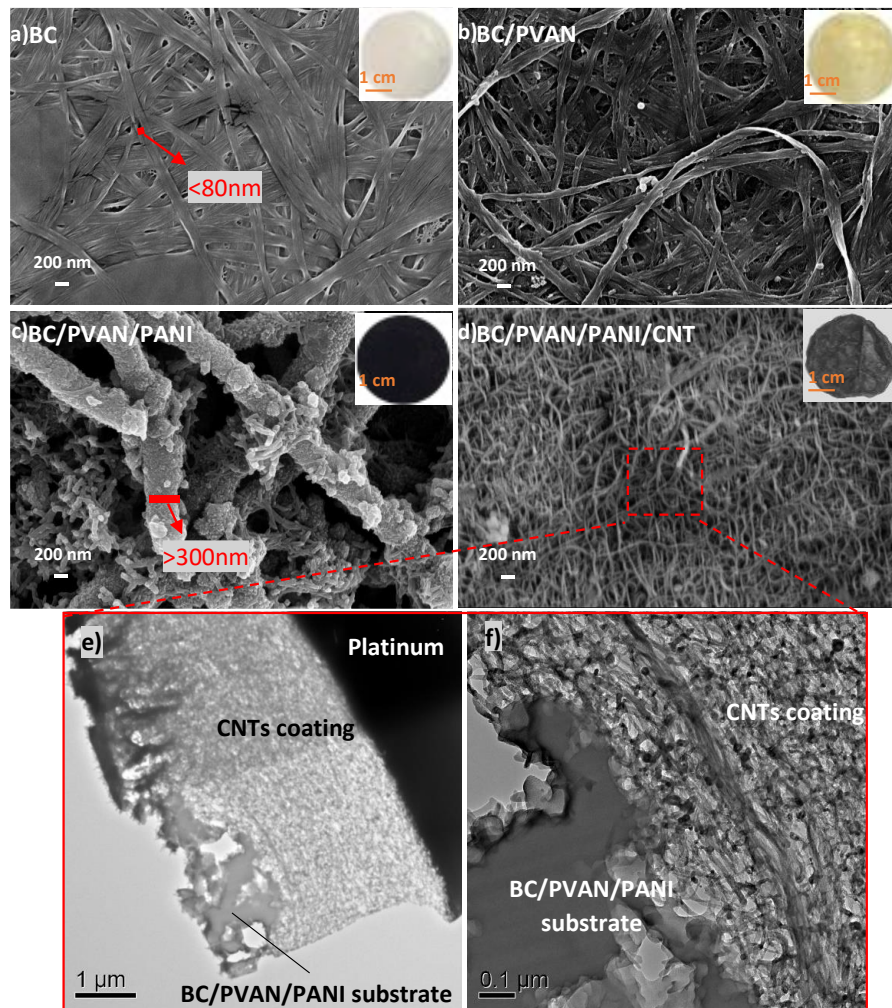


Figure 7.3. SEM images of a) pristine BC, b) BC/PVAN, c) BC/PVAN/PANI and d) BC/PVAN/PANI/CNTs, membranes with e) and f) STEM images of a CNTs coating portion of BC/PVAN/PANI/CNTs accordingly identified. The pictures placed on the right corner in SEM images correspond to the respective nanocomposites. The circle area indicates PANI-nanorods.

SEM-EDX mapping sustains the former results, demonstrating an abundant carbon content of the CNTs-reinforced nanocomposites of over 90% atomic weight in the selected area (Figure 7.4e). Carbon $1K\alpha$ distribution represented with a highly dense red dots area visible in EDX layered image of Figure 7.4a, corroborates the uniform impregnation of CNTs layer. Certain amounts of sulphur are also seen (Figure 7.4c,e) which can be attributed to residual APS from COP reaction.

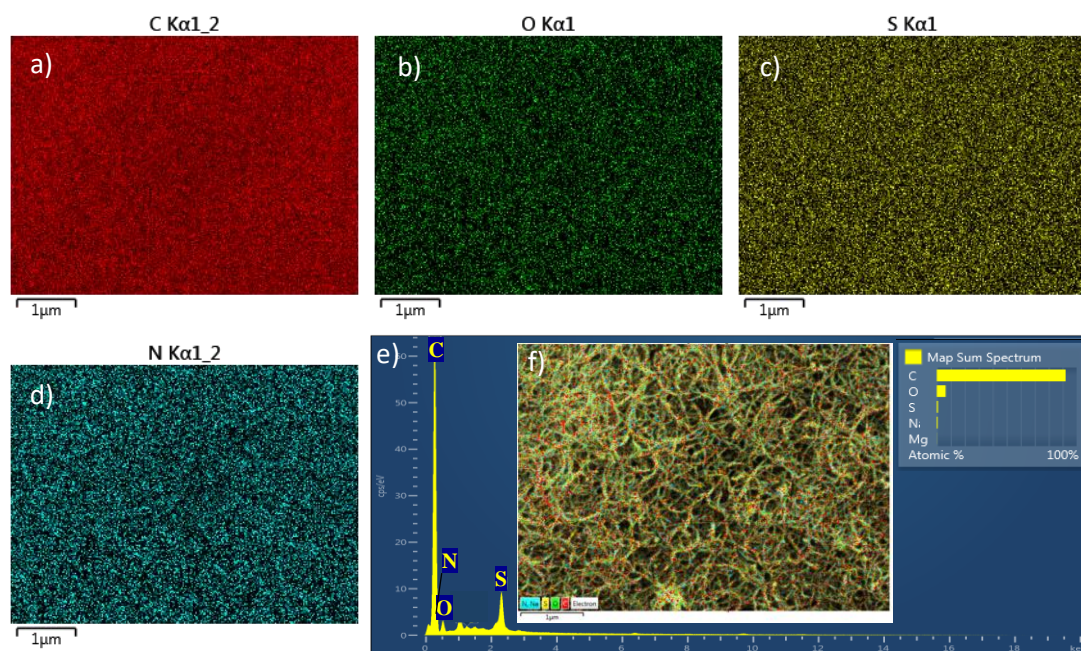


Figure 7.4. SEM-EDX of BC/PVAN/PANI/CNTs membranes. a-d) X-ray maps of the selected area f) and e) respective sum map spectrum.

7.1.2 Chemical Characterisation

X-Ray Diffraction

Representative XRD spectrum in Figure 7.5 was acquired for CNTs-reinforced membranes, which was directly compared with that of BC/PVAN/PANI (Figure 7.5b). The two main diffraction peaks observed at 14.5° and 22.7° in all spectra were ascribed to BC. As previously concluded in Chapter 5, the progressive decrease, broadening and slight shifting of the diffraction peaks after BC modification were attributed to the successful incorporation of PVAN and PANI, despite the non-detection of new peaks. After immersion of BC/PVAN/PANI membranes in CNTs, no significant changes could be seen, as shown in Figure 7.5a. However, with the high magnification of both spectra (Figure 7.5b), it is possible to be recognised a new diffraction peak measured at 26.6° that can be assigned to the plane 002 of CNTs (002_c) due to the reflection of graphite, which is the strongest and sharpest peak indexed to pristine CNTs [251]. The crystallite size of the CNTs as-calculated with the Scherrer equation (equation 3.5) is 39.4 nm, which is within the range found in the literature [252]. Therefore, it can be concluded CNTs were effectively coated on BC/PVAN/PANI nanocomposites, endorsing the previous gathered results on the optical and morphological analysis.

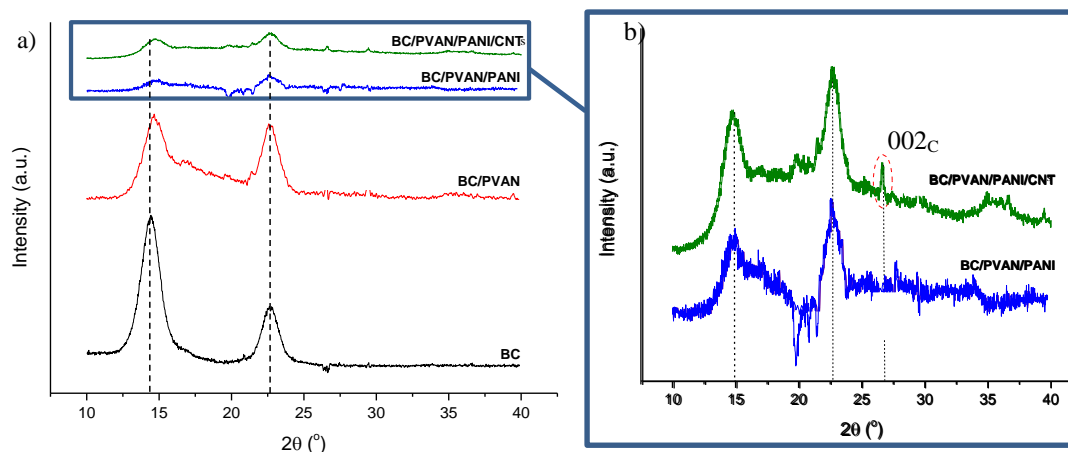


Figure 7.5. a) XRD spectra of BC, BC/PVAN, BC/PVAN/PANI and BC/PVAN/PANI/CNTs, b) with the corresponding magnification of the selected squared area. The curves were smoothed with FFT using Origin@2015 software.

X-Ray Photoelectron Spectroscopy

XPS conducted on BC nanocomposites corroborates the systematic reaction successfully achieved. The comparative wide scans displayed in Figure 7.6, acquired at a sampling area of $400 \mu\text{m} \times 400 \mu\text{m}$, showed that all nanocomposites have binding energies (BE) consistent with carbon 1s (C1s) and oxygen 1s (O1s) core shells, with a significant increased content in carbon after CNTs loading along with an expected escalating difference of C1s/O1s, as duly marked in the spectra [253]. The existence of nitrogen 1s core shell (N1s) in BC/PVAN (Figure 7.6b) and BC/PVAN/PANI (Figure 7.6c) composites reflected the efficient grafting of PVAN/PANI bilayer on pristine BC, as previously concluded in Chapter 5. In CNTs-reinforced nanocomposites, however, there are not apparent signs of the presence of nitrogen, indicative of full and uniform coverage of a CNTs on PVAN/PANI bilayer [254].

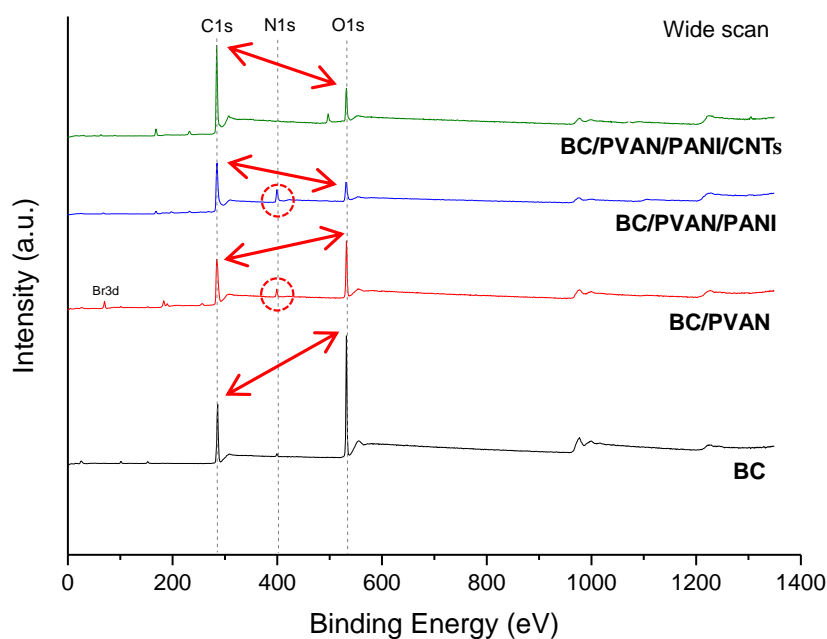


Figure 7.6. Comparative XPS spectra of wide scans acquired for un-modified BC, and BC/PVAN, BC/PVAN/PANI and BC/PVAN/PANI/CNTs nanocomposite membranes. The double sized arrows point out to the contrasting peak intensities of C1s and O1s after the inclusion of the successive coatings onto BC, and the circular areas in BC/PVAN and BC/PVAN/PANI spectra identify the peaks ascribed to N1s.

Distinct carbon bonds associated to individual contributions can also be distinguished in high-resolution C1s spectra over the sequential BC functionalisation steps. The core-level spectrum of C1s in BC manifests (Figure 7.7) the typical BE relative to pristine BC at 285.0 eV (C-C/C-H), 286.6 eV (C-O) and 288.1 eV (O-C-O) [74]. Upon SI-ATRP, a small deconvoluted peak emerged at 284.2 eV, that can be ascribed to C-C from PVAN aromatic ring, coupled with another peak at 289.4 eV, related to O-C=O bonding between BC and BiBB in ATRP initiation step [255]. The carbon-rich PVAN is witnessed with the intensification of C-C and C-H bonds compared to that of unmodified BC, to which C-Br from BiBB may have also accounted for. The subsequent functionalisation with PANI resulted in a rearrangement of the peak intensities, in particular at 285.0 eV for possible additional contributions of C-N and C=N bonds, and at 285.7 eV for C-N⁺ and C=N⁺ bonds [256]. However, the presence of CNTs into BC/PVAN/PANI nanocomposites led to an increased peak intensity of BE of the carbon bonding in contrast to what was observed in BC and other BC nanocomposites, indicating the possible presence of structural defects. A higher contribution of the peak at 284.2 eV can be assigned to C=C sp²

hybridisation of CNTs; while different relative intensities of the peaks at 284.2 eV and 285.0 eV compared to non-CNTs-treated membranes suggests that sp^3 hybridisation of C-C and C-N at 285.0 eV may be also present due to some possible interactions of CNTs with the aromatic rings and nitrogen atoms of protonated PANI [80, 257]. This supports that CNTs inclusion into BC/PVAN/PANI nanocomposites was efficiently accomplished.

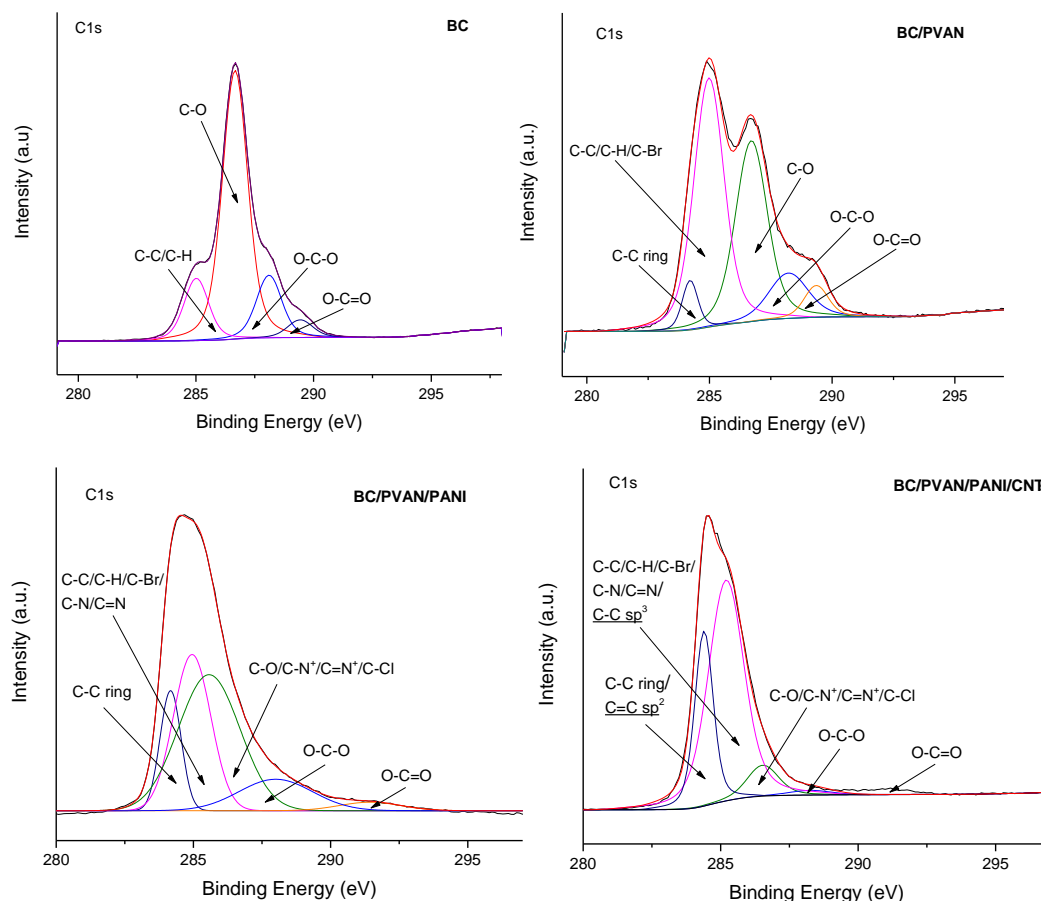


Figure 7.7. High-resolution core-level spectra of C1s of BC, BC/PVAN, BC/PVAN/PANI and BC/PVAN/PANI/CNTs nanocomposites, extracted from XPS wide scans of Figure 7.6. Highlighted are the contributions of CNTs to BC/PVAN/PANI/CNTs nanocomposites.

7.1.3 Electrical Conductivity

CNTs-reinforcement of BC/PVAN/PANI was completed through the dipping/drying process repeatedly performed five times to add an extra conductive layer. The frequency of this process was determined based on the highest electrical conductivity that could be achieved, which was monitored every step with the four-

point probe until a stable value was read (Figure 7.8). Similar to what was observed in Chapter 6, different electrical conductivities were obtained according to the membrane side, which was attributed to contrasting nanofibres density of BC, as such different grafting yields of PVAN/PANI bilayer are obtained upon ATRP and COP reactions.

No significant increase in the electrical conductivity of the nanocomposites can be noticed after soaking in CNTs twice. However, from the third time, the conductivity on the dense side raised considerably from $(3.5 \pm 0.8) \times 10^{-2}$ up to $(1.3 \pm 0.4) \times 10^{-1}$ S.cm⁻¹ on the last dip, and the average conductivity of both sides increased from $(2.8 \pm 0.6) \times 10^{-2}$ up to $(1.0 \pm 0.3) \times 10^{-1}$ S.cm⁻¹. This may be related to the better permeabilisation of CNTs solution inside BC membrane.

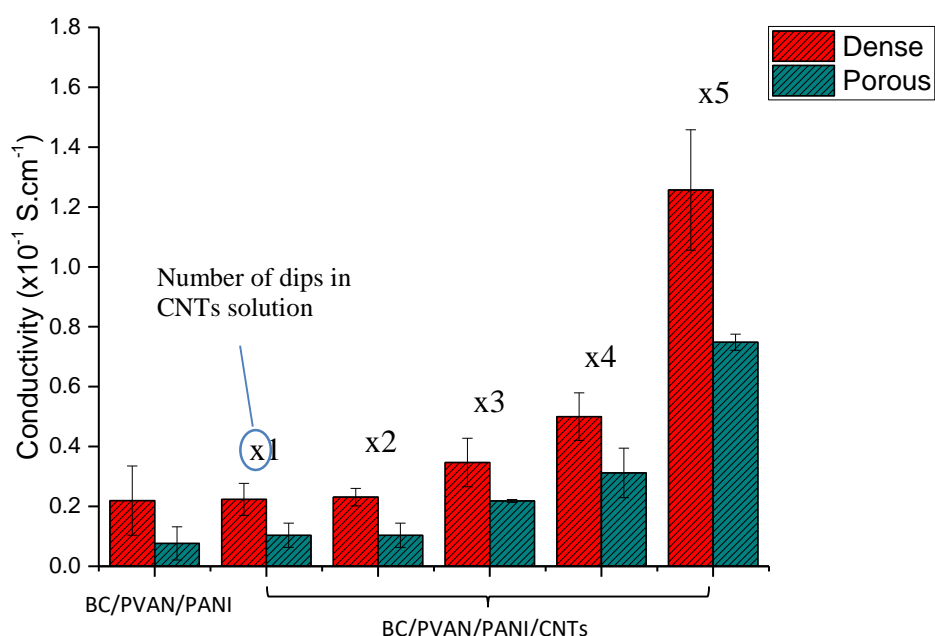


Figure 7.8. Electrical conductivity of BC/PVAN/PANI nanocomposites before and after immersion in CNTs dispersion for one up to five times.

7.1.4 Electrochemical Properties

Electrochemical Impedance Spectroscopy

CNTs-reinforced nanocomposites were subject to EIS analysis as displayed in Figure 7.9a, to further assess the electrical properties. The data was curve-fitted using the equivalent Randles circuit shown in Figure 7.9b. The results as-fitted by the circuit are discriminated in Table 7.1. Changes in the electrochemical behaviour of the

nanocomposites are mainly bestowed by the presence of both PANI and CNTs, whereas BC confers appropriate support for the accommodation of those electroactive moieties, while building a protonic conduction path (Chapter 4).

Table 7.1. Average values (3 samples) of the elements of the equivalent Randle circuit used to fit the data of Figure 7.9.

Element	BC/PVAN/PANI	BC/PVAN/PANI/CNTs
R_s (Ω)	51.3±5.3	31.0±6.8
R_{ct} (Ω)	21.2±5.1	23.4±4.4
CPE₁ (F)	(26.7±0.2)×10 ⁻⁶	(21.2±0.6)×10 ⁻⁶
R_p (Ω)	(1.1±0.005)×10 ¹²	308.1±24
CPE₂ (F)	(1.5±0.2)×10 ⁻⁶	(5.4±0.3)×10 ⁻²

As earlier discussed in Chapter 6, the solution resistance (R_s), marks the beginning of the first semicircle seen in the Nyquist plots and can be attributed to the electrolyte resistivity and the uncompensated resistance [232], as well as the resistance derived from the contact electrodes [73]. The parallel combination of the electrode/electrolyte charge transfer resistance (R_{ct}) with the corresponding faradaic capacitance (CPE_1) describes the first semicircle formed at high frequencies [231], that is followed by a second semicircle drawn at low frequencies which can be curve-fitted with a polarisation resistance (R_p) in parallel with a double layer capacitance (CPE_2) [234]. CPE_1 and CPE_2 are expressed in terms of constant phase elements as this accounts for the non-ideal capacitor behaviour resulted from heterogeneous porosity and PANI/CNTs distribution of the nanocomposite membranes [236], causing charge scattering at the electrode/electrolyte interface (depressed semicircles) and the deviation of the diffusion line from the 45° slope at low frequencies [258].

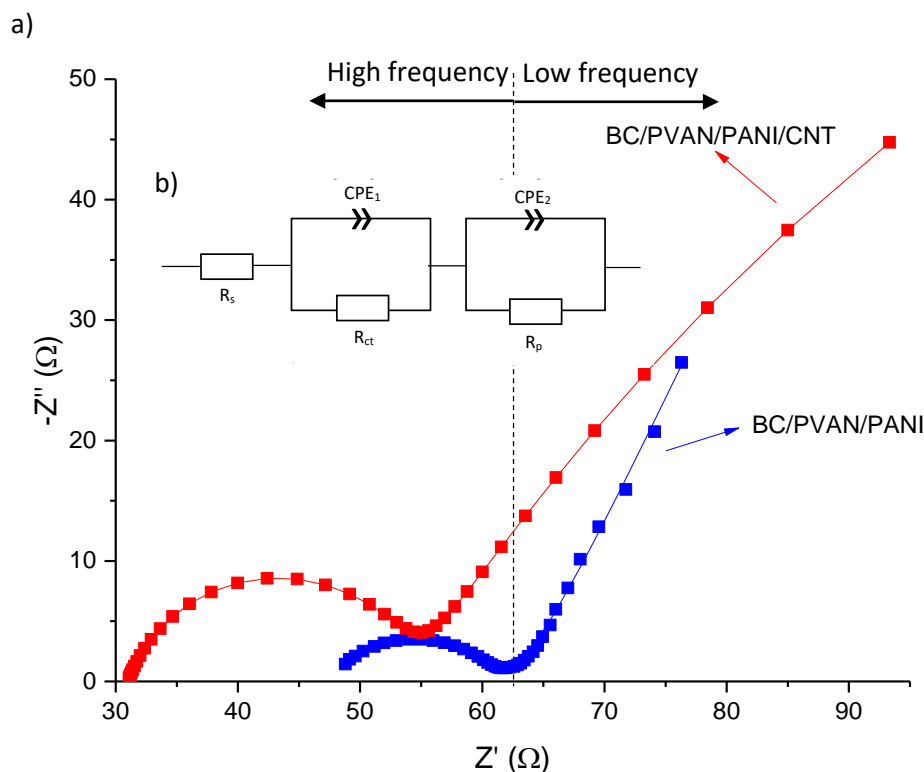


Figure 7.9. a) Representative Nyquist plots of BC/PVAN/PANI and BC/PVAN/PANI/CNTs nanocomposite membranes BC/PVAN/PANI, with the respective b) equivalent Randles circuit used to fit the data. R_s stands for solution resistance, R_{ct} for charge transfer resistance, R_p for polarisation resistance, and CPE_1 and CPE_2 for constant phase element of the corresponding R_{ct} and R_p parameters. Square dots (■) represents the acquired experimental data and solid lines (—) for the fitting.

R_s lowers after CNTs-reinforcement, which suggests ionic diffusion was facilitated [259]. Concurrently, R_{ct} and CPE_1 did not change significantly, which implies PANI may be the main responsible for the electrochemical behaviour over the high frequency range (first semicircle), while CNTs dominated in the low frequency region (second semicircle) with possible additional contribution of PANI/CNTs interface resistance [236]. In fact, it can be seen R_p decreases substantially from 1.1 TΩ to 308 Ω with a pronounced increase of the corresponding double layer capacitance (CPE_2) in 4 orders of magnitude from 1.5 μF to 54 mF. This corroborates the enhanced electrical conductivity and the new electrochemical properties upon BC/PVAN/PANI functionalisation with CNTs. The remarkable charge storage capacity shown is imparted by the large aspect ratio and surface area of CNTs, which may act as a conducting bridge between PANI domains [80]. The extended π structure of CNTs not only furnishes the nanocomposites with a more efficient electron transference, as it facilitates the ionic transport from the electrolyte that can traverse the nanotube length

through the bore upon an applied potential. This leads to an increased in the protonic conductivity [260]. It is also anticipated that the porosity of CNTs coating may have contributed further for the enhancement of the protonic conductivity, as it is established the interconnected porosity is favourable [261]. In addition, it is known and also revealed in high resolution XPS spectra, CNTs can strongly interact with the aromatic rings of PANI structures, establishing π -stacking and CH- π interactions [80], that contributes to boost the overall electrical properties of the nanocomposite.

7.1.5 Thermogravimetric Analysis

The thermal stability of BC/PVAN/PANI/CNTs nanocomposites was assessed via TGA recorded from room temperature to 800 °C. CNTs are characterised for its high thermal stability, with monotonical decomposition for temperatures over 500 °C [262]. The weight loss of the nanocomposites, however, demonstrate multiphase thermogravimetric profiles, which can be categorised into three main stages, accordingly indicated in Figure 7.10. Table 7.2 summarises the information related to the onset, offset and peak temperatures of the several degradation stages of the BC composites (T_{onset} , T_{offset} and T_{peak}), extracted from the graphic of Figure 7.10. Initially, there is a minimal decomposition below 5 %, followed by a sharp weight loss, from which a *plateau* is reached with an insignificant degradation. The first stage (I) can be attributed to some remaining moisture inside the samples [208], while the second stage (II) can be associated to the main chain decomposition of BC [79], PVAN [263] and PANI with deprotonation of EM salt and acid release [264] and the last stage can be assigned to the residual and irreversible polymer chain decomposition, along with some CO₂ emission resulting from the initial reaction between carbon from CNTs and oxygen from about 500 °C [174]. Despite the weight loss pursued the same trend for all BC nanocomposites, the extent of the stages varied slightly after BC modification. This observation is particularly evident in the first two degradation stages which differed from those of pristine BC by approximately 200 °C. The lower temperatures at which the decomposition of BC/PVAN/PANI/CNTs started are in the range of the temperatures corresponding to the degradation phases of the individual components of the nanocomposites abovementioned, which means the functionalised layers may serve as protective coating against thermal degradation of the underneath layers [72].

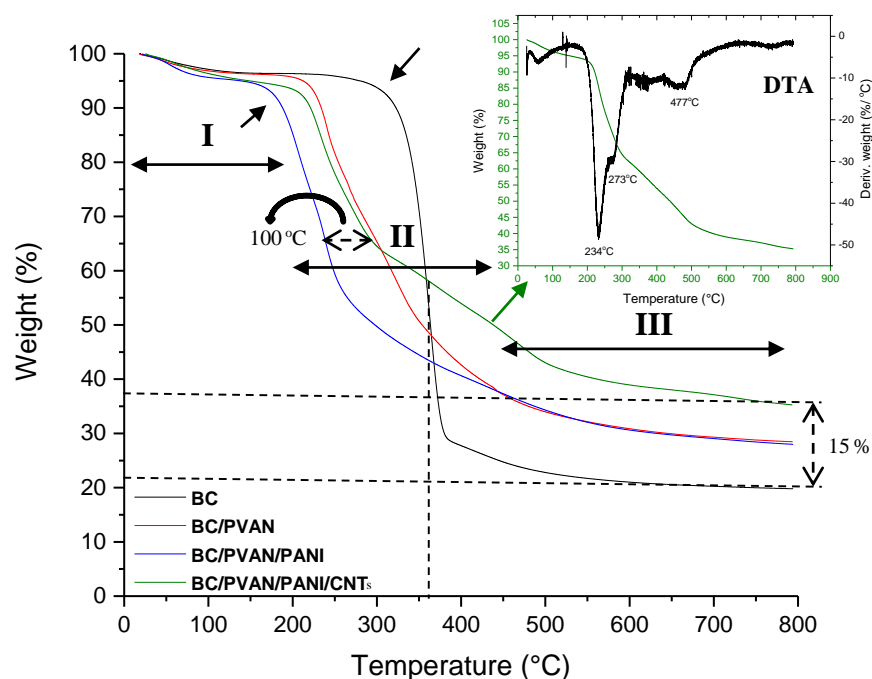


Figure 7.10. Thermogravimetric curves of BC nanocomposites characterized by three weight loss stages accordingly marked as I, II and III. The differential thermal curve of BC/PVAN/PANI/CNTs (DTA) is also shown.

After CNTs-reinforcement, the BC/PVAN/PANI nanocomposites become more thermally resistance by over 100 °C (see Figure 7.10), from 200 °C to 350 °C. In addition, CNTs-coated membranes seemed to be the most thermally stable nanocomposite, displaying a final vestigial weight of 37%, exceeding nearly 20% of that of pure BC (see Figure 7.10) [265]. Because CNTs possess elevated thermal stability, such event can be attributed to an eventual synergetic π -stacking interaction established between the quinoid rings of PANI and the CNTs π -bonding, as seen with XPS analysis. Moreover, stage II in BC/PVAN/PANI/CNTs can be further portioned into two phases (1st derivative plot of Figure 7.10) from 206 °C (T_{onset1}) and 232 °C (T_{onset2}), respectively, with the highest weight change (peak temperatures) at 234 °C (T_{peak1}) and 273 °C (T_{peak2}) previously assigned to polymer chain decomposition (Table 7.2). The last degradation stage visible from 420 °C (T_{onset3}) marks the beginning of CNTs burning that reaches its peak at 477 °C (Table 7.2) [262]. This assumes CNTs furnishes a supplemental thermally stable and also heatproof coating at high temperatures in addition to the enhanced conductivity rendered to the nanocomposites.

Table 7.2. Onset, peak and offset temperatures extrapolated from the first derivative curves of TGA shown in Figure 5.9b.

	BC	BC/PVAN	BC/PVAN/PANI	BC/PVAN/PANI/CNTs
T _{onset1} /°C	323	223	171	206
T _{peak1} /°C	362	242	202	234
T _{offset1} /°C	390	251	296	290
T _{onset2} /°C	-	202	213	232
T _{peak2} /°C	-	324	241	273
T _{offset2} /°C	-	377	267	310
T _{onset3} /°C	-	-	-	420
T _{peak3} /°C	-	-	-	477
T _{offset3} /°C	-	-	-	509

7.2 DISCUSSION

CNTs was successfully incorporated within BC/PVAN/PANI nanocomposites primarily for augmented electrical properties. CNTs-reinforced membranes were easily accomplished through a simple dipping and drying process herein described, forming a uniform coating that possesses nanofeatures and electrostatic interactions that were responsible for the outstanding electrical conductivity and capacity verified. The electrical conduction mechanisms of PANI and CNTs differ significantly. As discussed in Chapter 6, the conductivity of PANI is concerned with charge carries raised from redox processes, whereas in CNTs, it results from the π -stacking along with its nanostructure and high surface area to volume ratio which towers the charge carrier mobility. In spite of the contrasting conducting mechanisms, both are affected by changes in the respective morphologies [266]. In theory, smaller diameters of CNTs vertically aligned are known to provide higher conductivity, as seen in Chapter 2.

CNTs-functionalisation of BC/PVAN/PANI caused a significant increase of the electrical conductivity to values reported in literature for similar blends [72]. The high conductivity achieved was also determined by the extraordinary absorption capacity of BC substrate that can accommodate large amounts of CNTs within its network, while contributing for a protonic conduction pathway on the hydrated surface. The lowering values compared to that of pristine CNTs is, among others, related to the

randomly orientated CNTs nanofibres, the blending process and the substrate used, as different physicochemical interactions can be established. Although, mainly electrostatically adhered to BC/PVAN/PANI through Van der Waals forces, there is reported evidence that CNTs can strongly bind to the existing PANI, as testified from XPS analysis [267]. As this may provide a more stable coating, the inherent characteristics of CNTs, such as the electrical properties, may also be affected. It has been suggested that CNTs may act as dopant of PANI owing to the charge transfer from quinoid unit to CNTs, forming a charge-transfer complex which enhance the overall conductivity of BC/PVAN/PANI nanocomposite (Figure 7.11) [80].

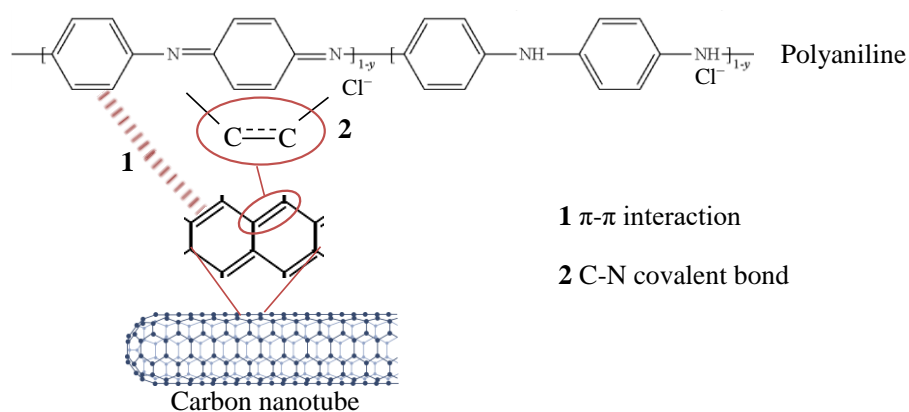


Figure 7.11. Schematic illustration of the possible interactions established between PANI and CNTs. 1 shows the pi-stacking interaction between the aromatic rings of both PANI and CNT and in 2, CNTs competes with chloride (Cl^-) to dope PANI and form a covalent C-N bond (adapted from [80]).

The electrochemical analysis extended the understanding of the electrical conduction mechanisms of this complex nanocomposite system, which is a mixed of electronic and protonic conductivities, brought in part by the long and continuous range of π -stacking chain across CNTs with its hollow nanostructure, as well as those created with PANI. Accordingly, the lowering resistivity and enlarged capacitance measured is a result of CNTs embodied within BC/PVAN/PANI membranes. Moreover, the electrochemical behaviour previously attributed to PANI was preserved after CNTs blending.

The increased thermal stability of the nanocomposites in wide temperature range, ensures the overall properties will be thermally preserved up to 234 °C with

very slow weight loss up to 270 °C, as such it is an essential requisite for bioelectronic devices (human body temperature 37 °C). This increased thermal stability of the nanocomposites seen is endowed by CNTs coating and the bonding with PANI [268]. Along with the interconnected porosity yet cohesive CNTs coating, it is also anticipated positive synergy with cells through a suitable flow of oxygen and nutrients, for encouraging suitable cell-cell interaction, cell adhesion, migration, proliferation and differentiation [269], aspects that are further inspected in Chapter 8. To conclude, these newly developed nanocomposites reinforced with CNTs reveals improved capabilities that may be employed as potential neural interfaces.

7.3 CONCLUSION

Electrical reinforcement of CNTs layer nanocomposites was efficiently accomplished with a dip-coating process. CNTs impregnation was confirmed with SEM-EDX, HRTEM, XRD and XPS analysis. PANI/CNTs interaction embodies BC substrate with special electrical properties, which can house large amounts of these moieties, while providing a path for protonic conductivity. CNTs considerably boosted the electrical conductivity from $\sim 10^{-2}$ to $\sim 10^{-1}$ S.cm⁻¹ and charge storage capacity up to 54 mF with an impressive decrease of the polarisation resistance in nine orders of magnitude to some hundreds of ohms. This is attributed to π - π interactions established with PANI with a possible dopant effect, as well as the large surface area provided by the nanorod-like arrangement. PANI/CNTs imparted a protective bilayer against thermal degradation of BC substrate, with no substantial weight loss measured under 234 °C. CNTs improved the electrical properties of the formerly produced BC/PVAN/PANI and the thermal stability.

Chapter 8: Biocompatibility of the Functionalised BC-based Nanocomposites

The content of this chapter is partially included in the published scientific article “Rebelo A, Liu Y, Liu C, Schäfer K-H, Saumer M, Yang G. Poly(4-vinylaniline)/polyaniline bilayer functionalized bacterial cellulose membranes as bioelectronics interfaces. *Carbohydr Polym.* Elsevier; 2019 Jan 15; 204:190–201” and the accepted manuscript for publication “Rebelo A, Liu Y, Liu C, Schäfer K-H, Saumer M, Yang G. Carbon nanotubes-reinforced poly(4-vinylaniline)/polyaniline bilayer grafted bacterial cellulose for bioelectronic applications. *Biomaterials Science & Engineering of American Chemical Society*, February 2019”.

The biocompatibility of a material involves several aspects in a certain context to induce appropriate host response in a specific situation. In general, a biomaterial must comply with some basic cellular responses, such as non-cytotoxicity and non-immunogenicity, while maintaining the cell integrity and supporting the ordinary cellular functions [270]. This chapter is devoted to a careful analysis on the biocompatibility aspects for evaluation of the safe usage of the as-developed nanocomposites for biomedical purpose, in particular in the nervous system. Accordingly, *in vitro* neural cell cultures were conducted in the presence of pristine BC and BC-based nanocomposites, with special attention given primarily to cell viability and differentiation, in order to evaluate any possible toxic and functional effects on cells (Figure 8.1).

Two different neural cell models – PC-12 Adh and SVZ cells – were selected for this aim (Figure 8.1). In the first set of experiments, adherent cells derived from the pheochromocytoma of embryonic rat adrenal medulla (PC-12 Adh cells) were used to evaluate both cell proliferation and neuronal differentiation [271]. PC-12 Adh cells were incubated for 7 days with BC-based nanocomposites and the cell viability was assessed using PrestoBlue® reagent, with the cell morphology examined at the end of the culture period. Neural differentiation was induced with nerve growth factor (NGF)

in the presence of the different materials and observed with fluorescence staining. Thereafter, primary neural stem cells (NSCs) isolated from the subventricular zone of the brain of postnatal mice (SVZ cells) were cultured with BC nanocomposites for a closer perception of the cells behaviour. The viability of SVZ cells was assessed with LIVE/DEAD assay after 7 days of incubation with BC and its composites. Neurogenesis was induced with NGF on the different substrates and was tracked at different time points using a green fluorescence staining (CFSE). On the last day of culture, the induced cells were immunostained for visualisation of neurons and glial cells using specific cell markers.

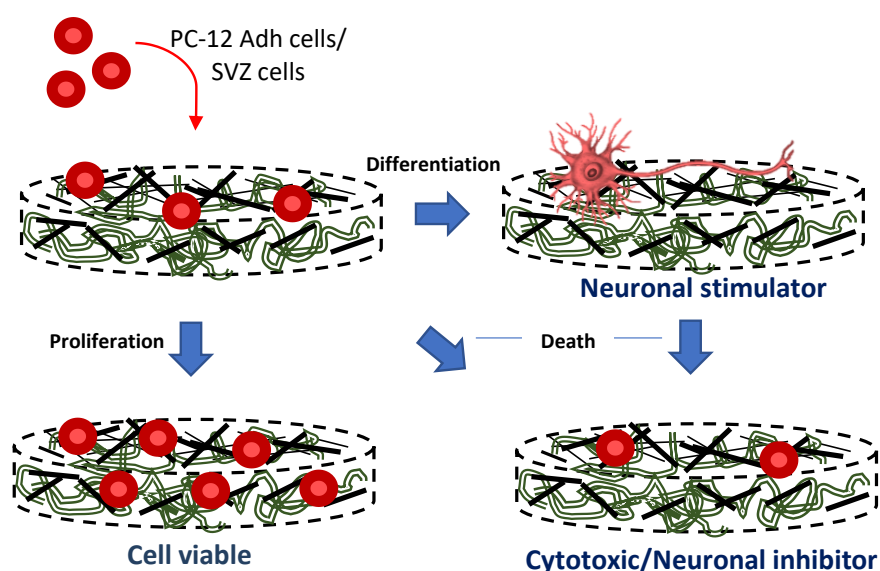


Figure 8.1. Schematic diagram of the possible cellular responses of PC-12 Adh and SVZ cells studied in this chapter after contact with the electrically conductive BC nanocomposites *in vitro* to conclude on their cytocompatibility: Cell proliferation and cell differentiation.

8.1 RESULTS

8.1.1 Cytocompatibility with PC-12 Adh Cells

Cell Viability

When being incubated with the as-synthesised BC/PVAN, BC/PVAN/PANI and BC/PVAN/PANI/CNTs loaded with different PVAN grafting yields, cell viability was determined through the assessment of cell adhesion and proliferation of PC-12 Adh

cells using PrestoBlue assay, which was compared with that on TCTP and BC. Cells were seeded on BC nanocomposites at a density of 2×10^4 cells per cm^2 , kept in culture at 37°C for 7 days. Cell adhesion was ensured within 24 hours after seeding and the proliferation was evaluated thereafter every 2 days until the end of the culture period. The absorbance read at 570 nm were normalised to 600 nm, and TCTP and BC were used as controls.

In the first set of experiments, cell viability was tested for BC/PVAN and BC/PVAN/PANI nanocomposites synthesised with different BiBB:VAN molar ratios, which were accordingly compared to that of TCTP and BC, as shown in Figure 8.2.

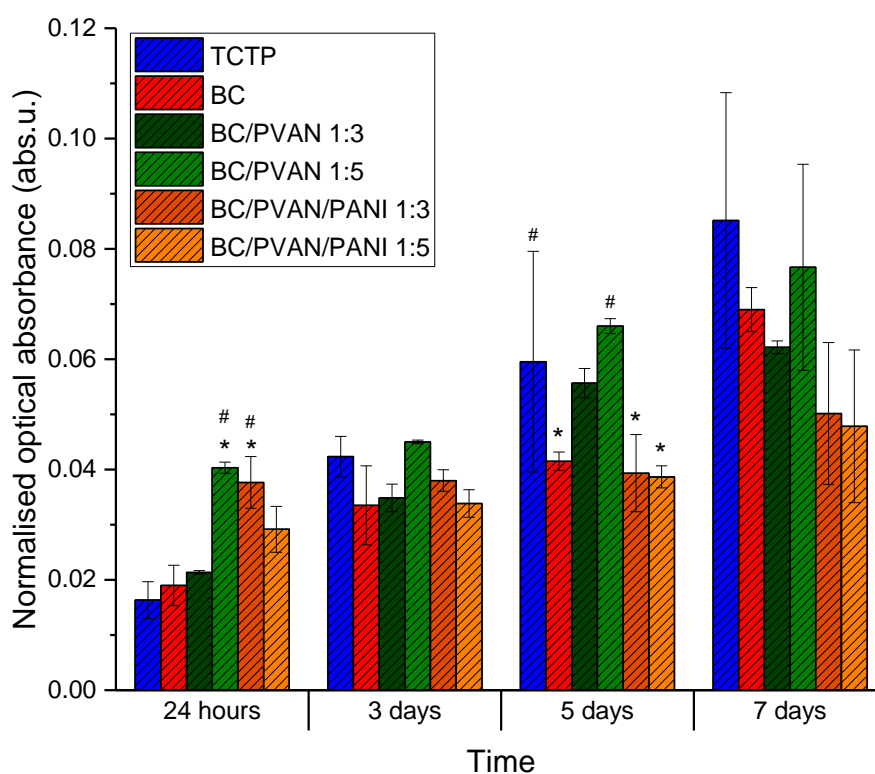


Figure 8.2. Cell activity of PC-12 Adh cells cultured on pristine BC, BC/PVAN (at 1:3 and 1:5) and BC/PVAN/PANI (at 1:3 and 1:5). The results are shown in terms of means \pm standard deviations of optical absorbance measured. * and # indicates statistical significance ($p < 0.05$) compared to TCTP and BC, respectively, according to one-way ANOVA testing.

After 24 hours of incubation, considerably higher optical absorbance (OA) was detected on BC/PVAN ($p < 0.05$). It can be also observed a trend for an increase OA on

BC/PVAN/PANI nanocomposites over time (Figure 8.2) to which cells seemed to be strongly anchored (Figure 8.3). Followed the initial 24 hours, the OA gradually increased on all substrates at a steady rate till the end of the culture period, in spite of being visibly higher on BC/PVAN in particular for higher VAN molar contents ($p < 0.05$). On the last day, statistically equivalent OA can be observed on all substrates, which approximately doubled in relation to the first day, although this was apparently slightly lower on BC/PVAN/PANI compared to that on TCTP.

Despite this observation, the adhered neural cells on BC-based substrates on the 7th day (Figure 8.3) show what seems to be a flat and fully spread shape over the surface.

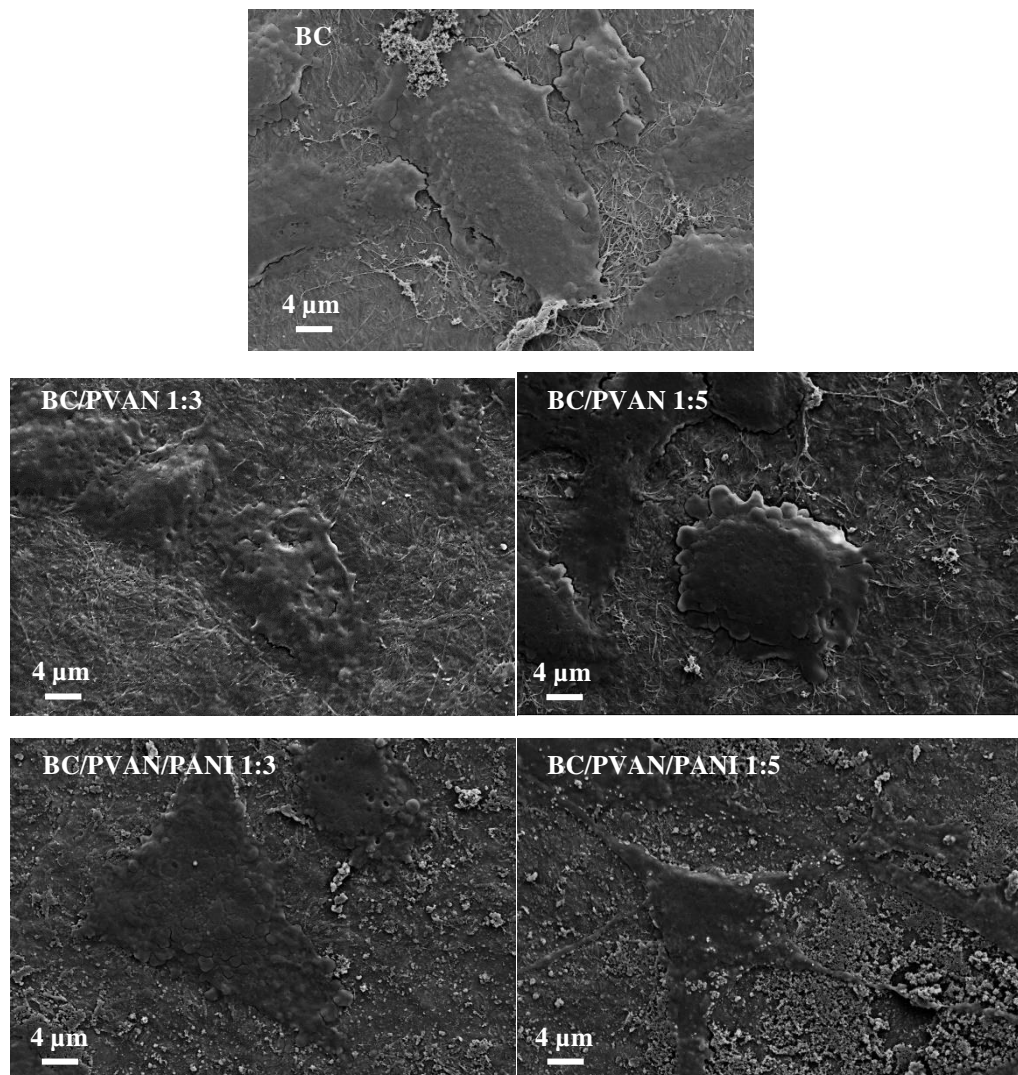


Figure 8.3. SEM images showing the morphology of PC-12 Adh cells cultured on BC, BC/PVAN (BiBB:VAN=1:3 and 1:5) and BC/PVAN/PANI (BiBB:VAN=1:3 and 1:5) after 7 days of culture.

Upon CNTs-reinforcement of BC/PVAN/PANI nanocomposites prepared from BiBB:VAN=1:5 molar ratio (BC/PVAN/PANI/CNTs), higher OA was identified 24 hours after seeding in comparison with BC ($p<0.05$) (Figure 8.4). However, in the following days, no statistical differences were detected on the average values despite significant dispersibility (long standard deviation bars). Notwithstanding, a trend to be slightly higher on BC/PVAN/PANI/CNTs can be observed. This shows that the inclusion of CNTs did not dramatically affect the OAs measured for the BC-based nanocomposites and it seems there was a trend to further increase. This also shows identical results to those obtained on BC/PVAN/PANI, and similar to what has been observed for pristine BC.

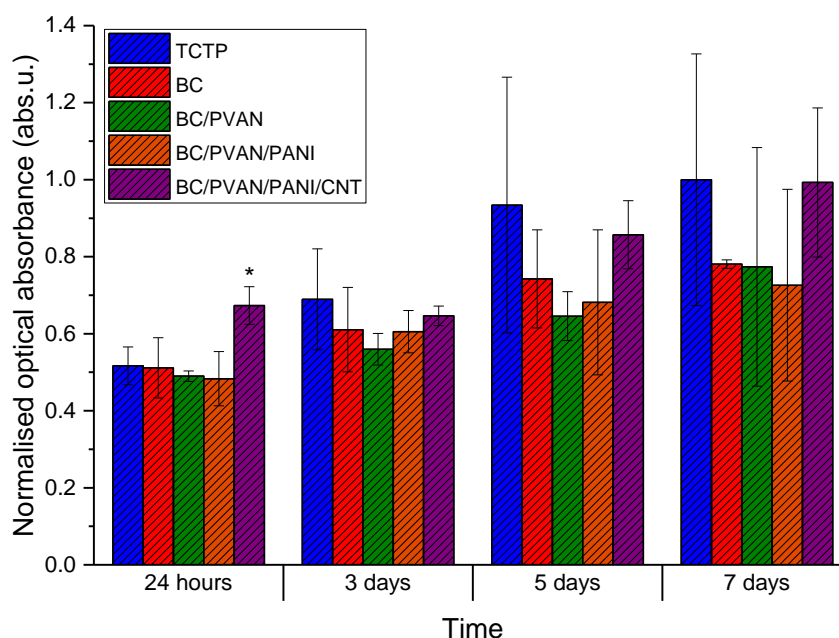


Figure 8.4. Cell activity of PC-12 Adh cells cultured on pristine BC, BC/PVAN (at 1:3 and 1:5) and BC/PVAN/PANI (at 1:3 and 1:5). The results are shown in terms of means±standard deviations of optical absorbances measured. * indicates statistical significance ($p<0.05$) compared to TCTP and BC according to one-way ANOVA testing.

Cell Differentiation

Differentiation of PC-12 Adh cells were induced on the diverse BC substrates and their responses were accordingly evaluated and compared with that on TCTP. Cell adhesion was ensured with incubation within the initial 24 hours after harvesting, when

culture media was replaced by NGF-enriched medium and replenished every 2 days for 7 days. In the end of the culture period, the DNA of the cell nucleus and the actin present in the neurites were stained with DAPI (blue) and Alexa Fluor® 488 (green), respectively, for visualisation with fluorescence microscope (Figure 8.5) and later quantitative analysis (Figure 8.6).

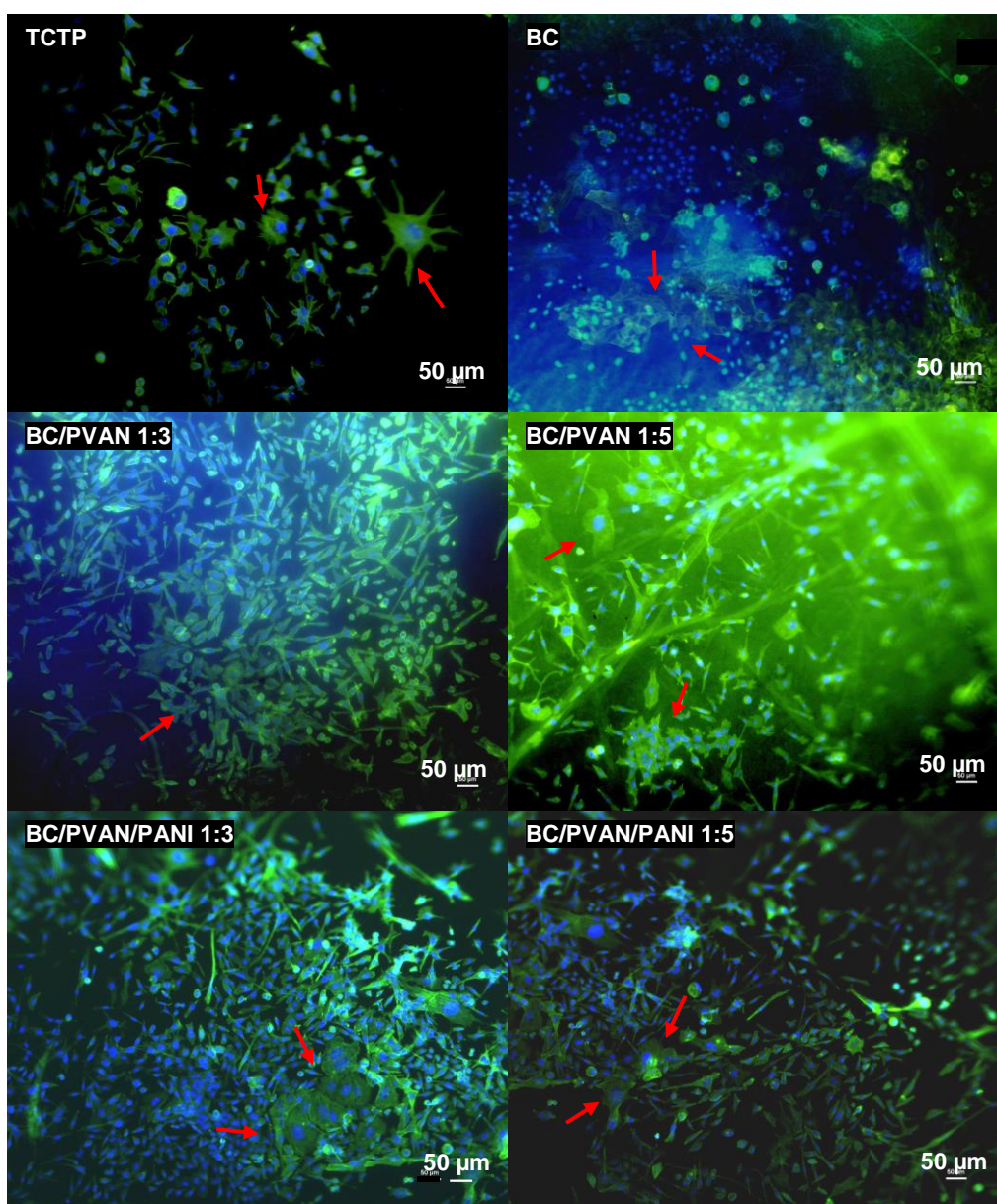


Figure 8.5. Fluorescence images of induced PC-12 Adh cells after 7 days incubated with NGF on TCTP, BC, and BC/PVAN and BC/PVAN/PANI prepared with different BiBB:VAN molar ratios. The nuclei are represented in blue (DAPI) and the cell projections are shown in green (Alexa Fluor® 488). The indexes 1:3 and 1:5 refer to BiBB:VAN molar ratios. Red arrows identify glial-type cell.

As shown in Figure 8.5, appreciable cell number showed high neurite outgrowth with long projections on both BC/PVAN and BC/PVAN/PANI substrates. In contrast, cells on BC adopted mostly rounded shape with multiple but very short projections, morphology that is typical of early differentiated glial-type cells or completely undifferentiated cells. With BC functionalisation, the differentiation degree practically doubled (Figure 8.6a) and a dramatic increase in neurite length occurred from 17 ± 5 μm on BC up to 77 ± 29 μm on BC/PVAN/PANI (Figure 8.6b). As such, the functionalised BC, in particular BC/PVAN/PANI, may have triggered neuronal differentiation unlike pristine BC, that apparently acted as a neuritogenesis inhibitor despite the good support provided for cell adhesion and proliferation when non-NGF treated.

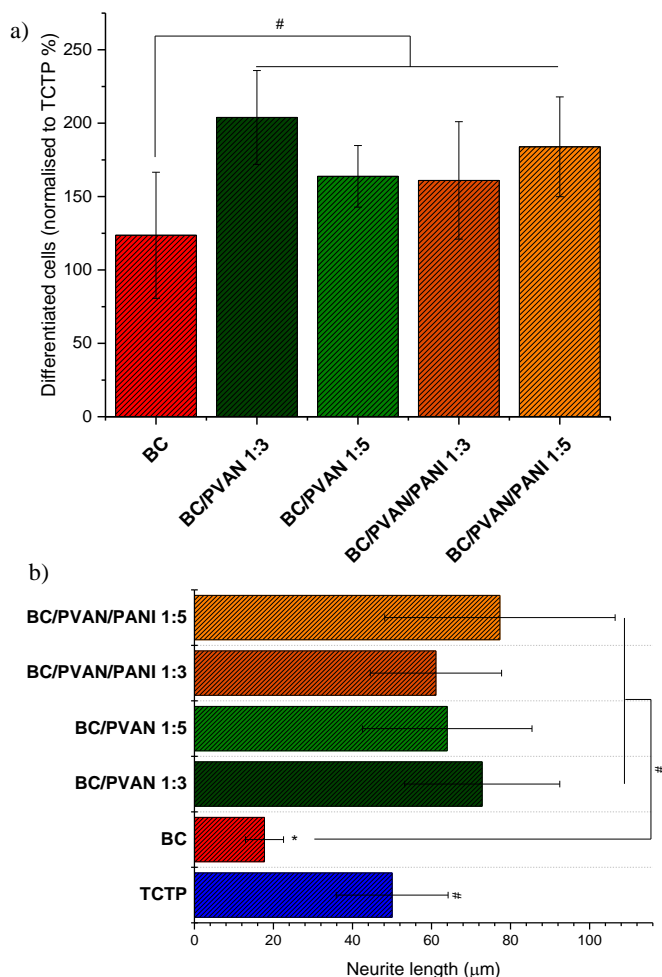


Figure 8.6. a) Percentage of differentiated cells on pristine BC and BC nanocomposites relative to TCTP and b) Neurite length of cell projections on the different substrates. * and # indicate statistical significance ($p < 0.05$) compared to TCTP and BC, respectively, according to one-way ANOVA testing.

8.1.2 Cytocompatibility with SVZ Cells

Cell Viability

To substantiate the former results on the neural cell viability of the newly developed functionalised BC composites prepared under the standard conditions (BiBB:PVAN=1:5), SVZ cells were isolated from postnatal mice and cultured with the grafted BC membranes for 7 days, as such their responses were evaluated and compared with that of pristine BC and TCTP, which were used as control. Representative images of the SVZ cells on the functionalised BC are depicted in Figure 8.7, in which live cells were stained green with calcein-AM and dead cells were stained red with propidium iodide.

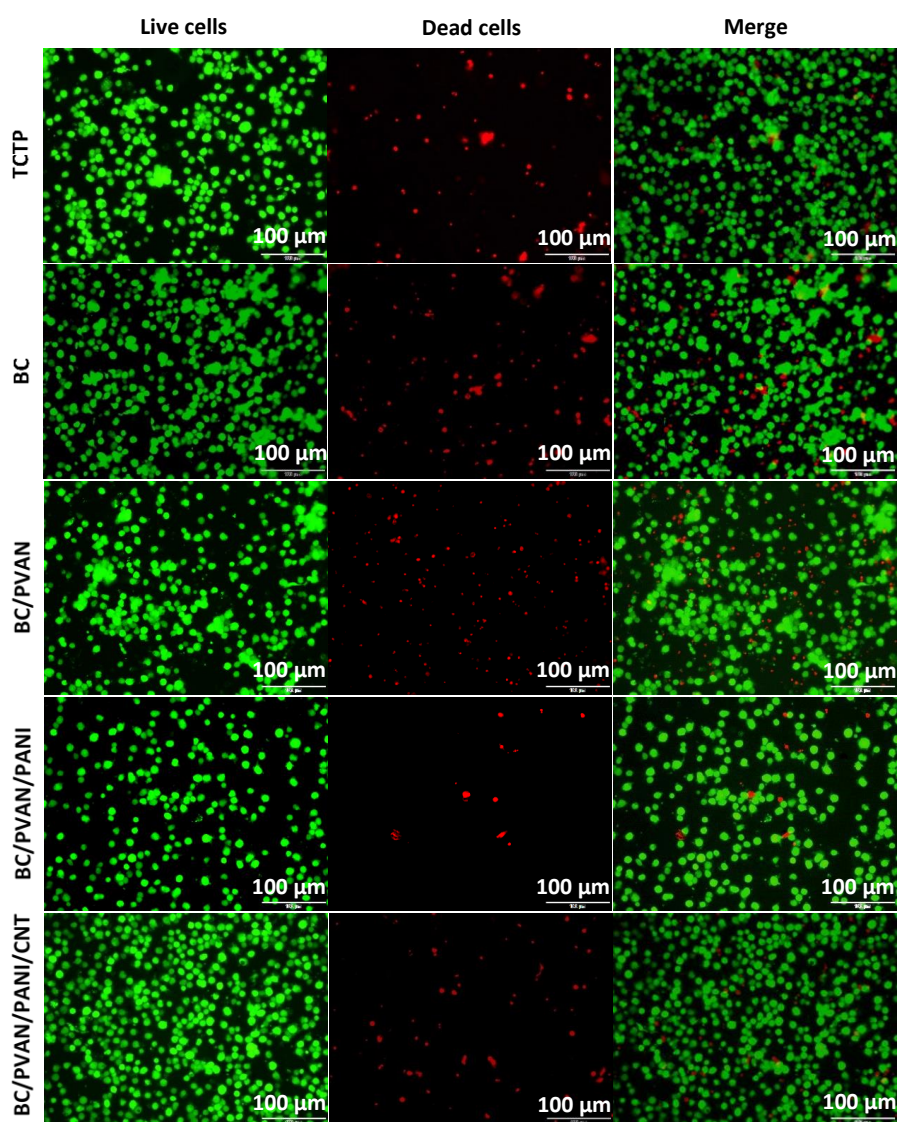


Figure 8.7. Live (green) and dead (red) stained SVZ cells, and corresponding merge images, using calcein-AM and propidium iodide, respectively, after 7 days of incubation with TCTP, BC, BC/PVAN, BC/PVAN/PANI and BC/PVAN/PANI/CNT's substrates.

The cell viability and cell number relative to the TCTP are shown in Figure 8.8a,b. 1×10^4 cells per cm^2 were seeded equally to all BC composites and TCTP. After 7 days of culture, over 80% of cells were viable in all conditions, reaching up to approximately 90% of viability on PANI- and CNT-reinforced BC, which suggests the substrates are not cytotoxic. However, there was an apparent lower cell number ($p < 0.05$) on BC/PVAN/PANI nanocomposites compared to that of control TCTP (Figure 8.7 and Figure 8.8b). However, after CNT reinforcement, this effect was not perceptible ($p < 0.05$)

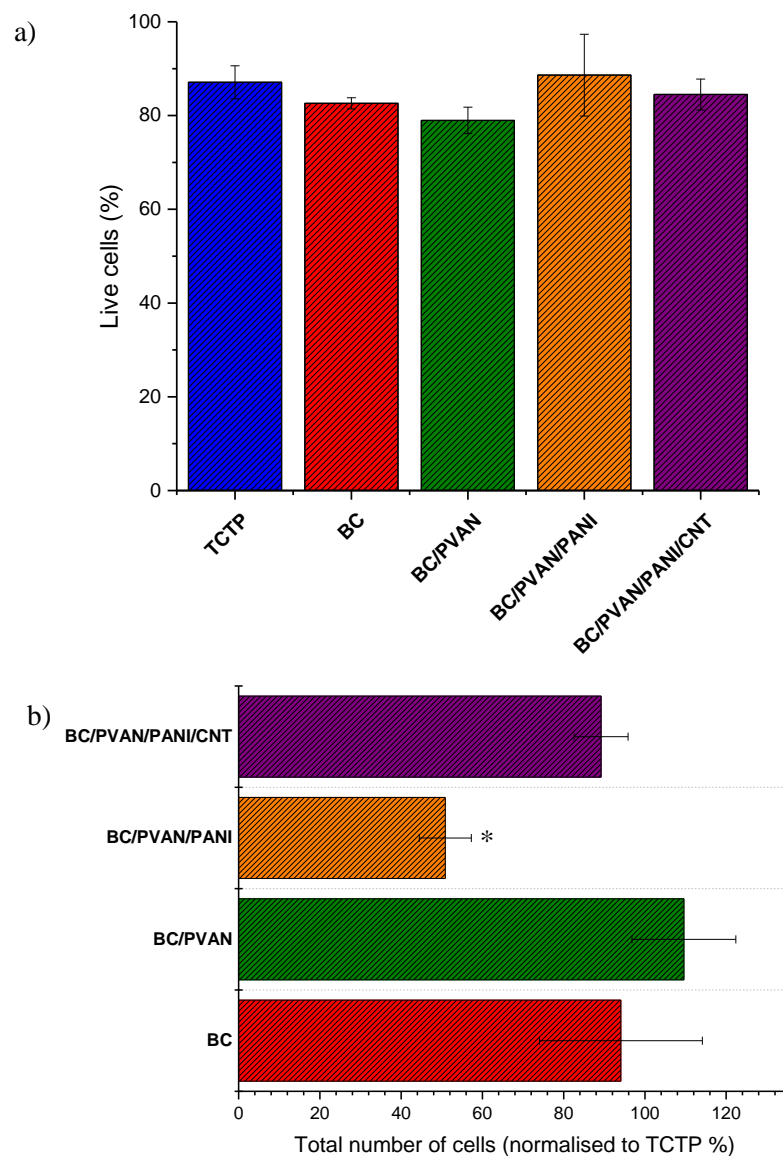


Figure 8.8. Viability of SVZ cells, as determined with LIVE/DEAD assay, after 7 days of culture with pristine BC and BC composites. a) Percentage of viable (live) cells and b) percentage of total number of cells relative to TCTP, with standard deviation error bars. Statistical significance between the different substrates (groups) tested is denoted as $*p < 0.05$, according to one-way ANOVA testing.

Despite these observations, it is very promising to see that almost 90% of cells were viable on BC/PVAN/PANI and BC/PVAN/PANI/CNTs nanocomposites. Further, a considerably higher cell number on BC/PVAN composites indicates PVAN provided good support for cell proliferation, that could be attributed to the enhanced surface hydrophilic properties, that may have also led to an improvement of the cell viability of the BC membranes containing PANI and CNTs [108]. This suggests that the electrically conductive BC nanocomposites with enhanced conductivity did not cause any cytotoxicity to SVZ cells.

Cell Differentiation

Neural differentiation was accomplished in the presence of the BC nanocomposites, which were incubated with SVZ cells for 7 days with NGF-enriched differentiation medium. ECM coating (laminin-based protein) was added to all substrates (coverslip and BC-based membranes) 1 hour before harvesting to facilitate cell adhesion and subsequent differentiation. Early cell differentiation stage was checked at two set time points (2 hours and 24 hours) using CFSE dye, and later differentiation stage was analysed on the last day of culture through immunostaining with β -tubulin III and α -GFAP for specific detection of neurons and glial cells, respectively. Induced cells on BC and BC nanocomposites were accordingly compared with those on coverslip (Figure 8.10).

Initial cell extensions sprouting from soma can be seen in Figure 8.9 shortly after seeding (2 hours), evincing well-adhered neural cells at early differentiation stage. Following 24 hours, cell processes became progressively longer and particularly pronounced on PANI- and CNT-treated BC membranes, which suggests the occurrence of neuronal maturation. Despite a lower cell density observed on conductive BC nanocomposites as expected from the previous results, the number of differentiated cells was significantly higher on BC/PVAN/PANI and BC/PVAN/PANI/CNTs ($p < 0.05$), in which approximately 70% and 80% of cells respectively, successfully developed neurites, in contrast with a modest 50% on coverslip and BC. This indicates the differentiation degree was particularly expressive on the electrically conductive substrates, on which the neural phenotype was preserved till the end of the culture period. In fact, neurite length on PANI- and CNTs-reinforced membranes is significantly higher ($p < 0.05$) from that measured on pristine coverslip

and BC ($<53 \mu\text{m}$) for all selected set time points, showing the most impressive neurite outgrowth on BC/PVAN/PANI from $56 \pm 15 \mu\text{m}$ after 2 hours up to $115 \pm 24 \mu\text{m}$ after 7 days (Figure 8.9).

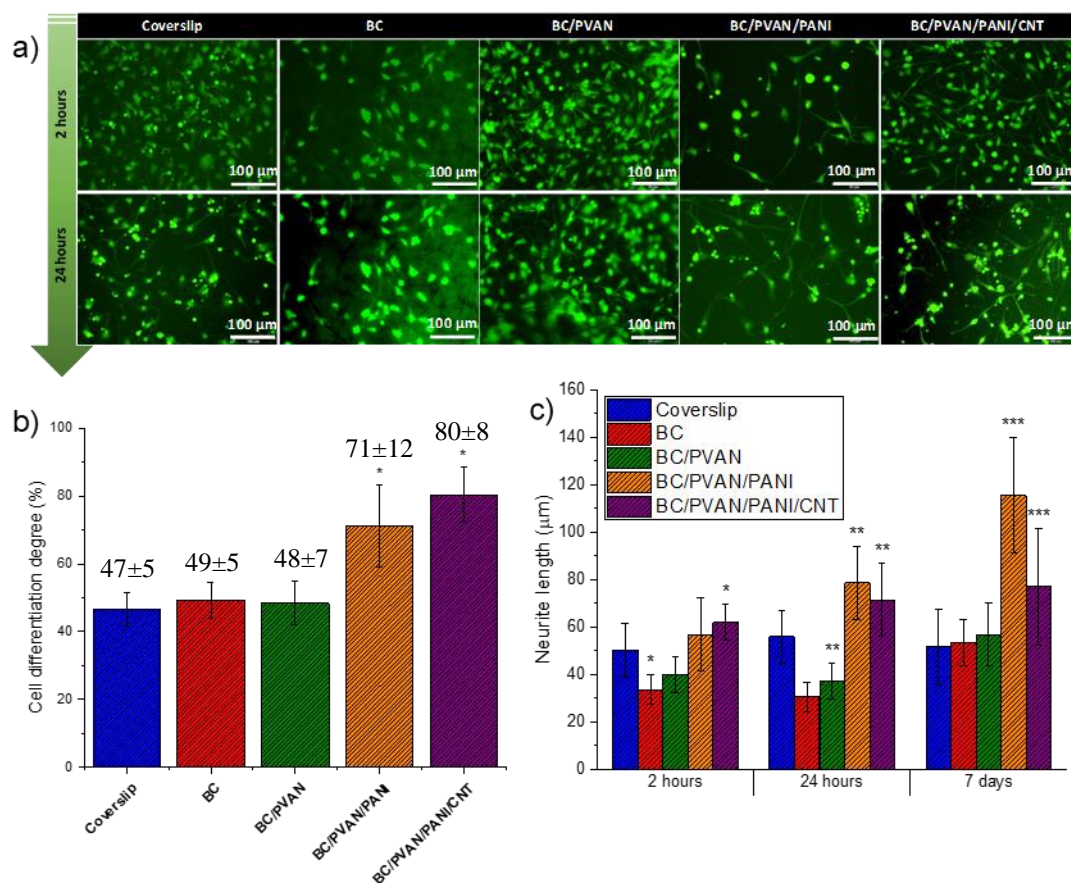


Figure 8.9. Neural differentiation of SVZ cells on different substrates over time. a) Induced cells labelled with CFSE after 2 hours and 24 hours of harvesting on coverslip, BC, BC/PVAN, BC/PVAN/PANI and BC/PVAN/PANI/CNTs substrates. b) Differentiation degree (%) on the 7th day of culture as determined differentiation on the different substrates. c) Neurite length evolution measured at different cultured periods (2 hours, 24 hours and 7 days). * $p < 0.05$ denotes statistical significance compared to coverslip, according to one-way ANOVA testing.

Immunostaining performed on the last day of culture corroborated these findings, showing positive expression of mature neural markers, β -tubulin III and α -GFAP (Figure 8.10). Compared to the induced cells on coverslip and BC, stronger expression of β -tubulin III can be seen on BC/PVAN/PANI and BC/PVAN/PANI/CNTs nanocomposites, which implies superior neuronal

differentiation. Despite the higher cell number seen on coverslip and BC/PVAN, it is evident that conductive BC-based composites promoted statistically higher differentiation degree with very well-developed neurons and extended neurites compared to other conditions, as concluded before. Furthermore, from Figure 8.10 it seems that more cells were preferentially differentiated into neurons (GFP) on conducting membranes, whereas in other conditions astrocytes (RFP) were the predominant neural lineage. This neuronal prevalence on BC/PVAN/PANI and BC/PVAN/PANI/CNTs was already suggested with PC-12 Adh cells. These new functional properties of BC nanocomposites may act as exogenous factors to trigger neuronal differentiation and stimulate the growth of well-developed axons (Figure 8.8). On BC/PVAN/PANI/CNTs, neurite outgrowth was slightly lower in comparison with BC/PVAN/PANI, measuring up to $76 \pm 25 \mu\text{m}$ at the end of the culture period.

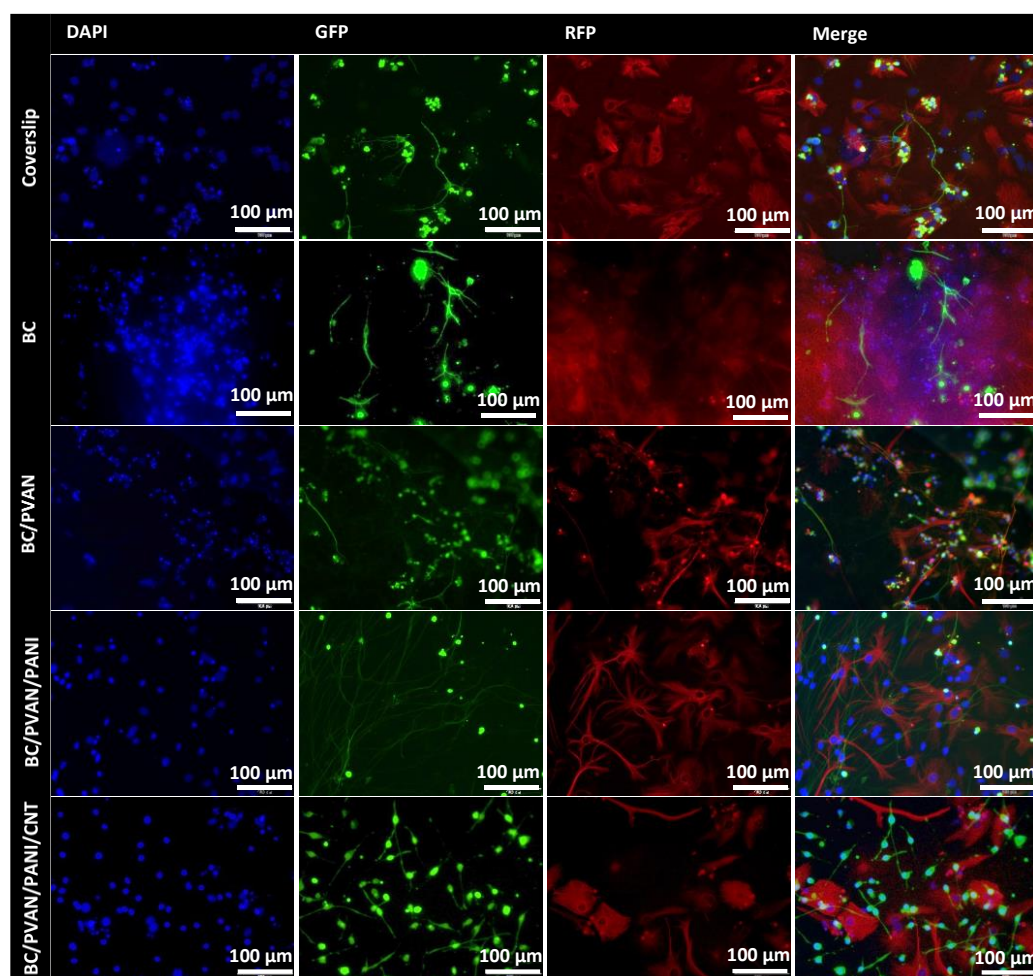


Figure 8.10. Immunofluorescent images of differentiated SVZ cells into neurons (GFP) and glia-like cells (RFP) cultured on BC, BC/PVAN, BC/PVAN/PANI, BC/PVAN/PANI/CNTs and coverslip for 7 days. Cell nuclei are stained in blue (DAPI) with merged pictures on the right.

8.2 DISCUSSION

BC has a long track record of accepted biocompatibility for a wide range of biological systems. Results from multiple studies performed both *in vitro* and *in vivo*, has led to be approved by US FDA for uses in biomedical applications. Some of the factors contributing to the outstanding biocompatible properties of BC are the non-cytotoxicity, high hydrophilicity and surface area, interconnected porosity with appropriate pore size for cell migration and flow of nutrients and oxygen, which makes BC an exceptional candidate for developing hybrid biocompatible electronic devices upon appropriate functionalisation. Therefore, for biological authentication of the as-prepared electrically conductive BC nanocomposites, the biocompatibility was initially tested in terms of cell viability and differentiation ability *in vitro* using secondary (PC-12 Adh) and primary (SVZ) cell models, with later demonstration of the mechanistic of the functionalised BC as neural interfaces.

8.2.1 Different Cell Models for Cytocompatibility of BC-based Nanocomposites: PC-12 Adh versus SVZ

Neural cells isolated from pheochromocytoma have been widely used as a standard secondary cell line for biocompatible trials, as regards neurotoxicological and neuronal differentiation studies. These cells are immortalised and as such, they can continuously grow, being able to acquire some of the intrinsic properties of sympathetic neurons when exposed to NGF, and hence, it serves as a useful comparison model [272]. An adherent variant, PC-12 Adh, was used to favour the adhesion and growth on the substrates. However, primary cells are often preferred owing to the non-immortalised characteristics and thus, a closer reproducible behaviour to that *in vivo* [273]. Therefore, neural stem cells isolated from the subventricular zone of the brain were also used for a more reliable comparison. SVZ cells are present in both embryonic and adult brains, showing ability to undergo differentiation into nerve cells (neurons) and several types of neuroglia (supporting elements), such as astrocytes, oligodendrocytes and ependymal cells, which makes them a powerful model of study [274].

Cell adhesion, proliferation and differentiation are strongly dependent on the surface properties of the material, that must comprise characteristics like hydrophilicity, certain degree of topographical features (roughness) yet sufficiently

smooth, and with functional and biomolecules cues, such as ECM, and other proteins and molecules.

In the first series of experiments, cell viability of PC-12 Adh cells was assessed with PrestoBlue® assay. PrestoBlue® reagent can estimate the number of live cells by measuring their mitochondrial metabolism activity, from which resazurin is reduced to resofurin, that can be detected via changes in the OA [275]. High metabolic cell activity implies higher resazurin conversion rate, and hence, elevated absorbance intensities. Therefore, higher OAs can be in principle ascribed to higher cell number, whereas lower OA indicates lower cell number. Based on these assumptions, cell activity on BC-based nanocomposite substrates seemed to be comparable to that on BC and TCTP, with demonstrated propensity to support cell adhesion, growth and differentiation. Particularly higher cell number was observed on PVAN-functionalised BC, which was corroborated with the data from SVZ cells. This may be related with the surfactant properties of PVAN that can lead to an improvement of the hydrophilicity of the overall material, and decreased number of PANI aggregates with homogeneous distribution (discussed in Chapter 5), which is especially important for the cell attachment of adherent cells like PC-12 Adh [276]. Hydrophilic surfaces, differences in electrical charge and wettability represent crucial factors for cell adhesion and subsequent growth [277]. However, it seems the intrinsically hydrophobic nature of PANI [278] did not impede greatly cell attachment, but low proliferation rate was detected for both cell types. The possible existence of some remaining chemicals left upon PANI synthesis may be underlying the low cell density witnessed, despite the several purification steps performed, which were relied on neutralisation and mass diffusion. In particular, Cl^- ions, as seen in XPS and SEM/TEM-EDX mapping (Chapter 5, sections 5.3 and 5.4), may be related to the possible existence of HCl that may not have been completely neutralised, creating an acidic environment which is cytotoxic [279]. Some unreacted aniline monomer and other oligomers may have also been retained within BC network, contributing to reduce further the cell growth rate. However, additional tests need to be performed to confirm this, as the results showed not to be statistically significant. Upon CNTs-reinforcement of BC/PVAN/PANI nanocomposites (BC/PVAN/PANI/CNTs), a trend for a slightly higher proliferation rate of both cell types could be observed. This fact may be due to the surface nanofeatures of CNTs, that provided a smoother but still

rough surface with a larger area for cell attachment than that of BC/PVAN/PANI [280]. Although SVZ cells were maintained under nonadherent conditions unlike PC-12 Adh cells, it has been demonstrated that the surface features of the substrate play a crucial role on cell growth, including SVZ cells that can grow as adherent monolayers subject to surface coating treatments [281]. Nevertheless, the results showed that the inclusion of CNTs did not affect negatively the cell viability of the BC-based nanocomposites but apparently facilitated cell-cell interactions and cell-substrate [282].

Despite a certain degree of inhibition seen of the seeded cells on PANI-based nanocomposites, both cell types attached in close contact with the substrate under induced differentiation conditions without neurogenesis being compromised. Similar to what was concluded for the cell viability tests, the relative low cell density observed during the culture period on BC/PVAN/PANI and BC/PVAN/PANI/CNTs was attributed to the reported poor hydrophilic properties of PANI and excessive surface roughness (Chapter 5), which may have prevented a portion of the cells to fully establish contact points with the substrate [283]. Comparable effect has been already reported when high PANI concentrations were used, which is anticipated to be related with the formation of big aggregates that increased the roughness heterogeneity and that could further enclose unreacted chemicals difficult to be completely removed [284]. At the same time, there are also evidences that a suitable surface roughness, at nano- and microscopic scale can create a heterogeneous surface energy distribution that, along with its electrical properties, may have favoured the neurogenesis of the attached cells witnessed on these substrates [271]. In fact, neuronal differentiation with well-developed neurites was superior on BC/PVAN/PANI and BC/PVAN/PANI/CNTs than on pristine BC; whereas unmodified BC and BC/PVAN membranes facilitated cell adhesion and stimulated cell proliferation of most of the cell population, which was particularly evident on BC/PVAN. BC/PVAN was also able to support cell differentiation, with higher differentiation degree and neuritogenesis than on BC, yet lower than on the electrically conductive substrates. These observations were frequently noticed for both PC-12 Adh and SVZ cells. The existence of charge carriers arising from both PANI and CNTs may have interacted with the ionic exchanges taken place at the cell membrane. This can generate electrical currents with a spatial

distribution of surface potentials which can act as an exogenous factor to trigger cell differentiation and thus, as a differentiation regulator [284].

8.3 CONCLUSION

The cytocompatibility of the BC nanocomposites was successfully assessed using two different neural cell models. Overall, the cellular responses of both PC-12 Adh and SVZ cells to unmodified and functionalised BC membranes were similar, which strengthened the results obtained and further confirms the suitability of PC-12 Adh cells as a model for cell viability and differentiation studies. The cellular friendly characteristics of neat BC benefited cell viability of BC-based nanocomposites, which was apparently improved with the presence of the PVAN grafted layer. Although lower cell density was seen on PANI-based membranes, no statistical differences could indicate generated cytotoxic effects. Moreover, neuronal differentiation was further encouraged on electrically functionalised BC-based composites than on non-functionalised ones, ascribed to the topographical electrical features, particularly demonstrated with SVZ cells. The results presented suggest the electrically conductive BC nanocomposites are not cytotoxic and can support and regulate neuronal differentiation.

Chapter 9: Conclusions and Future Recommendations

9.1 CONCLUSIONS

Electrically functionalised BC-based nanocomposite membranes with enhanced electrical conductivity and biocompatibility were successfully developed to eventually act as TENIs to detect and record electrical signals from the nervous system and/or artificially stimulate it. The fabrication of such devices requires the uses of biocompatible materials, in addition to the acceptable good electrical conductivity, long-term mechanical support and efficient bidirectional transducing paths between an electrical equipment and a biological structure.

BC has very interesting characteristics featuring a 3D network with high-water holding capacity, that is certified by US FDA for several biomedical applications. Owing to its 3D nanofibrillar nature with high surface area, the BC matrix can efficiently accommodate a diverse range of electroactive moieties, such as PANI and CNTs, to furnish BC with electrically conducting properties while affording physical support and taking advantage of its mechanical flexibility. With water comprising about 98% of the BC structure, slight changes to its content can be used to tailor specific behaviours according to the desired requirements, including the mechanical and electrochemical properties. In addition, and contrary to what has been overall accepted, never-dried pristine BC has also a measurable conductivity attributed to a proton source. This was imparted by the existing liquid (water), imbedded in the 3D network with large surface area, that increases the conductivity and the charge capacitance. Variations in the water content, and possibly in other electrolytes/solutions, may be controlled with the proposed model for the dehydration process of BC.

The electrically conductive properties were introduced to BC with a grafted PVAN/PANI bilayer achieved through SI-ATRP and COP in a three-step reaction. The chemical analysis confirmed the actual composition of PVAN/PANI which had been grafted onto BC nanofibres. The electrical properties of the newly developed BC membranes are closely related to the supramolecular PANI structures produced during

the chemical reaction. The PVAN interlayer inserted between PANI and BC enabled an increase of PANI yield with a more homogeneous distribution of its structural units in the form of nanorods-like shape, which could also be strengthened through denser PVAN brushes. This could be potentially applied onto other relevant substrates.

The polymerisation process employed to incorporate PVAN/PANI bilayer could be chemically controlled and optimised to achieve the desirable properties. It was found that the PVAN interlayer increased the conductivity of PANI-coated BC membranes in one order of magnitude, yielding BC/PVAN/PANI nanocomposites with a maximum electrical conductivity of $(4.5\pm 2.8)\times 10^{-2}$ S.cm⁻¹ when higher VAN monomer contents, HCl and aniline concentrations were used for extended reaction times. The grafting of CNTs in the modified BC matrix, accomplished with a simple dipping/drying process, further improved the electrical conductivity of the nanocomposites to a highest value up to $(1.3\pm 0.4)\times 10^{-1}$ S.cm⁻¹, showing also the largest charge storage capacity measure at 0 V of 54 ± 3 mF at low frequencies in contrast to 1.5 ± 0.2 μF measured on BC/PVAN/PANI due to the strong π - π interactions between PANI and CNTs and the high aspect ratio of CNTs structure. Furthermore, the PVAN/PANI coated BC nanocomposites were proven to be thermally stable up to nearly 200 °C, which could be extended to 234 °C after CNTs-reinforcement, confirming the suitability of the materials for both electronics and human body environments. Also, the weight loss was significantly reduced for a wider temperature spectrum. The different electrochemical responses to voltage changes arising from charge-transfer redox reactions indicated these nanocomposites can offer the quality and performance of smart materials. With this unprecedented electrochemical behaviour, electrically functionalised BC composites may act as an amplification mechanism for analysis and detection of electrical biosignals used in a wide range of biosensors, drug-delivery systems and TE scaffolds. The neurotoxicological and differentiation studies conducted with PC-12 Adh and SVZ cells ensured these BC-based nanocomposites may be safely utilised in biological environment, providing suitable cellular growth (over 80 % for SVZ cells) and functions (neurites as long as 115 ± 24 μm). Though, additional tests may be needed in order to verify potential strategies to improve the biocompatibility. Further, the optimal functional performance can be achievable to fulfil the specific biological requirements. This will be crucial to ultimately move forward with future prototypes and initial clinical trials.

9.2 FUTURE RECOMMENDATIONS

9.2.1 Potential Applications

On the basis of a multi-layered structure, the BC/PVAN/PANI/(CNTs) nanocomposites, developed by enclosing BC membrane within two electrically conductive coatings of PANI and CNTs enhanced with a PVAN interlayer, can be considered for constructing a bioelectronic device capable of stimulating and monitoring neural activity from BC/PVAN/PANI/(CNTs)-neuron interface. The possible switch of the electrochemical performance of PANI caused by redox reactions, as demonstrated in this study in Chapter 6 can act as pathway for appropriate signal amplification. PVAN interlayer can provide not only the desirable morphological and electrical properties of PANI coated on BC but it may also significantly improve the biocompatibility and tissue regeneration (Chapter 8). The extra CNTs layer strengthens the electrical properties, which has morphological nanofeatures demonstrated to enhance also cell adhesion, growth, while promoting neuronal differentiation. Also, with the excellent thermal stability as shown in Chapter 7, such CNTs-reinforcement can retard the overall thermal degradation of the BC nanocomposites. This ensures thermal feasibility from electronic and biological point of views.

Such electrically conductive system furnishes support for cell adhesion and growth by means of a substrate with suitable interconnected porosity and pore size provided at the first instances by the porous BC matrix (Chapter 4), enabling cell migration, and proper flow of nutrients and oxygen. Despite the non-conducting properties of BC, this peculiar matrix was shown to allow the passage and accumulation of charge carriers arising from PANI and CNTs. Also, the richness of BC in hydroxyl groups bounded to water/electrolyte and 3D arrangement may have contributed with protonic conductivity (Chapter 4), that is considered to actively interact with the surrounding environment and raise new electrochemical features, as discussed in Chapters 6 and 7.

It is therefore believed this may well perform and act as biosystem for building neural interfaces, by effectively detecting, recording and amplifying electrical signals from neurons. Ionic currents are established across the cell membrane of a neuron during an action potential (nerve impulse), which cause changes to ion concentrations

at both intra- and extracellular media. This generates a differential potential and hence, an electrochemical current at the surface membrane–electrolyte interface. Thus, the conductive PANI/CNTs surface layers can detect nerve impulses caused by ionic depolarisation of a neuron during an action potential. This generated ionic current may subsequently be converted into an electrical signal (transduction) and transmitted with aids of the excellent mass diffusion capacity of BC network, to be readable with a externally connected electrical device, as schematically represented in Figure 9.1.

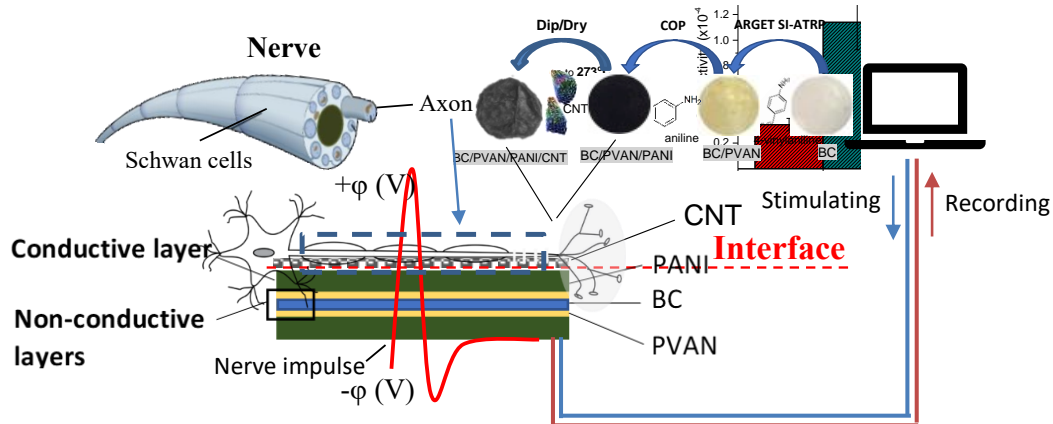


Figure 9.1. Schematic representation of flexible electrically conductive BC/PVAN/PANI/CNTs nanocomposite membranes, biologically interfacing with neurons for efficient nerve impulse conduction (Reproduced by permission from Carbohydr Polym, Elsevier, [188] copyright 2019).

Other possible biomedical applications can also be considered owing to the smart electrical behaviour of these flexible nanocomposite membranes, including drug-delivery systems, biosensors, wound dressings, TE and pacemaker devices (Figure 9.2). The micro- and nanoscopic dimensions of the biological components demand electrically conductive nanostructured materials to enable high sensitivity and performance for different biomedical devices.

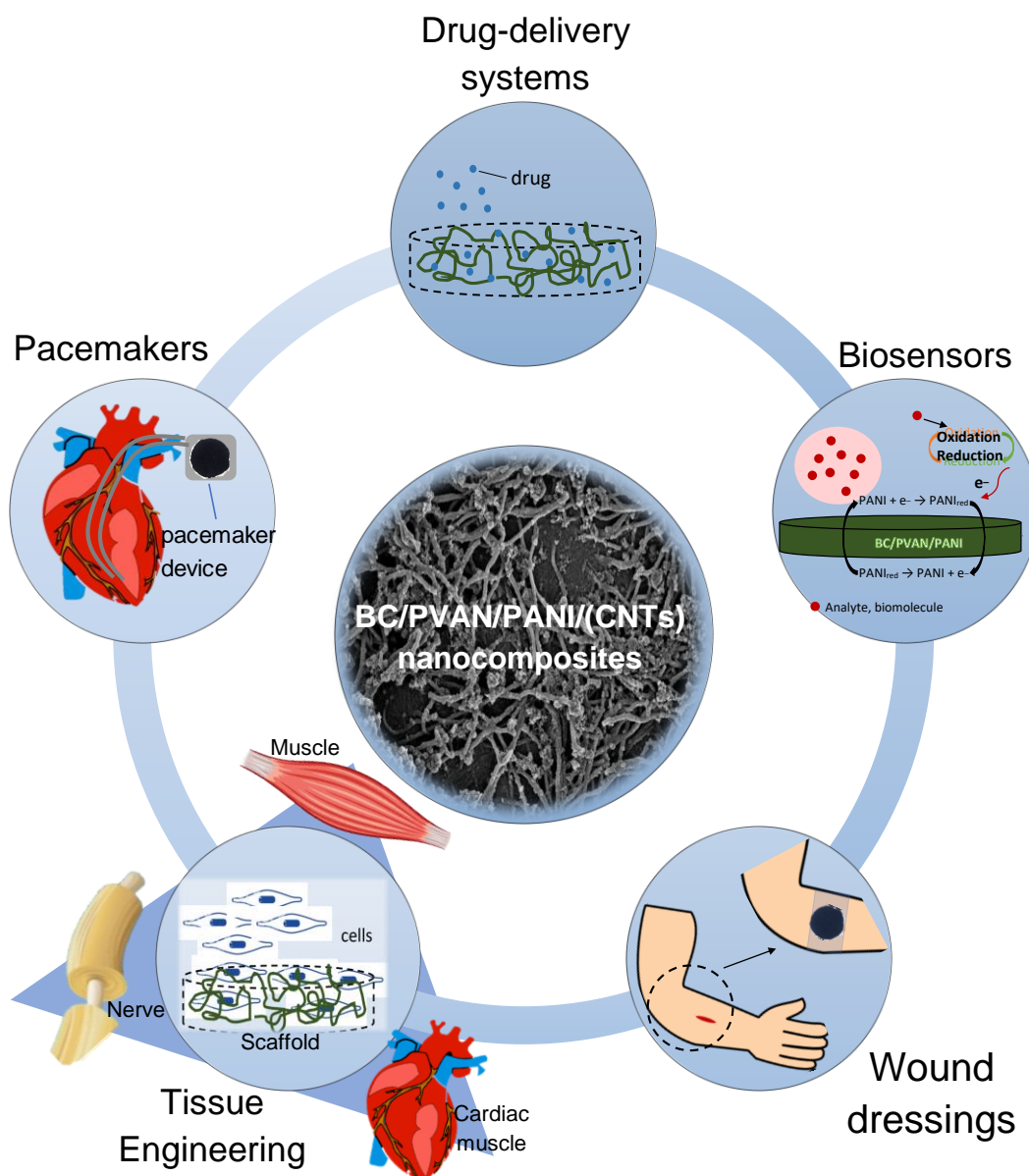


Figure 9.2. Examples of other potential biomedical applications of the as-developed electrically conductive BC nanocomposites as drug-delivery systems, biosensors, wound dressings, tissue engineering scaffolds and pacemakers.

For instances, BC/PVAN/PANI/(CNTs) nanocomposites can be used as drug-delivery systems owing to a nanofibrillar BC network that can efficiently encapsulate drugs, cells or other analytes within its porous 3D nanostructure and controllably be released upon a deliverable electrical stimulus, that induces the switching of the electrical behaviour of the PANI coating. As biosensors, these nanocomposites may efficiently detect an analyte or a physicochemical compound with aids of biological component integrated in the material to produce a measurable signal via biochemical

changes of the biomolecules that may induce redox reactions to PANI, to be later transduced into either amperometric or impedimetric responses. With similar mechanistic to neural interfaces, pacemakers may be built to control abnormal heart rhythms. The depolarisation and repolarisation of myocytes caused by different permeabilities to sodium, potassium and calcium generates an electrical current that can be detected by changes to the oxidation states of PANI layer and trigger an appropriate response through a pulse generator [285]. In TE applications, porous and electrically conductive nanofibrous membrane can act as tissue scaffolds to promote the regeneration of damaged tissue to fully recover its original functions. Such porous structure allows the revascularisation of the injured site, providing adequate flow of nutrients and migration of ‘first-aid’ cells, which accelerates tissue reconstruction. Scaffolds empowered with electrically conductive properties are demonstrated to offer advantages to regenerative processes of electrically-sensible tissues, including nerves, skeletal and cardiac muscle, and also bones [286]. Other possible applications involve wound dressings that combines the high-water holding capacity of BC with anti-bactericidal properties of PVAN/PANI/(CNTs) coating either by simply controlling PANI doping level or with controlled drug release [287]. Further combination of TE scaffolds with the other aforementioned applications can produce hybrid systems, which aims to overcome the major drawbacks of many bioelectronic devices currently available.

9.2.2 Improving the Biofunctional Performance

Despite the positive biological responses (Chapter 8), additional strategies must be followed to address the biocompatibility and functional requisites of these electrically conductive BC-based nanocomposites in order to fully exploit their advantages in the biomedical field, especially as regards neural interfaces. Based on this work and the published literature, this can be accomplished through continuous optimisation of the synthetic procedures to reach the desirable characteristics with later incorporation of biomolecular cues and cells. It will be critical to corroborate such results and complement them with other characterisation techniques.

According to William D. *et al* [288], ‘biocompatibility’ can be defined as “the ability of a material to perform well with an appropriate host response in a specific application”. Although a sustainable cell growth was noticed on the as-developed

PANI-containing BC nanocomposites, relatively low cell density was recurrently observed to both cell types. This effect could be attributed to the poor wettability properties of PANI, incomplete purification process and the highly heterogeneous surfaces, impeding proper cell attachment and hence, limiting the cell growth and differentiation. Some approaches were followed to prevent these limitations particularly raised from the surface properties of PANI agglomerates, that are commonly described in the literature. A PVAN interlayer was added on BC to ameliorate the conductivity of the post-grafted PANI, and may have contributed to increase the hydrophilicity of nanocomposite membrane with the dispersion of PANI particles into a more uniform coating. Also, washes were performed with appropriate solvents in the end of every reaction step, the acid used was neutralised after COP and dialysis was performed for one week.

Other steps may be followed in future research to lead to improvements in the cytocompatibility of the BC-based nanocomposites. One is the refinement of the purification steps for efficient removal of all chemicals and contaminants. PANI-based BC membranes were thoroughly washed with ethanol to dissolve any adsorbed PANI salt (emeraldine) and unreacted aniline monomer. However, other possible oligomers raised upon COP reaction may not be completely soluble in ethanol, as the solubility of these oligomers differs from that of emeraldine. Therefore, other solutions, such as N-methylpyrrolidinone (NMP) and n-dimethylsulfoxide [289] can be used to eliminate by-products of PANI synthesis. Other strategy relies on tuning the wettability surface properties of PANI emeraldine salt to acquire hydrophilic characteristics so that additional contact points between cells and the substrate can be established. It has been identified that the hydrophilicity of PANI is different according to its oxidation forms and it can be improved with the doping/dedoping process, i.e. by repeatedly converting emeraldine to leucoemeraldine, and vice-versa, without electrical conductive properties losses [278]. Furthermore, the reprotonation of PANI with other acids rather than HCl, such as DBSA [290] and phosphoric acid [291], has shown to increase the hydrophilicity of PANI. However, such properties need to be confirmed via contact angle measurements and complemented with other surface analysis, so that they can be adjusted accordingly to cellular requirements. The morphology of PANI-grafted BC membranes is another aspect that must be considered, since it can dramatically change the cell behaviour, but also the overall PANI properties of the composite. This

is particularly important, since the optimisation of the surface properties of PANI is anticipated to benefit both biological and electrical responses. The highly heterogeneous surface of PANI-based membranes compared to pristine BC, was seen in Chapter 5. Providing a more regular surface at nanoscale is expected to favour the focal contacts of cells with the substrate (better adhesion), as well as a more efficient circulation of the charge carriers (boosted conductivity). Although the grafted PVAN interlayer has led to a significant dispersion of PANI on the BC nanofibrils, the synthesis process, especially as regards that of PANI, still needs to be finely tuned. Continuous optimisation of the COP parameters must be carefully studied and developed further. In particular, as shown from this study, enabling longer reaction times and increasing aniline concentration may promote well-defined and more regular nanofibres structures with reduced dimensions, hence high-aspect-ratio. Different synthetic processes like interfacial polymerisation and template-assisted methods can be explored, and complemented with usage of other acids and oxidants that are known to favour the formation of more homogeneous PANI grafts. Yielding higher PVAN grafts and optimising its synthetic route on BC can also be reviewed. Owing to the high oxygen-reactivity of the SI-ATRP process, BC membranes must be subjected to solvent-exchange from water to oxygen-free solvents, that in the case of membranes, was only achievable by complete pre-dehydration. Customisation of this process as such that it can allow certain amounts of water, would be advantageous to fully exploit the potentials of BC-graft-PVAN, since the drying process inevitably affects the original structure of BC. In fact, certain amounts of water may be acceptable in ATRP; however, the problem relies mostly on the first step with the immobilisation of the initiator (BiBB) onto BC. Proper identification of non-water reactive initiators or other initiating paths that can efficiently act on never-dried BC membranes, can provide huge advances not only in the materials' properties, but also in chemistry. Investigation of solvent-exchange methods on never-dried BC membranes combined with the dehydration model of BC applied to other solvents/electrolytes, will possibly lead to improvements of the electrochemical properties of BC-based nanocomposites.

Despite no explicit cytotoxic signs were attributed to CNTs in this work, contrasting biological responses have been associated to its use. While its nanosized dimensions with large aspect-ratio may favour the cytocompatibility, this can also boost the adverse effects, as such nanosubstances can be more effectively absorbed by

cells if released in the host environment. Therefore, long-term acute effects must not be neglected when using CNTs, and nanomaterials in general. Dose-dependent toxicity is one important aspect that can be addressed by limiting the amount of loaded CNTs to that strictly necessary. For instances, through other routes to more efficiently incorporate CNTs into BC substrate, such as *in situ* synthesis of BC with CNTs added directly in the culture medium. More refined purification processes and pre-modification of CNTs, e.g. with biomolecules, may be needed, as most of the toxicological effects ascribed to CNTs are in fact arisen from the existing impurities, such as the catalyst and dispersant/surfactant.

The micro- and nanotopographical features of the BC composites and its electrical surface distribution must be carefully assessed, so that more reliable conclusions can be drawn for following steps. Such analysis must be supplemented with the evaluation of the mechanical properties (tensile and bend strengths) and electrical stability of the whole composite over time. For instances, the designed model for BC dehydration can be implemented to optimise further the mechanical and electrochemical properties. As an implantable medical device, these developed membranes have to withstand the forces and fluids naturally occurring in the human body. The electrochemical behaviour of the material and other possible interactions may occur while implanted in contact with the body fluids, which can be easily assessed in PBS solution loaded with some proteins to simulate the biological environment and adapt if needed. Electrostimulation tests *in vitro* may allow to draw some important conclusions about the electrical performance and potential beneficial effects for cells, especially neuronal differentiation and cell guidance, which *in vivo* would be shown in new well-oriented nervous tissue. The degradation of the materials must be assessed over time in PBS, to predict the stability of BC composites in the body and possible release of substances that may be toxic for cells.

A final remark is concerned with the incorporation of cells and modification of the surface with biomolecules naturally present in nervous tissue, that are mostly components of the ECM matrix. This will be valuable for improving the biocompatibility in terms of bimolecular recognition and cell proliferation, since cells respond primarily to the adsorbed proteins, rather to the surface itself.[292]. Thus, an efficient cell adhesion with multiple anchoring sites and cell differentiation can be promoted with the presence of ECM coating. Particularly on BC/PVAN/PANI/CNTs

nanocomposites, with the smooth and large surface area of CNTs, a better interaction between ECM and CNTs can be obtained. Putting these strategies into practise can lead to dramatic advances in the biocompatibility and functional performance of the materials to be safely employed in several biomedical devices.

Bibliography

- [1] Wickman F. North Korea ' s “ 2 MB of knowledge ” taunt : How many megabytes does the human brain. *Slate*. 2012; :24–5.
- [2] Rea P. Essential Clinically Applied Anatomy of the Peripheral Nervous System in the Head and Neck. *Essential Clinically Applied Anatomy of the Peripheral Nervous System in the Head and Neck*. 2016. 1-192 p.
- [3] Noback, Charles Robert Strominger N, Demarest R, Ruggiero D. The human nervous system: structure and function. *Springer Sci Bus Media. Humana Press*; 2005; 744:439.
- [4] Schmidt CE, Leach JB. Neural tissue engineering: strategies for repair and regeneration. *Annu Rev Biomed Eng*. 2003 Jan; 5:293–347.
- [5] The Central and Peripheral Nervous Systems | Biology for Majors II. [cited 2018 Sep 20]. Available from: <https://courses.lumenlearning.com/wm-biology2/chapter/the-central-and-peripheral-nervous-systems/>
- [6] Zhang S. Nervous Tissue and Nervous System. *An Atlas of Histology*. New York, NY: Springer New York; 1999. p. 67–109.
- [7] Cuevas J. The somatic nervous system. *xPharm: The Comprehensive Pharmacology Reference*. Elsevier; 2011. p. 1–13.
- [8] The Nervous System | SHEN Centre for Health and Wellness. [cited 2018 Nov 22]. Available from: <http://chw.spiritualeducation.org/phys/nervous-system>
- [9] Bankenahally R, Krovvidi H. Autonomic nervous system: anatomy, physiology, and relevance in anaesthesia and critical care medicine. *BJA Educ*. Oxford University Press; 2016 Nov 1; 16(11):381–7.
- [10] Sternini C. Organization of the peripheral nervous system: Autonomic and sensory ganglia. *Journal of Investigative Dermatology Symposium Proceedings*. 1997. p. 1–7.
- [11] Spinal Cord Anatomy - Parts and Spinal Cord Functions. [cited 2018 Oct 22]. Available from: <https://healthjade.com/spinal-cord/>
- [12] Nervous Tissue. [cited 2018 Nov 22]. Available from:

<http://oerpub.github.io/epubjs-demo-book/content/m46509.xhtml>

- [13] Mescher AL. Junqueira's Basic Histology. 13th ed. Mescher anthony L, editor. Text & Atlas; 2013.
- [14] Frantz C, Stewart KM, Weaver VM. The extracellular matrix at a glance. *J Cell Sci. Company of Biologists*; 2010 Dec 15; 123(24):4195–200.
- [15] Alan G. Brown. *Nerve Cells and Nervous Systems: An Introduction to Neuroscience* - Alan G. Brown - Google Books. Springer London; 1991. 268 p.
- [16] Bioninja. Nerve Impulses | BioNinja. 2018 [cited 2018 Oct 22]. Available from: <http://ib.bioninja.com.au/standard-level/topic-6-human-physiology/65-neurons-and-synapses/nerve-impulses.html>
- [17] Wang X-J, Rinzal J. *The Handbook of Brain Theory and Neural Networks*,| The MIT Press. MIT Press; 2002. 686-91 p.
- [18] Stackexchange. neurophysiology - Why does the intensity of an action potential once generated at the trigger zone remain undisturbed through the axon? - Biology Stack Exchange. [cited 2018 Oct 22]. Available from: <https://biology.stackexchange.com/questions/44154/why-does-the-intensity-of-an-action-potential-once-generated-at-the-trigger-zone>
- [19] SECHER NH. *The Physiology of. J Sports Sci. Elsevier Science*; 1983; 2008(December):187–96.
- [20] Cohen-Cory S. *The Developing Synapse: Construction and Modulation of Synaptic Structures and Circuits. Science (80-)*. 2002 Oct 25; 298(5594):770–6.
- [21] Purves D, Williams SM. *Neuroscience*. Sinauer Associates; 2001.
- [22] Robinson MM, Martin JM, Atwood HL, Cooper RL. Modeling biological membranes with circuit boards and measuring electrical signals in axons: student laboratory exercises. *J Vis Exp. MyJoVE Corporation*; 2011 Jan 18; (47).
- [23] Pinto TM, Wedemann RS, Cortez CM. Modeling the electric potential across neuronal membranes: The effect of fixed charges on spinal ganglion neurons

and neuroblastoma cells. Schulz DJ, editor. PLoS One. 2014 May 6; 9(5):96194.

- [24] Science Source Images - Website. [cited 2018 Oct 22]. Available from: <http://prints.sciencesource.com/>
- [25] Brown AG. Propagation of the Action Potential — The Nerve Impulse. Nerve Cells and Nervous Systems. London: Springer London; 1991. p. 45–52.
- [26] Peripheral neuropathy - Causes - NHS. [cited 2018 Sep 10]. Available from: <https://www.nhs.uk/conditions/peripheral-neuropathy/causes/>
- [27] Kaur S, Pandhi P, Dutta P. Painful diabetic neuropathy: an update. Ann Neurosci. Karger Publishers; 2011 Oct; 18(4):168–75.
- [28] Menorca RMG, Fussell TS, Elfar JC. Nerve physiology: mechanisms of injury and recovery. Hand Clin. NIH Public Access; 2013 Aug; 29(3):317–30.
- [29] Smith JK, Myers KP, Holloway RG, Landau ME. Ethical considerations in elective amputation after traumatic peripheral nerve injuries. Neurol Clin Pract. American Academy of Neurology; 2014 Aug; 4(4):280–6.
- [30] Shoichet MS, Tate CC, Baumann MD, Laplaca MC. Chapter 8 Strategies for Regeneration and Repair in the Injured Central Nervous System Strategies for Regeneration and Repair in the Injured Central Nervous System. Indwelling Neural Implants: Strategies for Contending with the In Vivo Environment. CRC Press/Taylor & Francis; 2011. p. 1–19.
- [31] Arslantunali D, Dursun T, Yucel D, Hasirci N, Hasirci V. Peripheral nerve conduits: Technology update. Medical Devices: Evidence and Research. Dove Press; 2014. p. 405–24.
- [32] Cianfoni A. Wallerian degeneration. Brain Imaging with MRI and CT: An Image Pattern Approach. Elsevier; 2010. p. 161–2.
- [33] Martinez de Albornoz P, Delgado PJ, Forriol F, Maffulli N. Non-surgical therapies for peripheral nerve injury. Br Med Bull. Oxford University Press; 2011 Dec 1; 100(1):73–100.
- [34] Robinson LR. AAEM MINIMONOGRAPH 28 TRAUMATIC INJURY TO PERIPHERAL NERVES. Muscle Nerve. 2000; 23:863–73.

- [35] Dahlin LB, Wiberg M. Nerve injuries of the upper extremity and hand. *EFORT open Rev. British Editorial Society of Bone and Joint Surgery*; 2017 May; 2(5):158–70.
- [36] Gu X, Ding F, Williams DF. Neural tissue engineering options for peripheral nerve regeneration. *Biomaterials*. 2014 Aug; 35(24):6143–56.
- [37] Geuna S, Perroteau I, Tos P, Battiston B. Tissue Engineering of the Peripheral Nerve: Stem Cells and Regeneration Promoting Factors. *Int Rev Neurobiol*. 2013; 108:285–323.
- [38] Peripheral nerve injuries - Diagnosis and treatment - Mayo Clinic. [cited 2018 Sep 13]. Available from: <https://www.mayoclinic.org/diseases-conditions/peripheral-nerve-injuries/diagnosis-treatment/drc-20355632>
- [39] Pacemaker implantation - NHS. [cited 2018 Sep 11]. Available from: <https://www.nhs.uk/conditions/pacemaker-implantation/>
- [40] Jaeger D, Jung R, editors. *Encyclopedia of Computational Neuroscience*. New York, NY: Springer New York; 2016.
- [41] Gu X, Ding F, Yang Y, Liu J. Construction of tissue engineered nerve grafts and their application in peripheral nerve regeneration. *Prog Neurobiol*. 2011 Feb; 93(2):204–30.
- [42] Aryan NP, Kaim H, Rothermel A. Stimulation and Recording Electrodes: General Concepts. 2015. p. 1–9.
- [43] Navarro X, Krueger TB, Lago N, Micera S, Stieglitz T, Dario P. A critical review of interfaces with the peripheral nervous system for the control of neuroprostheses and hybrid bionic systems. *J Peripher Nerv Syst*. 2005 Oct; 10(3):229–58.
- [44] Hoffmann KP, Koch KP, Doerge T, Micera S. New technologies in manufacturing of different implantable microelectrodes as an interface to the peripheral nervous system. *Proceedings of the First IEEE/RAS-EMBS International Conference on Biomedical Robotics and Biomechatronics, 2006, BioRob 2006*. 2006.
- [45] Tyler DJ. Electrodes for the Neural Interface. *Neuromodulation*. Academic Press; 2018. p. 239–74.

- [46] Boretius T, Yoshida K, Badia J, Harreby K, Kundu A, Navarro X, et al. A transverse intrafascicular multichannel electrode (TIME) to treat phantom limb pain Towards human clinical trials. Proceedings of the IEEE RAS and EMBS International Conference on Biomedical Robotics and Biomechatronics. 2012. p. 282–7.
- [47] Kim S-J, Manyam SC, Warren DJ, Normann RA. Electrophysiological Mapping of Cat Primary Auditory Cortex with Multielectrode Arrays. *Ann Biomed Eng.* Springer US; 2006 Feb 16; 34(2):300–9.
- [48] Abaya TVF, Diwekar M, Blair S, Tathireddy P, Rieth L, Clark GA, et al. Characterization of a 3D optrode array for infrared neural stimulation. *Biomed Opt Express.* Optical Society of America; 2012 Sep 1; 3(9):2200–19.
- [49] Akay M. Handbook of neural engineering. IEEE Press series in biomedical engineering. Wiley; 2007. 662 p.
- [50] Tyler D, Durand D. Flat interface nerve electrode and a method for use. USA: US Patent; 6456866 B1, 2002. p. 12.
- [51] E. Loeb G. Surgically implantable electrode for nerve bundles. USA: US Patent; 4940065, 1986.
- [52] Kotov NA, Winter JO, Clements IP, Jan E, Timko BP, Campidelli S, et al. Nanomaterials for Neural Interfaces. *Adv Mater.* 2009 Oct 26; 21(40):3970–4004.
- [53] Delivopoulos E, Chew DJ, Minev IR, Fawcett JW, Lacour SP. Concurrent recordings of bladder afferents from multiple nerves using a microfabricated PDMS microchannel electrode array. *Lab Chip.* 2012 Jul 21; 12(14):2540–51.
- [54] Spearman BS, Desai VH, Mobini S, McDermott MD, Graham JB, Otto KJ, et al. Tissue-Engineered Peripheral Nerve Interfaces. *Advanced Functional Materials.* 2018. p. 1701713.
- [55] Sahyouni R, Chang DT, Moshtaghi O, Mahmoodi A, Djalilian HR, Lin HW. Functional and Histological Effects of Chronic Neural Electrode Implantation. *Laryngoscope Investig Otolaryngol.* Wiley-Blackwell; 2017 Apr 1; 2(2):80–93.
- [56] Gao Y, Wang Y-L, Kong D, Qu B, Su X-J, Li H, et al. Nerve autografts and

tissue-engineered materials for the repair of peripheral nerve injuries: a 5-year bibliometric analysis. *Neural Regen Res.* Wolters Kluwer -- Medknow Publications; 2015 Jun; 10(6):1003–8.

- [57] de Ruyter GCW, Malessy MJA, Yaszemski MJ, Windebank AJ, Spinner RJ. Designing ideal conduits for peripheral nerve repair. *Neurosurg Focus.* 2009 Feb; 26(2):E5.
- [58] Esa F, Tasirin SM, Rahman NA. Overview of Bacterial Cellulose Production and Application. *Ital Oral Surg.* 2014; 2:113–9.
- [59] Suopajarvi T. Functionalized nanocelluloses in wastewater treatment applications. Doctoral Thesis. University of Oulu; 2015. 80 p.
- [60] McNamara JT, Morgan JLW, Zimmer J. A molecular description of cellulose biosynthesis. *Annu Rev Biochem.* NIH Public Access; 2015; 84:895–921.
- [61] Abeer MM, Mohd Amin MCI, Martin C. A review of bacterial cellulose-based drug delivery systems: their biochemistry, current approaches and future prospects. *J Pharm Pharmacol.* 2014 Aug; 66(8):1047–61.
- [62] Picheth GF, Pirich CL, Sierakowski MR, Woehl MA, Sakakibara CN, de Souza CF, et al. Bacterial cellulose in biomedical applications: A review. *Int J Biol Macromol.* Elsevier; 2017 Nov 1; 104:97–106.
- [63] Wang Y, Lian J, Wan J, Ma Y, Zhang Y. A supramolecular structure insight for conversion property of cellulose in hot compressed water: Polymorphs and hydrogen bonds changes. *Carbohydr Polym.* Elsevier; 2015 Nov 20; 133:94–103.
- [64] Rouabhia M, Asselin J, Tazi N, Messaddeq Y, Levinson D, Zhang Z. Production of Biocompatible and Antimicrobial Bacterial Cellulose Polymers Functionalized by RGDC Grafting Groups and Gentamicin. *ACS Appl Mater Interfaces.* American Chemical Society; 2014 Feb 12; 6(3):1439–46.
- [65] Cacicedo ML, Castro MC, Servetas I, Bosnea L, Boura K, Tsafrakidou P, et al. Progress in bacterial cellulose matrices for biotechnological applications. *Bioresour Technol.* Elsevier; 2016 Aug 1; 213:172–80.
- [66] Purified Cotton Fiber Manufacturer | Barnhardt Natural Fibers. [cited 2018 Oct 12]. Available from: <https://www.barnhardtcotton.net/>

- [67] PolySacDb. [cited 2018 Oct 12]. Available from:
http://polysac3db.cermav.cnrs.fr/discover_cellulose.html
- [68] Shi Z, Zhang Y, Phillips GO, Yang G. Utilization of bacterial cellulose in food. *Food Hydrocoll.* Elsevier; 2014 Mar 1; 35:539–45.
- [69] Zeng M, Laromaine Sagué A, Vallribera Massó A, Roig Serra A, Barcelona. UA de. Bacterial cellulose: fabrication, characterization and biocompatibility studies. TDX (Tesis Doctorals en Xarxa). Universitat Autònoma de Barcelona; 2014.
- [70] Dalglish T, Williams JMG., Golden A-MJ, Perkins N, Barrett LF, Barnard PJ, et al. Nanocellulose and Sustainability: Production, Properties, Applications, and Case Studies. *Sustainability: Contributions through Science and Technology.* 2007. 23-42 p.
- [71] Li J, Fang L, Tait WR, Sun L, Zhao L, Qian L. Preparation of conductive composite hydrogels from carboxymethyl cellulose and polyaniline with a nontoxic crosslinking agent. *RSC Adv.* The Royal Society of Chemistry; 2017 Nov 27; 7(86):54823–8.
- [72] Jasim A, Ullah MW, Shi Z, Lin X, Yang G. Fabrication of bacterial cellulose/polyaniline/single-walled carbon nanotubes membrane for potential application as biosensor. *Carbohydr Polym.* Elsevier; 2017 May 1; 163:62–9.
- [73] Shi Z, Li Y, Chen X, Han H, Yang G. Double network bacterial cellulose hydrogel to build a biology-device interface. *Nanoscale.* 2014 Jan 21; 6(2):970–7.
- [74] Shi Z, Zang S, Jiang F, Huang L, Lu D, Ma Y, et al. In situ nano-assembly of bacterial cellulose–polyaniline composites. *RSC Adv.* The Royal Society of Chemistry; 2012 Jan 17; 2(3):1040.
- [75] Chawla KK. *Composite materials - Science and Engineering.* Springer New York; 1985. 533 p.
- [76] Kaur G, Adhikari R, Cass P, Bown M, Gunatillake P. Electrically conductive polymers and composites for biomedical applications. *RSC Adv.* Royal Society of Chemistry; 2015 Apr 24; 5(47):37553–67.
- [77] S. Snow E, Perkins FK. *Capacitance and Conductance of Single-Walled*

- Carbon Nanotubes in the Presence of Chemical Vapors. *Nano Lett.* American Chemical Society; 2005; 5(12):2414–7.
- [78] Snow ES, Perkins FK, Houser EJ, Badescu SC, Reinecke TL. Chemical Detection with a Single-Walled Carbon Nanotube Capacitor. *Science* (80-). American Association for the Advancement of Science; 2005 Mar 25; 307(5717):1942–5.
- [79] Hu W, Chen S, Yang Z, Liu L, Wang H. Flexible electrically conductive nanocomposite membrane based on bacterial cellulose and polyaniline. *J Phys Chem B.* American Chemical Society; 2011 Jul 7; 115(26):8453–7.
- [80] Oueiny C, Berlioz S, Perrin F-X. Carbon nanotube–polyaniline composites. *Prog Polym Sci.* Pergamon; 2014 Apr 1; 39(4):707–48.
- [81] Wan H, Song D, Li X, Zhang D, Gao J, Du C. Failure Mechanisms of the Coating/Metal Interface in Waterborne Coatings: The Effect of Bonding. *Materials* (Basel). 2017 Apr 9; 10(4):397.
- [82] Bettinger CJ. Recent advances in materials and flexible electronics for peripheral nerve interfaces. *Bioelectron Med.* BioMed Central; 2018 Dec 23; 4(1):6.
- [83] Fielding LA, Hillier JK, Burchell MJ, Armes SP. Space science applications for conducting polymer particles: synthetic mimics for cosmic dust and micrometeorites. *Chem Commun* (Camb). 2015 Dec 11; 51(95):16886–99.
- [84] Prasad K, Bazaka O, Chua M, Rochford M, Fedrick L, Spoor J, et al. *Metallic Biomaterials: Current Challenges and Opportunities.* Mater (Basel, Switzerland). Multidisciplinary Digital Publishing Institute (MDPI); 2017 Jul 31; 10(8).
- [85] Sapurina Iy, Shishov M. Oxidative Polymerization of Aniline: Molecular Synthesis of Polyaniline and the Formation of Supramolecular Structures. *New Polymers for Special Applications.* 2012. p. 251–312.
- [86] Skotheim TA, Reynolds JR. *Handbook of conducting polymers.* 3rd ed. Skotheim TA, Reynolds J, editors. New York: CRC; 2007. 1680 p.
- [87] Balint R, Cassidy NJ, Cartmell SH. Conductive polymers: towards a smart biomaterial for tissue engineering. *Acta Biomater.* 2014 Jun; 10(6):2341–53.

- [88] Sapurina I, Stejskal J. The mechanism of the oxidative polymerization of aniline and the formation of supramolecular polyaniline structures. *Polym Int.* John Wiley & Sons, Ltd.; 2008 Dec 1; 57(12):1295–325.
- [89] Stejskal J, Bogomolova OE, Blinova N V, Trchová M, Šeděnková I, Prokeš J, et al. Mixed electron and proton conductivity of polyaniline films in aqueous solutions of acids: beyond the 1000 S cm⁻¹ limit. *Polym Int.* Wiley-Blackwell; 2009 Aug 1; 58(8):872–9.
- [90] Molapo KM, Ndangili PM, Ajayi RF, Mbambisa G, Mailu SM, Njomo N, et al. Electronics of Conjugated Polymers (I): Polyaniline. *Int. J. Electrochem. Sci.* 2012.
- [91] Covalent Bonds and Molecular Structure. [cited 2018 Oct 15]. Available from: http://wps.prenhall.com/wps/media/objects/4678/4790506/ch07_12.htm
- [92] Wan M, Yang J. Mechanism of proton doping in polyaniline. *J Appl Polym Sci.* 1995; 55(3):399–405.
- [93] Myasnikov EN, Myasnikova AE, Kusmartsev F V. Coherence of the lattice polarization in large-polaron motion. *Phys Rev B.* 2005 Dec 16; 72(22):224303.
- [94] Silva CHB, Da Costa Ferreira AM, Constantino VRL, Temperini MLA. Hybrid materials of polyaniline and acidic hexaniobate nanoscrolls: high polaron formation and improved thermal properties. *J Mater Chem A.* Royal Society of Chemistry; 2014 May 13; 2(22):8205–14.
- [95] de Albuquerque JE, Mattoso LHC, Faria RM, Masters JG, MacDiarmid AG. Study of the interconversion of polyaniline oxidation states by optical absorption spectroscopy. *Synth Met.* Elsevier; 2004 Oct 14; 146(1):1–10.
- [96] Choi BG, Park H, Im HS, Kim YJ, Hong WH. Influence of oxidation state of polyaniline on physicochemical and transport properties of Nafion/polyaniline composite membrane for DMFC. *J Memb Sci.* Elsevier; 2008 Oct 31; 324(1–2):102–10.
- [97] de Salas F, Pardo I, Salavagione HJ, Aza P, Amougé E, Vind J, et al. Advanced Synthesis of Conductive Polyaniline Using Laccase as Biocatalyst. Vazquez-Duhalt R, editor. *PLoS One.* Public Library of Science; 2016 Oct 14;

11(10):e0164958.

- [98] Shishov M, Moshnikov V, Sapurina I. Self-organization of polyaniline during oxidative polymerization: formation of granular structure. *Chem Pap*. 2013 Jan 1; 67(8).
- [99] Wang M. Template-Free Method to Conducting Polymer Micro/Nanostructures. *Conducting Polymers with Micro or Nanometer Structure*. Berlin, Heidelberg: Springer Berlin Heidelberg; 2008. p. 158–277.
- [100] Sapurina IY, Shishov MA. Oxidative Polymerization of Aniline: Molecular Synthesis of Polyaniline and the Formation of Supramolecular Structures. *New Polymers for Special Applications*. InTech; 2012. p. 251–312.
- [101] Xie Y, Kocafe D, Chen C, Kocafe Y. Review of Research on Template Methods in Preparation of Nanomaterials. *J Nanomater*. Hindawi; 2016 Jul 25; 2016:1–10.
- [102] Diez-Pascual AM. Preparation and characterization of polyphenylene sulfide nanocomposites. *Manufacturing of Nanocomposites with Engineering Plastics*. Woodhead Publishing; 2015. p. 127–65.
- [103] Cruz-Silva R, Escamilla A, Nicho ME, Padron G, Ledezma-Perez A, Arias-Marin E, et al. Enzymatic synthesis of pH-responsive polyaniline colloids by using chitosan as steric stabilizer. *Eur Polym J*. Pergamon; 2007 Aug 1; 43(8):3471–9.
- [104] Shi J. *Steric Stabilization*. MSE, The Ohio State University. 2002.
- [105] Liu M-C, Dai C-L, Chan C-H, Wu C-C, Liu M-C, Dai C-L, et al. Manufacture of a Polyaniline Nanofiber Ammonia Sensor Integrated with a Readout Circuit Using the CMOS-MEMS Technique. *Sensors*. Molecular Diversity Preservation International; 2009 Feb 10; 9(2):869–80.
- [106] Eisazadeh H, Ghorbani M. Nanoparticles Preparation of Aniline and Acrylonitrile Copolymer Using Various Surfactants. *World Appl Sci J*. 2008; 5(2):204–10.
- [107] Gabr Y. Gabr: Studies on the Copolymerization of 4-Aminostyrene With 4-Nitro-and 2,4-Dinitrostyrene Scientific paper Studies on the Copolymerization of 4-Aminostyrene With 4-Nitro-and 2,4-Dinitrostyrene. *Acta Chim. Slov*.

2007.

- [108] Yuan S, Tang S, Lv L, Liang B, Choong C, Pehkonen SO. Poly(4-vinylaniline) - Polyaniline Bilayer-Modified Stainless Steels for the Mitigation of Biocorrosion by Sulfate-Reducing Bacteria (SRB) in Seawater. *Ind Eng Chem Res. American Chemical Society*; 2012 Nov 14; 51(45):14738–51.
- [109] L. Y. Ji, Kang ET, Neoh KG, Tan KL. Surface Modification of Poly(tetrafluoroethylene) Film by Consecutive Graft Copolymerization with 4-Vinylaniline and Aniline. *Macromolecules. American Chemical Society*; 1999; 32(24):8183–8.
- [110] Fu GD, Zhao JP, Sun YM, Kang ET, Neoh KG. Conductive hollow nanospheres of polyaniline via surface-initiated atom transfer radical polymerization of 4-vinylaniline and oxidative graft copolymerization of aniline. *Macromolecules. 2007 Mar 20*; 40(6):2271–5.
- [111] Yokozawa T, Yokoyama A. Chain-growth polycondensation: The living polymerization process in polycondensation. *Prog Polym Sci. Pergamon*; 2007 Jan 1; 32(1):147–72.
- [112] Harrisson S, Liu X, Ollagnier J-N, Coutelier O, Marty J-D, Destarac M, et al. RAFT Polymerization of Vinyl Esters: Synthesis and Applications. *Polymers (Basel). Multidisciplinary Digital Publishing Institute*; 2014 May 20; 6(5):1437–88.
- [113] Arslan H. Block and Graft Copolymerization by Controlled/Living Radical Polymerization Methods. *Polymerization. InTech*; 2012.
- [114] Matyjaszewski K, Spanswick J. Controlled/living radical polymerization. *Mater Today. Elsevier*; 2005 Mar 1; 8(3):26–33.
- [115] Patten T, Matyjaszewski K. Atom transfer radical polymerization and the synthesis of polymeric materials. *Adv Mater. 1998*; 10(12):901–15.
- [116] Minko S. Grafting on Solid Surfaces: “Grafting to” and “Grafting from” Methods. *Polymer Surfaces and Interfaces. Berlin, Heidelberg: Springer Berlin Heidelberg*; 2008. p. 215–34.
- [117] Kim M, Schmitt S, Choi J, Krutty J, Gopalan P, Kim M, et al. From Self-Assembled Monolayers to Coatings: Advances in the Synthesis and Nanobio

Applications of Polymer Brushes. *Polymers* (Basel). Multidisciplinary Digital Publishing Institute; 2015 Jul 20; 7(7):1346–78.

- [118] Bhattacharya A, Misra BN. Grafting: a versatile means to modify polymers: Techniques, factors and applications. *Prog Polym Sci.* 2004; 29(8):767–814.
- [119] Hansson S, Östmark E, Carlmark A, Malmström E. ARGET ATRP for Versatile Grafting of Cellulose Using Various Monomers. *ACS Appl Mater Interfaces.* American Chemical Society; 2009 Nov 25; 1(11):2651–9.
- [120] Baughman RH, Zakhidov AA, de Heer WA. Carbon nanotubes--the route toward applications. *Science.* American Association for the Advancement of Science; 2002 Aug 2; 297(5582):787–92.
- [121] Nanocomp Technologies, Inc. - manufacturer of Miralon. 2016 [cited 2018 Oct 15]. Available from: <http://www.miralon.com/>
- [122] Technistro®, Multiwalled carbon nanotubes - MWCNT. 2012 [cited 2018 Oct 17]. Available from: <https://www.techinstro.com/multiwalled-carbon-nanotubes-mwcnt/>
- [123] Hunley DP. SYNTHESIS , INTEGRATION , AND PHYSICAL CHARACTERIZATION OF GRAPHENE AND CARBON NANOTUBES. Theses and Dissertations-Physics and Astronomy Physics and Astronomy. 2015.
- [124] Basic principles in organic chemistry: Tetravalent carbon and its hybridization – Open Teaching Project. [cited 2018 Oct 11]. Available from: <http://padakshep.org/otp/subjects/chemistry/organic-chemistry/tetravalent-carbon/>
- [125] Molecular Structure & Bonding. [cited 2018 Oct 11]. Available from: <https://www2.chemistry.msu.edu/faculty/reusch/virttxtjml/intro3.htm>
- [126] Ken Costello. Hybridization in covalent bonds. [cited 2018 Oct 17]. Available from: <http://www.chemistryland.com/CHM151S/09-CovalentBonds/Covalent.html>
- [127] Welcome to 7Active Studio. [cited 2018 Oct 11]. Available from: <http://www.7activestudio.com/>

- [128] Moisala A, Li Q, Kinloch IA, Windle AH. Thermal and electrical conductivity of single- and multi-walled carbon nanotube-epoxy composites. *Compos Sci Technol*. Elsevier; 2006 Aug 1; 66(10):1285–8.
- [129] Bussy C, Ali-Boucetta H, Kostarelos K. Safety considerations for graphene: lessons learnt from carbon nanotubes. *Acc Chem Res*. American Chemical Society; 2013 Mar 19; 46(3):692–701.
- [130] Kreupl F, Graham A., Duesberg G., Steinhögl W, Liebau M, Unger E, et al. Carbon nanotubes in interconnect applications. *Microelectron Eng*. Elsevier; 2002 Oct 1; 64(1–4):399–408.
- [131] Jiang S, Hou P-X, Chen M-L, Wang B-W, Sun D-M, Tang D-M, et al. Ultrahigh-performance transparent conductive films of carbon-welded isolated single-wall carbon nanotubes. *Sci Adv*. American Association for the Advancement of Science; 2018 May 4; 4(5):eaap9264.
- [132] Landi BJ, Ganter MJ, Cress CD, DiLeo RA, Raffaele RP. Carbon nanotubes for lithium ion batteries. *Energy Environ Sci*. Royal Society of Chemistry; 2009 Jun 2; 2(6):638.
- [133] High-Resolution TEM on Graphene - DTU Cen. [cited 2018 Oct 4]. Available from: <https://www.cen.dtu.dk/research/projects/actual-high-resolution-tem-on-graphene>
- [134] Yang W, Ratinac KR, Ringer SP, Thordarson P, Gooding JJ, Braet F. Carbon Nanomaterials in Biosensors: Should You Use Nanotubes or Graphene? *Angew Chemie Int Ed*. Wiley-Blackwell; 2010 Mar 15; 49(12):2114–38.
- [135] Mittal G, Dhand V, Rhee KY, Park S-J, Lee WR. A review on carbon nanotubes and graphene as fillers in reinforced polymer nanocomposites. *J Ind Eng Chem*. Elsevier; 2015 Jan 25; 21:11–25.
- [136] Kordrostami Z, Sheikhi MH, Mohammadzadegan R. Modeling electronic properties of multiwall carbon nanotubes. *Fullerenes Nanotub Carbon Nanostructures*. 2008; 16(1):66–77.
- [137] Carbon Lab, Department of Physics of the University of Rome Tor Vergata - Google Search. [cited 2018 Oct 19]. Available from: <https://www.google.co.uk/search?q=Carbon+Lab,+Department+of+Physics+o>

f+the+University+of+Rome+Tor+Vergata&safe=active&rlz=1C1CHBD_en-GBGB799GB799&source=Inms&tbn=isch&sa=X&ved=0ahUKEwj0nbnkvpLeAhWFe8AKHR9eCZ4Q_AUIDigB&biw=1918&bih=938#imgrc=HDXTASRpHV73AM

- [138] PUSKÁS R. Carbon Nanostructures with Different Dimensionality-From Synthesis to Applications. University of Szeged Department of Applied and Environmental Chemistry; 2015.
- [139] Tan CW, Tan KH, Ong YT, Mohamed AR, Zein SHS, Tan SH. Carbon nanotubes applications: Solar and fuel cells, hydrogen storage, lithium batteries, supercapacitors, nanocomposites, gas, pathogens, dyes, heavy metals and pesticides. Environmental Chemistry for a Sustainable World. Springer, Dordrecht; 2012. p. 3–46.
- [140] Mitchell LA, Gao J, Wal R Vander, Gigliotti A, Burchiel SW, McDonald JD. Pulmonary and Systemic Immune Response to Inhaled Multiwalled Carbon Nanotubes. Toxicol Sci. 2007 Nov; 100(1):203–14.
- [141] Ganesh EN. Single Walled and Multi Walled Carbon Nanotube Structure, Synthesis and Applications. Int J Innov Technol Explor Eng. 2013; (24):2278–3075.
- [142] Eatemadi A, Daraee H, Karimkhanloo H, Kouhi M, Zarghami N, Akbarzadeh A, et al. Carbon nanotubes: properties, synthesis, purification, and medical applications. Nanoscale Res Lett. Springer; 2014; 9(1):393.
- [143] Choy KL. Chemical vapour deposition of coatings. Prog Mater Sci. Pergamon; 2003 Jan 1; 48(2):57–170.
- [144] Szabó A, Perri C, Csató A, Giordano G, Vuono D, Nagy JB, et al. Synthesis Methods of Carbon Nanotubes and Related Materials. Materials (Basel). Molecular Diversity Preservation International; 2010 May 7; 3(5):3092–140.
- [145] Lu Y, Li T, Zhao X, Li M, Cao Y, Yang H, et al. Electrodeposited polypyrrole/carbon nanotubes composite films electrodes for neural interfaces. Biomaterials. Elsevier; 2010 Jul 1; 31(19):5169–81.
- [146] Dawouda HD, Altahtamounia TM, Zaghoa MM, Bensalahb N. A brief overview of flexible CNT/PANI super capacitors. Mater Sci Nanotechnol.

- Allied Academies; 2017; 1(2):23–36.
- [147] Gajendran P, Saraswathi R. Polyaniline-carbon nanotube composites. *Pure Appl Chem.* 2008; 80(11):2377–95.
- [148] Matyjaszewski K, Tsarevsky N V. Macromolecular engineering by atom transfer radical polymerization. *Journal of the American Chemical Society.* 2014. p. 6513–33.
- [149] Stejskal J, Sapurina I, Trchová M. Polyaniline nanostructures and the role of aniline oligomers in their formation. *Prog Polym Sci. Pergamon;* 2010 Dec 1; 35(12):1420–81.
- [150] Hu L, Pasta M, Mantia F La, Cui L, Jeong S, Deshazer HD, et al. Stretchable, porous, and conductive energy textiles. *Nano Lett.* 2010 Feb 10; 10(2):708–14.
- [151] Stokes DJ. *Principles and Practice of Variable Pressure/Environmental Scanning Electron Microscopy (VP-ESEM).* Chichester, UK: John Wiley & Sons, Ltd; 2008.
- [152] Smith DJ. *High Resolution Transmission Electron Microscopy. Handbook of Microscopy for Nanotechnology.* Boston: Kluwer Academic Publishers; 2005. p. 427–53.
- [153] Warren BE (Bertram E. *X-ray diffraction.* Dover Publications; 1990. 381 p.
- [154] Park S, Baker JO, Himmel ME, Parilla PA, Johnson DK. Cellulose crystallinity index: measurement techniques and their impact on interpreting cellulase performance. *Biotechnol Biofuels. BioMed Central;* 2010; 3(1):10.
- [155] Cullity BD (Bernard D, Stock SR. *Elements of x-ray diffraction.* Prentice Hall; 2001. 664 p.
- [156] Van der Heide P. *X-ray photoelectron spectroscopy : an introduction to principles and practices.* Wiley-Blackwell; 2012.
- [157] Belgacem MN, Czeremuszkina G, Sapiuha S, Gandini A. Surface by XPS characterization and inverse gas of cellulose fibres chromatography. *Cellulose.* 1995; 2(3):145–57.
- [158] Lei J, Li Q, He G. Accuracy measurement of grafting degree of radiation-

- induced surface graft polymerization by weighing. *Polym Plast Technol Eng.* 2002; 41(1):51–7.
- [159] Hay J, Herbert E. Measuring the Complex Modulus of Polymers by Instrumented Indentation Testing. *Exp Tech.* 2013 May 14; 37(3):55–61.
- [160] Alonso E, Faria M, Mohammadkazemi F, Resnik M, Ferreira A, Cordeiro N. Conductive bacterial cellulose-polyaniline blends: Influence of the matrix and synthesis conditions. *Carbohydr Polym.* Elsevier; 2018 Mar 1; 183:254–62.
- [161] Kissinger PT, Heineman WR. Cyclic voltammetry. *J Chem Educ.* 1983 Sep; 60(9):702.
- [162] Elgrishi N, Rountree KJ, McCarthy BD, Rountree ES, Eisenhart TT, Dempsey JL. A Practical Beginner's Guide to Cyclic Voltammetry. *J Chem Educ.* 2018 Feb 13; 95(2):197–206.
- [163] Lisdat F, Schäfer D. The use of electrochemical impedance spectroscopy for biosensing. *Anal Bioanal Chem.* 2008 Apr 16; 391(5):1555–67.
- [164] Macdonald DD. Reflections on the history of electrochemical impedance spectroscopy. *Electrochim Acta.* Pergamon; 2006 Jan 20; 51(8–9):1376–88.
- [165] Agarwal P. Measurement models for electrochemical impedance spectroscopy I. Demonstration of applicability. *J Electrochem Soc.* 1992; 139(7):1917–27.
- [166] Coats AW, Redfern JP. Thermogravimetric analysis. A review. *Analyst.* The Royal Society of Chemistry; 1963 Jan 1; 88(1053):906.
- [167] PerkinElmer. OA007-12-TR3-253 - OA00712TR3253A-750-A1.pdf.
- [168] Ramlan SNA, Basirun WJ, Phang S-W, Ang DT-C. Electrically conductive palm oil-based coating with UV curing ability. *Prog Org Coatings.* 2017 Nov; 112:9–17.
- [169] R. Rebelo A, Archer AJ, Chen X, Liu C, Yang G, Liu Y. Dehydration of bacterial cellulose and the water content effects on its viscoelastic and electrochemical properties. *Sci Technol Adv Mater.* Taylor & Francis; 2018 Dec 31; 19(1):203–11.
- [170] Lin H, Du C. Synthesis, Structure and Properties of Bacterial Cellulose/polyaniline/manganese Dioxide Nanocomposites via Layer-by-layer

Interfacial Polymerization. *Res Mater Sci.* 2014; 3(1):1–9.

- [171] Mathur G, Dua A, Das AR, Kaur H, Kukal S, Sharma P, et al. Bacteria Cellulose: Biopolymer from *Gluconacetobacter Xylinus*. *Macromol Symp.* 2015 Jan 23; 347(1):27–31.
- [172] Barud HS, Ribeiro CA, Crespi MS, Martines MAU, Dexpert-Ghys J, Marques RFC, et al. Thermal characterization of bacterial cellulose–phosphate composite membranes. *J Therm Anal Calorim.* 2007 Mar 7; 87(3):815–8.
- [173] Tsouko E, Kourmentza C, Ladakis D, Kopsahelis N, Mandala I, Papanikolaou S, et al. Bacterial Cellulose Production from Industrial Waste and by - Product Streams. *Int J Mol Sci.* 2015; 16:14832–49.
- [174] Wang F, Jeon J-H, Park S, Kee C-D, Kim S-J, Oh I-K. A soft biomolecule actuator based on a highly functionalized bacterial cellulose nano-fiber network with carboxylic acid groups. *Soft Matter.* 2016; 12(1):246–54.
- [175] Okiyama A, Motoki M, Yamanaka S. Bacterial cellulose II. Processing of the gelatinous cellulose for food materials. *Food Hydrocoll.* 1992 Nov; 6(5):479–87.
- [176] Esa F, Tasirin SM, Rahman NA. Overview of Bacterial Cellulose Production and Application. *Agric Agric Sci Procedia.* Elsevier; 2014; 2:113–9.
- [177] Yamanaka S, Watanabe K, Kitamura N, Iguchi M, Mitsuhashi S, Nishi Y, et al. The structure and mechanical properties of sheets prepared from bacterial cellulose. *J Mater Sci.* 1989; 24(9):3141–5.
- [178] Ruan C, Zhu Y, Zhou X, Abidi N, Hu Y, Catchmark JM. Effect of cellulose crystallinity on bacterial cellulose assembly. *Cellulose.* 2016 Dec 6; 23(6):3417–27.
- [179] Mikkelsen D, Flanagan BM, Dykes GA, Gidley MJ. Influence of different carbon sources on bacterial cellulose production by *Gluconacetobacter xylinus* strain ATCC 53524. *J Appl Microbiol.* Wiley/Blackwell (10.1111); 2009 Aug 1; 107(2):576–83.
- [180] Gofman IV, Buyanov AL. Unusual effect evidenced at the investigations of the mechanical behavior of composite hydrogels under cyclic compression. *J Mech Behav Biomed Mater.* 2017 Jul; 71:238–43.

- [181] Chen DTN, Wen Q, Janmey PA, Crocker JC, Yodh AG. Rheology of Soft Materials. *Annu Rev Condens Matter Phys.* 2010; 1:301–22.
- [182] Clasen C, Sultanova B, Wilhelms T, Heisig P, Kulicke W-M. Effects of Different Drying Processes on the Material Properties of Bacterial Cellulose Membranes. *Macromol Symp.* WILEY-VCH Verlag; 2006 Dec; 244(1):48–58.
- [183] Müller F, Ferreira CA, Azambuja DS, Alemán C, Armelin E. Measuring the Proton Conductivity of Ion-Exchange Membranes Using Electrochemical Impedance Spectroscopy and Through-Plane Cell. *J Phys Chem B.* American Chemical Society; 2014 Jan 30; 118(4):1102–12.
- [184] Kreuer K-D. Proton Conductivity: Materials and Applications. *Chem Mater.* American Chemical Society ; 1996 Jan; 8(3):610–41.
- [185] Zhang SS, Xu K, Jow TR. Electrochemical impedance study on the low temperature of Li-ion batteries. *Electrochim Acta.* Pergamon; 2004 Mar 15; 49(7):1057–61.
- [186] Mitra SK, Rangunathan P, Nayar MG. Porous nickel electrodes in water electrolysis 2. Use of porous nickel electrodes in multicell module. *Int J Hydrog Energy.* Pergamon Press Ltd; 1981; 6(5):497–507.
- [187] Stafford OA, Hinderliter BR, Croll SG. Electrochemical impedance spectroscopy response of water uptake in organic coatings by finite element methods. *Electrochim Acta.* Pergamon; 2006 Nov 12; 52(3):1339–48.
- [188] Rebelo A, Liu Y, Liu C, Schäfer K-H, Saumer M, Yang G. Poly(4-vinylaniline)/polyaniline bilayer functionalized bacterial cellulose membranes as bioelectronics interfaces. *Carbohydr Polym.* 2019; 204:190–201.
- [189] Bandeira RM, van Drunen J, Garcia AC, Tremiliosi-Filho G. Influence of the thickness and roughness of polyaniline coatings on corrosion protection of AA7075 aluminum alloy. *Electrochim Acta.* Pergamon; 2017 Jun 20; 240:215–24.
- [190] Yu Sapurina I, Stejskal J. Oxidation of Aniline with Strong and Weak Oxidants. *ISSN Russ J Gen Chem.* Pleiades Publishing, Ltd; 2012; 82(2):1070–3632.

- [191] Kuczynska A, Uygun A, Kaim A, Wilczura-Wachnik H, Yavuz AG, Aldissi M. Effects of surfactants on the characteristics and biosensing properties of polyaniline. *Polym Int.* John Wiley & Sons, Ltd.; 2010 Dec 1; 59(12):1650–9.
- [192] Li D, Kaner RB. How nucleation affects the aggregation of nanoparticles. *J Mater Chem.* 2007; 17(22):2279.
- [193] Tian Z, Yu H, Wang L, Saleem M, Ren F, Ren P, et al. Recent progress in the preparation of polyaniline nanostructures and their applications in anticorrosive coatings. *RSC Adv.* Royal Society of Chemistry; 2014 Jun 30; 4(54):28195.
- [194] Habibi Y. Key advances in the chemical modification of nanocelluloses. *Chem Soc Rev.* The Royal Society of Chemistry; 2014 Mar 7; 43(5):1519–42.
- [195] Wu Z-Y, Li C, Liang H-W, Chen J-F, Yu S-H. Ultralight, Flexible, and Fire-Resistant Carbon Nanofiber Aerogels from Bacterial Cellulose. *Angew Chemie.* WILEY-VCH Verlag; 2013 Mar 4; 125(10):2997–3001.
- [196] Shah N, Ul-Islam M, Khattak WA, Park JK. Overview of bacterial cellulose composites: A multipurpose advanced material. *Carbohydr Polym.* Elsevier; 2013 Nov 6; 98(2):1585–98.
- [197] Wang L, Wu Y, Men Y, Shen J, Liu Z. Thermal-sensitive Starch-g-PNIPAM prepared by Cu(0) catalyzed SET-LRP at molecular level. *RSC Adv.* 2015; 5(87):70758–65.
- [198] Gaspar D, Fernandes SN, de Oliveira AG, Fernandes JG, Grey P, Pontes R V, et al. Nanocrystalline cellulose applied simultaneously as the gate dielectric and the substrate in flexible field effect transistors. *Nanotechnology.* IOP Publishing; 2014 Mar 7; 25(9):094008.
- [199] Kluczka J, Korolewicz T, Zołotajkin M, Adamek J. Boron removal from water and wastewater using new polystyrene-based resin grafted with glycidol. *Water Resour Ind.* 2015; 11:46–57.
- [200] Verma N. Effect of Zinc Oxide Nano Particle Concentration in the Polyaniline-Zinc Oxide Nanocomposite on the Dielectric Property. *Mater Sci Res India.* 2014 Dec 31; 11(2):146–52.
- [201] Maity N, Kuila A, Das S, Mandal D, Shit A, Nandi AK. Optoelectronic and

- photovoltaic properties of graphene quantum dot–polyaniline nanostructures. *J Mater Chem A. Royal Society of Chemistry*; 2015 Oct 13; 3(41):20736–48.
- [202] Wang H, Zhu E, Yang J, Zhou P, Sun D, Tang W. Bacterial Cellulose Nanofiber-Supported Polyaniline Nanocomposites with Flake-Shaped Morphology as Supercapacitor Electrodes. *J Phys Chem C. American Chemical Society*; 2012 Jun 21; 116(24):13013–9.
- [203] Pleumphon C, Thiangtham S, Pechyen C, Manuspiya H, Ummartyotin S. Development of Conductive Bacterial Cellulose Composites: An Approach to Bio-Based Substrates for Solar Cells. *J Biobased Mater Bioenergy*. 2017 Aug 1; 11(4):321–9.
- [204] Wang H, Fu Y, Wang Z, Shao Z, Qin M. Regioselectivity in the Acylation of Cellulose with 2-Bromoisobutyryl Bromide under Homogeneous Conditions. *Cellul Chem Technol Cellul Chem Technol*. 2017; 51(12):11–21.
- [205] Tong Z, Yang Y, Wang J, Zhao J, Su B-L, Li Y. Layered polyaniline/graphene film from sandwich-structured polyaniline/graphene/polyaniline nanosheets for high-performance pseudosupercapacitors. *J Mater Chem A. Royal Society of Chemistry*; 2014 Mar 4; 2(13):4642–51.
- [206] Tanwar S, Ho J. Green Synthesis of Novel Polyaniline Nanofibers: Application in pH Sensing. *Molecules. Multidisciplinary Digital Publishing Institute*; 2015 Oct 13; 20(10):18585–96.
- [207] Lin Z, Guan Z, Huang Z. New Bacterial Cellulose/Polyaniline Nanocomposite Film with One Conductive Side through Constrained Interfacial Polymerization. *Ind Eng Chem Res. American Chemical Society*; 2013 Feb 27; 52(8):2869–74.
- [208] Liu DY, Sui GX, Bhattacharyya D. Synthesis and characterisation of nanocellulose-based polyaniline conducting films. *Compos Sci Technol. Elsevier*; 2014 Jul 30; 99:31–6.
- [209] Ludvig P, Calixto JM, Ladeira LO, Gaspar ICP. Using Converter Dust to Produce Low Cost Cementitious Composites by in situ Carbon Nanotube and Nanofiber Synthesis. *Materials (Basel)*. 2011 Mar 18; 4(3):575–84.
- [210] Wu Q, Qin Y-F, Chen L, Qin Z-Y. Conductive Polyaniline/Cellulose

Nanocrystals Composite for Ammonia Gas Detection. *Computer Science and Engineering Technology (CSET2015), Medical Science and Biological Engineering (MSBE2015)*. WORLD SCIENTIFIC; 2016. p. 670–5.

- [211] Beaumont PWR, Soutis C. Structural integrity of engineering composite materials: a cracking good yarn. *Philos Trans A Math Phys Eng Sci. The Royal Society*; 2016 Jul 13; 374(2071):20160057.
- [212] Goosey MT. Introduction to Plastics and their Important Properties for Electronic Applications. In: Goosey MT, editor. *Plastics for Electronics*. Dordrecht: Springer Netherlands; 1985. p. 1–24.
- [213] Wang T-L, Liu Y-Z, Jeng B-C, Cai Y-C. The Effect of Initiators and Reaction Conditions on the Polymer Syntheses by Atom Transfer Radical Polymerization. *J Polym Res*. 2005; 12:67–75.
- [214] Hansson S, Carlmark A, Malmström E, Fogelström L. Toward industrial grafting of cellulosic substrates via ARGET ATRP. *J Appl Polym Sci*. 2015 Feb 10; 132(6):41434–44.
- [215] Yamaguchi K, Hirao A, Suzuki K, Takenaka K, Nakahama S, Yamazaki N. Anionic living polymerization of p-N,N-bis(trimethylsilyl)-aminostyrene. Synthesis of linear poly(p-aminostyrene) with a narrow molecular weight distribution. *J Polym Sci Polym Lett Ed. Wiley-Blackwell*; 1983 May; 21(5):395–401.
- [216] Matyjaszewski K. Atom Transfer Radical Polymerization (ATRP): Current status and future perspectives. *Macromolecules*. 2012 May 22; 45(10):4015–39.
- [217] Heinze T, Schwikal K, Barthel S. Ionic Liquids as Reaction Medium in Cellulose Functionalization. *Macromol Biosci. Wiley-Blackwell*; 2005 Jun 24; 5(6):520–5.
- [218] Riede A, Helmstedt M, Sapurina I, Stejskal J. In situ polymerized polyaniline films. 4. Film formation in dispersion polymerization of aniline. *J Colloid Interface Sci*. 2002 Apr 15; 248(2):413–8.
- [219] Hong S-Y, Park S-M. Electrochemistry of Conductive Polymers 36. pH Dependence of Polyaniline Conductivities Studied by Current-Sensing Atomic

- Force Microscopy. *J Phys Chem B*. American Chemical Society; 2005; 109(19):9305–10.
- [220] Focke WW, Wnek GE, Wei Y. Influence of Oxidation State, pH, and Counterion on the Conductivity of Polyaniline. *J Phys Chem*. 1987; 91(20):5813–8.
- [221] Jelmy EJ, Ramakrishnan S, Devanathan S, Rangarajan M, Kothurkar NK. Optimization of the conductivity and yield of chemically synthesized polyaniline using a design of experiments. *J Appl Polym Sci*. 2013 Oct 15; 130(2):1047–57.
- [222] Mahalakshmi B, Vedhi C. Synthesis and Characterization of Perfluorooctanoic Acid Anionic Surfactant Doped Nanosize Polyaniline. *Open J Synth Theory Appl*. 2014; 3(3):57–68.
- [223] Xie H-Q, Ma Y-M, Feng D-S. Preparation of organosoluble conductive polyaniline via precipitation polymerization and study of its conductivity. *Eur Polym J*. 2000 Oct; 36(10):2201–6.
- [224] Bhadra S, Singha NK, Chattopadhyay S, Khastgir D. Effect of different reaction parameters on the conductivity and dielectric properties of polyaniline synthesized electrochemically and modeling of conductivity against reaction parameters through regression analysis. *J Polym Sci Part B Polym Phys*. Wiley Subscription Services, Inc., A Wiley Company; 2007 Aug 1; 45(15):2046–59.
- [225] John R, Wallace GG. Doping-dedoping of polypyrrole: a study using current-measuring and resistance-measuring techniques. Elsevier Sequoia SA. 1993; 354:145–60.
- [226] Lindner D. Triumph Des Ensembles Und Der Regiearbeit. *Osterr Musik*. 1959; 14:476–7.
- [227] Jamadade VS, Dhawale DS, Lokhande CD. Studies on electrosynthesized leucoemeraldine, emeraldine and pernigraniline forms of polyaniline films and their supercapacitive behavior. *Synth Met*. Elsevier; 2010 May 1; 160(9–10):955–60.
- [228] Huang W-S, Humphrey BD, Macdiarmid AG. Polyaniline, a Novel

- Conducting Polymer Morphology and Chemistry of its Oxidation and Reduction in Aqueous Electrolytes. *J Chem SOC, Faraday Trans 1*. 1986; 82:2385–400.
- [229] Mi H, Zhang X, Yang S, Ye X, Luo J. Polyaniline nanofibers as the electrode material for supercapacitors. *Mater Chem Phys*. Elsevier; 2008 Nov 15; 112(1):127–31.
- [230] Zhu H, Peng S, Jiang W. Electrochemical properties of PANI as single electrode of electrochemical capacitors in acid electrolytes. *ScientificWorldJournal*. Hindawi Publishing Corporation; 2013; 2013:940153.
- [231] Chang KC, Lai MC, Peng CW, Chen YT, Yeh JM, Lin CL, et al. Comparative studies on the corrosion protection effect of DBSA-doped polyaniline prepared from in situ emulsion polymerization in the presence of hydrophilic N⁺-MMT and organophilic organo-MMT clay platelets. *Electrochim Acta*. 2006; 51(26):5645–53.
- [232] Amirudin A, Thiény D. Application of electrochemical impedance spectroscopy to study the degradation of polymer-coated metals. *Prog Org Coatings*. Elsevier; 1995 Aug 1; 26(1):1–28.
- [233] Guan L, Yu L, Chen GZ. Capacitive and non-capacitive faradaic charge storage. *Electrochim Acta*. Pergamon; 2016 Jul 10; 206:464–78.
- [234] Park S-M, Yoo J-S. Electrochemical Impedance Spectroscopy for Better Electrochemical Measurements. *Anal Chem*. 2003; 75(21):455 A-461 A.
- [235] Xu J, Wang K, Zu S-Z, Han B-H, Wei Z. Hierarchical Nanocomposites of Polyaniline Nanowire Arrays on Graphene Oxide Sheets with Synergistic Effect for Energy Storage. *ACS Nano*. 2010 Sep 28; 4(9):5019–26.
- [236] Huang VM-W, Vivier V, Orazem ME, Pébère N, Tribollet B. The Apparent Constant-Phase-Element Behavior of a Disk Electrode with Faradaic Reactions A Global and Local Impedance Analysis. *J Electrochem Soc*. 2006; 154(2):99–107.
- [237] Mori S, Asano A. Light Intensity Independent Electron Transport and Slow Charge Recombination in Dye-Sensitized In₂O₃ Solar Cells: In Contrast to the Case of TiO₂. *J Phys Chem C*. American Chemical Society; 2010 Aug 5;

114(30):13113–7.

- [238] Le TH, Kim Y, Yoon H. Electrical and electrochemical properties of conducting polymers. *Polymers (Basel)*. 2017; 9(150):1–32.
- [239] Colomban P, Tomkinson J. Novel forms of hydrogen in solids: the “ionic” proton and the “quasi-free” proton. *Solid State Ionics*. Elsevier; 1997 May 1; 97(1–4):123–34.
- [240] Tzou K, Gregory RV. Kinetic study of the chemical polymerization of aniline in aqueous solutions. *Synth Met*. Elsevier; 1992; 47(3):267–77.
- [241] Shokry Hassan H, Elkady MF, Kawi MAA El, Alian MF. Preparation and Characterization of Polyaniline Nanotubes. *Am J Appl Chem. Science Publishing Group*; 2015 May 13; 3(3):54.
- [242] Tran HD, Li D, Kaner RB. One-Dimensional Conducting Polymer Nanostructures: Bulk Synthesis and Applications. *Adv Mater*. Wiley-Blackwell; 2009 Apr 20; 21(14–15):1487–99.
- [243] Yu Q-Z, Shi M-M, Deng M, Wang M, Chen H-Z. Morphology and conductivity of polyaniline sub-micron fibers prepared by electrospinning. *Mater Sci Eng B*. Elsevier; 2008 Apr 25; 150(1):70–6.
- [244] Mostafaei A, Zolriasatein A. Synthesis and characterization of conducting polyaniline nanocomposites containing ZnO nanorods. *Prog Nat Sci Mater Int*. Elsevier; 2012 Aug 1; 22(4):273–80.
- [245] Yang Z, Coutinho DH, Sulfstede R, Balkus KJ, Ferraris JP. Proton conductivity of acid-doped meta-polyaniline. *J Memb Sci*. Elsevier; 2008 Apr 10; 313(1–2):86–90.
- [246] Wu X, Lu C, Xu H, Zhang X, Zhou Z. Biotemplate synthesis of polyaniline@cellulose nanowhiskers/natural rubber nanocomposites with 3D hierarchical multiscale structure and improved electrical conductivity. *ACS Appl Mater Interfaces*. American Chemical Society; 2014 Dec 10; 6(23):21078–85.
- [247] Qiang Z, Liang G, Gu A, Yuan L. The interaction between unique hyperbranched polyaniline and carbon nanotubes, and its influence on the dielectric behavior of hyperbranched polyaniline/carbon nanotube/epoxy resin

- composites. *J Nanoparticle Res.* Springer Netherlands; 2014 May 18; 16(5):2391.
- [248] Lv P, Feng Q, Wang Q, Li D, Zhou J, Wei Q. Preparation of Bacterial Cellulose/Carbon Nanotube Nanocomposite for Biological Fuel Cell. *Fibers Polym.* 2016; 17(11):1858–65.
- [249] Wen Z, Shen C, Lu Y. Air Electrode for the Lithium-Air Batteries: Materials and Structure Designs. *Chempluschem.* Wiley-Blackwell; 2015 Feb; 80(2):270–87.
- [250] Branca C, Frusteri F, Magazù V, Mangione A. Characterization of Carbon Nanotubes by TEM and Infrared Spectroscopy. *J Phys Chem B.* American Chemical Society; 2004; 108(11):3469–73.
- [251] H S, N Y, MK B, L K, M S, M B, et al. Synthesis of Carbon Nanotubes for Oil-water Interfacial Tension Reduction. *Oil Gas Res.* OMICS International; 2015 Nov 5; 1(1).
- [252] Qing R, Sigmund W. Morphological and crystallite size impact on electrochemical performance of electrospun rutile and rutile/multiwall carbon nanotube nanofibers for lithium ion batteries. *Ceram Int.* Elsevier; 2014 May 1; 40(4):5665–9.
- [253] Jeong HK, Echeverria E, Chakraborti P, Le HT, Dowben PA. Electronic structure of cyclodextrin–carbon nanotube composite films. *RSC Adv.* Royal Society of Chemistry; 2017 Feb 10; 7(18):10968–72.
- [254] Ramana G V., Srikanth VVSS, Padya B, Jain PK. Carbon nanotube–polyaniline nanotube core–shell structures for electrochemical applications. *Eur Polym J.* Pergamon; 2014 Aug 1; 57:137–42.
- [255] Liu P-S, Chen Q, Liu X, Yuan B, Wu S-S, Shen J, et al. Grafting of Zwitterion from Cellulose Membranes via ATRP for Improving Blood Compatibility. *Biomacromolecules.* American Chemical Society; 2009 Oct 12; 10(10):2809–16.
- [256] Golczak S, Kanciurzevska A, Fahlman M, Langer K, Langer JJ. Comparative XPS surface study of polyaniline thin films. *Solid State Ionics.* Elsevier; 2008 Dec 15; 179(39):2234–9.

- [257] Al-Gamal AG, Farag AA, Elnaggar EM, Kabel KI. Comparative impact of doping nano-conducting polymer with carbon and carbon oxide composites in alkyd binder as anti-corrosive coatings. 2018; 25(11):959–80.
- [258] Zoltowski P. On the electrical capacitance of interfaces exhibiting constant phase element behaviour. *J Electroanal Chem. Elsevier*; 1998 Feb 10; 443(1):149–54.
- [259] Jin L, Jiang Y, Zhang M, Li H, Xiao L, Li M, et al. Oriented Polyaniline Nanowire Arrays Grown on Dendrimer (PAMAM) Functionalized Multiwalled Carbon Nanotubes as Supercapacitor Electrode Materials. *Sci Rep. Nature Publishing Group*; 2018 Dec 19; 8(1):6268.
- [260] Pilgrim GA, Leadbetter JW, Qiu F, Siitonen AJ, Pilgrim SM, Krauss TD. Electron Conductive and Proton Permeable Vertically Aligned Carbon Nanotube Membranes. *Nano Lett. American Chemical Society*; 2014 Apr 9; 14(4):1728–33.
- [261] Liu M, Chen L, Lewis S, Chong SY, Little MA, Hasell T, et al. Three-dimensional protonic conductivity in porous organic cage solids. *Nat Commun. Nature Publishing Group*; 2016 Sep 13; 7:12750.
- [262] Arulmani S, Wu JJ, Anandan S. Amphiphilic Triblock Copolymer guided Polyaniline embraced CNT nanohybrid with outcropping whiskers as an energy storage electrode. *Electrochim Acta. Pergamon*; 2017 Aug 20; 246:737–47.
- [263] Sun C, Zhang S, Qu R, Sun T, Zhang Y, Zhang X, et al. Synthesis of polystyrene, poly(styrene/4-vinylpyridine), poly(p-nitrostyrene) and poly(p-aminostyrene)-coated silica and their extraction capabilities for amphetamine. *Mater Chem Phys. Elsevier*; 2010 Nov 1; 124(1):298–304.
- [264] Morávková Z, Trchová M, Tomšík E, Čechvala J, Stejskal J. Enhanced thermal stability of multi-walled carbon nanotubes after coating with polyaniline salt. *Polym Degrad Stab. Elsevier*; 2012 Aug 1; 97(8):1405–14.
- [265] Ho Park S, Goo Lee S, Kim SH. Thermal decomposition behavior of carbon nanotube reinforced thermotropic liquid crystalline polymers. *J Appl Polym Sci. Wiley-Blackwell*; 2011 Nov 5; 122(3):2060–70.

- [266] Nigam R, Habeeb S, Priyadarshi A, Jaggi N. Electrical conductivity of metal-carbon nanotube structures: Effect of length and doping. *Bull Mater Sci*. Springer India; 2014 Aug 20; 37(5):1047–51.
- [267] Salvatierra RV, Zitzer G, Savu S-A, Alves AP, Zarbin AJG, Chassé T, et al. Carbon nanotube/polyaniline nanocomposites: Electronic structure, doping level and morphology investigations. *Synth Met*. Elsevier; 2015 May 1; 203:16–21.
- [268] Ruoff RS, Lorents DC. Mechanical and thermal properties of carbon nanotubes. *Carbon N Y*. Pergamon; 1995 Jan 1; 33(7):925–30.
- [269] Bružauskaitė I, Bironaitė D, Bagdonas E, Bernotienė E. Scaffolds and cells for tissue regeneration: different scaffold pore sizes-different cell effects. *Cytotechnology*. Springer; 2016 May; 68(3):355–69.
- [270] Kulkarni AA, Rao PS. Synthesis of polymeric nanomaterials for biomedical applications. *Nanomaterials in Tissue Engineering: Fabrication and Applications*. Woodhead Publishing; 2013. p. 27–63.
- [271] Lamour G, Journiac N, Souès S, Bonneau S, Nassoy P, Hamraoui A. Influence of surface energy distribution on neuritogenesis. *Colloids Surfaces B Biointerfaces*. Elsevier; 2009 Sep 1; 72(2):208–18.
- [272] Das KP, Freudenrich TM, Mundy WR. Assessment of PC12 cell differentiation and neurite growth: a comparison of morphological and neurochemical measures. *Neurotoxicol Teratol*. Pergamon; 2004 May 1; 26(3):397–406.
- [273] Gordon J, Amini S, White MK. General overview of neuronal cell culture. *Methods Mol Biol*. NIH Public Access; 2013; 1078:1–8.
- [274] Kriegstein A, Alvarez-Buylla A. The glial nature of embryonic and adult neural stem cells. *Annu Rev Neurosci*. NIH Public Access; 2009; 32:149–84.
- [275] Xu M, McCanna DJ, Sivak JG. Use of the viability reagent PrestoBlue in comparison with alamarBlue and MTT to assess the viability of human corneal epithelial cells. *J Pharmacol Toxicol Methods*. 2015 Jan; 71:1–7.
- [276] Sun Y, Xing Z, Xue Y, Mustafa K, Finne-Wistrand A, Albertsson AC. Surfactant as a critical factor when tuning the hydrophilicity in three-

dimensional polyester-based scaffolds: Impact of hydrophilicity on their mechanical properties and the cellular response of human osteoblast-like cells. *Biomacromolecules*. 2014; 15(4):1259–68.

- [277] Webb K, Hlady V, Tresco PA. Relative importance of surface wettability and charged functional groups on NIH 3T3 fibroblast attachment, spreading, and cytoskeletal organization. *J Biomed Mater Res. NIH Public Access*; 1998 Sep 5; 41(3):422–30.
- [278] Leng W, Zhou S, Gu G, Wu L. Wettability switching of SDS-doped polyaniline from hydrophobic to hydrophilic induced by alkaline/reduction reactions. *J Colloid Interface Sci. Academic Press*; 2012 Mar 1; 369(1):411–8.
- [279] Rotin D, Robinson B, Tannock IF. Influence of hypoxia and an acidic environment on the metabolism and viability of cultured cells: potential implications for cell death in tumors. *Cancer Res. American Association for Cancer Research*; 1986 Jun 1; 46(6):2821–6.
- [280] Cho Y, Borgens R Ben. The effect of an electrically conductive carbon nanotube/collagen composite on neurite outgrowth of PC12 cells. *J Biomed Mater Res Part A*. 2010 Jul 27; 95A(2):510–7.
- [281] Guo W, Patzlaff NE, Jobe EM, Zhao X. Isolation of multipotent neural stem or progenitor cells from both the dentate gyrus and subventricular zone of a single adult mouse. *Nat Protoc. NIH Public Access*; 2012 Nov; 7(11):2005–12.
- [282] Szulcek R, Bogaard HJ, van Nieuw Amerongen GP. Electric Cell-substrate Impedance Sensing for the Quantification of Endothelial Proliferation, Barrier Function, and Motility. *J Vis Exp. MyJoVE Corporation*; 2014 Mar 28; 85(e51300):1–12.
- [283] Bayat A, Ebrahimi M, Moshfegh AZ. Correlation between surface roughness and hydrophobicity of GLAD RF sputtered PTFE/W/Glass nanorod thin films. *Vacuum. Pergamon*; 2014 Mar 1; 101:279–82.
- [284] Sirivisoot S, Pareta R, Harrison BS. Protocol and cell responses in three-dimensional conductive collagen gel scaffolds with conductive polymer nanofibres for tissue regeneration. *Interface Focus. The Royal Society*; 2014

Feb 6; 4(1):20130050.

- [285] Norlin A, Pan J, Leygraf C. Investigation of Electrochemical Behavior of Stimulation/Sensing Materials for Pacemaker Electrode Applications II. Conducting Oxide Electrodes. *J Electrochem Soc. The Electrochemical Society*; 2005 Jul 1; 152(7):J85.
- [286] Qazi TH, Rai R, Boccaccini AR. Tissue engineering of electrically responsive tissues using polyaniline based polymers: A review. *Biomaterials*. 2014 Aug; 35(33):9068–86.
- [287] dos Santos MR, Alcaraz-Espinoza JJ, da Costa MM, de Oliveira HP. Usnic acid-loaded polyaniline/polyurethane foam wound dressing: preparation and bactericidal activity. *Mater Sci Eng C. Elsevier*; 2018 Aug 1; 89:33–40.
- [288] Williams DF (David F. *The Williams dictionary of biomaterials*. Liverpool University Press; 1999. 343 p.
- [289] Stejskal J, Trchová M. Aniline oligomers versus polyaniline. *Polym Int*. 2012; 61(2):240–51.
- [290] Haba Y, Segal E, Narkis M, Titelman GI, Siegmann A. Polyaniline–DBSA/polymer blends prepared via aqueous dispersions. *Synth Met. Elsevier*; 2000 Apr 17; 110(3):189–93.
- [291] Blinova N V, Stejskal J, Trchová M, Trchová T, Prokě J. Control of polyaniline conductivity and contact angles by partial protonation. *Polymer International Polym Int*. 2008.
- [292] Khalili AA, Ahmad MR. A Review of Cell Adhesion Studies for Biomedical and Biological Applications. *Int J Mol Sci. Multidisciplinary Digital Publishing Institute (MDPI)*; 2015 Aug 5; 16(8):18149–84.

Appendices

Appendix A

Protocol of BC synthesis

Protocol for BC production:

1. Weight 6.8 g of disodium hydrogen phosphate dodecahydrate, 5 g peptone, 5 g yeast extract, 1.5 g citric acid and 20 g glucose;
2. Put everything together into a jar of over 1 L of capacity and add 1 L of pure water, following by continuous agitation with a glass rod;
3. After complete dissolution, distribute the prepared solution into 4 Erlenmeyer flasks of 500 mL capacity, with 250 mL each;
4. Cover the flasks with filter paper and tight around with a piece of rope/line, as illustrated in the Figure A.1;

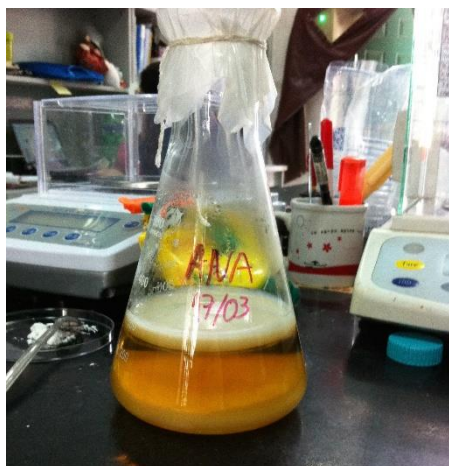


Figure A.1. BC membrane in an Erlenmeyer flask covered with filter paper.

5. Place the covered flasks into the autoclave at 121 °C for 20 min for medium sterilisation;
6. After completed the sterilisation cycle, remove carefully the sterilised medium and transfer them into a biosafety cabinet with a sterile environment. Ensure the medium is cooled down to about 30 °C to prevent bacteria death;

7. Remove, with a strippete, 10 % V/V from an ongoing BC culture into the flasks containing medium, i.e. 25 mL of bacteria culture into each flask;
8. Transfer the medium containing the inoculated bacteria into TCTP plates with a 5 mL pippete: 3.5 mL in 6-well or 1 mL in 24-well, accordingly;
9. Place the well plates into the incubator at 30 °C and 5 % CO₂, keeping a sterile environment and static conditions for 4 days;
10. Followed the 4 days of culture, remove the synthesised BC membranes with tweezers into a large container;
11. Thoroughly wash the membranes with pure water and leave them soaked (in pure water) for 2-3 days, exchanging the water 2 up to 3 times per day;
12. After the step 11., prepare 4 g.L⁻¹ sodium hydroxide solution by weighting 4 g of sodium hydroxide followed by addition of 1 L of pure water;
13. When sodium hydroxide is completely dissolved, insert the pre-washed BC membranes and place it on a hot plate at 100 °C. under magnetic stirring;
14. When the sodium hydroxide solution is boiling, count 40 min;



Figure A.2. BC membranes in a boiled NaOH solution.

15. After the 40 min, remove BC membranes and thoroughly wash with pure water several times (at least 3 times);
16. Leave membranes in pure water for several days until the pH goes down to 7. This normally occur in one week providing that the pure water is replaced 3 times per day;
17. The purified BC membranes can then be used for further treatment/modification.

Appendix B

Protocol of BC/PVAN/PANI synthesis

BC-initiator (prepare the mixture and wash the BC membrane initiator in a sealed container – flask with a rubber tap – and in a fume cupboard):

1. Put the needed amount of BC, roughly 1 g of dry mass of membranes (about 10 dried BC membranes), into a round bottom flask, mix with 30 mL of dried DMF, 5 mL TEA and 1 g DMAP;
2. Add 2 mL of BiBB drop-by-drop into the previous solution under magnetic stirring, ice-bath, and keep the reaction for 24 hours under argon atmosphere at room temperature;
3. The prepared BC membrane initiator is washed with DMF for three days.

Atom Transfer Radical Polymerisation of 4-vinylaniline onto BC-initiator surface (prepare the solution and wash the grafted BC in a sealed container – flask with a rubber tap – and in a fume cupboard):

4. Add 4-VAn (97 %, 2.6 mL, 20 mmol), PMEDTA:Van=1:250, CuCl₂ (0.1 mmol) and ascorbic acid (0.1 mmol) to 10 mL of DMF (or THF) and 1 mL of water in a round-bottom flask;
5. After degassing with argon for 30 min, the BC-initiator substrate is introduced into the reaction mixture under argon atmosphere (use a double-ended canula to transfer the solution into the flask containing the BC-initiator membrane). The reaction flask is sealed and kept at room temperature for 24 hours;
6. After the reaction, the PVAN-grafted BC (BC/PVAN) surface is washed thoroughly with an excess amount of THF and deionised water (do this step in the fume cupboard);
7. Finally, the BC/PVAN substrate is immersed in 20 mL of DMF for 24 hours to remove physically adsorbed PVAN homopolymer, if any (do this step in the fume cupboard).

In situ chemical oxidative polymerisation of aniline (prepare the solution and wash the grafted BC in a sealed container – flask with a rubber tap – and in a fume cupboard):

8. The chemical oxidative polymerisation of aniline on the free amine groups (–NH₂) of the covalently bonded PVAN molecules is carried out in a 30 mL of 1 M HCl aqueous solution, containing the BC/PVAn, 1 mL of aniline, and 2.45 g of APS;
9. The reaction is allowed to proceed at 0 °C in an ice bath for 6 hours;
10. Followed the 6 hours reaction, wash BC/PVAN/PANI membranes with deionised water and ethanol to ensure complete removal of the physically

adsorbed aniline homopolymer and reactants and until the pH raises up to 7.

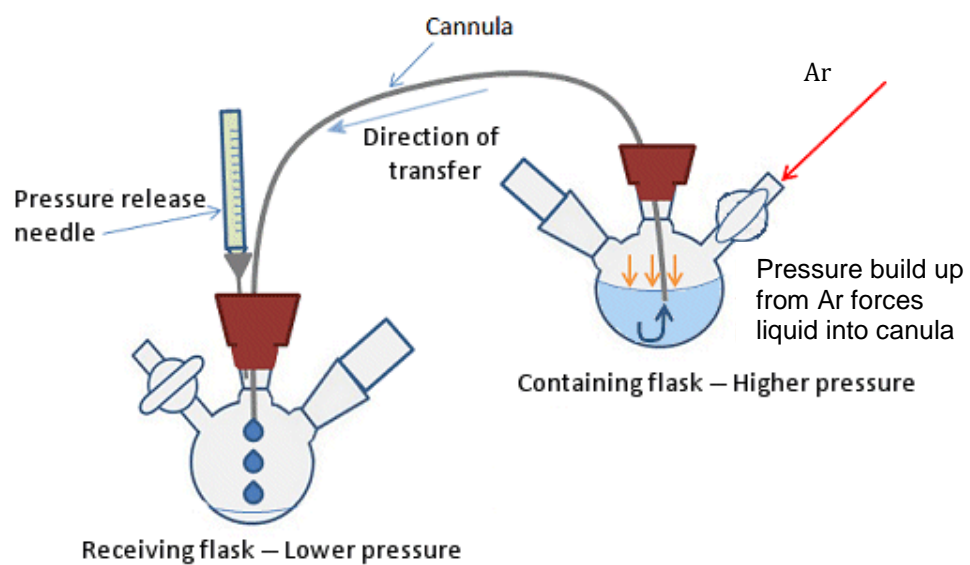


Figure B.1. Scheme of ATRP process setup.

Appendix C

Protocol of cell culture with PC12-Adh and SVZ cells

General Procedure of PC-12 Adh Cell Culture and Harvesting:

1. Remove one million of PC-12 Adh cells in 1 mL of freezing medium (DMEM+1% DMSO) from the cryostore bank and defrost in pre-warmed water bath;
2. Place the cells (1 mL) in a 15 mL centrifuge tube and add 4 mL of proliferation medium;
3. Centrifuge at 120 g for 7 min for removing DMSO;
4. Discharge the medium and resuspend the cells (pellet) in 5 mL of pre-warmed proliferation medium;
5. Transfer the content (one million cells in 5 mL of proliferation medium described in page 85) into a T25 flask and keep it in the incubator at 37 °C and 5% CO₂ for 7 days to reach confluency, with medium replenished every 2 days (remove old medium and add fresh medium);
6. Following the 7 days of culture, passage the cells with aids of scraper: detaching gently the cells from the T25 flask;
7. Transfer the cells from the T25 flask into a 15 mL centrifuge tube (take a certain amount for cell counting) and centrifuge at 120 g for 7 min;
8. According to the obtained number of cells, either using haemocytometer or cell counter, resuspend the cells with the needed proliferation medium in order to have 1×10^4 cells.cm⁻²: 200 µl x number of wells.
9. With the pre-sterilised BC nanocomposite membranes placed in the bottom of 24-well TCTP plates, add 200 µl of cell suspension on the membranes, just the enough to cover it;
10. Incubate for 2 hours to allow cell adhesion, before adding 800 µL of proliferation medium to make the total of 1 mL per well.

General Procedure of Presto Blue Assay:

1. 24 hours after seeding cells, add Presto Blue® reagent at 10% V/V in fresh and pre-warmed proliferation medium (described in page 85), previously prepared in 15 mL centrifuge tube;
2. Remove old culture medium from each well of the 24-well TCTP plate with 1 mL pipette, exchanging the tips for every single well;
3. Add the medium containing Presto Blue® reagent and incubate for 2 hours at 37 °C and 5 % CO₂, before measuring the optical absorbance with a microplate reader) at 570 nm and 600 nm;
4. Wash the cells on membranes with 1 mL of PBS in each well for three times before adding fresh and pre-warmed medium;
5. Repeat the procedure every two days for 7 days.

General Procedure of Cell Differentiation of PC-12 Adh Cells:

1. 24 hours after seeding cells as described above in “General Procedure of PC-12 Adh Cell Culture and Harvesting”, replace the proliferation medium by differentiation medium (described in page 86), adding 1m mL of this in each well;
2. Replace the differentiation medium every 2 days afterwards until the end of the culture period.

General Procedure of SVZ Cell Isolation, Culture and Harvesting:

1. Place the removed the tissues from the dissection procedure in 1 mL of dissection medium (DMEM/F12 GlutaMAX+1% pen/strep) in a centrifuge tube of 2 mL capacity with 1 % Trypsin;
2. Aspirate and dispense gently three times with 1 mL tip pipette and place into the incubator for 30 min laid down at 37 °C and 5 % CO₂;
3. Elapsed the time, proceed to the dissociation steps:
 - Aspirate and dispense gently with 1 mL tip pipette for 5 times;

- Aspirate and dispense gently with 200 μ L tip pipette for 5 times;
 - Aspirate and dispense gently with syringe and cannula of 23 G for 3 times;
 - Aspirate and dispense gently with syringe and cannula of 27 G for 2 times;
4. If after the dissociation steps, there is still some tissue, aspirate and dispense gently again with 1 mL tip pipette for 3 times maximum;
 5. Centrifuge the dissociated tissues for 5 min at 100 g and discharge the medium with trypsin;
 6. Resuspend gently the cells in 1 mL of pre-warmed proliferation medium (described in page 87);
 7. Count the cells with a haemocytometer by mixing 2 μ l of cell suspension and 2 μ l of Trypan Blue, and place the total 4 μ l into a chamber of the haemocytometer;
 8. Add the cell suspension (1 mL) into a T25 flask and complete with 4 mL of pre-warmed proliferation medium;
 9. Incubate the cells for 6 days or until enough neurospheres have been created.

Appendix D

Residuals R^2 Mathematical Model of Dehydration of BC Membranes:

Figure D.1 shows the graphic of the residuals calculated for the weight loss of the samples with different dimensions. The random distribution of the points around zero in T8D8 samples indicates that this is a good model for BC weight loss. However, when the sample size is reduced, the model does not provide so good adjustment since it seems to be a certain degree of autocorrelation.

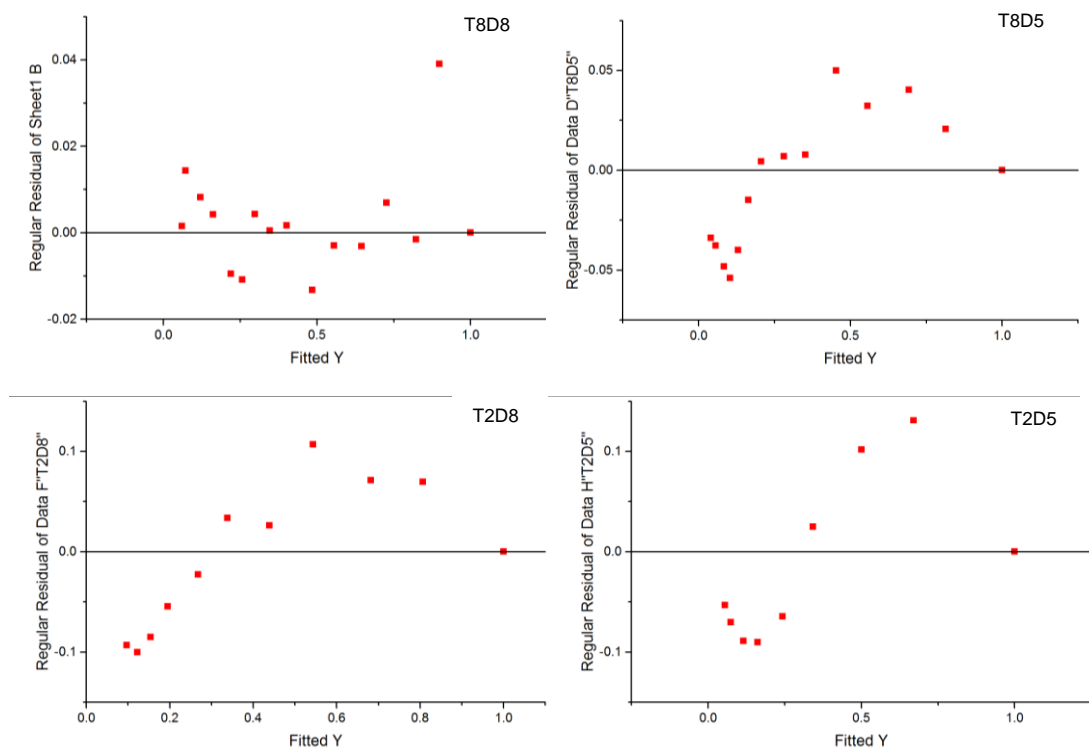


Figure D.1. Graphics of the residuals of the fitted weight loss ("Y") for each size of membrane.